The University Of Sheffield.

Modelling of active flow control devices using hybrid RANS/LES techniques

Verónica Palma González García

Supervised by Prof. Ning Qin

Department of Mechanical Engineering

The University of Sheffield

This thesis is submitted to The University of Sheffield in partial fulfilment of the requirement for the degree of

Doctor of Philosophy

August 2015

To my parents, my brother and my auntie.

To Ryan.

"Just keep swimming. Just keep swimming. Just keep swimming, swimming, swimming. What do we do? We swim, swim".

- Dory, Finding Nemo (Disney, 2003)

Abstract

The focus of the present thesis is on the effects of two active flow control devices on the periodic components of the turbulent shear layers and the Reynolds stresses. One of the main aims is to demonstrate the capability to control individual structures that are larger in scale and lower in frequency against the richness of the time and spatial scales in a turbulent boundary layer.

In order to carry out this investigation, computational fluid dynamics CFD simulations are performed. The turbulence modelling approach for the two dimensional initial cases is RANS and URANS and with regards to 3D simulations IDDES, a hybrid RANS/LES technique, is applied. The geometry for the studies is taken from experimental configurations for each case; both cases comprise a turbulent flow over a backward facing step (BFS), where separation is induced after the step edge. The results from the simulations are compared to the experimental data for both cases with and without control.

The first active flow control device is a single DBD plasma actuator located upstream of the step. The effects of quasi-steady and unsteady – or pulsated- plasma actuation using two different phenomenological models are studied. The resulting turbulent structures, Reynolds stresses, skin friction and velocity profiles are analysed applying the aforementioned models to simulate the plasma actuation. The results for quasi-steady plasma mode show very good agreement with the available experimental data and a reduction of the reattachment length which matches the experimental data is observed. Regarding modulated actuation of the DBD plasma device, three dimensional simulations were carried out and the results also showed excellent agreement of the overall behaviour flow when compared to the experimental data.

The second flow control device is a novel device known as spanwise vortex generators. It consists of a strip of magnets placed along the span of the BFS upstream of step and the device oscillates at a given frequency and amplitude. Like for the first control device, turbulent structures, Reynolds stresses, skin friction distributions and velocities are analysed and compared to the experimental measurements. A remarkable effect of the device is observed especially in the reattachment length which is considerably reduced. Experimental measurements for the baseline case were available and a comparison with such data is performed.

Acknowledgements

My foremost gratitude and thanks are for my supervisor, Professor Ning Qin, for his supervision, guidance and support throughout the completion of this thesis. I have been encouraged by him and I have had the opportunity to learn from his deep knowledge, his insightful views, enlightening ideas and wise suggestions during these four years. I have found strong motivation in his experience and scientific attitude in aerodynamics and turbulence modelling techniques which has allowed me to enrich myself in terms of rational approach, knowledge and professional attitude. All these will be always deeply appreciated.

Thanks to Prof. Qin as well for the financial support to carry out my research enjoying a PhD studentship from the Manipulation of Reynolds stress for Separation Control and Drag Reduction, EC MARS, project No. 266326 funded by the 7th RTD Framework European Programme during the first three years of my PhD studies.

Thank you to my colleagues from the Aerodynamics Group, especially thanks to Ben Hinchliffe and Raybin Yu for their help, support and friendship: I never expected to find good friends in such a competitive world but I did. Thanks to Dr. Wei Wang for her help to understand the in-house code and her patience and guidance with regards to dealing with all kind of programming issues I found during this journey. I would also like to thank her and Dr. Spirious Siouris for our work together in the MARS project.

Thanks to all the collaborators from MARS project which was the starting point of inspiration and foundation for my thesis, in particular thanks to Dr. Jordi Pons from CIMNE for his kind help and attention. I wish to thank to the experimental partners Dr. Nicola Bernard from Poitiers and Prof. Ming Xiao from Nanjing for our collaboration in this study.

I would like to remark how I appreciate all the HPC resources granted from the University of Sheffield: the lovely Iceberg HPC system and the Greengrid cluster and also the N8 HPC system, Polaris.

Thank you to my manager at Grayson Thermal Systems, Jagjit Golar, for his support and time conceded to work on the final stages of writing up this thesis.

And last but not least, my most sincere and deepest thank you to my family who have been there to help me when I struggled in the deepest valleys and to share my happiness when I reached the top of the brightest mountains. Thank you to my boyfriend, Ryan Rees, for his unconditional love and support when I was going through the hardest moments and for his joy when I was step by step succeeding. You all know I would have never got here without your love and encouragement.

Table of Contents

List of Figures

List of Tables

Nomenclature

Roman Symbols

$\mathbf{A}$	(= A_i) Vector of a surface area
$\mathbf{A_c}$	Conservative Jacobian matrix
C	A constant number
C_{DES}	A constant in DES
C_f	Coefficient of skin friction
c_ρ, c	Speed of sound
c_p	Specific heat capacity at constant pressure
C_{ROY}	Constant applied to Singh and Roy's model
c_v	Specific heat capacity at constant volume
d	Length scale in hybrid RANS/LES techniques Wall distance, the distance from a point to the nearest wall
E	Specific total energy
$\boldsymbol{E}$	Electric field
e	Electron charge
f	Flow control frequency Constants in DES Blending/damping function
F_{x0}, F_{y0}	Constants in Singh and Roy's model
$\mathbf{F}$	Vector of convective flux
$\mathbf{F_d}$	Vector of dissipation flux in the Roe scheme
$\mathbf{G}$	Vector of viscous flux
H	Specific total enthalpy or height of the step in BFS
K	Parameter in Roe's scheme
k	Specific kinematic energy or turbulence kinetic energy
k_1, k_2	Constants in Shyy's model
L	Characteristic length scale of flow

l	Length of eddies
L_{LES}	LES length scale
l_{hyb}	Hybrid length scale of turbulence and RANS average
l_{RANS}	RANS length scale
l_{turb}	Turbulence length scale
M	Mach number
$\mathbf{n}$	(= ni) Normal vector of a surface, i = 1, 2, 3
N_{face}	Face number
n_r	A random number with magnitude less than a unity
N_z	Cell number along a span
p	Fluid static pressure
$\mathbf{A_p}$	Primary Jacobian matrix
Pr	Prandtl number
$\mathbf{Q}$	Vector of primary variables, $\mathbf{Q}$ = (p, $u1$, $u2$, $u3$, T)T
$\mathbf{q}$	(= qi) Heat flux vector, i = 1, 2, 3
$\mathbf{R}$	Residual vector in the N-S equations
$\mathbf{r}$	A displacement vector form one point to another
R	The ideal gas constant for air, R = 287.04 J Kg−1 K−1
Re	Reynolds number
$\mathbf{S}$	Source term in Navier-Stokes equations
$\boldsymbol{S}$	(= S_{ij}) Rate of strain tensor, or a vector of the source term in the N-S equations
T	Fluid absolute temperature
t	Physical time
T_0	The reference temperature in the Suntherland's law, T_0 = 273.11 K, or a time interval
Δt	Physical time step
Δt*	Dimensionless time step, $\Delta t* = \Delta t/(L/U_\infty)$
T_{FT}	Flow-through time period
$\mathbf{v_g}$	Velocity vector on a moving surface

u	(= u_i) Velocity vector, i = 1, 2, 3
U_∞, U	Free stream velocity
u_n	The real normal velocity of a surface of a control volume, u_n = (**u** - **ug**) · **n**
u_τ	Friction velocity, $u_\tau = \sqrt{\nu(\partial u/\partial y)}$
u'u', v'v',w'w'	Normal Reynolds stress components
u'v', u'w', v'w'	Reynolds shear stress components
u, v, w	Instantaneous velocity components in Cartesian coordinates
V	Volume of fluid
W	Vector of conserved variables
X_R	Reattachment length after the step
x, y, z	Cartesian coordinates

Greek Symbols

α	Thermal diffusivity Coefficients in physical term discretisation using backward Euler scheme Parameter in AUSM
β	Parameter in AUSM
β_x, β_y	Dielectric constants used in Singh and Roy's model
δ	Boundary layer thickness
δ_{ij}	Kronecker's delta symbol
Δτ	Pseudo time step
Δx	Characteristic length of a control volume
ϵ	Energy dissipation rate, or a small number
ϑ	Frequency of applied AC voltage in Shyy's model
Φ_0	Applied voltaje in Singh and Roy's model
η	Kolmogorov's length scale
γ	Heat capacity ratio, $\gamma = c_p/c_v$
Γ	The transformation matrix in the preconditioning

$\mathbf{\Gamma_{nc}}$	A transition format of the transformation matrix in the preconditioning
$\varkappa$	Von Karman constant, $\varkappa = 0.41$
λ	Thermal conductivity coefficient Bulk elasticity or second coefficient of viscosity, or spacial interval between two adjacent jets
$\mathbf{\Lambda}$	$(= \lambda_k)$ Diagonal matrix of eigenvalues, $k = 1, 2, ...5$
Λ_c	Spectral radii of the convective flux
Λ_v	Spectral radii of the viscous flux
μ	Dynamic viscosity
μ_0	The reference viscosity in the Suntherland's law, $\mu 0 = 1.716 \times 10^{-5}$ m^{-1} Kg s^{-1}
ν	Kinematic viscosity
ν_t	Turbulent kinematic viscosity
$\mathbf{\Omega}$	$(= \Omega_{ij})$ Vorticity tensor
ω	Specific dissipation ratio in k- ω turbulence model
$\boldsymbol{\omega}$	$(= \omega_i)$ Vector of angular velocity
Ψ	A low-Reynolds number correction in DES and its variations
ϱ	Fluid density
σ	Van Neumann number
τ	Pseudo time
$\tau_{i,j}$	Reynolds stress tensor
$\tau_{ij}\vert_{mod}$	The modelled Reynolds stresses
$\tau_{ij}\vert_{res}$	The resolved Reynolds stresses
$\tau_{ij}\vert_{TOT}$	The total Reynolds stresses
Θ	A replacement of ϱp in the preconditioning
ε	Coefficients in the backward Euler's discretization Dissipation of turbulence kinetic energy
$\varepsilon_{i,j,k}$	$\varepsilon i,j,k$ The Levi-Civita symbol

Superscripts

$+$	Dimensionless distance, $y^+ \equiv u_\tau y/\nu$
L	The left side of a surface
M	Modelled variables
m	Time step of the pseudo time
n	Time step of the physical time
$'$	Flow fluctuation
R	The right side of a surface, or the Reynolds Averaged variable
S	Sub-grid scale filtered variable
T	Transposition of a vector or a matrix

Subscripts

exp	Experimental data
i	i = 1, 2, 3 corresponds to Cartesian coordinates, x, y, z
j	j = 1, 2, 3 corresponds to Cartesian coordinates, x, y, z
m	Measured variables in experiments

Other Symbols

$\hat{\cdot}$	Roe averaged values
$\langle\cdot\rangle$	Spatial averaged
$\bar{\cdot}$	Time averaged
$\tilde{\cdot}$	Modified variables in the S-A model
∇	Local mesh spacing
∂	Derivative operator

Acronyms

2D	Two Dimensional
3D	Three Dimensional
ALE	Arbitrary Lagranigan-Eulerian
AUSM	Advection Upstream Splitting Method
BFS	Backward Facing Step
CFD	Computational Fluid Dynamics
CFL	Courant-Friedrichs-Lewy condition or number
DBD	Dielectric Barrier Discharge
DES	Detached Eddy Simulation
DDES	Delayed Detached Eddy Simulation
DGDES	Dynamic Grid Detached Eddy Simulation in-house code
DNS	Direct Numerical Simulations
EHD	Electro-hydro-dynamic plasma force
FVM	Finite Volume Method
GCL	Geometric Conservation Law
IDDES	Improved Delayed Detached Eddy Simulation
LHS	Left Hand Side
LES	Large Eddy Simulation
MARS	Manipulation of Reynolds stress for Separation Control and Drag Reduction
MPI	Message Passing Interface platform for core's communication
N-S	Navier-Stokes
NUAA	Nanjing University of Aeronautics and Astronautics
RANS	Reynolds-Averaged Navier-Stokes
RHS	Right Hand Side
RNG	Re-Normalisation Group method for k-ε turbulence model

SGS	Sub-grid Scale
SLAU	Simple Low-dissipation Scheme of AUSM-family
SST	Shear Stress Transport turbulence model
SVG	Spanwise Vortex Generators
URANS	Unsteady Reynolds-Averaged Navier-Stokes
WMLES	Wall-Modelled Large Eddy Simulation

1 Introduction

1.1 Background and motivations

The manipulation of a flow field, widely known as flow control, by means of active or passive devices has been a subject of high importance throughout the history of Fluid Mechanics. The changes introduced in the flow are basically related to investigating their effects in flow separation control, skin friction and drag reduction, laminar to turbulent transition investigation and so on.

Numerous methods have been developed since the beginning of the XX century up to nowadays. Passive control implies the introduction of changes with regards to the variation of the geometry of the domain of the flow. On the other hand, active control includes the introduction of external energy into the flow field to change the original flow field as it will be later explained.

Drag reduction and separation control are directly related to more efficient air transportation and less emission of harmful gases into the environment. While the aerospace industry is striving to have more and more optimised designs, it is still some way away from the targets set out in the ACARE 2020 vision for 50% reduction in aircraft emissions. Separation control and drag reduction contribute directly towards this target and active flow control could play an important role in achieving it. Active flow control provides an additional dimension for further improving aircraft performance, in particular, for performance at different operational points, such as at cruise and take-off and landing. After many decades of development, the highly optimised aircraft designs make further large improvements difficult without a game changing technology such as active flow control.

Going deeper into the concept, the turbulent Reynolds stress is the most important dynamic quantity affecting the mean flow as it is responsible for a major part of the momentum transfer in a wall bounded turbulent flow. It has a direct relevance to both skin friction (for a turbulent boundary layer) and flow separation (occurs when skin friction drops to zero). The near wall region for a turbulent boundary layer can

be divided into the viscous sub-layer, where the mean viscous stress is important; and the approximately constant Reynolds stress region where the viscous stress drops to zero and the Reynolds stress peaks. As the Reynolds number increases, the peak Reynolds stress approaches the value of the viscous stress at the wall. Therefore active manipulation of the Reynolds stress can directly lead to changes in the viscous stress at the wall so as to effectively control the flow.

Active flow manipulation is directly related to control of separation and a reduction of the drag yielding to more efficient air transportation and to eco-friendlier aircraft performance reducing the emission of harmful gases to the atmosphere.

The capability to control individual flow structures that are larger in scale and have lower frequency compared to the richness of the time and spatial scales in a turbulent boundary layer will be demonstrated. This thesis analyses two novel active flow control means: a dielectric barrier discharge plasma actuator and spanwise vortex generators. To explain the basic strategy in manipulating Reynolds stresses through the dynamic components of the turbulent shear layers, it is helpful to start with the triple decomposition proposed by Reynolds and Hussain, 1972, for an instantaneous velocity, U, where

$$U = U_{avg} + \tilde{u} + u'$$

The first term on the RHS is the time averaged mean velocity. If we attempt to control this via flow control then most devices offer little gain in efficiency on a global energy basis, i.e. change in energy out is equal to energy in. The second term on the RHS is the periodic/dynamic component of the flow and for some specific flow scenarios this can be shown to be dominant in determining the flow state and characteristics. The stresses produced from this term are referred as the periodic stresses. It offers some interesting opportunities for demonstrating the way in which to deploy flow control technologies for dynamic environments (responsive environments, smart inputs and sensible control). This also implies that, for statistically steady flows where the second term disappears, artificial introduction of the periodic term may be necessary for effective control. The final term on the RHS represents the broadband "random" turbulent fluctuations from which the Reynolds

stresses are defined. Whilst direct control of the "random" components is the ultimate goal, the current project aims to investigate the control of the periodic stresses, the dynamic components of the flow, in order to manipulate the Reynolds stress for the benefit of flow control.

Different types of flow control have been widely investigated during the past two centuries [Prandtl, 1904; Schubauer and Skramstand, 1947; Gad-el-Hak and Bushnell, 1991; Choit et al., 1994; Gad-el-Hak, 1998, 2003]. As mentioned before, flow control devices can be classified into passive and active flow control devices. Passive flow control comprises changes in the geometry via the installation of devices such as the classic vortex generators which will create or destroy large turbulent structures of the flow. Active flow control, on the other hand, introduces energy into the flow field from external devices such as moving or oscillating surfaces, synthetic jets, etc., and consequently the original flow field is perturbed.

Passive devices offer a limited effectiveness on flow control as they are operational in a single or small range of operation points whereas active flow control offers a much broader possibility of development by investigating the techniques to enhance their ability to control turbulent flows in a wide variety of configurations and applications.

By understanding the interaction of the flow control devices and the resulting flow field, a deeper insight into the effectiveness of active flow control can be achieved.

Within the Manipulation of Reynolds stress for Separation Control and Drag Reduction, MARS, project an investigation of flow control devices to enhance the performance of such devices was carried out in order to achieve an improvement of aircraft performance. In this project, an active collaboration of experimental and numerical partners allowed a further understanding of a wide range of flow control devices to reduce skin friction and manipulate Reynolds stress. Two different test cases were chosen to study the effects of various flow control devices. This thesis focuses on the flow over a backward facing step, BFS, and the aforementioned investigated flow control devices were a single dielectric barrier discharge plasma actuator and spanwise vortex generators.

In order to analyse and research these devices, thanks to the development of technology during the current and past centuries, different computational techniques and tools have been developed. Therefore, the numerical investigation by means of such methods will provide a much better understanding of the effects of active flow control devices which will potentially have an application in real life, leading to development of the current devices, the introduction of new ones and optimisation of their realistic configurations. The final and ultimate motivation is the achievement of more efficient, safer and greener performance of the different means of transport in the aerospace industry.

1.2 Aims and objectives of this work

This thesis was defined and performed as a part of the MARS project hence the objectives are directly related to this project's goals. The global aims for this study can be defined as,

- To validate via simulation and comparison the implementation of a single DBD plasma actuator and spanwise vortex generators into the in-house code DGDES performing CFD URANS and IDDES simulations.
- To investigate the relation of discrete dynamic structures generated by a single DBD plasma and SVG flow control devices installed on a backward facing step flow and the configuration of these two devices.
- To simulate and understand the impact of the devices on the turbulent structures of two different cases of a flow over a BFS and their effects on the turbulent shear layer to obtain a reduction of the separation region.
- To establish the relation –if any – between the control parameters of the devices and the resulting Reynolds stress and skin friction distribution.

1.3 Outline of the thesis

In this study, several 2D RANS and URANS and 3D IDDES are performed to prove the consistency and reliability of such simulations as all of the calculations will be validated and compared to two different experimental databases. For the single DBD plasma actuator, simulations are carried out according to the setup of the experimental partner from the University of Poitiers. Secondly, the spanwise vortex generators case will be compared and simulated following the configuration from

Nanjing University of Aeronautics and Astronautics. Both experimental partners also contributed with their work for the MARS project.

A brief outline of the chapters is given here:

- **Chapter 1**: In this current chapter, the background and motivations and the objectives and aims are presented. A brief introduction to the two main chapters of this thesis is also provided.
- **Chapter 2**: The main features of turbulence and its modelling approaches and the most popular active flow control devices are described and presented.
- **Chapter 3**: A full description of the governing equations and how the flow solver DGDES works is given in this chapter. The methodology and numerical schemes are described. Moving mesh techniques and plasma models implementation into the in-house code are described.
- **Chapter 4**: The complete plasma actuation study carried out for this thesis is provided. First of all a comparison of the solver DGDES is performed against a 2D calculation using a commercial code. Then, the case from Poitiers where the plasma device was experimentally investigated is analysed. First of all, 2D study for initial Singh and Roy's model validation is carried out. Once the model is adjusted, several three dimensional studies are performed to validate the model completely. A mesh dependency study is performed for both baseline and plasma actuation cases to choose a proper mesh for the investigation. An eight million cells grid is selected for further investigation of Poitiers case as it shows closer results to the experimental data. A series of Singh and Roy's constants are then tested and compared to the data from the experimental partner and a final assessment with the final selected constant for steady and unsteady plasma actuation is shown. Final overall conclusions are also included in this chapter.
- **Chapter 5**: The second flow control device study is presented in this chapter. A description of the experimental facilities for the investigation of the spanwise vortex generators in NUAA is firstly done. The mesh for this case is the eight million cells mesh which was utilised for the DBD plasma study

as it showed very good results. Both uncontrolled and controlled cases are analysed and compared to the available experimental data. The SVG setup and simulations are then described and the analysis of the coherent structures of the turbulent flow, velocity profiles, reattachment length comparison with the baseline and experimental case is included in this chapter. The conclusions of the investigation are finally presented.

- **Chapter 6**: A final assessment of the work conducted in the thesis is given in this chapter. Achievements are discussed and several ideas and proposals for future work involving DGDES, the plasma actuator and the SVG are provided.
- **Appendix**: Two different 2D simulations, uncontrolled and controlled, were carried out to explore the skin friction distribution along the streamwise direction for the baseline and controlled cases with the spanwise vortex generators.

Finally, the **References** part contains the most relevant books and technical papers for this research.

2 Literature Review

2.1 Introduction

In this chapter the basics of turbulence and its modelling and the active flow control devices used to perform the numerical simulations carried out for the completion of this thesis will be introduced among some other flow control devices.

In order to solve the turbulent flow behaviour accurately, first of all, one must understand the nature of turbulence and its different ways of modelling. A brief explanation regarding the different available methodologies will be given, from the Reynolds Average Navier Stokes (RANS) method to the most complex, Direct Numerical Simulations or DNS. In this work the main technique for resolving turbulence was the hybrid RANS/LES procedure.

Secondly, what active flow control is and how it is been achieved will be described including the active flow control devices which have been investigated in this thesis, i.e., dielectric barrier discharge, DBD, plasma actuators and spanwise vortex generators, SVG. Only a theoretical explanation is given, its modelling and implementation in the computational code will be analysed later on in this thesis.

2.2 Turbulence: definition and modelling

2.2.1 What is turbulence

In this study, the flow was always considered turbulent therefore an explanation of its nature and main features will be given.

Turbulence is a property of a flow not of a fluid: the same fluid can produce laminar or turbulent flows depending on the flow characteristics. Also, and before going any deeper into turbulence and its characteristics, it is really important to clarify that turbulence is a continuum phenomenon: even the smallest turbulent scales are larger than molecular scales. Even though the vortices distribution in a turbulent flow is highly irregular, it is continuous.

In order to assess whether a flow is laminar or turbulent, the Reynolds number is used. This number is a non-dimensional parameter defined as the ratio of inertial to viscous forces. When Reynolds number is a small number, the flow is strongly characterised by viscous effects, therefore instabilities are suppressed by the viscosity. In fluid mechanics, a laminar flow occurs when a fluid flows in parallel layers, with no disruption between the layers. At low velocities, the fluid tends to flow without lateral mixing and adjacent layers slide past one another like a deck of playing cards. Laminar flow is characterised by high momentum diffusion and low momentum convection.

Figure 2.1 Examples of turbulence in real life

On the other hand, when a flow is characterised by a high Reynolds number, there is a high interaction between diffusive –viscous- terms and convective –inviscid- terms and the flow is remarkably rotational and irregular with an increase of instabilities as a consequence, and it is known as turbulent flow. So in reality, most of flows present in real life are turbulent, Fig. 2.1, from the smoke of a candle to the flow of a river or the wake of an airplane. All these flows are found to be highly non-linear characterised by a chaotic and stochastic behaviour of the fluid itself. The flow contains eddies which result in lateral mixing with a rapid variation of velocity and

pressure both in space and time. The properties of a turbulent flow vary in a random way. Hence, it is really difficult to provide an accurate definition for turbulence. Nevertheless, turbulence can be highly characterised by the following points:

- Irregularity: turbulent flows are very irregular. That is why turbulence is always treated statistically: a turbulent flow is unique and it will never be repeated in the exact same way in nature.

- Diffusivity: In turbulent flows, the mixing is improved due to the available supply of energy in them. Turbulent flows enhance the mixing and also increase the rate of mass, momentum and energy transports.

-Rotationality: In turbulent flows, three dimensional vortex stretching is always present and the flow has vorticity, i.e., the turbulence is always 3D rotational. Vortex stretching is responsible of the turbulence energy cascade phenomena where unsteady vortices appear and interact with each other. The stretching mechanism makes the vortices go thinner due to the volume conservation of fluid elements, therefore the larger vortices break down into smaller flow structures until these small structures are small enough so their kinetic energy is overwhelmed by the fluid's molecular viscosity and dissipated in heat form. [Batchelor, 1953; Pope, 2000]

- Energy cascade: Turbulent flows are a continuum phenomenon and they contain a wide variety of scales of motion. The energy cascade occurs from the largest scales to the smallest scales. The largest scales are responsible for the transport and generation of turbulence whereas the smallest scales dissipate the energy coming from the larger scales into internal energy in form of heat as mentioned previously. Consequently, turbulence flows can be interpreted as a superposition of eddies with a wide range of uncontrollable and non-symmetric length scales upon a mean flow. Velocities have also random fluctuations. The hierarchy from bigger eddies to the smallest ones is determined by the energy spectrum which measures the energy in the fluctuations of the velocity for each wave number. According to this, length scales are divided in three categories. In first place, the largest scales in the energy spectrum are known as integral length scales. Eddies obtain the energy from the mean flow and also from each other. They have low frequencies and large velocity fluctuations. Taylor

microscales are the intermediate scales. They pass energy from the largest scales to the smallest and they are not dissipative. And finally, the Kolmogorov length scales are the smallest scales in the spectrum. They have high frequencies and lower velocity fluctuations. In this range of the energy spectrum, the energy drain from viscous dissipation and energy input from nonlinear interaction are in balance.

- Dissipation: Turbulent flows are highly dissipative. Viscosity effects at smallest scales result in the conversion of kinetic energy of the flow into hear or internal energy. Accordingly, in order to maintain a turbulent regime a constant supply of energy is required.

2.3 Modelling turbulence

As discussed in the previous section, an exact definition for turbulence cannot be given; consequently when a simulation of a turbulent flow is going to be performed models are needed to represent the scales of the flow which cannot be resolved due to their unpredictable behaviour. In order to solve aerodynamic problems numerically, the mathematical solution of the equations of motion for fluid flow can be obtained for a wide range of different cases. Different techniques have been developed derived from Navier-Stokes equations. The computational fluid dynamics, CFD, approach chosen for a particular case depends on which accuracy the solution of the problem requires and also it depends on the high performance computing resources available in terms of computational time and cost.

A description of the main approaches will be provided in the next sections: from the less demanding Reynolds-averaged Numerical Simulation, RANS, approach to the Direct Numerical Simulation, DNS, and the approaches in between.

2.3.1 Reynolds-averaged Navier-Stokes equations Modelling (RANS)

RANS approach is the most common used to solve the real life flows by applying the statistical mean average directly to the solution: the flow is resolved in terms of time and space averaged variables only by means of the Reynolds averaging method, where every variable in the Navier-Stokes equations is decomposed in a mean quantity and its fluctuating component over time,

$$U(x_i, t) = \overline{U\,(x_i)} + u'(x_i, t) \tag{2.1}$$

This decomposition results in an equation for the average flow variables, $\overline{U\,(x_i)}$, and additional fluctuating quantities, $u'(x_i, t)$, known as Reynolds stresses. These stresses represent the momentum transfer due to the fluctuations to the mean flow. Reynolds stresses are characterised by its randomness nature and therefore, the resulting equations need to be closed by using turbulence models. RANS can be seen as an approach where turbulent scales are not resolved but all the turbulence effects on the mean flow are modelled. This approach requires less computational time and provides decent solutions of the turbulent flows in the near wall region.

However, when a not statistically stationary flow is going to be resolved, RANS does not provide an accurate solution as in this approach the flow is considered to be steady [Iaccarino, 2003]. A variation of RANS called unsteady RANS or URANS would be applied in such case. URANS introduces a new term in the variables decomposition known as phase-average or conditional statistical average term. This quantity represents the coherent behaviour in the flow dynamics. When the flow is periodic in time, an URANS simulation must be averaged over one period in order to be able to compare with time-averaged data. Despite the time dependence and large vertical structures, URANS is not a simulation of the turbulence, only of its statistics. A definition of URANS is given by Merzari et al. (2009), based on the ensemble averaging over different realisations of the flow fields. URANS is regarded as a generalised filter in both time and space with characteristic filter spatial scales and filter temporal scales.

2.3.2 Large Eddy Simulations (LES)

LES resolves the large scales of the turbulent flow and the rest of smaller scales are modelled using a subgrid scale (SGS) model which statistically affects the large scale motion of the flow. In a turbulent flow, the major part of energy and momentum transfer to the mean flow is mainly caused by the larger scales of the flow into the smaller scales; for such reason, this method turns out to be very interesting from the engineering point of view. Computationally speaking LES is more demanding than RANS but less demanding than DNS, but also it is expected to be more accurate as it

resolves the large scales directly. In LES all the scales with size smaller than the grid size are filtered and will be modelled afterwards. Filtering the Navier-Stokes equations means basically to remove eddies smaller than the filter, usually defined by the grid size. All these removed eddies will be the modelled part of LES approach and this modelling is the necessary closure for the approach. Bearing this in mind, the total velocity field will be the result of the sum of the resolved velocity field and the modelled component.

Different subgrid scales, SGS, models can be used. The first model used for LES filtering was the Smagorinski model, [Smagorinsky, 1963]. The applied constant in this model was estimated from isotropic homogeneous flows and it results in a highly dissipative model for most of real but simple flows. Later on, in order to sort this problem out Germano et al. (1991) proposed a variation to the Smagorinski model by using two filters instead of one to calculate the Smagorinski coefficient dynamically based on local transient flow fields.

In the past years, many different SGS models were proposed such as wall-adapting local eddy-viscosity model [Nicoud and Ducros, 1999], where a spatial filter related to the wall distance and cell volume was introduced and it guaranteed a zero turbulent viscosity for laminar shear flows or one of the most recent models by You and Moin (2007) who proposed a method which can be used in complex geometries.

2.3.3 Direct Numerical Simulations (DNS)

DNS is by far the most complex technique when resolving an aerodynamic problem. Direct Numerical Simulations, as its own name indicates, provides a complete description of turbulent variables and resolves Navier Stokes equations directly without any modelling. The whole range of turbulent scales, from the large scale eddies to the Kolmogorov dissipative scales, is resolved.

In order to capture all the turbulent length scales numerically, both time step and grid space sizes must be smaller than the smallest eddy sizes, the Kolmogorov scales and its characteristic time scales. DNS simulations are, therefore, highly demanding in time and computation costs. For this reason, the applicability of this technique is limited to low Reynolds number flows and other approaches such as the previously

described RANS and LES and the following described in the next sections were developed to be able to tackle the turbulent flow problems at high Reynolds numbers.

2.3.4 Hybrid RANS/LES techniques

In this section, different hybrid RANS/LES methods will be described. A deeper analysis of these approaches will be made as this work is based in hybrid RANS/LES computations. These techniques were designed to combine the best aspects of RANS and LES approaches. Regarding RANS, its best aspect taken is the near wall region/boundary layer treatments and regarding LES its features when tackling separated flows were taken for the different hybrid approaches. As discussed previously, LES requires a very fine mesh near the walls and a high computational cost, but RANS can be applied close to the wall as a feasible method at high Reynolds number cases and LES would be applied away from the walls, resolving the large scales of the flow.

Detached Eddy Simulation, DES, is one of the most widely used hybrid RANS/LES approaches. It was firstly proposed by Spalart et al (1997). It was initially developed to be applied in high Reynolds number flows where a massive separation occurs, such as aerospace and ground transportation problems.

Essentially, it *"senses"* the grid density and compares the grid spacing in all directions in order to assign the near wall region to RANS and SGS model in the rest of regions. It can be defined then as "a three-dimensional unsteady numerical solution using a single turbulence model, which functions as a subgrid-scale model in regions where the grid density is fine enough for a LES simulation and as a Reynolds-averaged model in regions where it is not" [Shur et al., 1999]. Therefore, the boundary layer would be treated by RANS and regions with massive separation would be treated by LES. The space between these two areas, known as the grey area, may be problematic as it has to be wisely decided when to switch to RANS or LES, but this issue will be addressed later in this section.

DES proposed by Spalart et al. is based in the Spalart-Allmaras one-equation turbulence model, [Spalart, 1992]. In RANS mode, the length scale, d, is defined as

the shortest distance from any point to the closest wall in RANS model. In DES, d is replaced as the minimum distance from the wall to the length proportional to the local mesh spacing, ∇,

$$d_{DES} = \min(d, C_{DES}\nabla) \tag{2.2}$$

where C_{DES} is a constant which can take different values but 0.65 is the most common. [Shur et al, 1999].

The local grid spacing will be dependent on the type of mesh: when using a structured mesh, ∇ will be the maximum grid spacing over the three directions x, y, z. If, on the other hand, an unstructured mesh is used, ∇ will be the maximum edge length connecting the centroids of the neighbouring cells. DES will be in RANS mode using Spalart-Allmaras turbulence model when $d_{DES} = d$ and will be operating in LES mode otherwise, using the Spalart-Allmaras as the subgrid scale model.

There is a problem known as the grey area in this hybrid approach. DES only depends on the grid and length scales and when a mesh refinement is performed, it may trigger to LES mode when the boundary layer is fully attached: when the grid spacing parallel to the wall is less than the boundary layer thickness, the LES method takes over as the length scale is fine enough for the detached eddy simulation to switch into a LES model from RANS mode; however, the grid spacing is partially inside the boundary layer and the resolved Reynolds stresses in LES mode do not completely replace the modelled Reynolds stresses from the RANS mode. This leads to a depletion of the stresses which in turn leads to an over prediction of the separation area producing a reduction of the skin friction computation which is not physically real, [Panguluti, 2007]. In order to solve the grey area issue, different variants of the DES were developed. A deeper explanation will be provided in the next Chapter of this thesis.

2.3.5 RANS, LES or DES?

To close section 3 of this chapter, a brief assessment of RANS, LES and DES simulations will be given. Nowadays, it is well-known that RANS performance is not able to produce accurate results when it comes to problems which imply massive separations. Due to this lack of success, researchers have applied other flow techniques to resolve the dynamics of the flow such as LES or even DNS. However, these other techniques are still computationally too expensive as it has already been commented previously in this work.

Regarding LES, it was shown by Spalart et al. (1997), that for flow simulations in which Reynolds number was about 10^7 a grid of 10^{11} cells would be necessary in order to obtain a sufficiently accurate solution of the problem. Although computers are in constant development, a grid of such number of cells is still too expensive in the sense of computational requirements. This situation gave place to the beginning of development of hybrid RANS/LES techniques.

Breuer et al. (2003) made a comparison of three different approaches such as DES, RANS and LES for a separated flow around a flat plate at high incidence was carried out.

It was soon shown that RANS due to its time-averaged characteristics has got a lack of resolving the unsteadiness of massively separated flows and then it can be concluded that RANS is not able to produce reliable results as it lacks to reproduce the unsteady characteristics of the separated flow field. LES, on the other hand, provides good and reliable results when facing separated flows as it resolves the larger structures of the flow and models the smaller turbulent structures after the SGS filter is applied. However, and it is worth mentioning it again, it is an expensive computational technique as it demands a really fine mesh to predict the resolved turbulent structures. And finally, DES the hybrid RANS/LES method combines the best features of the two approaches: near the walls within the boundary the flow is solved via RANS and a turbulence model such as Spalart-Allmaras is applied and in the rest of the domain where the bigger turbulent structures are present a LES simulation is performed. Therefore, the application of hybrid RANS/LES is appropriate and recommended when the problem to solve consists of unsteady

turbulent flows with large separation regions. The two cases analysed in this thesis accomplish such condition: when the flow of air moves over the backward facing step, a massive separated bubble occurs after the step and in order to achieve accurate and computationally affordable simulations, a variant of DES was the approach chosen for this study. Furthermore, certain issue –the aforementioned grey area problem- was found when using DES, but this will be addressed in Chapter 3, in which a deep analysis of DES and its variants is provided.

2.4 Flow Control

As a basic concept, it is well-known that drag reduction and separation control are directly related to more efficient air transport with a lower emission of harmful gases into the environment. Separation control and drag reduction contribute directly towards greener aircraft efficiencies and active flow control plays a vital role in achieving it.

Reynolds stress is the dynamic quantity responsible for transferring the majority of momentum in a wall bounded flow. Hence, it has a direct influence into both skin friction and flow separation. It was said in the introduction of this thesis that in the viscous sublayer of the turbulent boundary layer in the near wall region the mean viscous stress is definitely more influent on the flow than the Reynolds stresses and in the constant Reynolds stress region, the viscous stress drops to zero and the Reynolds stress peaks. Increasing the value of the Reynolds number, the peak Reynolds stress approaches the value of the viscous stress at the wall. For this reason, an active manipulation of the Reynolds stress can directly lead to changes in the viscous stress at the wall so as to flow control.

However, there is a lack of current understanding of the inter-relationship between the various flow control devices such as piezoelectric oscillating surfaces, synthetic jets, dielectric plasma actuators, oscillating vortex generators, etc., and the Reynolds stresses in the flow field these devices generate. A better understanding can potentially and significantly improve the effectiveness of flow control as the Reynolds stresses are closely related to the flow behaviour at the surface for effective separation control or drag reduction. A variety of control devices are available and new ones are invented but which one for what purpose is an open question yet to be

fully answered. The vast majority of previous work so far has focused on the introduction of changes to the mean flow that resulted in changes to the Reynolds stress. In this thesis, it is proposed to reverse that process and consider the long term goal of controlling dynamic structures that then influence the Reynolds stress that in turn change the mean flow. This radical approach recognises that we are still away to implement the concept at flight scales but it is an aim to establish a first important step towards this ultimate ambition. The focus of the present section will be on describing the different types of actuators and the types of flow control. The complete explanation of these two active flow control devices investigated in this thesis is fully contained in Chapter 4 and Chapter 5 where their effects on the discrete dynamic components of the turbulent shear layer and the Reynolds stress will be discussed.

There are two possible ways of flow control: passive and active. Passive control implies no input of energy into the flow but it is modified by placing fixed physical devices into the geometry such as vortex generators, riblets, surface roughness, bumps, cavities and so on. The other kind of control is known as active control, where there is an external form of energy introduced into the flow to manipulate its state. All the work carried out in this thesis is only focused on active flow control.

With regards to actuation, active flow control devices are nowadays locally applied and their only requirement is an electrical power input. Seifert et al (1996) showed that separation control using periodic addition of momentum at frequencies a bit higher than the natural frequency of the vortex shedding of a flow could produce similar performance improvement as when a steady blowing actuation is applied.

There are different types of active flow control devices such as,

- Piezoelectric actuators: These devices are installed normally along the spanwise direction of the surface of the studied geometry, such an aerofoil or wall. Fig. 2.2 shows the configuration of piezoelectric actuators in a wind tunnel at the University of Manchester for the MARS project, [Wang et al, 2014]. The piezoelectric actuators are excited by an electric current and as a result the device behaves as an oscillating surface enhancing the flow

momentum in the boundary layer and suppressing the turbulent intensity. [Wang, 2013].

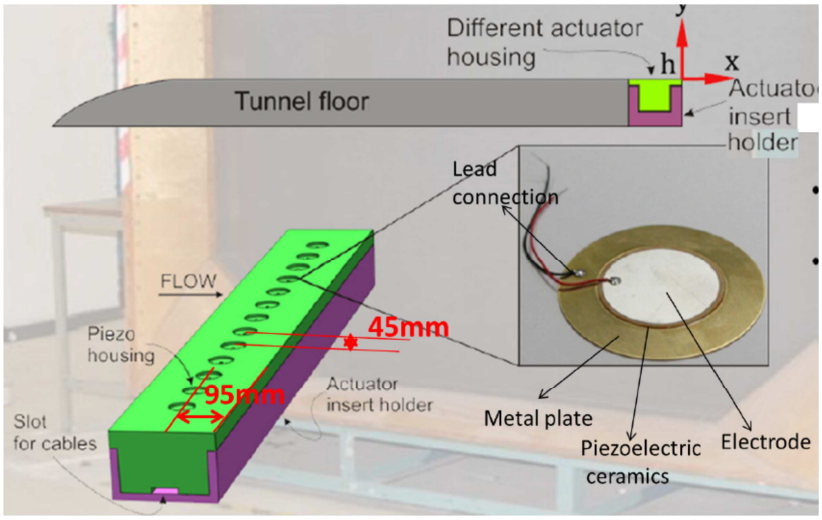

Figure 2.2 Piezoelectric actuators at the University of Manchester wind tunnel.

- Suction/blowing devices: These devices consist of nozzles where either constant suction or blowing affecting the boundary layer is performed. Different suction/blowing velocities will produce different effects on the air flow. Different configurations and locations of the nozzles/slots/slits in a backward facing step can be found in the literature. The slots can also have different shapes such as rectangular, triangular/serrated [Uruba et al, 2007] or circular shapes. With regards to the location of the slots, a typical and widely seen configuration is at the bottom of the step on the vertical wall, Fig.2.4(A),[Sakuraba et al 2004; Uruba et al, 2007; Bakhshan et al, 2012]; also the slit is typically located at the edge of the step, Fig.2.4(B) [Chung, 1996; Yoshioka et al, 1999, 2001; Dejoan, 2004; Mehrez, 2010]. Multichannel cases can also be configured such as the location of multiple slots along the vertical wall of the step, Fig.2.4(C) [Emami-Naeini et al, 2006].

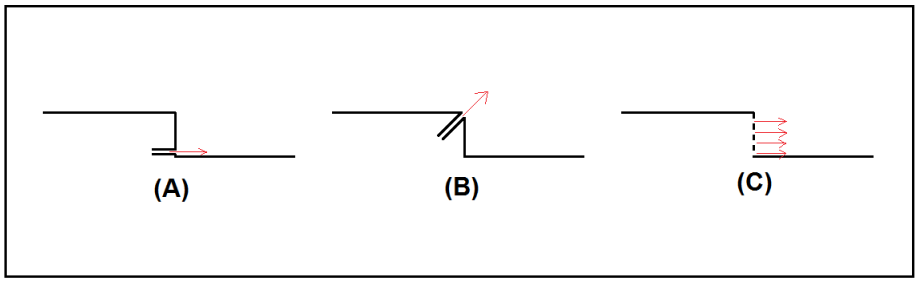

Figure 2.3 Suction/blowing locations on a backward facing step. (A) Bottom corner of step; (B) Step edge; (C) Multichannels along vertical wall of step

- Synthetic jets: These devices are a sort of zero-net mass flux jets which means the working fluid is used without any external mass source or sink. This actuator consists of a series of orifices placed along the streamwise direction of the geometry. Inside the nozzles there is a chamber where there is a membrane oscillating at a certain amplitude and frequency generating a suction/blowing effect at the exit of the nozzle, Fig 2.4, [Ming, 2013]. Another configuration could be where instead of a membrane oscillating, there is a moving wall producing the synthetic jet effects [Cadirci and Gunes, 2012]. Different simulations have been carried out with regards to this device. The jet direction can be in the streamwise direction of the flow [Valencia, 1997; Dandois et al, 2007] or perpendicular to the flow direction, [Okada et al, 2009].

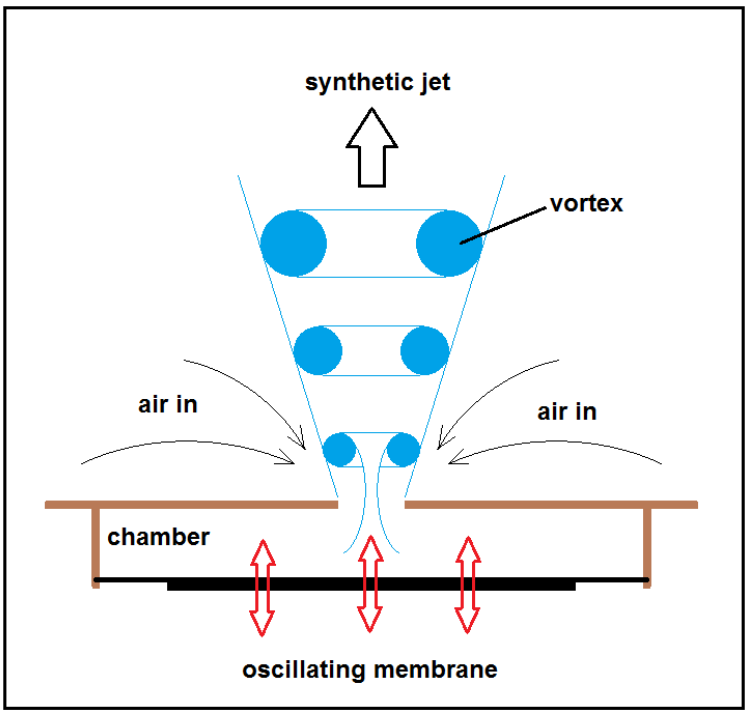

Figure 2.4 Schematics of synthetic jet

- Dielectric barrier plasma actuators: A DBD plasma actuator, Fig. 2.5, is a device where a high voltage is applied between two electrodes placed on both sides –top and bottom- of a dielectric material and as a result a weakly ionized region above the dielectric material appears, [Moreau, 2007; Enloe et al, 2004]. The interaction between the generated plasma and the surrounding air results in the production of a local wall tangential jet flow caused by the addition of momentum into the air flow. Different configurations of the DBD actuators are available and have been studied [Dinef, 2009; Erfani, 2015; Forte et al, 2007] however, in this thesis, the analysis is carried out based on an experimental investigation and this configuration is then analysed later on in Chapter 4.

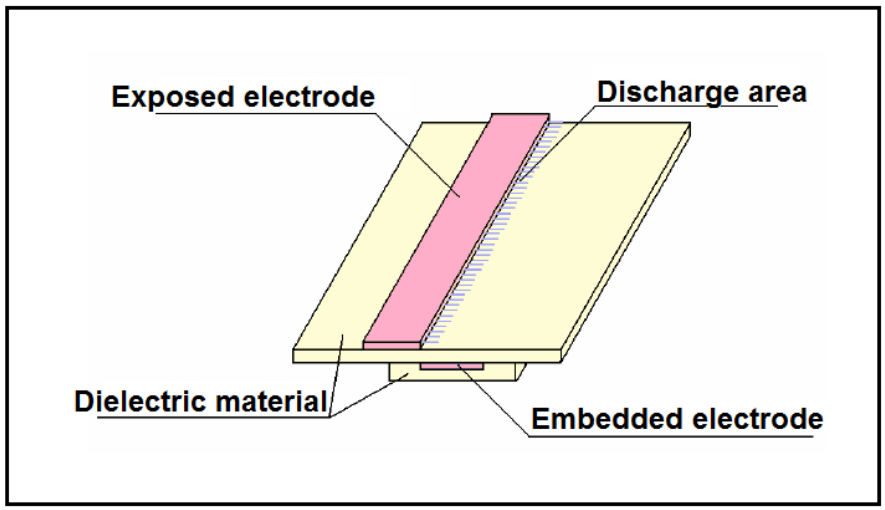

Figure 2.5 Schematics of a DBD plasma actuator

- Oscillating vortex generators: In this work, the oscillating vortex generators consist of a strip of magnets located along the span of the geometry. Alternative current is then applied to this strip and as a consequence the strip oscillates at a certain given amplitude and frequency, introducing turbulent fluctuations into the mean flow. The implementation and effects of the spanwise vortex generators are further investigated in Chapter 3 and mainly in Chapter 5. Similar studies have been performed using water as shown by Inaoka et al, 2004. In the experiment it was observed that the larger the amplitude of the oscillation is larger disturbances are introduced and a better heat transfer was captured. In this thesis, heat transfer was not analysed as the main objective is to analyse the effects of the device on the physics of the flow but the influence of the actuator frequency on the flow field was clearly identified. Weier et al, 2011 performed experimental work using electromagnetic excitation in the streamwise direction of the flow over a backward facing step to reduce the reattachment length after the step. In this thesis, the magnet's oscillation was induced in the normal direction of the flow and the strip is not located exactly at the wall but slightly above. Further review of this device is shown in Chapter 5 where the spanwise vortex generator was fully studied and analysed.

The investigation, both computational and experimental, of these devices can provide a further understanding of their capabilities to control different types of flows and in the latest stage of the study, their application in real-life cases. This is one of the aims of this thesis.

To finish this section, a brief description of how active control is performed is given. Active control can be classified under two categories: open loop control or closed loop control, [Gad-el Hak, 2007]. Open loop control means there is no feedback from the output to assess whether the system has achieved the desired objective and the controller calculates the input into a given system using only the current state and the model of the system. On the other hand, in a closed loop control, the flow state is measured in real time and the measurement is used as feedback which will be used by different models to re-adjust the flow state to a desired state. The challenging side of the closed loop control is to find or develop a proper model to achieve the desired flow conditions. In order to measure the current flow state, sensors are placed in the domain or geometry and they will measure a specific parameter which is the one to be controlled. Then, the control device will change its actuation according to the results of the model given the sensors measurements: the flow is being continuously modified in real time in an interactive way. A further and deeper explanation of the control methods can be found at Gad-el Hak (2007).

2.5 Summary

A description of turbulence and the basic description of its modelling have been done in this chapter. An assessment of the different techniques to solve aerodynamic problems numerically has been presented, too. When the problem to resolve is a complex unsteady flow DNS, LES and the different hybrid RANS/LES techniques are the most adequate; however, their application is limited by the computational resources due to the high demand of such resources. Hybrid RANS/LES approaches are the least demanding of the three aforementioned methods, having a reduced mesh resolution requirement. As this study focuses on active flow control devices which potentially will be applied in the aerospace industry, hybrid RANS/LES will be the most appropriate method to carry out the research.

The major challenge regarding hybrid RANS/LES techniques is to model correctly the so-called grey area, the area of transition between RANS and LE; however, different proposals to tackle this issue have been investigated in the recent years. A deeper discussion of such proposals will be made in the next chapter where all the methodology is explained thoroughly.

Finally what flow control is and the most popular devices for active flow control have been discussed. Passive flow control implies only the introduction of a change in the geometry which presents fewer challenges to model, computationally speaking. On the other hand, active flow control devices presents a more challenging situation when they are simulated using hybrid RANS/LES techniques as these devices imply moving parts, active introduction of momentum in the flow or modification of large structures in the flow that needs to be properly modelled. This challenge is overcome in this thesis showing successful simulations of two active flow control devices.

Regarding plasma control, the main challenge was to implement properly the model producing realistic results. The assumptions when the models were implemented will be stated later on in the thesis. In the case of synthetic vortex generators, simulations shown to be much more computationally demanding as the reading of the nodes of the mesh needs to be performed and updated every single time step because there is a moving boundary. This will lead to much longer computational time requirements.

3 Methodology: Governing equations and numerical schemes

3.1 Introduction

In this chapter, the flow solver will be analysed in detail, providing its assumptions, limitations, governing equations, temporal and spatial discretisation methods, dynamic mesh treatment techniques and implementation of turbulence and active flow control models.

3.2 Flow solver: description of analytical methods

In the field of aerodynamics, there are several ways to analyse a given flow field: experimental methods such as wind tunnel experiments; computational fluid dynamics –CFD – analysis or mathematical descriptions.

Computational fluid dynamics is a tool developed along the past two centuries. It is defined as a series of numerical methods and algorithms to resolve the flow field produced by a certain fluid in a given domain. The simulations are carried out using more or less computational resources depending on the demands of every case under investigation. CFD techniques are in constant development but this tool has already shown its capability to provide reliable results for a very wide range of different cases which has led to a very extensive use of it both in Academic and Industrial fields. In order to perform a CFD calculation, several requirements need to be fulfilled such as a definition of a domain and of a set of boundary conditions which will limit that domain. CFD comprises different approaches to produce realistic and reliable results and it also requires of a mathematical discretisation technique in order to achieve the final numerical solution of the flow. This project focuses in turbulence modelling and other related numerical issues such as modelling of the flow control devices to enable realistic configurations by means of CFD simulations.

Regarding turbulence modelling, DES (hybrid of RANS and LES) calculations are performed to be able to represent the contribution of the periodic velocity fluctuations to the total Reynolds stresses due to the random and periodic velocity fluctuations.

For that, the CFD code used in this work is called Dynamic Grid Detached Eddy Simulation, DGDES. DGDES is an in-house solver developed at the University of Sheffield based on the conservation form of the basic governing equations of fluid dynamics (Navier-Stokes equations) in their integral form. It is completely developed using the FORTRAN 90 programming language and the OpenMPI library to run parallel jobs. The code is designed based on the cell centred Finite Volume Method (FVM) formulation and unstructured grid data architecture for flexibility in handling complex geometries. It includes the Roe's flux difference splitting and Advection Upstream Splitting Method (AUSM) schemes for inviscid flux calculations. In addition, it incorporates the central difference for viscous flux calculations and higher order spatial accuracy is achieved by piecewise linear reconstructions. Through time integrations, it uses dual time formulations with first and second order backward Euler schemes in physical time term and Runge-Kutta four stage for time-stepping in the pseudo-time term. The dynamic grid related quantities are updated every physical time step by invoking the subroutines implemented with the geometry similarity, the spring analogy, geometrical similarity and the Delaunay mapping moving grid algorithms. The solver is parallelised applying the Message Passing Interface (MPI) platform for communications between processors, which is essential for the three dimensional unsteady flow problems. A one-equation Spalart-Allmaras turbulent model based on the transport equation for turbulent viscosity was employed to model the effect of the small and unresolved turbulent scales within the DES methodology and its variants.

3.3 Assumptions

Several assumptions were made when DGDES was developed which means the application of the solver will be limited to a certain range of aerodynamic cases. These main assumptions will be described in the following paragraphs.

First of all, the fluid is considered as a continuum. The fluid is continuous and indivisible. By making this assumption, when it comes to discretisation techniques, the volumes can be resolved by the application of differential calculus but still assuring these volumes are much larger than atoms or molecules but small enough to be considered microscopic.

The second assumption is that the fluid is considered to be compressible, Newtonian and isotropic. In a Newtonian fluid, the viscous tensor and the strain rate are related by a constant, i.e., there is a linear dependency between these terms. Besides, isotropy is a property of a fluid in which its mechanical properties are the same along any direction, and applying this concept to a Newtonian fluid, the result is a reduction of the 9x9=81 linear coefficients of the stress tensor, $\bar{\tau}$, to just two coefficients: μ, known as the coefficient of dynamic viscosity; and λ is the second coefficient of the viscosity known as bulk elasticity or dilatational viscosity. Taking into account these statements, the shear stress of a Newtonian fluid can be expressed as,

$$\tau_{ij} = \mu\left(\frac{\partial u_i}{\partial x_j} + \frac{\partial u_j}{\partial x_i}\right) + \lambda\left(\frac{\partial u_l}{\partial x_l}\right) \tag{3.1}$$

The molecular viscosity μ and the bulk elasticity λ are related by the Stokes hypothesis,

$$\lambda = \frac{2}{3}\mu \tag{3.2}$$

In this study Sutherland's law is applied to the molecular viscosity so it is a function of the temperature according to this law's equation,

$$\frac{\mu}{\mu_0} = \left(\frac{T}{T_0}\right)^{\frac{3}{2}} \frac{T_0 + 110.56}{T + 110.56} \tag{3.3}$$

where the subscript "0" denotes the reference state, i.e., at temperature $T_0 = 273.11\text{K}$, the molecular viscosity $\mu_0 = 1.716 \times 10^{-5}$ kg m^{-1}s^{-1}.

In third place, the fluid is considered to follow the equation for an ideal gas and it also behaves as a calorically perfect gas. The equation of an ideal gas is,

$$pV = mRT \xrightarrow{\rho=\frac{m}{V}} \rho = \frac{p}{RT} \tag{3.4}$$

Where R is the ideal gas constant for air and it is equal to $R = 287.04$ $Jkg^{-1}K^{-1}$.

In DGDES it is assumed that the air follows the Fourier's law of heat conduction,

$$q_j = -\kappa \frac{\partial T}{\partial x_j} \tag{3.5}$$

Where q_j is the heat flux in the j direction and κ is is the thermal conductivity coefficient and can be expressed as a function of the molecular viscosity as follows,

$$\kappa = \frac{c_p}{Pr}\mu \tag{3.6}$$

In which c_p is the specific heat at constant pressure and Pr is the Prandtl number.

Furthermore, total energy E is related to the enthalpy H and total temperature T of the fluid by

$$E = H - \frac{p}{\rho} \tag{3.7}$$

$$H = c_p T + \frac{1}{2}(u^2 + v^2 + w^2) \tag{3.8}$$

Finally, the Navier-Stokes equations in DGDES will be discretised and treated according to the previous stated assumptions.

3.4 Governing Equations

The fundamental governing equations in DGDES are as aforementioned the unsteady Navier-Stokes equations. Their formulation and discretisation will be described in this section and its subsections.

3.4.1 Unsteady Navier Stokes Equation

For a given control volume domain, V, limited by the surface ∂V the three dimensional Navier-Stokes equations in their integral form are written as,

$$\frac{\partial}{\partial V}\iiint_V \boldsymbol{W}dV + \iint_{\partial V}(\boldsymbol{F}-\boldsymbol{G})\cdot\boldsymbol{n}dA = \int_{\partial V}\boldsymbol{S}\partial V \tag{3.9}$$

Where the conserved variables, $\boldsymbol{W}$, inviscid flux $\boldsymbol{F}$ and viscous flux $\boldsymbol{G}$ are given by,

$$\boldsymbol{W} = \begin{pmatrix} \rho \\ \rho u \\ \rho v \\ \rho w \\ \rho E \end{pmatrix} \tag{3.10}$$

$$\boldsymbol{F} = \begin{pmatrix} \boldsymbol{F}_x \\ \boldsymbol{F}_y \\ \boldsymbol{F}_z \end{pmatrix} \tag{3.11}$$

$$\boldsymbol{G} = \begin{pmatrix} \boldsymbol{G}_x \\ \boldsymbol{G}_y \\ \boldsymbol{G}_z \end{pmatrix} \tag{3.12}$$

And ρ is the density of the fluid, u, v, w are the three Cartesian velocity components in $x, y\ z$ directions respectively and E is the total energy expressed per unit mass. $\boldsymbol{F}_x, \boldsymbol{F}_y, \boldsymbol{F}_z$ are the components of $\boldsymbol{F}$ in the three dimensions and $\boldsymbol{G}_x, \boldsymbol{G}_y, \boldsymbol{G}_z$ are also the three components of the viscous flux in $x, y\ z$ directions. Every component can be written as follows,

$$\boldsymbol{F_x} = \begin{pmatrix} \rho u \\ \rho uu + p \\ \rho uv \\ \rho uw \\ \rho uE + p \end{pmatrix} \quad \boldsymbol{G}_x = \begin{pmatrix} 0 \\ \tau_{xx} \\ \tau_{xy} \\ \tau_{xz} \\ u\tau_{xx} + v\tau_{xy} + w\tau_{xz} - q_x \end{pmatrix} \tag{3.13}$$

$$\boldsymbol{F_y} = \begin{pmatrix} \rho v \\ \rho vu + p \\ \rho vv \\ \rho vw \\ \rho vE + p \end{pmatrix} \quad \boldsymbol{G}_y = \begin{pmatrix} 0 \\ \tau_{yx} \\ \tau_{yy} \\ \tau_{yz} \\ u\tau_{yx} + v\tau_{yy} + w\tau_{yz} - q_y \end{pmatrix} \tag{3.14}$$

$$\boldsymbol{F_z} = \begin{pmatrix} \rho w \\ \rho wu + p \\ \rho wv \\ \rho ww \\ \rho wE + p \end{pmatrix} \quad \boldsymbol{G}_z = \begin{pmatrix} 0 \\ \tau_{zx} \\ \tau_{zy} \\ \tau_{zz} \\ u\tau_{zx} + v\tau_{zy} + w\tau_{zz} - q_z \end{pmatrix} \tag{3.15}$$

Where $\boldsymbol{p}$ is the static pressure, q_i are the three components of the heat flux vector and τ_{ij} are the components of the viscous stress $\boldsymbol{\tau}$ which are,

$$\tau_{xx} = 2\mu\frac{\partial u}{\partial x} + \lambda\left(\frac{\partial u}{\partial x} + \frac{\partial v}{\partial y} + \frac{\partial w}{\partial z}\right) \tag{3.16}$$

$$\tau_{yy} = 2\mu\frac{\partial v}{\partial y} + \lambda\left(\frac{\partial u}{\partial x} + \frac{\partial v}{\partial y} + \frac{\partial w}{\partial z}\right) \tag{3.17}$$

$$\tau_{zz} = 2\mu\frac{\partial w}{\partial z} + \lambda\left(\frac{\partial u}{\partial x} + \frac{\partial v}{\partial y} + \frac{\partial w}{\partial z}\right) \tag{3.18}$$

$$\tau_{xy} = \mu\left(\frac{\partial u}{\partial y} + \frac{\partial v}{\partial x}\right) = \tau_{yx} \tag{3.19}$$

$$\tau_{yz} = \mu\left(\frac{\partial v}{\partial z} + \frac{\partial w}{\partial y}\right) = \tau_{zy} \tag{3.20}$$

$$\tau_{zx} = \mu\left(\frac{\partial w}{\partial x} + \frac{\partial u}{\partial w}\right) = \tau_{xz} \tag{3.21}$$

The RHS term of the Navier-Stokes equations (3.9) is the source term. It comprises all the rest of body forces acting on the fluid such as gravity, magnetic fields, etc.

3.4.2 Arbitrary Lagrangian Eulerian formulation

The Arbitrary Lagrangian Eulerian, ALE, formulation was firstly developed by Noh [Noh, 1964] and it has been widely used when the boundaries of the flow move during a simulation. In fact, it is a frequent approach when a deformation response or distortion of a material structure or a fluid system is to be analysed.

In this thesis, one of the two active flow control devices investigated comprises the analysis of the unsteady fluid flow which spanwise vortex generators will produce. Therefore, as one of boundaries in the domain is moving, ALE formulation will be used taking the advantage of its simplicity and flexibility.

The word arbitrary in ALE indicates that the flow could be looked at as either Lagrangian or Eulerian or anywhere between these two classical descriptions of motion and it combines the best advantages of both methods. In a pure Lagrangian description of a medium, each particle which belongs to this medium is tracked as an individual particle; on the other hand in an Eulerian approach the computational domain is fixed and all the particles will move with respect to this fixed reference system. So, in ALE the computational mesh can move and each node will be treated in a Lagrangian way whereas if one of the domain boundaries moves it can also be treated in an Eulerian way during numerical computations.

To reflect this principle into the Navier-Stokes equations, a re-formulation will be done. The previous control volume domain V and its boundary surface ∂V will now be time-dependent: $V = V(t)$ and $\partial V = \partial V(t)$. If the velocity of the moving surface, call it $\partial V(t)$, is written as $\boldsymbol{v}_g = (u_g, v_g, w_g)$, then the inviscid flux vector in

the integral form of the Navier-Stokes will be affected and can be expressed as follows after recasting its terms in convective and pressure terms,

$$\boldsymbol{F}_x = \rho(u - u_g)\begin{pmatrix}1\\u\\v\\w\\E\end{pmatrix} + p\begin{pmatrix}0\\1\\0\\0\\u\end{pmatrix} \tag{3.22}$$

$$\boldsymbol{F}_y = \rho(v - v_g)\begin{pmatrix}1\\u\\v\\w\\E\end{pmatrix} + p\begin{pmatrix}0\\0\\1\\0\\v\end{pmatrix} \tag{3.23}$$

$$\boldsymbol{F}_z = \rho(w - w_g)\begin{pmatrix}1\\u\\v\\w\\E\end{pmatrix} + p\begin{pmatrix}0\\0\\0\\1\\w\end{pmatrix} \tag{3.24}$$

And it is clearly seen that only the convective terms are affected by the movement of the surface because the net flux through it has changed.

When $\boldsymbol{v}_g = 0$, Navier-Stokes equations are purely Eulerian and when $\boldsymbol{v}_g \neq 0$ the Navier-Stokes equations are solved according to the ALE formulation.

3.4.3 Discretisation of Time

Generally, two methods have been used along history of CFD to solve the time dependent Navier-Stokes equations. First one is called pressure-based method, wherein a pressure correction is applied in order to solve the equations in a segregated manner. This method is mainly applied when an incompressible flow at low Reynolds number is analysed. The second method is density-based, and it employs a series of time-marching procedures to solve the governing equations using either explicit or implicit methods. It was developed in order to be able to solve compressible flows. However, there could be a case where a mixed of compressible

and incompressible flow is simulated and in such case, a preconditioning technique [Durrani, 2009] must be applied in order to solve the governing equations by means of a density-based solver.

3.4.3.1 Dual time stepping

The alteration of the governing equations caused by the application of the preconditioning matrix changes the temporal behaviour of the flow leading to a lack of accuracy of the governing equations. For unsteady flows the loss of accuracy needs to be carefully treated. In order to tackle this issue, the physical time is kept and a pseudo-time step which will not affect the original physical time step is introduced into the equations. The main idea of this dual time stepping approach [Jameson, 2007] is to achieve a steady state by using different numerical methods such as a multistage Runge-Kutta scheme.

The physical time step is determined by the flow physics and it will be discretised using a backward Euler scheme. In every physical time step, the pseudo time step will converge to a steady state or to a satisfactory level and then the physical time will march one step forward and so on. According to this, it is important to determine the maximum number of pseudo time iterations for each single physical time step before the latter moves to the next physical time step. The solver will continue running until the maximum number of iterations and/or the convergence criterion in pseudo time step loop previously specified in the initialization is reached.

As it has already been mentioned, preconditioning destroyed the physical time accuracy as it is an artificial temporal term introduced in the original Navier-Stokes equations. The way this issue is tackled will be explained next.

The Navier-Stokes equations with dual time stepping are expressed as,

$$\frac{\partial}{\partial t}\iiint_V \boldsymbol{W}\partial V + \frac{\partial}{\partial \tau}\iiint_V \boldsymbol{W}\partial V + \iint_{\partial V}(\boldsymbol{F}-\boldsymbol{G})\cdot\boldsymbol{n}dA = \int_V \boldsymbol{S}dV \tag{3.25}$$

Where t is the physical time and τ is the pseudo time step.

Leaving the pseudo time term on the left hand side of the equation it will read as,

$$\frac{\partial}{\partial \tau}\int_V \boldsymbol{W}\partial V = -\left[\frac{\partial}{\partial t}\iiint_V \boldsymbol{W}\partial V + \iint_{\partial V}(\boldsymbol{F}-\boldsymbol{G})\cdot\boldsymbol{n}dA\right] + \int_V \boldsymbol{S}dV \tag{3.26}$$

According to what has already been discussed, the pseudo time step, which is the inner iteration in the dual time stepping (LHS of the previous equation) should drop to zero inside every physical time step – so that this term does not affect the latter-, called the outer loop in the dual time stepping treatment. After this is accomplished, the Navier-Stokes equations are recovered and the physical time step will advance.

Finally, in DGDES the preconditioning matrix multiplies the pseudo time derivative term rather than the physical time. In this way, the destruction of the physical time because of the preconditioning is reduced and the Navier-Stokes equations will be finally written in terms of the conservative and primitive variables as follows,

$$\frac{\partial}{\partial t}\iiint_V \boldsymbol{W}\partial V + \boldsymbol{\Gamma}\frac{\partial}{\partial \tau}\iiint_V \boldsymbol{Q}\partial V + \iint_{\partial V}(\boldsymbol{F}-\boldsymbol{G})\cdot\boldsymbol{n}dA = \int_V \boldsymbol{S}dV \tag{3.27}$$

Where $\boldsymbol{Q}$ is the primitive variable matrix given by,

$$\boldsymbol{Q} = \begin{pmatrix} p \\ u \\ v \\ w \\ T \end{pmatrix} \tag{3.28}$$

And $\boldsymbol{\Gamma}$ is the preconditioning matrix.

3.4.3.2 Physical time step

The physical time step is the outer iteration in the dual stepping method as already mentioned in the previous subsection. This time step is treated as a part of the residual so equation (3.27) can be written as,

$$\boldsymbol{\Gamma}\frac{\partial}{\partial\tau}\iiint_V \boldsymbol{Q}\partial V = -\boldsymbol{R} - \frac{\partial}{\partial t}\iiint_V \boldsymbol{W}\partial V \tag{3.29}$$

In which $\boldsymbol{R}$ is the residual,

$$\boldsymbol{R} = \iint_{\partial V} (\boldsymbol{F}-\boldsymbol{G})\cdot\boldsymbol{n}dA - \int_V \boldsymbol{S}dV \tag{3.30}$$

Applying the ALE formulation to this equation it can be expressed as,

$$\boldsymbol{\Gamma}\iiint_V \frac{\partial}{\partial\tau}\boldsymbol{Q}\partial V = -\boldsymbol{R} - \iiint_V \frac{\partial}{\partial t}\boldsymbol{W}\partial V \tag{3.31}$$

If the integrals are replaced by summations, the resulting equation is semi-discretised,

$$\boldsymbol{\Gamma}\frac{\partial(\boldsymbol{Q}V)}{\partial\tau} = -\boldsymbol{R} - \frac{\partial(\boldsymbol{W}V)}{\partial t} \tag{3.32}$$

Most time stepping methods for steady flows can be applied to solve the semi-discretised equation. One of these methods is the second-order backward Euler's method. It is applied to the physical time step term in the (3.32) equation becoming,

$$\left[\boldsymbol{\Gamma}\frac{\partial(\boldsymbol{Q}V)}{\partial\tau}\right]^n = -\boldsymbol{R}^n - \frac{\alpha_0(\boldsymbol{W}V)^n + \alpha_1(\boldsymbol{W}V)^{n-1} + \alpha_2(\boldsymbol{W}V)^{n-2}}{\Delta t} \tag{3.33}$$

where α_i are coefficients determined by the time accuracy order and their values can be seen at Table 3.1. The superscripts $n, n-1, n-2$ are the current, last and previous to the last time steps, respectively.

Accuracy order	α_0	α_1	α_2
First order	1	0	1
Second order	3/2	-2	1/2

Table 3.1 α_i values for the first and second order temporal accuracies

In order to resolve the pseudo time derivative for a fixed physical time step, n, explicit or implicit techniques can be applied.

If an explicit scheme is applied to the pseudo time term (3.33) equation will be,

$$\left[\boldsymbol{\Gamma}^m \frac{(\Delta Q)^m V}{\Delta\tau}\right]^n = -\boldsymbol{R}^{m-1,n} - \frac{\alpha_0(\boldsymbol{W}V)^{m,n} + \alpha_1(\boldsymbol{W}V)^{n-1} + \alpha_2(\boldsymbol{W}V)^{n-2}}{\Delta t} \quad (3.34)$$

In which the superscripts $m, m-1$ denote the current and previous pseudo time steps, respectively.

In order to address instability problems regarding the physical time step –as it can be seen in (3.34), when Δt tends to zero the RHS term dramatically increases- it will be discretised using implicit methods, [Melson et al., 1993].

3.4.3.3 Pseudo Time Stepping

In the present work, a fourth order Runge-Kutta scheme [Jameson et al., 1981] is applied to the pseudo time step term.

As stated previously, the inner iteration within every pseudo time step should get close to a steady state before the physical time step marches to a next time step. However and especially when facing problems where unsteady flows are going to be present as those investigated in this thesis, the number of required time steps until

the residual drops to an acceptable small value may be a large number –up to thousands- and it needs to be carefully selected.

3.4.3.4 Determination of time step sizes

In CFD there are always numerical stability issues associated with the explicit temporal schemes. For this reason, the size of the time step has to be restricted to be within a certain limit.

Regarding the physical time step, it has already been mentioned it could be determined by the flow physics. In general, the smaller the physical time step, the faster the convergence rate in the pseudo time step but larger computational time will be required. On the other hand, when the physical time step size is increased, the unsteady characteristics of the flow may not be captured although the computational time to perform a simulation is considerably reduced. When solving flows where there is a dominant frequency, such as the flow control device frequency or if it is the case where a vortex shedding is going to occur, the physical time step must be small enough to capture these frequencies and to obtain enough time steps within every period to properly capture the unsteady phenomena which is taking place in the flow.

When it comes to the pseudo time step size, as an explicit temporal scheme was applied, the size of this step size is determined by the Courant-Friedrichs-Lewy (CFL) condition, [Blazek, 2001].

This condition has been applied for Euler and Navier-Stokes solvers using explicit time scheme. The pseudo time step size $\Delta\tau$ is then a function of the CFL number,

$$\Delta\tau = \frac{CFL\,\Delta x}{\lambda_{max}} \tag{3.35}$$

where Δx is the local grid spacing and λ_{max} is the maximum eigenvalue of the system.

For viscous flow problems, Navier-Stokes equations behave like a diffusive equation, therefore another condition is included in addition to the CFL condition. Hence, a Van Neumann condition is applied to limit the time step size as follows,

$$\Delta\tau = \frac{\sigma\,\Delta x^2}{\nu} \tag{3.36}$$

where σ is the Van Neumann number and ν is the kinematic viscosity, $\nu = \mu/\rho$.

In DGDES both CFL and Van Neumann equations are integrated so the use of unstructured meshes is permitted within the solver. Consequently, the pseudo time step size is described as,

$$\Delta\tau = \frac{CFL\,V}{\sum_{i=1}^{nfaces}(\lambda_i^{inv} + \lambda_i^{vis})A_i} \tag{3.37}$$

Where V is the cell volume and $\lambda_i^{inv}, \lambda_i^{vis}$ are given by,

$$\begin{cases} \lambda_i^{inv} = \left|(\boldsymbol{v} - \boldsymbol{v}_g)\cdot \boldsymbol{n}_i\right| + c_i \\ \lambda_i^{vis} = \dfrac{\mu}{\rho|\Delta \boldsymbol{r}_i|} \end{cases} \tag{3.38}$$

Where $\boldsymbol{v}_g$ is the grid velocity as in the ALE formulation, $\boldsymbol{n}_i$ is the face unit normal vector, c_i is the speed of sound; and $\Delta\boldsymbol{r}_i$ is the inter cell centroid across face i.

3.4.4 Finite Volume Spatial Discretization

DGDES is a finite volume solver, which means the domain is divided in individual cells where the conservative and primary variables are stored at the same location, the cell centroid in this case as the code has got implemented a cell-centred scheme. The solver can handle complex geometries and both structured and/or unstructured meshes. Regarding the convective flux variables, the schemes are upwind methods and for the viscous flux calculations, central difference schemes are applied.

3.4.4.1 Discretisation of inviscid flux

3.4.4.1.1 Roe's flux difference splitting scheme

Roe's flux difference splitting scheme [Roe, 1981] is a widely used upwind scheme in the fluid dynamics field [Weiss, Smith, 1998; Wilcox, 1998; Frink, 1991]. In this method the linearised Riemann problem is solved directly [Toro, 1997].

The discrete inviscid flux vector, $\boldsymbol{F}$, is decomposed into the summation of a central term plus a dissipation term,

$$\boldsymbol{F} = \boldsymbol{F}_{central} + \boldsymbol{F}_{dis} \tag{3.39}$$

The central term is normally calculated by averaging the convective fluxes at the "left" and "right" sides of the cell face as,

$$\boldsymbol{F}_{central} \cdot \boldsymbol{n} = \frac{1}{2}(\boldsymbol{F}_c\rfloor_L + \boldsymbol{F}_c\rfloor_R) \cdot \boldsymbol{n} \tag{3.40}$$

And the dissipation term is written as

$$\boldsymbol{F}_{dis} = -\frac{1}{2}|\boldsymbol{A}|\Delta\boldsymbol{W} \tag{3.41}$$

Where $\boldsymbol{A}$ is the conservative jacobian in the normal direction $\partial \boldsymbol{F}_n / \partial \boldsymbol{W}$ and $\Delta(\cdot) = (\cdot)_R - (\cdot)_L$, the difference of the variables at the right and left sides.

In order to express $|\boldsymbol{A}|\Delta\boldsymbol{W}$ in the primitive form, the following change is made,

$$|\boldsymbol{A}|\Delta\boldsymbol{W} = \underbrace{|\boldsymbol{A}|\frac{\partial \boldsymbol{W}}{\partial \boldsymbol{Q}}}_{|\boldsymbol{A_p}|}\Delta\boldsymbol{Q} = |\boldsymbol{A_p}|\Delta\boldsymbol{Q} \tag{3.42}$$

And the dissipation term then becomes,

$$\boldsymbol{F}_{dis} = -\frac{1}{2}\left|\boldsymbol{A}_{\boldsymbol{p}}\right|\Delta\boldsymbol{Q} \tag{3.43}$$

The primitive Jacobian $\left|\boldsymbol{A}_{\boldsymbol{p}}\right|$ is given by the following expression,

$$\left|\boldsymbol{A}_{\boldsymbol{p}}\right| = \widehat{\boldsymbol{R}}\left|\widehat{\boldsymbol{\Lambda}}\right|\left(\widehat{\boldsymbol{R}}\right)^{-1} \tag{3.44}$$

Where $\hat{\cdot}$ stands for the Roe's averaged values at the interface and $\widehat{\boldsymbol{R}}$ is the right eigenvector matrix of $\partial\boldsymbol{F}/\partial\boldsymbol{Q}$ and $\widehat{\boldsymbol{\Lambda}}$ is the diagonal matrix in which

$$\hat{\lambda}_{1,2,3} = \hat{v}_n,\ \hat{\lambda}_4 = \hat{v}_n + \hat{c} \quad \text{and} \quad \hat{\lambda}_5 = \hat{v}_n - \hat{c} \tag{3.45}$$

where v_n is the normal velocity on the surface: $v_n = (\boldsymbol{v} - \boldsymbol{v}_g)\cdot\boldsymbol{n}$.

The resultant dissipation term is rearranged and expressed in the following form according to Liu (1989),

$$\boldsymbol{F}_{dis} = -\frac{1}{2}\left[\left|\hat{\lambda}_1\right|\cdot\begin{pmatrix}\Delta\rho\\ \Delta(\rho\boldsymbol{v})\\ \Delta(\rho E)\end{pmatrix} + \delta U\begin{pmatrix}\hat{\rho}\\ \hat{\rho}\hat{\boldsymbol{v}}\\ \hat{\rho}\hat{H}\end{pmatrix} + \delta p\begin{pmatrix}0\\ \boldsymbol{n}\\ \hat{v}_n\end{pmatrix}\right] \tag{3.46}$$

with

$$\delta U = \frac{\hat{\lambda}^+ - \left|\hat{\lambda}_1\right|}{\hat{\rho}\hat{a}^2}\cdot\Delta p + \frac{\hat{\lambda}^-}{\hat{a}}\Delta v_n \tag{3.47}$$

$$\delta p = \frac{\hat{\lambda}^-}{\hat{c}}\cdot\Delta p\left(\hat{\lambda}^+ - \left|\hat{\lambda}_1\right|\right)\cdot\hat{\rho}\cdot\Delta v_n \tag{3.48}$$

And $\hat{\lambda}^{+}$ and $\hat{\lambda}^{-}$ are defined as

$$\hat{\lambda}^{+} = \frac{1}{2}\left(|\hat{\lambda}_4| + |\hat{\lambda}_5|\right) = \begin{cases} \hat{a} & \text{if subsonic} \\ v_n & \text{if supersonic} \end{cases} \tag{3.49}$$

$$\hat{\lambda}^{-} = \frac{1}{2}\left(|\hat{\lambda}_4| - |\hat{\lambda}_5|\right) = \begin{cases} v_n & \text{if subsonic} \\ \hat{a} & \text{if supersonic} \end{cases} \tag{3.50}$$

As seen in (3.46) the numerical dissipation is expressed as a summation of three terms. The first term is described as the effect of upwinding the convective variables [Weiss, 1995]. The second term is responsible to ensure the pressure-velocity coupling and the third term is a modification to the pressure at the interface having an important role with regards to accuracy [Li, 2009].

In (3.46) the variables on the interface are the Roe-averaged values defined as,

$$\hat{\rho} = \sqrt{\rho_L + \rho_R} \tag{3.51}$$

$$\hat{\boldsymbol{v}} = \frac{\sqrt{\rho_L}\boldsymbol{v}_L + \sqrt{\rho_R}\boldsymbol{v}_R}{\sqrt{\rho_L} + \sqrt{\rho_R}} \tag{3.52}$$

$$\hat{H} = \frac{\sqrt{\rho_L}H_L + \sqrt{\rho_R}H_R}{\sqrt{\rho_L} + \sqrt{\rho_R}} \tag{3.53}$$

The Roe's scheme, however, may violate the entropy condition as it may occur the case where there is no dissipation, for example when a sonic expansion takes place and Roe's solver will propagate unphysical entropy. Harten, [Harten, 1984] and Liou and Van Leer, [Liou and Van Leer, 1988] developed a entropy scheme which introduces a modification into the eigenvalues as,

$$|\hat{\lambda}_{new}| = \begin{cases} \dfrac{\hat{\lambda}^2{}_{old} + \varepsilon^2}{2\varepsilon}, & \text{if } |\hat{\lambda}_{old}| < \varepsilon \\ |\hat{\lambda}_{old}|, & \text{otherwise} \end{cases} \tag{3.54}$$

Where ε is defined as,

$$\varepsilon = K \max(\lambda_R - \lambda_L, 0) \tag{3.55}$$

The parameter K is given the value $K = 2$ in this study.

The entropy fix allows the shock expansion to dissipate and completely disappear in the computational domain, producing more physically meaningful computational solutions. A low dissipation approach, SLAU, can be found at Wang, 2013.

3.4.4.1.2 AUSM flux splitting scheme

The Advection Upstream Splitting Method scheme was already implemented in the code. It combines the efficiency of flux vector splitting and the accuracy of flux-difference splitting Liou et al., 1993 developed this mathematical scheme and its variants. [Liou and Van Leer, 1988, 2003] Considering the inviscid terms of the Navier-Stokes equations and rewriting the inviscid flux on face i and separating convective terms from pressure terms,

$$\boldsymbol{F}_i \cdot \boldsymbol{n} = \rho(\boldsymbol{v} - \boldsymbol{v}_g) \cdot \boldsymbol{n} \begin{pmatrix} 1 \\ u \\ v \\ w \\ H \end{pmatrix} + p \begin{pmatrix} 0 \\ \boldsymbol{n} \\ 0 \end{pmatrix} \triangleq \dot{m}\psi + p\phi \tag{3.56}$$

Where $\dot{m} = \rho(\boldsymbol{v} - \boldsymbol{v}_g) \cdot \boldsymbol{n}$

AUSM scheme is generally described in an upwind form:

$$(\boldsymbol{F}_i \cdot \boldsymbol{n})_{1/2} = \dot{m}_{1/2} \begin{cases} \psi_L \; if \; \dot{m}_{\frac{1}{2}} > 0, \\ \psi_R \; otherwise \end{cases} + p_{1/2}\phi \tag{3.57}$$

Where $\dot{m}_{1/2}$ and $p_{1/2}$ are expressed as,

$$\dot{m}_{\frac{1}{2}} = c_{\frac{1}{2}} M_{\frac{1}{2}} \begin{cases} \rho_L & if\ M_{\frac{1}{2}} > 0 \\ \rho_R & \text{otherwise} \end{cases} \tag{3.58}$$

And $c_{\frac{1}{2}}$ is the interface sound speed and $M_{\frac{1}{2}}$ is the splitting Mach number:

$$M_{1/2} = \boldsymbol{\mathcal{M}}^{+}_{(m)}(M_L) + \boldsymbol{\mathcal{M}}^{-}_{(m)}(M_R) \tag{3.59}$$

And the splitting pressure is written as,

$$p_{1/2} = \boldsymbol{\mathcal{P}}^{+}_{(n)}(M_L)p_L + \boldsymbol{\mathcal{P}}^{-}_{(n)}(M_R)p_R \tag{3.60}$$

The subscript ½ indicates the variable has got the interface quantity on face *i* and L and R stand for left and right sides, respectively. The Mach numbers M_L and M_R are defined as,

$$\begin{cases} M_L = \dfrac{\left(\boldsymbol{v} - \boldsymbol{v}_g\right)_L \cdot \boldsymbol{n}}{c_{\frac{1}{2}}} \\ M_R = \dfrac{\left(\boldsymbol{v} - \boldsymbol{v}_g\right)_R \cdot \boldsymbol{n}}{c_{\frac{1}{2}}} \end{cases} \tag{3.61}$$

The rest of the elements in the equations represent polynomial functions of different degrees: $\boldsymbol{\mathcal{M}}^{\pm}_{(m)}$of degree m=1, 2 and 4 and $\boldsymbol{\mathcal{P}}^{\pm}_{(m)}$ of degree n=5.

$$\boldsymbol{\mathcal{M}}^{\pm}_{(1)}(M) = \frac{1}{2}(M \pm |M|) \tag{3.62}$$

$$\boldsymbol{\mathcal{M}}^{\pm}_{(2)}(M) = \pm\frac{1}{4}(M \pm 1)^2 \tag{3.63}$$

$$\mathcal{M}_{(m)}^{\pm}(M) = \begin{cases} \mathcal{M}_{(1)}^{\pm} \;\; if \; |M| \geq 1 \\ \mathcal{M}_{(2)}^{\pm}\left(1 \mp 16\beta \mathcal{M}_{(2)}^{\pm}\right) \;\; \text{otherwise} \end{cases} \tag{3.64}$$

$$\mathcal{P}_{(m)}^{\pm} = \begin{cases} \frac{1}{M}\mathcal{M}_{(1)}^{\pm} \;\; if \; |M| \geq 1 \\ \mathcal{M}_{(2)}^{\pm}\left[\pm 2 - M\right) \mp 16\alpha M \mathcal{M}_{(2)}^{\mp}\right] \text{otherwise} \end{cases} \tag{3.65}$$

Finally, parameters α and β are set to be 1/8 and 3/16 respectively.

AUSM scheme generates better shock capabilities than the previously discussed Roe's scheme and it also inherits the simplicity of flux-vector splitting techniques.

3.4.4.2 Discretisation of viscous flux

The discretisation of the viscous terms is basically the calculation of the variables $p, v \; and \; T$ and their gradients at the interface. A simple central scheme can be used to obtain the variables on the interface of the left and right cells as follows,

$$\varphi_{\frac{1}{2}} = \frac{1}{2}(\varphi_L + \varphi_R) \tag{3.66}$$

In which φ represents any of the aforementioned variables stored at the cell centres.

This central difference is, as one can easily see, an arithmetic average. For meshes with good quality, this discretisation is adopted as less calculation is required.

In the solver DGDES, the variables are stored in the cell centres. Several methods are applied to calculate the approximate values of all variables on the face and also the higher order reconstruction of the data is fully provided at Xia, 2005.

3.5 Hybrid RANS/LES formulation

3.5.1 Introduction

This section of Chapter 3 is crucial, as the hybrid RANS/LES techniques and the turbulence model applied in each of them will be fully described.

Back in section **3.5 RANS, LES or DES?**, it was stated why a hybrid RANS/LES approach has been adopted in all the studies carried out in this thesis: hybrid RANS/LES techniques combine the advantages of RANS and LES. RANS advantages are present in the near wall region, where LES mesh requirements are highly demanding therefore computational resources are saved by using RANS in this area. On the other hand, LES advantages lean on its capabilities to resolve the large turbulent structures of the flow which occur in the regions away from walls.

Before explaining the hybrid RANS/LES method and its turbulence approach implemented in DGDES, several definitions and three main assumptions will be explained in the following paragraphs.

First of all, definitions of mean rate of the strain tensor and the vorticity tensor will be given. From the general state of deformation of flowing fluids theory, the deformation tensor can be expressed as,

$$\frac{\partial u_i}{\partial x_j} \equiv \frac{1}{2}\left(\frac{\partial u_i}{\partial x_j} + \frac{\partial u_j}{\partial x_i}\right) + \frac{1}{2}\left(\frac{\partial u_i}{\partial x_j} - \frac{\partial u_j}{\partial x_i}\right) = S_{ij} + \Omega_{ij} \qquad (3.67)$$

S_{ij} is defined as the rate of strain tensor and Ω_{ij} is defined as the vorticity tensor. The rate of strain tensor is also known as the rate of deformation tensor and every component of the vorticity tensor is related to the angular velocity vector, $\boldsymbol{\omega}$ as follows, [Schlichting, 1979],

$$\boldsymbol{\omega} = \frac{1}{2}\nabla \times \boldsymbol{\Omega} \qquad (3.68)$$

Bearing those definitions in mind, the assumptions will now be discussed:

1) The relation of the Reynolds/subgrid scale stresses and the mean/filtered velocity gradients through the eddy viscosity is achieved by the application of the Boussinesq hypothesis to both RANS and LES approaches.

Recalling Chapter 2, it was explained that due to the application of averaging to the Navier-Stokes equations, new variables appeared and they needed to be addressed somehow in order to close the system of equations. This is known as the closure problem which needs to be solved. In order to close the equations, turbulence models are applied and they are able to relate Reynolds stresses –the resulting term containing the fluctuating part of the variables when Navier-Stokes equations are averaged- with the rest of variables. One of the solutions for the closure problem is the Boussinesq hypothesis [Boussinesq, 1897]. It relates turbulence stresses to the mean flow via a new concept called eddy viscosity, which describes the momentum transfer due to turbulent eddies.

$$-\overline{u'_i u'_j} = 2\nu_t S_{ij} - \frac{2}{3} k \delta_{ij} \tag{3.69}$$

where S_{ij} is the mean rate of the strain tensor, ν_t is the aforementioned turbulent eddy viscosity, k is the turbulent kinetic energy and δ_{ij} is the Kronecker's delta.

2) Instead of using filters to achieve the hybrid RANS/LES methods, hybrid of RANS and LES models are applied.

The type of averaging used for RANS is time average whereas in LES, the averaging is spatial, as a spatial filter is applied to make the distinction between the larger structures from the smaller. From a physical point of view, the sizes of the eddies are related to their duration in time as well as it is the cascade of energy, so a combination of both types of averaging from RANS and LES although lacking theoretical fundamentals will make such combination feasible and physically reasonable. So, as a conclusion, a hybrid combination of RANS/LES models/variables is carried out in DGDES as it has also been done in most of commercial CFD codes.

3) Regarding the implicit filter for LES, spatial filter and differentiation is assumed to be commutative.

This assumption means the following: for time-averaging in RANS,

$$\overline{\frac{\partial(\overline{\rho u_i u_j})}{\partial x_j}} = \frac{\partial(\overline{\rho u_i u_j})}{\partial x_j} \tag{3.70}$$

So it can be seen time average and the differential commute. However, this assumption is not true for spatial averaging, i.e., LES: the spatial average and the differential calculus do not commute except, as stated at Pope, (2001): if the spatial filter is uniform in space, such filter and the differential can commute. In DGDES it is always assumed this way, always commutative.

To end up this introduction, all the hybrid RANS/LES variants implemented in DGDES are based on the one-equation model Spalart-Allmaras (S-A), firstly published at 1992, [Spalart, 1992]. It will be explained next, previous to the full description of the three hybrid RANS/LES methods available in DGDES: DES, DDES and iDDES.

3.5.2 Turbulence model for hybrid RANS/LES techniques

In aerodynamics, the Spalart-Allmaras, S-A, model is one of the most widely applied approaches. As it was mentioned earlier, it is a one-equation model which consists of a partial differential transport equation for the eddy viscosity. The governing equation was derived by "using empiricism and arguments of dimensional analysis, Galilean invariance and selective dependence on the molecular viscosity."

S-A model has got a series of good advantages with respect to other turbulence models. The first advantange is that S-A is local which means the solution at one point is independent from the solution at any other point; this gives the model the ability to be compatible with any type of grid, i.e., two or three dimensional and structured or unstructured meshes. It was also proved that S-A produces faster convergence to a steady state than other two-equation models such as k-ε model. In Spalart-Allmaras model, wall and free stream boundary conditions are trivial and

regarding laminar-turbulent transition, it is made in a smooth manner at the points where the user has specified transition has to occur. Finally, this model predicts satisfactorily boundary layers in the presence of pressure gradients.

The Spalart-Allmaras model consists, as mentioned before, of a one-equation for the transport of a modified kinetic viscosity, $\tilde{\nu}$,

$$\underbrace{\frac{D\tilde{\nu}}{Dt}}_{\substack{1)Material\\ derivative}} = \underbrace{c_{b1}[1-f_{t2}]\tilde{S}\tilde{\nu}}_{\substack{2)Production\\ terms}} + \underbrace{\frac{1}{\sigma}\left[\nabla\left((\nu+\tilde{\nu})\nabla\tilde{\nu}\right)+c_{b2}(\nabla\tilde{\nu}^2)\right]}_{\substack{3)Diffusion\\ terms}} - \underbrace{\left[c_{w1}f_w-\frac{c_{b1}}{\kappa^2}f_{t2}\right]\left[\frac{\tilde{\nu}}{d}\right]^2}_{\substack{4)Destruction\\ terms}} + \underbrace{f_{t1}\Delta U^2}_{5)Tripping\ term} \tag{3.71}$$

On the left hand side of the equation, there is the material derivative of the turbulent kinetic viscosity which is equal to the temporal derivative plus the convective term as follows,

$$\frac{D\tilde{\nu}}{Dt} = \underbrace{\frac{\partial\tilde{\nu}}{\partial t}}_{\substack{time\\ derivative}} + \underbrace{\frac{\partial(\tilde{\nu}u_i)}{\partial x_i}}_{\substack{convective\\ term}} \tag{3.72}$$

The right hand side of the transport equation of the turbulent viscosity comprises the production terms, the diffusion terms, the destruction terms and the tripping terms. Production terms are

$$Production = \underbrace{c_{b1}\tilde{S}\tilde{\nu}}_{(1)} - \underbrace{f_{t2}\tilde{S}\tilde{\nu}}_{(2)} \tag{3.73}$$

composed by a basic production term, (1), and the laminar limitation on production term(2). The subscript "b" stands for basic and subscript "t" stands for trip. The modified eddy viscosity $\tilde{\nu} = \frac{\nu_t}{f_{v1}}$ was introduced to resolve the buffer layer and the viscous sub-layer so that its transport behaves linearly near the wall. $\tilde{\nu}$ will be equal to the turbulent viscosity, ν_t, everywhere except in the viscous region. This was achieved by introducing a damping function near the wall,

$$f_{v1} = \frac{\chi^3}{\chi^3 + {c_{v1}}^3} \tag{3.74}$$

$$\text{with } \chi = \frac{\tilde{\nu}}{\nu} \tag{3.75}$$

And the "*v*" subscript stands for viscous in this case and $c_{v1} = 7.1$. In both terms, the scalar norm of the deformation tensor, $S = \sqrt{2S_{ij}S_{ij}}$, was replaced by $\tilde{S}$ in order to maintain its log layer behaviour all the way to the wall,

$$\tilde{S} \equiv S + \frac{\tilde{\nu}}{\kappa^2 d^2} f_{v2} \tag{3.76}$$

$$\text{with} \quad f_{v2} = 1 - \frac{\chi}{1 + \chi f_{v1}} \tag{3.77}$$

where d is the distance to the wall and $\kappa = 0.41$ is the von Karman constant. Regarding term (2) in equation (3.73), $f_{t2}\tilde{S}\tilde{\nu}$, it was again introduced to deal with laminar flows and flow transition with tripping,

$$f_{t2} = c_{t3}\exp(-c_{t4}\chi^2) \tag{3.78}$$

And c_{t3} and c_{t4} are constants which take 1.1 and 2.0, respectively.

The second term of the RHS of the S-A equation (3.71) is the diffusion terms. It includes the conservative and the non-conservative diffusion terms,

$$Diffusion = \underbrace{\frac{1}{\sigma}\left[\nabla\left((\nu+\tilde{\nu})\nabla\tilde{\nu}\right)\right]}_{(3)} + \underbrace{\frac{1}{\sigma}\left[c_{b2}(\nabla\tilde{\nu}^2)\right]}_{(4)} \tag{3.79}$$

Where σ would correspond to the traditional Prandtl number but in this case it is equal to $2/3$ and $c_{b2} = 0.622$. The term denoted by (3) in equation (3.79) is the conservative diffusion and term (4) is the non-conservative diffusion term. Term (3) is a spatial derivative of the modified turbulent kinematic viscosity; this can be seen when rearranging the term as follows,

$$\frac{1}{\sigma}\left[\nabla\left((\nu+\tilde{\nu})\nabla\tilde{\nu}\right)\right] = \frac{1}{\sigma}\frac{\partial}{\partial x_i}\left[(\nu+\tilde{\nu})\frac{\partial\tilde{\nu}}{\partial x_i}\right] \tag{3.80}$$

On the other hand, term (4) breaks the conservation of the integral as its own name indicates. This term involves the first derivatives introduced by Spalart and Allmaras in their paper [Spalart, 1992] through an analogy to other two-equation models.

Going back to the transport equation of $\tilde{\nu}$, the third term in (3.71) includes the destruction terms,

$$Destruction = \underbrace{c_{w1}f_w\left[\frac{\tilde{\nu}}{d}\right]^2}_{(5)} - \underbrace{\frac{c_{b1}}{\kappa^2}f_{t2}\left[\frac{\tilde{\nu}}{d}\right]^2}_{(6)} \tag{3.81}$$

Where the subscript "w" refers to wall and term (5) in (3.81) $c_{w1}f_w\left[\frac{\tilde{\nu}}{d}\right]^2$ is the destruction term at the wall and f_w is a function which controls the damping of the modified eddy viscosity from outside of the boundary layer to the wall; it is based on algebraic models and in Spalart-Allmaras model takes the following form,

$$f_w(r) = g\left[\frac{1+c_{w3}^6}{g^6+c_{w3}^6}\right]^{1/6}, \quad g = r + c_{w2}(r^6 - r) \tag{3.82}$$

where $c_{w3} = 2.0$ and $c_{w2} = 0.3$. And r is defined as $r \equiv \frac{\tilde{\nu}}{\tilde{S}\kappa^2 d^2}$, the ratio of the modelled mixing length to the wall distance.

This term includes the wall distance d to reduce the values of the eddy viscosity in the log layer and in the laminar sub-layer. Term (6) in (3.81), on the other hand, is an optional term which was introduced in the equation in order to deal with the production of $\tilde{\nu}$ in the case of a laminar flow.

Finally, the last term in S-A transport equation (3.71) is known as the trip term which was introduced to tackle the transition problem: it is a source term added to the equation in order to produce a smooth transition compatible with any grid. This term is non-zero in regions where the transition is desired and it should not extend outside of the boundary layer,

$$Trip = f_{t1}\Delta U^2 \tag{3.83}$$

$$\text{with} \quad f_{t1} = c_{t1} g_t \exp\left(-c_{t2}\frac{\omega_t^2}{(\Delta U)^2}(d^2 + g_t^2 d_t^2)\right) \tag{3.84}$$

Where the factor $g_t \equiv \min\left(0.1, \frac{\Delta U}{\omega_t \Delta x}\right)$ and it guarantees that the trip term is non-zero over several stream wise stations. Δx is the grid spacing along the wall at the trip. Furthermore, f_{t1} is a function which comprises the domain of influence of the trip; in it, $c_{t1} = 1.0$ and $c_{t2} = 2.0$. The parameter ω_t is the magnitude of the vorticity at the trip point.

The presence of tripping terms in the transport equation of Spalart-Allmaras was necessary as one needs to have control over laminar regions of shear layer keeping flow laminar where desired and also making the transition to take place when desired.

3.5.3 Hybrid RANS/LES techniques in DGDES

In DGDES, three hybrid RANS/LES methods are available. One variant is the original DES from 1997; later on delayed DES, DDES, was implemented and finally improved DDES, iDDES was included for the code. The most applied turbulence models for these hybrid techniques are the Spalart-Allmaras model and also the SST model [Menter, 1994]. However, it has been said before in DGDES, S-A model was adopted to implement the hybrid RANS/LES approaches.

3.5.3.1 DES

This approach was briefly explained back in **Chapter 2**, section **3.4**. DES97 or just DES was initially proposed by Spalart et all based on their original model [Spalart, 1992]. In RANS mode, the length scale, d, is defined as the shortest distance from any point to the closest wall in RANS model. In DES, d is replaced as the minimum distance from the wall to length proportional to the local mesh spacing, ∇,

$$d_{DES} = \min(d, C_{DES}\nabla) \tag{3.85}$$

Where C_{DES} is a constant which takes the value of 0.65, chosen from the energy spectra decay in isotropic turbulence, [Shur et al., 1999]. The grid spacing ∇ depends on the type of mesh. Shur et al (2008) proposed it to be defined as the largest dimension of the local grid cell,

$$\nabla = \max(\nabla_i) \tag{3.86}$$

where $i = 1, 2, 3$, is the three directions in space. This form is the most suitable for structured grid, where ∇_i would be the largest length of a cell edge. However, when dealing when unstructured grid, ∇_i will be defined as follows,

$$\nabla_i = max|\Delta r_{i,n}| \tag{3.87}$$

which will be: for the local cell referred as to i, the local grid spacing is the maximum distance between the cell centroid and all the cell's neighbours centroids. Note that if the mesh is structured, ∇_i will still be the largest cell edge and this equation

$$\nabla = \max(\nabla_i) \tag{3.88}$$

is still perfectly correct.

3.5.3.2 DDES

The previous approach, DES, only takes into account the distance to the wall and the grid spacing when switching from RANS to LES or vice versa. However, a very fine mesh in the near wall region may switch from RANS to LES within still attached boundary layer areas. The resolved Reynolds stresses may not be replacing the modelled Reynolds stress due to lack of mesh resolution or because of delays of instabilities generation and this may lead to a premature separation of the flow. In order to prevent this from happening, delayed DES or DDES was proposed by Spalart et al. in 2006 providing a dynamic transition between RANS/LES. In this new version of DES they used a blending function as those applied by Menter and Kuntz to the SST model, [Menter, 2004]. The distance to the wall was therefore re-defined introducing a blending function which depends on instantaneous fields,

$$d_{DDES} = \min[d, (1 - f_d)d + f_d C_{DES}\nabla] \tag{3.89}$$

Where f_d is the aforementioned blending function defined as

$$f_d \equiv 1 - tanh[(C_1 r_d)^{C_2}] \tag{3.90}$$

r_d, in which "*d*" subscript refers to delayed, is defined as

$$r_d = \frac{\nu_t + \nu}{\sqrt{U_{i,j}U_{i,j}}\kappa^2 d^2} \tag{3.91}$$

The constants C_1 and C_2 are 8.0 and 3.0 for the original formulation of DDES; κ is the von Karman constant and d is the distance to the wall. The blending function will be in the range of (0, 1) and the transition of RANS mode, i.e., $f_d = 0$, to LES mode, $f_d = 1$, will be more or less smoother depending on the values of the constants C_1 and C_2, [Gritskevich et al, 2012]. In the S-A model, $\nu_t + \nu = \tilde{\nu}$

So, the introduction of the blending function has created important changes in the definition of the distance to the wall: without the function, the model is the previous variant, DES and with it, it does not only depend on the distance to the wall and grid spacing but also on the eddy viscosity field. The advantages DDES brought can be sum up as follows: the model is now able to detect whether a point is inside a boundary layer or not by judging the value of r_d. If separation then occurs, the blending function increasy abruptly from 0 to 1 and LES takes over faster than DES did and the grey area [Panguluri, 2007] is then narrower when applying DDES rather than DES.

3.5.3.3 iDDES

Improved DDES was developed by Shur et al. in 2008. It was aimed at wall modelling in LES, improving the original DES model. Such improvements have got empirical character providing a huge increase of the resolved turbulence near the wall and providing an adjustment to the resolved log layer and the modelled log layer which is the solution to the grey area issue also known as the log layer mismatch. In DDES, the switch from/to RANS/LES depended on, apart from distance to wall and grid spacing, the eddy viscosity field; iDDES ensures the switch no matter whether the simulation has or has not got initial turbulent content by introducing a new definition of the sub-grid scale and a coordination of two different branches as explained next: basically, when there is no inflow turbulence information, iDDES behaves as a DDES -RANS where the flow is attached and DES for massive separations- and as wall-modelled LES, WMLES, when inflow turbulent content is provided. The coordination of these two branches, i.e., DDES and WMLES is carried out by a set of empirical functions which control the mode in which iDDES is operating and it also couples both approaches, ensuring a favourable combination of the two methods depending on the initial conditions of the simulation.

The definition of the new LES scale was made according to two requirements: the SGS should be fairly isotropic far from the wall and it should depend on grid spacing parallel to the wall in very close to wall regions. In the rest of the domain, it should be just function of the grid spacing and the wall distance as in DES. Based on this, the new sub-grid scale definition is,

$$\nabla = \min[\nabla_{max}, \max(c_w d, c_w \nabla_{max}, \nabla_{wn}] \tag{3.92}$$

where ∇_{max} is the same as $\nabla_i = max|\Delta r_{i,n}|$. ∇_{wn} is the grid step in the direction normal to the wall, but in this study is assumed to be ∇_{min} to reduce computational cost. c_w is an empirical constant which is equal to 0.15 based on a wall-resolved LES channel flow.

The LES length scale is given by,

$$l_{LES} = \Psi C_{SGS} \nabla \tag{3.93}$$

Where Ψ is a low-Reynolds correction defined at the original DDES paper as,

$$\Psi^2 = \min\left(100, \frac{1 - \frac{c_{b1}}{c_{w1}\kappa^2 f_w^*}[f_{t2} + (1 - f_{t2})f_{v2}]}{f_{v1}\max(10^{-10}, 1 - f_{t2})}\right) \tag{3.94}$$

where $f_w^* = 0.424$.

The RANS length scale is given by, $l_{RANS} = d$

So in iDDES the wall distance, d, is replaced by l_{hyb}defined as,

$$l_{hyb} = \tilde{f}_d(1 + f_e)l_{RANS} + (1 - \tilde{f}_d)l_{LES} \tag{3.95}$$

Where the blending function, $\tilde{f}_d$,

$$\widetilde{f_d} = \max(f_B, 1 - f_{dt}) \text{ with } f_{dt} \equiv 1 - tanh[(C_1 r_{dt})^{C_2}] \quad (3.96)$$

And the empirical function $f_B = min[1.0, 2\exp(-9\alpha^2)]$ with $\alpha = 0.25 - \frac{d}{\nabla_{max}}$.

The function f_e is the elevating empirical function aimed to prevent an excesive reduction of the modelled Reynolds stresses in the blending region tackling with log layer mismatch issue and it reads,

$$f_e = \max(0, 1 - f_{e1}) \cdot \Psi f_{e2} \quad (3.97)$$

Where

$$f_{e1} = \begin{cases} 2\exp(-11.09\alpha^2) & if\ \alpha \geq 0 \\ 2\exp(-9\alpha^2) & if\ \alpha < 0 \end{cases} \quad (3.98)$$

And

$$f_{e2} = 1.0 - \max(f_t, f_l) \quad (3.99)$$

f_{e2} includes two functions defined as follows,

$$f_t \equiv 1 - tanh[(C_t^2 r_{dt})^3] \text{ with } r_{dt} \equiv \frac{\nu_t}{\kappa^2 d^2 \cdot max\sqrt{S_{ij}S_{ij}, 10^{-10}}} \quad (3.100)$$

$$f_l \equiv 1 - tanh[(C_l^2 r_{dl})^{10}] \text{ with } r_{dl} \equiv \frac{\nu}{\kappa^2 d^2 \cdot max\sqrt{S_{ij}S_{ij}, 10^{-10}}} \quad (3.101)$$

where the subscripts "t" and "l" stand for turbulent and laminar, respectively.

3.5.4 Resolved and modelled variables in DES

In this Chapter the governing equations and the numerical schemes and models employed for the solver have been described. It has also been explained in previous sections the hybrid RANS/LES techniques in which part of the fluctuations are

resolved and the other part is modelled. In this section, the distinction from resolved and modelled will be explained according to Fadai-Ghotbi et al. (2010).

In an instantaneous field the instantaneous velocity can be decomposed into a resolved part, $\tilde{u}_i$, which contains the mean flow and the large-scale fluctuations corresponding to the LES part and a residual part, $u_i^{"}$, which will be modelled via the application of a turbulence model as already discussed along this Chapter. According to this, the instantaneous velocity can be written as,

$$u_i = \tilde{u}_i + u_i^{"} \tag{3.102}$$

Where $\tilde{u}_i$ is the resolved velocity composed by

$$\tilde{u}_i = \underbrace{U_i}_{mean} + \underbrace{U_i'}_{large-scale\ fluctuations} \tag{3.103}$$

Therefore, the total fluctuation of the velocity can be written as,

$$u'_i = U_i' + u_i^{"} \tag{3.104}$$

According to this, the resolved Reynolds stresses in LES mode are given as,

$$\tau_{ij}\big|_{res} = \rho\left(\overline{\tilde{u}_i\tilde{u}_j} - U_iU_j\right) \tag{3.105}$$

And the modelled Reynolds stresses will be

$$\tau_{ij}\big|_{mod} = \rho\overline{\langle u_i^{"}u_j^{"}\rangle} \tag{3.106}$$

As the turbulence modelled in DGDES is the one-equation Spalart-Allmaras model in which the only transported variable is the turbulent viscosity, the turbulence kinetic energy k was approximated by Durrani and Qin, (2011) based on the Bradshaw's hypothesis, [Bradshaw and Ferris, 1967] as,

$$k = \frac{\nu_t \sqrt{2 S_{ij} S_{ij}}}{\sqrt{C_\nu}} \tag{3.107}$$

where S_{ij} is been given in equation (3.67) and $C_\nu = 0.09$.

With this turbulent kinetic energy and the resolved turbulent viscosity ν_t in the Spalart-Allmaras model, the modelled stresses are calculated using the equation (3.80)

Finally the total Reynolds stresses are defined as,

$$\tau_{ij}\big|_{total} = \tau_{ij}\big|_{res} + \tau_{ij}\big|_{mod} \tag{3.108}$$

3.6 Boundary Conditions treatment

3.6.1 Introduction

In CFD, one of the most important tasks to do before running a simulation is the determination of the boundary conditions which will limit the computational domain. An inappropriate selection of boundary conditions can lead to an inaccurate solution of a given problem. An explanation of the most common boundary conditions can be found at Blazek, (2001).

In DGDES several boundary conditions can be applied when defining the domain. The description of the most common boundary conditions such as inlet, wall, farfield implemented in DGDES can be found at Xia, (2005). Also, the turbulent inlet condition will be used in order to simulate the turbulent inlet data provided by the experimental side of every case; a full description of the treatment for a turbulent inlet boundary condition in DGDES can be found at Wang's thesis, [Wang, 2013]. However, as a DBD plasma actuator and spanwise vortex generators are the key cases in this thesis, the introduction of new boundary conditions had to be implemented in the solver. First of all, the plasma boundary condition will be described. In second and last place, the moving boundary condition will be presented.

3.6.2 Plasma Boundary Condition

In the code, a no-slip boundary condition is given to the generic walls. When the fluid flows over a surface which has been defined as a wall, it means that there are two conditions to be achieved: the first one, no-penetration of the fluid through the surface and secondly, the no-slip condition which means the velocity at the wall is zero. Together with the condition for the temperature, i.e., the wall is considered either adiabatic or isothermal, the no-slip condition conforms the wall boundary condition in DGDES. Hence, at the wall,

$$\begin{cases} u = u_w \\ v = v_w \\ w = w_w \\ T = T_w \; or \; \left.\dfrac{\partial T}{\partial n}\right|_w = 0 \end{cases} \tag{3.109}$$

When plasma is set as a boundary condition, it will be taken into account in the simulation as a wall, but the body force term will be added to the Navier-Stokes equations as it has already been discussed in previous sections of this thesis.

3.6.3 Moving wall Boundary Condition

In this thesis, by moving wall boundary condition we are referring to the moving wall which corresponds to the dimensions and geometry of the spanwise vortex generators within the fixed domain.

A moving wall is a wall as it name indicates but a non-zero velocity is introduced into the original no-slip wall. Therefore, the velocity for this boundary condition can be calculated in a simple way,

$$\left(\boldsymbol{v}_b - \boldsymbol{v}_g\right) \cdot n = 0 \tag{3.110}$$

where $\boldsymbol{v}_b$ is the velocity of the moving wall.

Regarding pressure, it can be calculated based on the condition which states that the pressure gradient in the normal direction to the wall is equal to zero.

3.7 Dynamic Grid Techniques for the Spanwise Vortex Generators

3.7.1 Introduction

In this thesis, the study of the spanwise generators flow control device involves the necessity of moving mesh due to obvious reasons as described back on Chapter 2. Consequently, the availability of dynamic grid options was crucial to carry out appropriate simulations of this device.

Dynamic grid technique was firstly introduced by Batina [Batina, 1990, 1991] in his work for solving unsteady Euler algorithms using unstructured dynamic meshes. Later on, based on Delaunay graph mapping different proposals for moving grids were developed and published by Liu, Qin and Xia, (2006).

In the present thesis, however, a different dynamic grid method is applied. It was developed by Wang, (2013) and, unlike Spring Tension or Delaunay Graph Mapping in which changes in the grid points all over the solution domain are considered, this method only implies a small region where the movement of the mesh is performed and the rest of the domain remains intact, involving therefore much less computational time and requirements. The use of this method is justified when the flow control device movement, normally treated as a boundary condition, is small compared to the characteristic length and domain size.

So, in DGDES there are three different types of dynamic grid techniques available: Spring Tension Analogy, Delaunay graph mapping and Geometrical Similarity method. Delaunay graph mapping and Spring Tension Analogy descriptions can be found at Xia, 2005. A brief description of the Geometrical Similarity method will be provided here.

3.7.2 Geometric Conservation Law

In the case of running a simulation which implies grid movement, the Geometric Conservation Law needs to be applied to the ALE formulation. In this section the discretisation of the mesh movement is given.

When a simulation requires mesh deformation the solver has to be able to predict the solution of a uniform flow as it is predicted when a fixed mesh is used. Besides, despite of the movement of the grid no disturbances should be produced by such movement or by any other movement for a uniform flow. Because of these statements, the mesh movement terms need to be carefully discretised so the freestream is preserved and the Geometric Conservation Law, GCL, is applied for such purpose.

The continuity equation for a uniform velocity and constant density field is,

$$\frac{\partial V}{\partial t} + \iint_{\partial V(t)} (\boldsymbol{v} - \boldsymbol{v}_g) \cdot \boldsymbol{n} dA = 0 \tag{3.111}$$

where $\partial V(t)$ is the boundary of the control volume which is time dependent. If, as mentioned earlier, the velocity is considered to be uniform

$$\boldsymbol{v} \cdot \iint_{\partial V(t)} \boldsymbol{n} dA = 0 \tag{3.112}$$

Then (3.111) would be re-written as,

$$\frac{\partial V}{\partial t} + \iint_{\partial V(t)} \boldsymbol{v}_g \cdot \boldsymbol{n} dA = 0 \tag{3.113}$$

The discretisation of this equation must be conserved at all the time steps and for all the control volumes or cells in our case. This is the Geometric Conservation Law formulation and it must be discretised using the same methods used for the discretisation of the governing equations of the flow in order to achieve a self-consistent solution for the local cell volumes.

If a backward Euler scheme is applied to the GCL equation a cell-wise discretisation is presented,

$$\frac{V^n - V^{n-1}}{\Delta t} = \sum_{j=1}^{nface} (\boldsymbol{v}_g)_j^n \cdot \boldsymbol{n}_j^n A_j \tag{3.114}$$

where $(\boldsymbol{v}_g)_j^n$ is the averaged velocity of the face j of the moving mesh at time step n. $\boldsymbol{n}_j^n$ is face normal vector and A_j is the area of the face at time step n. Both of them, $\boldsymbol{n}_j^n$ and A_j are determined by the instantaneous node positions. Finally, the averaged velocity of the cell will be the face centroid velocity which obtain from the position vector, $\boldsymbol{x}_c$, following the same backward Euler scheme as above,

$$(\boldsymbol{v}_g)_j^n = \frac{(\boldsymbol{x}_c)_j^n - (\boldsymbol{x}_c)_j^{n-q}}{\Delta t} \tag{3.115}$$

$\boldsymbol{x}_c$ is calculated from the average of the nodes which the face consists of.

3.7.3 Geometry Similarity Method

As it was already stated in the introduction of this section, when the movement of the boundary condition is much smaller than the characteristic length, a smaller domain can be defined as the only region of the whole domain which is affected by the moving flow control device. Fig. 3.1 shows a diagram of the geometry similarity approach.

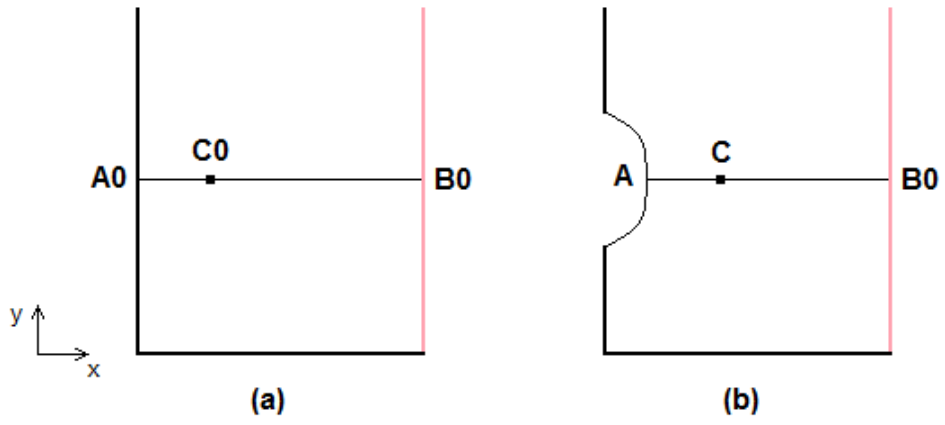

Figure 3.1 Geometry similarity diagram

There are three steps in this moving mesh method which are:

1) Definition of a reduced moving zone.
2) Define the movement of the boundary.
3) Obtain the new position of the nodes using the geometry similarity.

Step number 1) has already been described. Also, a main direction of the movement of the boundary needs to be defined; in the example shown in Fig. 3.1 it would be the x axis direction. In step number 2) the movement of the boundary is performed according to the flow control device, i.e., in this study, the spanwise vortex generator follows a sinusoidal oscillation $P = P_0 \sin(\omega t)$ where P is the instantaneous position and P_0 is the maximum amplitude and ω is the frequency of the movement. And finally, the moving nodes will only move in the main direction defined in step number 1) and the other nodes follow the geometry similarity: For example in Fig 3.1 if x is taken as the main directions, the geometrical similarity is,

$$\frac{x_{B0} - x_{A0}}{x_{B0} - x_{C0}} = \frac{x_{B0} - x_A}{x_{B0} - x_C} \tag{3.116}$$

However, although this method saves a large amount of computational time and it is a robust method, it has got some limitations. The first limitation is when the mesh deformation follows a complex movement. Second limitation is that the mesh has to be quite fine in the moving boundary region because if the mesh quality in such region is poor, this method loses robustness and finally, the third limitation is that the orthogonality of the fitting meshes in the moving boundary region cannot be maintained; however as the mesh movement is normally quite small, the orthogonality damage is in most of cases negligible.

3.8 DBD Plasma Models and their Implementation

In the current section, a dielectric barrier discharge, DBD, plasma actuator will be described. In order to perform appropriate simulations using this control device, two different models were implemented in the solver: Shyy's model, [Shyy, 2002] and the model provided by Singh and Roy, [Singh and Roy, 2008].

Plasma actuators have shown several advantages in aerospace applications when compared to other flow control devices actuating at a wide range of speed regimes [Low speed: Roth, 2003; Enloe et al., 2004. High speed: Miles, 2000; Leonov, 2007]. For instance and unlike other active flow control devices, plasma actuators have no mechanical components and the required power to operate them is moderate; furthermore, the actuation has a quick response and the generated force is significant.

3.8.1 General Description of a Dielectric Barrier Discharge Plasma Device

Several studies have been carried out in past to investigate how the plasma force is generated when using a DBD plasma actuator and its effects when applied to different cases such a BFS or other geometries such as aerofoils under different initial configurations, [Gregory et al., 2007; Roy et al., 2006, 2007; Corke et al, 2010; Mertz, 2011; Opaits, 2012; Bernard et al., 2007, 2008, 2009, 2014]. A single DBD plasma actuator consists of two electrodes asymmetrically placed at different sides of a flat dielectric plate, [Pons, 2005]; however, different configuration of the electrodes and the dielectric material can be configured, [Corke et al, 2010; Hoskinson and Hershkowitz, 2008; Santhanakrishnan and Jacob, 2006; Roy, 2009]. Nevertheless, the chosen configuration in this thesis is shown in Fig. 3.2 where a brief diagram of how plasma is generated is depicted: two electrodes are located on both sides of a dielectric material of certain thickness (in the order of micro/millimetres). A high voltage is applied between the electrodes by means of a transformer and the air in the indicated regions is ionised and turned into plasma, Fig. 3.3. Plasma actuation consists in generating an electrical discharge at the wall within the boundary layer. The objective is to add momentum with the discharge-induced electro-hydro-dynamic force and electric wind.

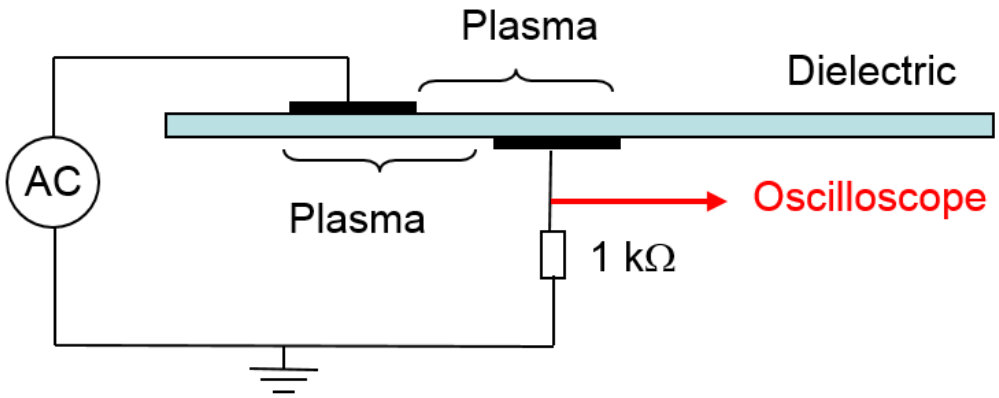

Figure 3.2 Basic principle of an axisymmetric DBD plasma actuator

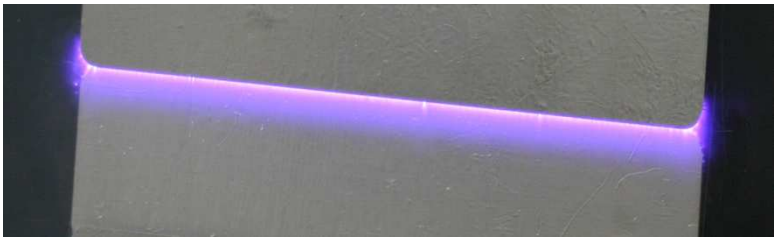

Figure 3.3 Plasma visualisation along the spanwise of wind tunnel at University of Poitiers

In the work carried out by the experimental partner, the electrode downstream of the flow is grounded and insulated, so the plasma will be generated only on the upper surface of the dielectric surface. Due to the distance between the electrodes along the streamwise direction and due to the difference of pressure produced by the application of high voltage, a discharge barrier is created in the adjacent region to the exposed electrode and it ionises the air surrounding this region and an optical glow appears as shown in Fig. 3.3. This plasma is highly collisional: due to the added energy, the air dissociates because of the collisions of particles whose molecular binding energy is lower than the thermal kinetic energy. This effect together with the electric body force induces a momentum transfer from the electric field into the flow field, influencing the near-wall boundary layer. In another arrangement, a pulsation frequency –much lower than the AC frequency- can be applied. In this case, the excitation induces an unsteady force which will influence the natural large-scale flow structures of the flow rather than the near-wall boundary layer.

The generated force will be dependent on the applied voltage – applied waveform and voltage -, the applied frequency –normally in the range of radio frequency wave lengths- and the geometry and material characteristics of the device, i.e., distance and thickness of electrodes and thickness and permittivity of dielectric material.

Two different models were implemented in DGDES: Shyy's model and Singh and Roy's model. A complete explanation and description of these models is given in the following sections of the present thesis.

3.8.2 Plasma Models in DGDES

In this section an explanation of two different models implemented in the solver is going to be given. In both cases, the force generated by the plasma device is considered as a body force and it will be added as a source term in the Navier – Stokes governing equations of the flow.

The first implemented model which is going to be described is the model developed by Shyy et al at their paper "Modelling of glow discharge-induced fluid dynamics" (2002). In this article, fluid dynamics and heat transfer induced by plasma were investigated. However, in this study –and for both models- only the fluid dynamics produced by the plasma were investigated, as the interest of this research was focused on weakly ionised plasma or non-thermal plasma. Secondly, the model proposed by Singh and Roy on their paper "Force approximation for a plasma actuator operating in atmospheric air" (2008) is mathematically explained and it was implemented in the code after Shyy's model. Singh and Roy's model implementation and validation was one of the aims of this thesis and it will be described in the next sections.

3.8.2.1 Shyy's model and its implementation into DGDES

As it has already been mentioned previously, Shyy et al modelled the fluid dynamics and heat transfer induced by an asymmetric dielectric barrier discharge plasma actuator. In their work, a single DBD plasma actuator was installed on a flat plate and the effects of the generated plasma were investigated. A formulation for the body force and its addition into the governing equations was obtained.

The DBD actuator operated at atmospheric pressure and plasma was generated by applying a certain frequency and voltage. Regarding the order of frequency and voltage, the frequency was in the range of kilohertzs and the voltage was also in the range of a few kilovolts.

Since the electric field lines emerge from the exposed electrode to the grounded electrode, in Shyy's model plasma is considered to interact with air inside a triangular region defined by the position of the electrodes, Fig. 3.4. The electric field lines are assumed to be linear and moving from A to B so the electric field, hence the induced force is strongest near the edge of the exposed electrode and weakens as moving beyond the embedded electrode and beyond line A-B.

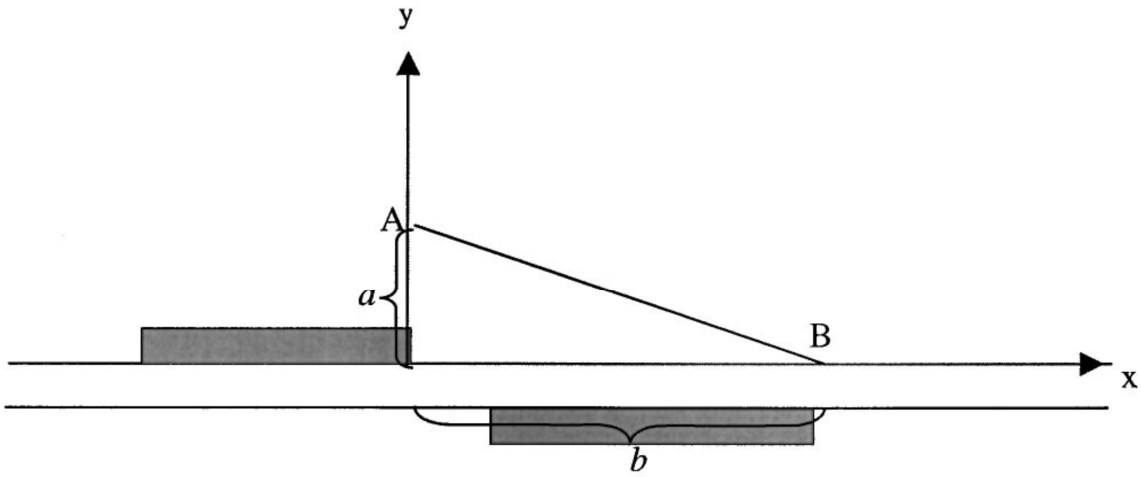

Figure 3.4 Triangular area of actuation of plasma in Shyy's model

According to these assumptions, an equation for the electric field variation can be written as,

$$|E| = E_0 - k_1 x - k_2 y \tag{3.76}$$

Where E_0 is the electric field in the region between the left edge of the exposed electrode and the right edge of the left electrode and it is approximated to be,

$$E_0 = \frac{V}{d} \tag{3.77}$$

Where d is the distance between electrodes in the x-direction. k_1 and k_2 are constants whose values were obtained by means of the condition that "the field strength is the breakdown value at the plasma-fluid boundary". Regarding the electric field, $\vec{E}$, it is restricted to be two dimensional in this approximation, their components were the x-direction component given by,

$$E_x = \frac{Ek_2}{\sqrt{k_1^2 + k_2^2}} \tag{3.78}$$

and the y component was,

$$E_y = \frac{Ek_1}{\sqrt{k_1^2 + k_2^2}} \tag{3.79}$$

The force components were obtained by multiplying each electric field component by the electron charge, e (C) and the electron number density, ρ_c (m^{-3}),

$$f_x = E_x \rho_c \, e \tag{3.80}$$

$$f_y = E_y \rho_c \, e \tag{3.81}$$

However, this force only influences the area where the plasma is present, i.e., the triangular region therefore a blending function δ is needed to make sure plasma acts in the correct region in the whole domain,

$$\begin{cases} \delta = 1 \; for \; E < E_{crit} \\ \delta = 0 \; for \; E \geq E_{crit} \end{cases} \tag{3.82}$$

E_{crit} is the aforementioned breakdown electric field strength.

In addition to this, as plasma is a highly collisional phenomenon, a constant named α was also introduced to account for the collision efficiency. Taking into account the blending function and the efficiency assumptions, the final effective force components can be easily obtained,

$$f_{effx} = \alpha f_x \delta \tag{3.83}$$

$$f_{effy} = \alpha f_y \delta \tag{3.84}$$

Finally, this body force is not acting constantly but when plasma is formed during Δt time, which is half cycle of the AC voltage as explained in Shyy's paper. However, as the frequency of the applied voltage is high, the acting force is considered to be steady, hence a time averaged force was obtained,

$$F_{tavex} = \vartheta f_{effx} \Delta t \tag{3.85}$$

$$F_{tavey} = \vartheta f_{effy} \Delta t \tag{3.86}$$

Note that ϑ is the frequency of the applied AC voltage.

These two components were added then as a source term in the momentum equations and the effects of plasma were analysed.

At high frequencies, plasma shows to dramatically increase the streamwise component of the velocity.

3.8.2.2 Singh and Roy's model and its implementation into DGDES

K.P Singh and S. Roy stated in their paper "Force approximation for a plasma actuator operating in atmospheric air" that resolving all mechanisms involved in presence of a plasma actuator is a very complicated task: following the principles of plasma, in order to get an accurate solution of the influence of a plasma device one would have to solve continuity equations of different species, Poisson's equation [Roy, 2007] and Navier-Stokes equation which would be a really expensive methodology, computationally speaking. For such reason, they proposed a rather

simple and straightforward model for obtaining the electro-hydro-dynamic force generated by a simple DBD actuator.

In the model proposed by Singh and Roy, several assumptions were made: a sinusoidal voltage was applied to the exposed electrode and in this case the embedded electrode was grounded as well as in Shyy's model. The current flows perpendicular to the dielectric surface and no slip condition was assumed for this surface. The generated force was assumed to be two dimensional, therefore it will only be defined by two components in the x and y direction, respectively and the air was considered to be a quiescent gas flow. The formulation does not include the frequency of the AC voltage applied so if in reality the plasma actuation is quasi-steady –radiofrequency waves – this model considers the plasma actuation as steady.

With regards to the area where plasma has got influence in the flow field, unlike in Shyy's model where the plasma region is limited to a triangle defined by the geometry of the device, in Singh and Roy's model plasma is considered to have influence in the whole domain. Furthermore, the value of each EHD force component will be dependent on the distance and position with respect to the DBD actuator location.

According to these ideas and assuming the time averaged force interacts with air, the body force was approximated by a fourth order polynomial equation dependent on the applied voltage, ϕ_0 and the DBD geometry,

$$\begin{aligned}\vec{F} = {} & F_{x0}\phi_0^4 exp\left(-\left\{\frac{[x-x_0-(y-y_0)}{y}\right\}^2\right. \\ & \left.-\beta_x(y-y_0)^2\right)\vec{\imath} \\ & + F_{y0}\phi_0^4 exp\left\{-\left[\frac{(x-x_0)}{y}\right]^2\right. \\ & \left.-\beta_y(y-y_0)^2\right\}\vec{\jmath}\end{aligned} \tag{3.87}$$

where the values for the following constants: F_{x0} and F_{y0} were taken from the paper

and their values are obtained by averaging the solution of the body force obtained when solving air-plasma coupled equations. These values were obtained after performing a study of the plasma actuator under nine conditions explained in the original paper therefore the model will require further adjustment when the air is moving/flowing. Besides, β_x and β_y are constants that depend on the dielectric material characteristics and their values were initially and for test purposes assumed to be equal as those provided in Singh and Roy's paper. However, and because of taking such values for the above mentioned constants, when Singh and Roy's model was implemented in the flow solver, several problems due to large generated plasma force values were found in the first CFD simulations. A solution for this problem was later found in another paper [Roy and Wang, 2009] and will be shown in Chapter 4 where this plasma model is fully analysed.

Finally, x_0 and y_0 are the midpoint between the electrodes and the thickness of the dielectric material, respectively, Fig. 3.5.

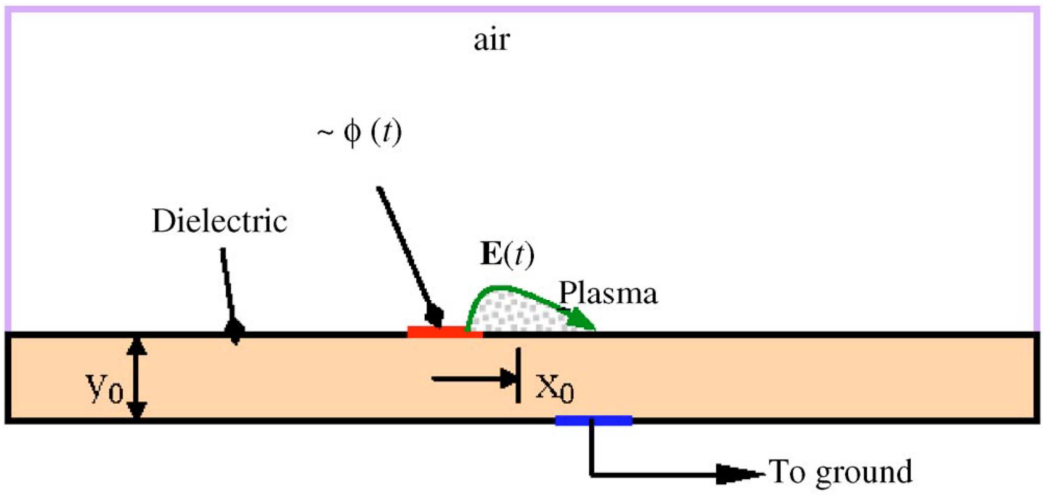

Figure 3.5 Single DBD plasma actuator diagram according to Singh and Roy's model

It can be seen from the force equation that its value over the domain of actuation is spatial dependent: the closer to the actuator, the more intense the force will be. This is one of the main differences with the formulation provided by Shyy in which the plasma only operates in a triangular area and it does not have any effect beyond the limits of such triangle.

With regards to its implementation into DGDES, the model assumes the generated body force follows the equation (3.87). In this study, the only investigated configuration of the two electrodes considered is the one depicted back in Fig. 3.5.

As already discussed, in the original plasma model formulation several conditions were assumed and tested in order to obtain all the coefficients needed to produce the values of the plasma force which matched the experimental measurements. This means that the force given by the model is sensitive to the initial conditions. In this thesis, the initial conditions of the analysed experimental case are completely different to the original paper formulation. Because of that, a constant needs to be applied to the plasma equation as it will be seen later on. Apart from that reason, according to experimental results the efficiency of the plasma actuator is not 100% and both components of the force would have to be multiplied by a constant in order to match the experimental results. In addition to all this, due to the original Singh and Roy's plasma model formulation, in which the magnitude of the force increases with the fourth power of the maximum applied voltage, when high voltages such as the experimental case carried out in the MARS project framework are applied (which can reach up to 25kV), the resulting EHD force is a huge number which leads to not physically reasonable values for the force hence an assumption was made: the plasma body force term had to be reduced by the application of another constant which would multiply both components of the force. Another important assumption as already mentioned before in this section, the plasma actuation when it is really quasi-steady – in the order of kilohertzs – Singh and Roy's model consider the actuation as purely steady and constant plasma actuation.

With regards to the introduction of a constant into the force components using the original Singh and Roy's model formulation, the application of such constant was later on found in the paper "Bulk flow modification with horseshoe and serpentines plasma actuators" by Roy and Wang on 2009. Supported by that reason, a re-formulation of the original equation was performed by introducing a constant, C_{ROY}, which multiplies both force components,

$$\vec{F} = C_{ROY}\, F_{x0}\phi_0^4 exp\left(-\left\{\frac{[x - x_0 - (y - y_0)}{y}\right\}^2 - \beta_x(y - y_0)^2\right)\vec{\imath} + C_{ROY}\, F_{y0}\phi_0^4 exp\left\{-\left[\frac{(x - x_0)}{y}\right]^2 - \beta_y(y - y_0)^2\right\}\vec{\jmath} \quad (3.88)$$

In this thesis, a few studies to select an appropriate value for the model's constant were performed and it will be fully analysed in Chapter 4. In the adjustment, both components of the body force will be multiplied by the same constant which will contain both plasma efficiency and the constant used at Roy and Wang, (2009).

Regarding the implementation of Singh and Roy's model into DGDES, it is clear that the model is a electromagnetical phenomenological model and therefore the generated force was included as a source term in the Navier-Stokes equations, which means, when plasma is switched on in Equation (3.9),

$$\frac{\partial}{\partial t}\iiint_V \boldsymbol{W}\partial V + \frac{\partial}{\partial \tau}\iiint_V \boldsymbol{W}\partial V + \iint_{\partial V}(\boldsymbol{F} - \boldsymbol{G})\cdot \boldsymbol{n}dA = \int_V \boldsymbol{S}dV \quad (3.117)$$

The term $\int_V \boldsymbol{S}dV$ is the summation of the all the body forces such as electric fields, magnetic fields, gravity, etc. will be equal to the force generated by the plasma actuator. When the plasma device is deactivated, $\int_V \boldsymbol{S}dV = 0$.

3.9 Summary

In Chapter 3 the governing equations, mathematical schemes and models in DGDES have been described. The Navier-Stokes equations and the ALE formulation have been explained for simulations with fixed/moving boundaries. Discretisation of time and space has also been given. The different hybrid RANS/LES techniques such as DES, DDES and iDDES with the Spalart-Allmaras turbulence model have been presented and its implementation in DGDES has also been discussed. The boundary conditions treatment has been explained and the dynamic grid techniques applied for the spanwise vortex generator study have been introduced.

Finally, a general description of the DBD plasma devices and the implementation of both Shyy's and Singh and Roy's plasma phenomenological models have been presented. As the main interest of this study is to investigate the flow behaviour, not chemistry was included in the model of the plasma actuator.

Regarding Singh and Roy's model, when the plasma actuation is in reality quasi-steady the model resolves the plasma force as a purely steady actuation. Despite this assumption, it will be seen in the next Chapter of this thesis that the results simulating quasi-steady plasma using Singh and Roy's model are very accurate when they are compared to the experiment, proving that the formulation of the model even though it is only a phenomenological model is clearly reliable. On the other hand, Shyy's model limitation comes with the region of actuation of the plasma, only a triangular region dependent on the dimensions of the electrodes. For this reason, Shyy's application leads to different flow behaviour and development as it will be shown in the next chapter.

4 Active flow control with a single DBD plasma actuator over a backward facing step

4.1 Introduction

The problem of a turbulent flow over a backward facing step, BFS, has been widely investigated both experimentally and numerically [Armaly et al., 1983; Driver and Seegmiller, 1985; Lien and Leschziner, 1994; Le, Moin, and Kim, 1997; Chiang, 1998; Fadai-Ghotbi et al., 2008; Barri et al., 2010]. One of the most comprehensive BFS cases is Driver and Seegmiller's, D&S, case which was tested in order to validate our in-house code by Wang, (2013). In this thesis a 2D validation of D&S case was performed at early stages of the PhD studies using commercial software and also DGDES. However, in the framework of the Manipulation of Reynolds stress for Separation Control and Drag Reduction (MARS) project different geometries and configurations of the BFS were investigated.

Generally, a backward facing step problem consists of the following main features depicted in Fig.4.1: when the air flow arrives at the edge of the step, the attached boundary layer upstream of the step separates and a massive recirculation region is created downstream of the step. Therefore, there are two differentiated regions: the air which flows over the step at the free stream velocity, known as the inviscid core, and the air bubble originated in the region below the free shear layer and in the downstream direction which contains low-velocity flow recirculating, creating thusly reversed flow towards the step as indicated in Fig.4.1. Part of the shear layer reattaches to the wall and a new boundary layer is then growing forward from that area. This region is known as the reattachment region or point, one of the main investigated characteristic parameters of a flow over a BFS, as it is very sensitive to the inflow parameters. One of the goals of this study is to control the size of this reattachment area, i.e., separation control. In order to achieve such control, different devices can be used. In this chapter, a DBD plasma actuator is investigated and then in Chapter 5, spanwise vortex generator, SVG, is studied.

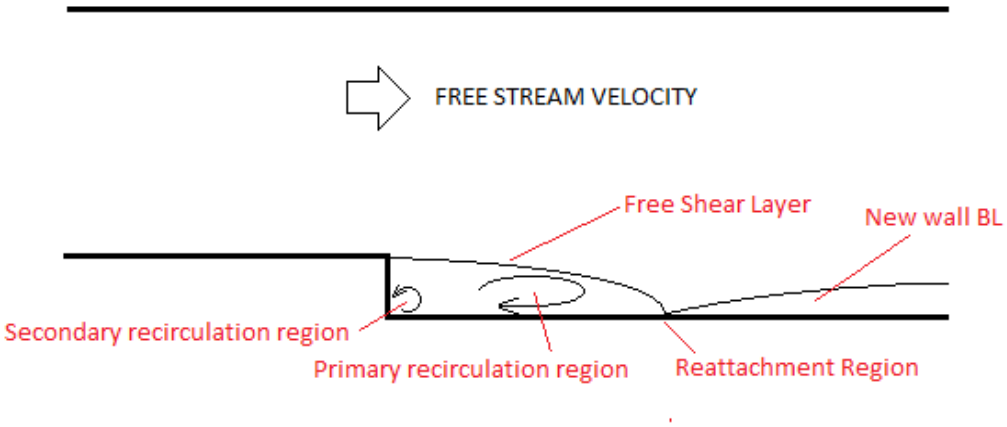

Figure 4.1 Scheme of a flow over a BFS

An investigation of different Singh and Roy's model constants was performed in this chapter in order to match the experimental case and to compare the performance of Singh and Roy's model versus Shyy's model as well. Finally, an unsteady forcing study was carried out as this plasma operation mode experimentally showed to be more effective regarding the reduction of the reattachment area of the flow, [Sujar-Garrido et al., 2012].

4.2 Driver and Seegmiller's baseline case: Evaluation of RANS and URANS methods for Flow over a Backward Facing Step

4.2.1 Introduction: RANS and URANS results comparison simulating Driver and Seegmiller's case

During the first year of the PhD degree, the activities and tasks were directed towards performing different studies of well-known aerodynamic problems such as a backward facing step and a compression ramp (the latter not included in this thesis) with the main objective of training and acquiring good knowledge of the different phenomena which take place in the above mentioned cases. The means used were two-dimensional calculations with two Computational Fluid Dynamics codes and then a comparison was performed. Only the main results are shown here. All the work done focused on flow behaviour understanding and analysis. After this first

period, all the work was directed towards flow control cases in order to get fully involved with the MARS project, which was the project funding this PhD course. The most relevant work and results are gathered in this thesis.

In this initial stage, the methodology followed was based on the evaluation of different turbulence models using Reynolds Average Navier Stokes, RANS, and unsteady RANS, URANS, for solving the equations of motion for the fluid flow with the purpose of evaluating their ability when predicting the reattachment length in every specific case of study.

In the case of a BFS, the reattachment length is one of the most important variables studied in order to assess the accuracy of the utilised models as stated in the introduction of this chapter. In order to make proper assessment of the models, an experimental case was used as the experimental reference database and all the results were compared to these experimental available data.

As mentioned previously, the well-known problem of a backward facing step based on the experiments carried out by Driver and Seegmiller, (1985) was the starting point and reference for every performed calculation. Initially, the flow analysis was done with a commercial code. The problem was to set up as a two dimensional, incompressible flow over the backward facing step. The pressure-based solver with the SIMPLE algorithm was used as the calculations were considered to be steady.

In the second stage of the study, after evaluating the performance of 2D RANS, the model considered to be the closest to the experimental data was compared to a SA-URANS case using the DGDES in-house code.

DGDES was the selected code to run all the analysis in this study due to its capability to capture the unsteadiness of the flow using hybrid RANS/LES techniques and all the advantages of hybrid methods which have already been discussed in previous sections of this thesis.

With regards to RANS, RNG k-ε turbulence model using in a commercial CFD code, ANSYS Fluent 13 showed the closest results to the experiment carried by Driver and Seegmiller, (1985). The comparison with URANS will show the better capabilities of

this method versus RANS and also the advantages of using the in-house code against a commercial code will be discussed.

4.2.2 Methodology, Results and Conclusions

For RANS, the flow was considered subsonic and incompressible in a turbulent steady state. The simulation which showed the closest reattachment length to the experimental value was run using RNG k-ε turbulence model.

The step height, H, was 1.27×10^{-2} m and the Reynolds number based on momentum thickness was 5000 at 4H upstream of the step. The free stream velocity was 44.2m/s at atmospheric conditions. According to this, the computational domain and mesh were designed. In all cases, dimensionless wall distance y+ must be in order of 1, thus enhanced wall functions were used when possible, [Kim, 2005]. Consequently given these conditions, the minimum wall spacing was 6.3×10^{-6} m. Values of y+ in the order of 6 were accepted in computations.

The computational mesh is shown in Fig. 4.2,

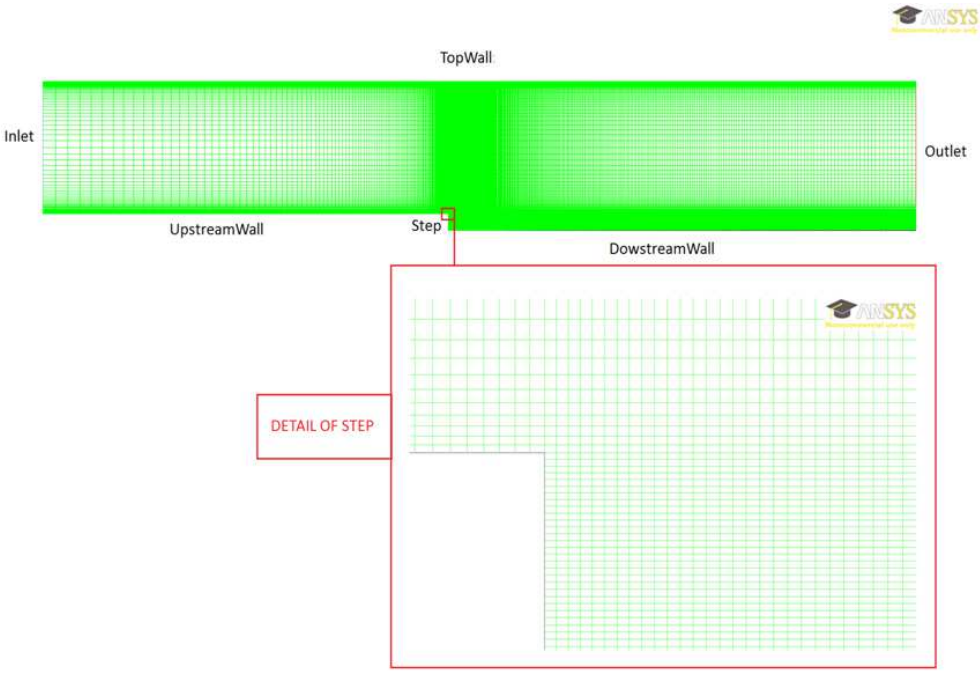

Figure 4.2 Computational Mesh

The mesh was clustered in the step region in order to capture recirculation zone, reattachment length and other parameters such as skin friction and velocities more precisely.

Mesh details are arranged in the following table,

Face	Length (m)	Cells
Inlet	0.1016	90
Outlet	0.1143	290
Upstream Wall	0.33	148
Downstream Wall	0.381	421
Step	0.0127	200
Top Wall	0.711	569

Table 4.1 B.C. for D&S case. Fluent's mesh.

Regarding numerical setup, calculations were run using the pressure-based solver in all cases with pressure-velocity coupling SIMPLE. Spatial discretisation was second order upwind for momentum, turbulent kinetic energy and dissipation rate and convergence criterion was 10^{-8} for all variables.

The boundary conditions were uniform free stream velocity inlet for the inlet, pressure outlet for the outlet and the rest of boundaries were walls with no-slip condition.

For every case, initial turbulence values must be given; the equations used to calculate these values are Equations (4.1) to (4.4).

First, in Fluent, the kinetic turbulent energy is defined by the turbulence normal stresses,

$$k = \frac{1}{2}(u'^2 + v'^2 + w'^2) \tag{4.1}$$

If $u'^2 = v'^2 = w'^2$, then $k = \frac{3}{2}u'^2$. (4.2)

And ε, the turbulent kinetic dissipation is,

$$\varepsilon = \frac{C_{\mu}^{0.75}\ k^{1.5}}{l} \tag{4.3}$$

The turbulence intensity, $I = \frac{u\prime}{U_{avg}}$, (4.4) was chosen to be a 5% and l was 10%H.

The URANS case using DGDES was run in order to investigate and evaluate the quality of the predicted results for RANS and URANS over the BFS. The pure RANS calculation failed to predict the unsteady characteristics of the separation flow. On the other hand, URANS simulation yielded reasonably the shedding phenomenon.

In the case using the in-house code DGDES, the real time-step size was 5.0×10^{-5}, running 90,000 total time-steps in order to allow the flow to be fully developed in time. The turbulence model was Spalart-Allmaras. A comparison with RANS of the y+, the x-velocity streamlines (time-average) and also the reattachment length is done.

First of all, a comparison of the meshes is shown,

Face	Length (m)	Cells-FLUENT	Cells-DGDES
Inlet	0.1016	90	90
Outlet	0.1143	290	90+70
Upstream Wall	0.33	148	148
Downstream Wall	0.381	421	400
Step	0.0127	200	70
Top Wall	0.711	569	148+400

Table 4.2 Comparison of meses for the two different solvers for D&S validation case

It is important to point out that DGDES mesh was "pseudo-3D", as it has one cell on the z direction of 1 mm.

The y+ of RNG k-ε RANS (FLUENT) and S-A URANS (DGDES) is shown in the following figure,

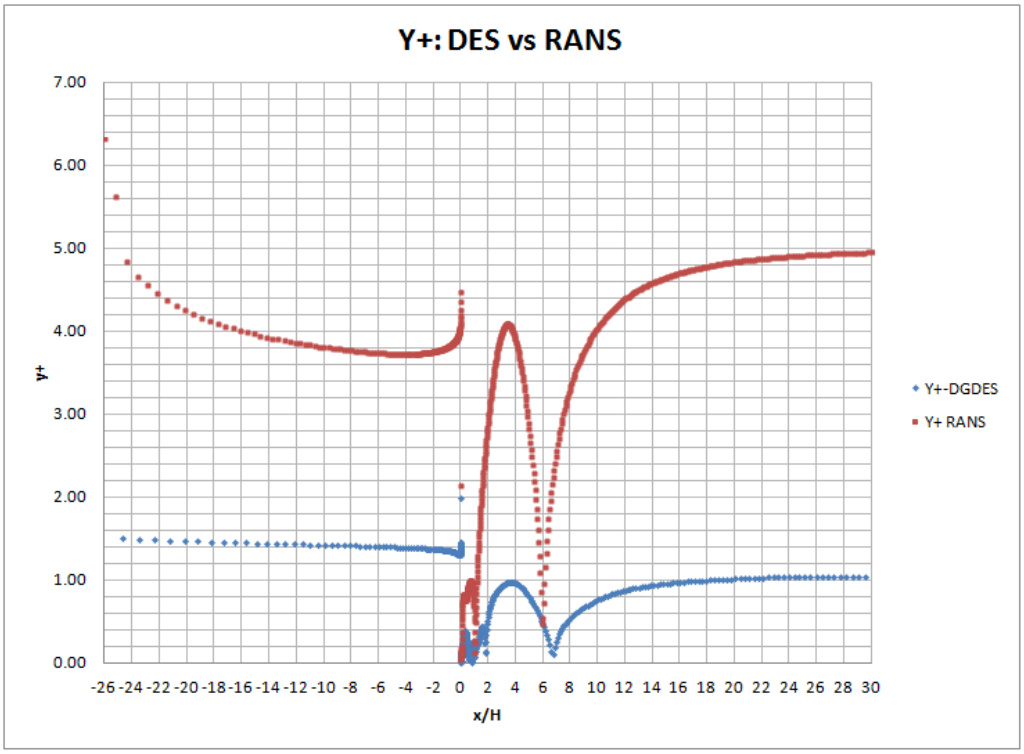

Figure 4.3 Y+: DGDES vs RANS (Fluent)

It can be seen both methods provide a reasonable value of y+, although DGDES y+ is lower.

The next figure shows the comparison of velocity streamlines, where in the S-A URANS case, it is the time-averaged streamlines in order to be comparable with RNG k- ε RANS,

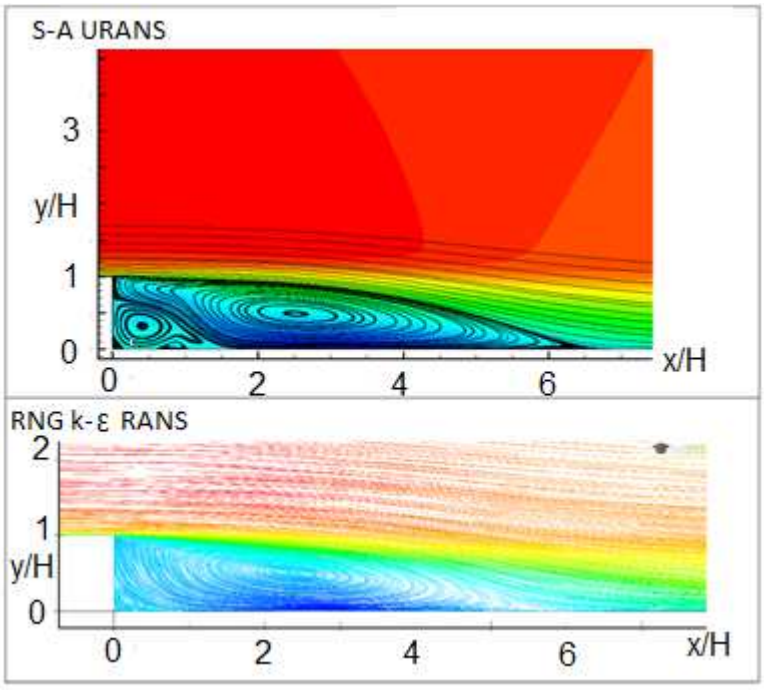

Figure 4.4 Velocity streamlines: S-A URANS vs RNG k- ε RANS

In the figure, the turbulent structures are similar, although, the secondary bubble in the corner is bigger in URANS than in RANS.

Skin friction coefficient was also compared, Fig.4.5, and it is seen how both configurations under-predict the skin friction coefficient, C_f before reattachment area. In this figure, Spalart-Allmaras model using Fluent was included in order to compare C_f in both Fluent and DGDES with the same turbulence model and the experimental data,

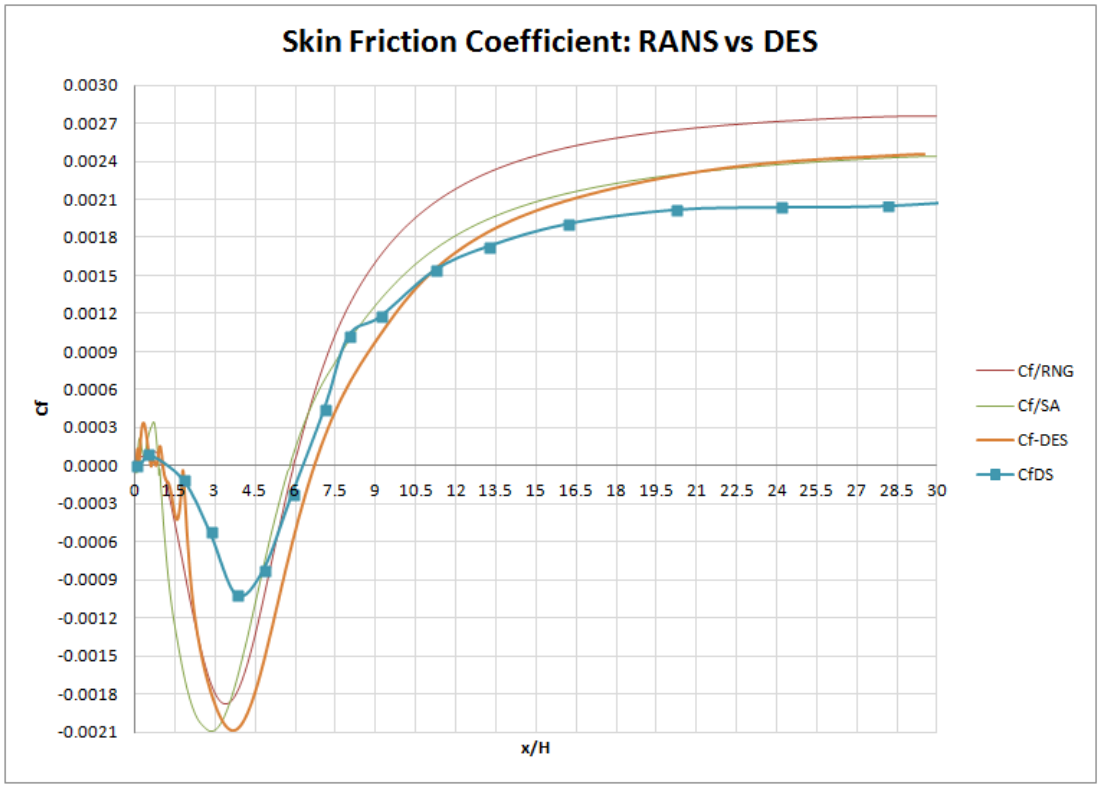

Figure 4.5 Skin Friction Coefficient Distributions

Finally, the following table shows the reattachment lengths of all cases, where it is shown URANS over-predicts reattachment length due to the 3D requirement for this simulation technique.

Reattachment Length	**FLUENT**		**DGDES**
Experimental	RNG k-ε	S-A	S-A
6.28H	5.95H	5.82H	~6.6H

Table 4.3 Reattachment length comparison using two different solvers for the D&S validation case

As a conclusion of this RANS vs. URANS comparison, the latter has proved, as expected, more reliability when predicting separated flows than pure RANS. Additionally, this was only a starting point and the rest of cases will be three dimensional and active flow control devices with different frequencies and amplitudes will be analysed. Also, different models and moving mesh techniques will

be implemented and analysed hence an open code using an unsteady methodology to capture the unsteadiness of the flow is necessary.

The cases investigated in this thesis are strongly characterised by unsteadiness and periodicity induced by the active flow control devices. Additionally, turbulence is a three dimensional phenomenon therefore three dimensional simulations will be needed in order to obtain reasonable solution for the physics of the flow. For these reasons, hybrid RANS/LES will be the most appropriate method to carry out the research.

4.3 Flow over a backward facing step using a DBD plasma actuator – CNRS PPRIME Poitiers case

4.3.1 Case Configuration: Description of University of Poitiers experimental configuration

In order to validate Singh and Roy's model implemented into DGDES, initial two dimensional S-A URANS tests were carried out based on Poitier's experimental case, [Sujar-Garrido et al., 2012].

Experiments performed at the wind-tunnel in Poitiers facilities, Fig. 4.6, were characterised by the following configuration: the step height, H, was 0.03m with a spanwise length of 0.3m. The wind tunnel test section is 0.3x0.3x1. Measurements were taken at the middle section covering x/H= {-2, 7} and y/H= {-1.5, 2}.

Experiments were carried out for a free stream velocity of 15m/s, therefore the Reynolds number based on step height is 30,000. The boundary layer thickness was calculated by means of velocity profiles measurement at various locations upstream of the step and it was determined to be approximately 13mm at 1H before the step edge.

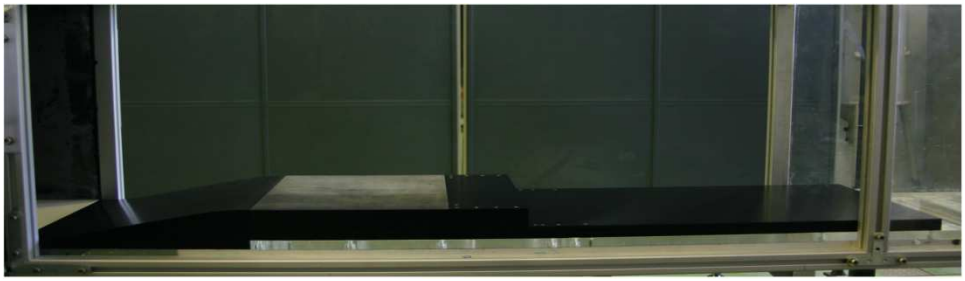

Figure 4.6 BFS model in wind-tunnel (CNRS PPRIME Poitiers)

The actuator was mounted as shown in Fig. 4.7,

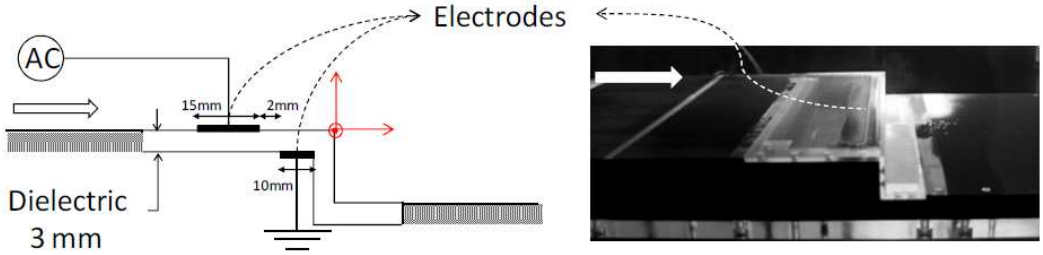

Figure 4.7 DBD plasma actuator configuration

As it can be seen in Fig. 4.7, the exposed electrode is 0.015m long. The embedded electrode, on the other hand, is located 0.002m downwards the exposed and it is 0.01m long. The dielectric thickness in this case is 0.003mm.

The actuator design was described back in Chapter 2, where the dielectric barrier discharge plasma actuators were presented. Just as a reminder, the plasma actuation consists in generating an electrical discharge at the wall within the boundary layer of the air flow, adding momentum with the discharge-induced electro-hydro-dynamic force and the electric wind. Additionally, DBD plasma actuators can be operated in two different modes; the first one known as quasi-steady or steady forcing – depending on the AC frequency – modifies the near-wall flow imparting flow perturbations in the boundary layer at the frequency of the applied electrical signal. In this case, the frequency of the alternating current was 1kHz so it is quasi-steady actuation of the device; however, in the simulations with Singh and Roy's model, the plasma actuation will be considered purely steady as this model does only consider the applied voltage and not the AC frequency as stated in the previous chapter. For

such reason and for comfort, steady actuation will be the term used when referring to steady or quasi-steady actuation of the plasma in the simulations; nonetheless this assumption needs to be borne in mind.

The second DBD plasma mode is referred to as unsteady forcing and it interacts with surrounding natural large-scale flow structures. In the experiment, the plasma discharge frequency was 125Hz.

In the initial two-dimensional study, a steady force was applied in order to validate Singh and Roy's model testing a set of different constants and compare them with the baseline and the experimental database. This 2D study allowed an appropriate assessment of the correctness of the implementation of Singh and Roy's plasma model into DGDES solver.

4.3.2 Two dimensional study for initial Singh and Roy's model validation

4.3.2.1 Geometry and Computational mesh for two dimensional initial study

The backward facing step mesh based on step height is shown in Fig. 4.8. The total height of the domain is 10H, from -1H to 9H. Regarding x-direction, the numerical inlet was located at 10H upstream of the step so that the flow at the inlet is not influenced by the flow downstream. On the other hand, the outlet was set 45H downstream of the step in order to assure proper outlet flow convection. Finally, regarding the spanwise direction, as simulations are 2D the mesh has got only one cell in z-direction.

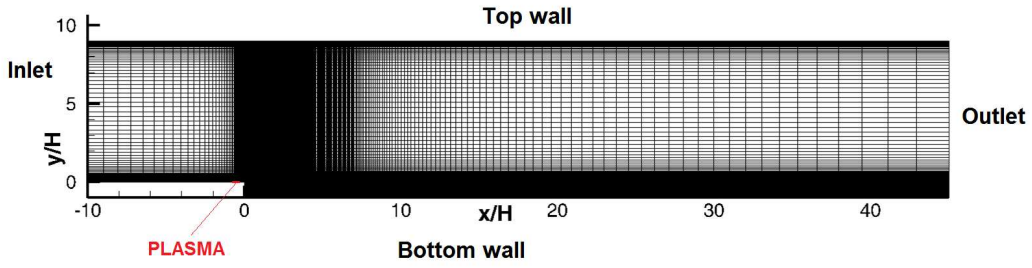

Figure 4.8 Computational 2D mesh, x-y view

As it can be seen in Fig. 4.8 and Fig. 4.9 the mesh is entirely structured and it is clustered near the step and downstream of it close to the bottom wall in order to capture the phenomena taking place in the recirculation area, the reattachment region and also the mixing layer region between the inviscid core and the air bubble areas. In the following figure, Fig. 4.9, the mesh area close to the step has been magnified in order to obtain a better appreciation of the mesh resolution in the aforementioned interesting areas in the BFS study.

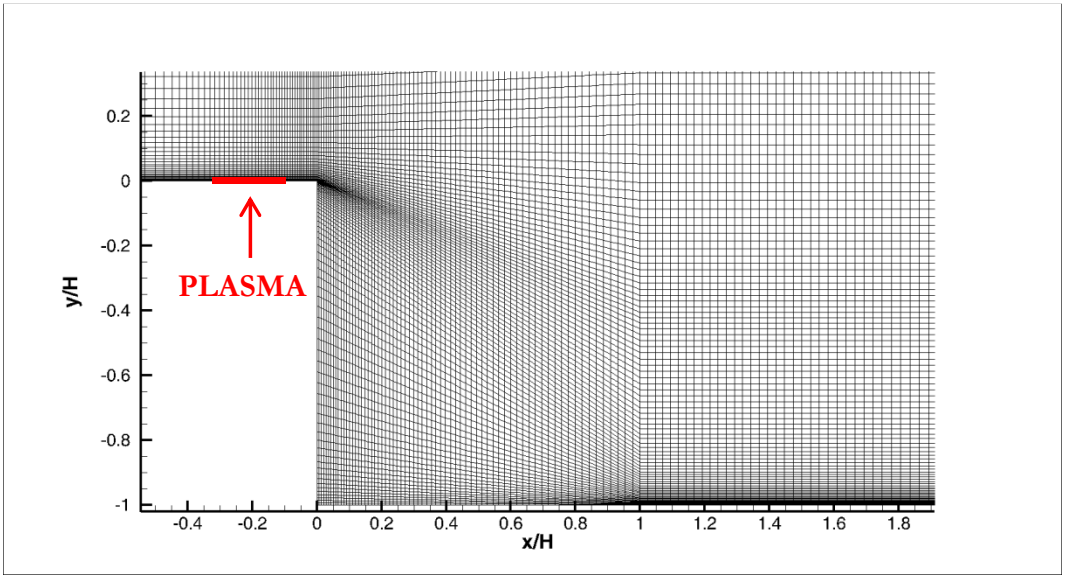

Figure 4.9 Detail of mesh at step region, x-y view

The mesh had a total number of cells of 56,127.

4.3.2.2 Boundary Conditions

As mentioned previously, the free stream velocity for the experimental case was 15m/s and the Reynolds number based on step height was 30,000. Besides, experimental velocity profiles were provided and therefore utilised at the inlet of the domain as the inflow conditions. The outlet was set as a non-reflective convective boundary condition and the top wall was set as a no-slip wall in this case. Regarding the sides, a periodic boundary condition was set for each of them. The bottom wall was also specified as no-slip wall and finally the plasma actuator was set to be plasma boundary condition, as described in the previous Chapter of this thesis.

The time step was $0.01H/U_\infty$, and 8 flow-through time periods, $T_{FT} = \frac{length}{U_\infty}$, proved to be enough to reach a statistically steady state as it will be soon shown.

4.3.2.3 Model adjustment: selection of model's constant

As a start point, a baseline simulation was run in order to assess the performance of a 2D case compared to the real experiment. The reattachment point in the experimental case from Poitiers was located at ~5.8H from the step and the results from the 2D simulation produced a reattachment point of 6.4H, Fig. 4.10. The reason this point was over-predicted in the simulation is due to the strong three dimensional characteristics of the turbulence and a 2D case does not allow the flow to develop in the spanwise direction producing, therefore, a "stretched" version of the real flow.

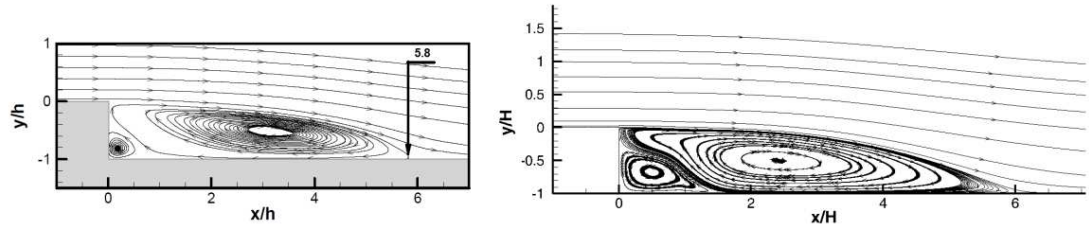

Figure 4.10 Baseline streamlines, experimental and simulation respectively

In experiments, when the DBD plasma device was operating in steady forcing mode, a reduction from 5.8H to 5.6H was achieved which is a 3.4% reduction. Bearing this in mind, a set of various very different constants, referred to as C_{ROY}, were initially chosen to be tested to tune the model so it would match the experimental reduction from baseline to steady forcing plasma actuation as it can be seen in Table. 4.5,

	Baseline	C_{ROY}= $1x10^{-5}$	C_{ROY} = $1x10^{-6}$	C_{ROY} = $1x10^{-7}$	C_{ROY} = $1x10^{-8}$	C_{ROY} = $1x10^{-10}$	C_{ROY} = $1x10^{-15}$
X_R (H-based)	6.4	1.3	2.3	4.5	6.15	6.39	6.4
% reduction	-	79.78%	64.1%	29.7%	3.3%	0%	0%

Table 4.4 Set of constants for Roy's model adjustment in 2D cases

In the following figure, Fig. 4.11, the streamlines together with the streamwise velocity contours is depicted to better see the effects of the various constants in the reattachment point.

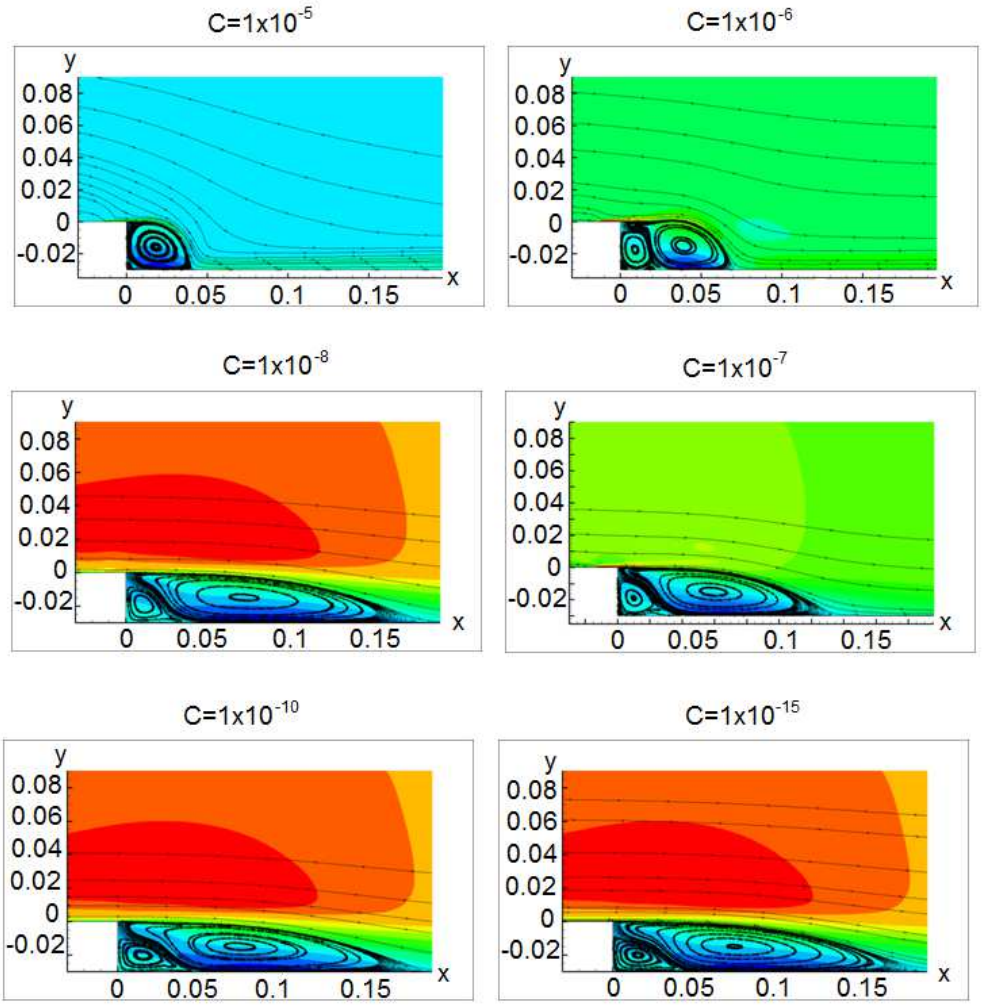

Figure 4.11 Streamlines and streamwise velocity contours for a set of different C_{ROY} constants

Hence, the chosen constant was $C_{ROY}=1x10^{-8}$ which produced a reduction of a 3.3% of the reattachment point when plasma is steady.

4.3.2.4 Comparison with Shyy's model after adjustment

Once Singh and Roy's model was initially adjusted, a comparison with Shyy's model case was analysed. A quick 2D simulation was carried out using the same mesh with the original Shyy's formulation with an efficiency of the plasma of a 30%. Finally it was compared with Singh and Roy's case with the selected constant of $1x10^{-8}$. In the following figures the controlled cases, experimental and simulations with both models, are shown

Shyy's model produced a reattachment location at 6.15H from step, whereas reattachment point using Singh and Roy's model as seen previously is located at 6.2H downstream of the step. The difference is less than 1% and Singh and Roy's model was considered to be correctly implemented and validated, Fig. 4.12 and Fig. 4.13.

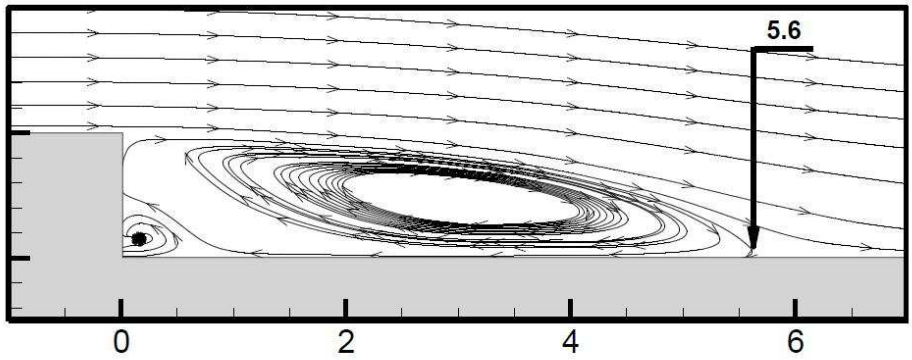

Figure 4.12 Streamlines for steady forcing. Experimental case

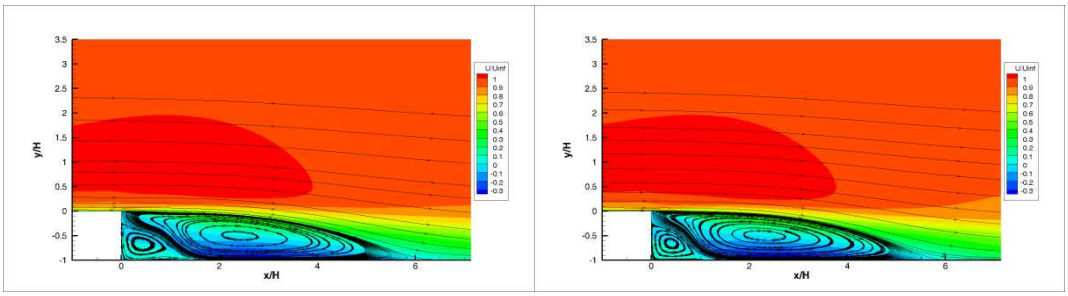

Figure 4.13 Streamlines and U/U_∞ contours: Singh and Roy's and Shyy's models, respectively

4.3.2.5 Conclusions of the 2D study

A validation of Singh and Roy's model for the case of a turbulent flow over a BFS was successfully carried out using 2D simulations in section. A comparison with experiments and another phenomenological model was performed and the model proved to be valid and reliable. Since the model was validated using only a set of two dimensional cases, further three-dimensional studies were carried out to be able to provide a complete assessment of the performance of Singh and Roy's model when using both steady and unsteady forcing for a DBD plasma actuator.

4.3.3 Three dimensional study: DBD plasma actuation over a backward facing step (Poitiers) applying quasi-steady actuation of plasma.

Once Singh and Roy's model was correctly implemented in DGDES solver, two three dimensional studies were carried out. Initially, a three million mesh was created and then an eight million mesh was utilised to simulate the experiments from Poitiers.

The 3M mesh was created from the 2D initial mesh, extruding it in the spanwise direction and having a total of 50 cells of 0.001m/cell. On the other hand, the 8M mesh was inherited from previous studies; it is a finer mesh similar to the finest mesh for Driver and Seegmiller's validation. It is completely structured to avoid high numerical dissipation due to the high skewness ratio which can be found in unstructured meshes.

Three different Singh and Roy's constant were also tested in order to assess the accuracy of the model in 3D cases: when using Shyy's model in 3D, efficiency of the plasma actuation had to be 65% and not a 30% applied in 2D simulations to match experimental results, hence a corresponding constant was researched for when using Singh and Roy's model in 3D calculations. The three chosen constants were investigated using both 3M and 8M meshes to evaluate the influence of the constants themselves and also the mesh influence when resolving turbulence structures and the flow behaviour.

Finally, after the model constant's adjustment, a comparison the experimental data from Poitiers will be presented.

4.3.3.1 Geometry and Computational Domain

The BFS configuration is exactly the same as it was for the 2D studies of the plasma devices. As mentioned in the previous section, an exploration of two computational meshes was carried out and then and finally a study for the unsteady forcing of the plasma actuator was investigated.

Regarding numerical schemes and turbulence modelling, the classic Roe scheme was selected for all cases and IDDES was the turbulence approach for all 3D cases as it

resolves more turbulence structures in both the recirculation and recovery regions and deals well with the grey area issue.

4.3.3.2 Boundary Conditions and selection of time step

The boundary conditions for the 3D simulations are the same as they are for the 2D cases. The difference is the number of cells in the spanwise direction –as stated earlier in 2D there was only one cell in z-direction- but the boundary conditions remained the same. At the inlet, the incoming turbulent profile provided by the experimental partner was used. The bottom wall was set as no-slip wall and the DBD plasma actuator was set to be plasma boundary condition. Regarding the top surface, for the 3M mesh the total height was 10H and it was set as no-slip wall as the BFS model in Poitiers. However, when using the 8M mesh, the total height of the mesh was 5H and the top surface was set to be symmetry boundary condition so the flow at the bottom wall or regions above it is not affected by the top wall boundary layer. Finally, the outlet was located further downstream of the step and it was set as non-reflective convective outlet.

The time step was chosen to be the same for both 3D cases, i.e., $0.01H/U_\infty$. Time averaging was done after a $5T_{FT}$ and it was calculated for a period of time corresponding to $400H/U_\infty$ for both 3M and 8M cases.

4.3.3.3 Study of mesh dependency: 3 million versus 8 million grids

The 3M mesh consists of an extrusion from the original 2D mesh; therefore, the x-y plane of the mesh is exactly the same as shown in previous sections of this chapter, Fig. 4.8, and in the spanwise direction the mesh had 50 cells with a total spanwise length of 1.4H and $8.4x10^{-4}$ m each cell. The total number of cells of this mesh is 2,573,550.

The 8M mesh resolution was finer than the 3M mesh. Previous studies with this mesh showed good results and good agreement with experimental data when simulating different uncontrolled/controlled cases so it was taken to investigate DBD plasma cases for this work. It has 7,685,496 cells, 84 in the spanwise direction with and total length of 1.4H and an x-y plane of the computational domain can be seen in Fig. 4.14 with a detail of the step edge below.

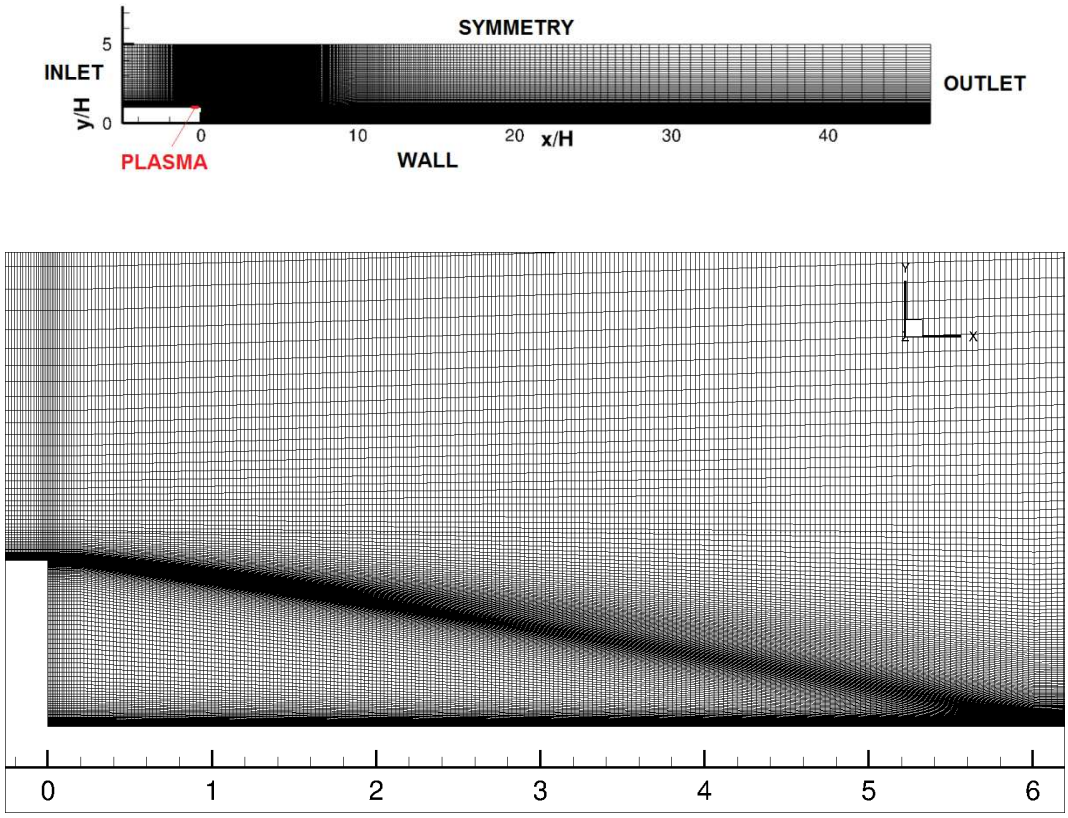

Figure 4.14 x-y plane of 8M computational mesh (top) and detail of step region (bottom)

4.3.3.3.1 Baseline cases comparison

The differences between a coarser and a finer mesh will be analysed based on the results of the baseline cases. A comparison of the time-averaged streamlines and a comparison of the vorticity magnitude will be shown in this section.

Fig. 4.15 shows the streamwise velocity contours together with streamlines for both cases and the experimental baseline streamlines,

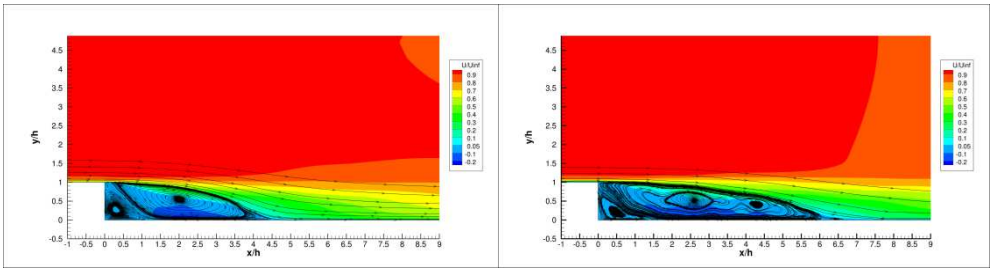

Figure 4.15 Streamlines comparison: 3M versus 8M mesh

As it can be seen, the 3M mesh reattachment point is located at 4.5H from the step edge, which is an under-prediction of a 23% compared to experimental results. On

the other hard the 8M mesh produces a much closer to experiment results as X_R is located at almost 6H and the experimental reattachment point is located at ~5.8H.

A comparison of the profiles of normalised streamwise velocity and Reynolds stresses between the results from simulations and the only available experimental data is shown next. The experimental data was only available at certain x/H locations so the results from computations will be depicted at such locations to assess the accuracy of both meshes.

First of all, the normalised streamwise velocity is shown at 1H, 4H and 6H respectively, Fig. 4.16.

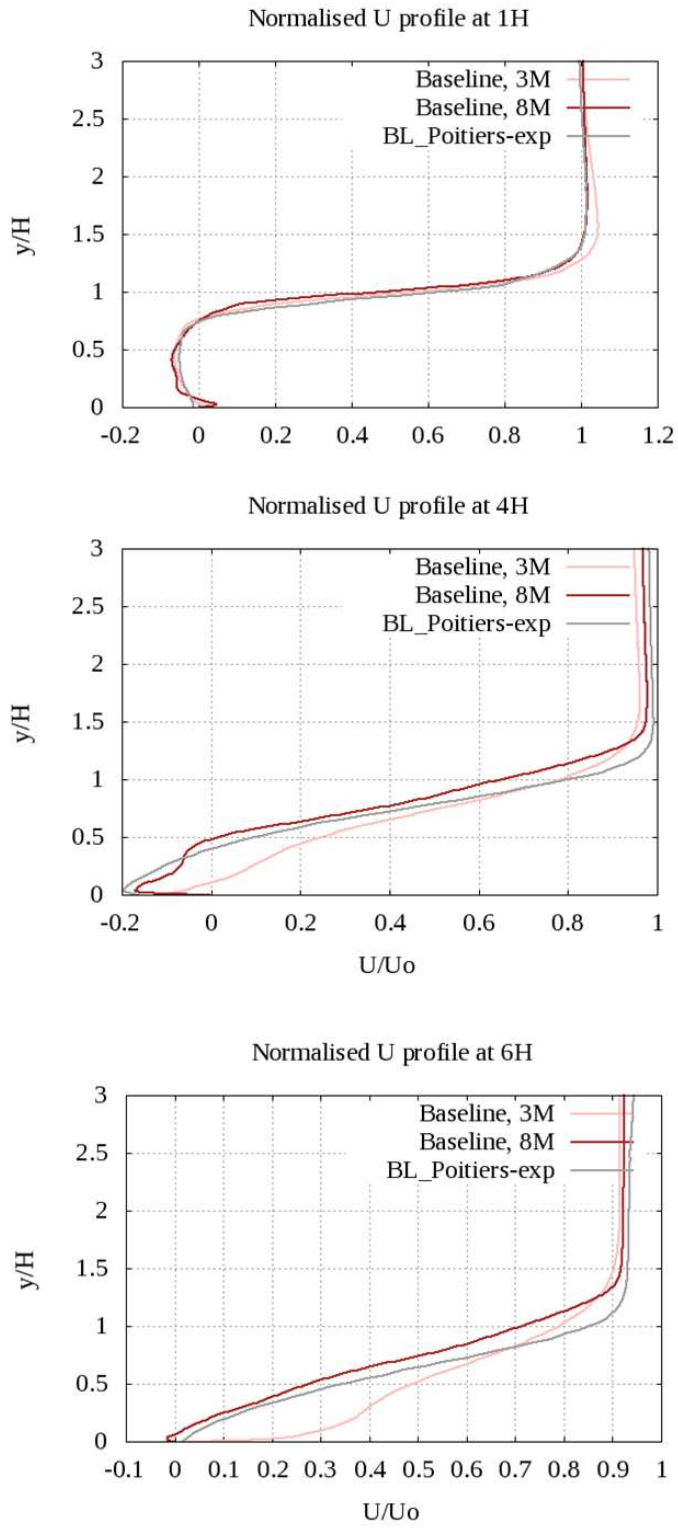

Figure 4.16 Time and spanwise averaged streamwise velocities at three different x/H locations

As it can be seen, the 8M mesh produces much closer velocity profiles when compared to experiments, whereas the 3M mesh results show an over prediction of the velocity near the wall which means the flow is already attached and the new boundary layer is developing at 6H as the velocity is much larger than the experimental and 8M cases.

An important aim in this study is to understand the behaviour of Reynolds stresses. First the profiles of normalised Reynolds stresses, $\langle u'u' \rangle$ and $\langle v'v' \rangle$, at the same three locations -1H, 4H and 6H-, Fig. 4.17, is shown and then a comparison of the three normal stresses contours, Fig. 4.18 is depicted.

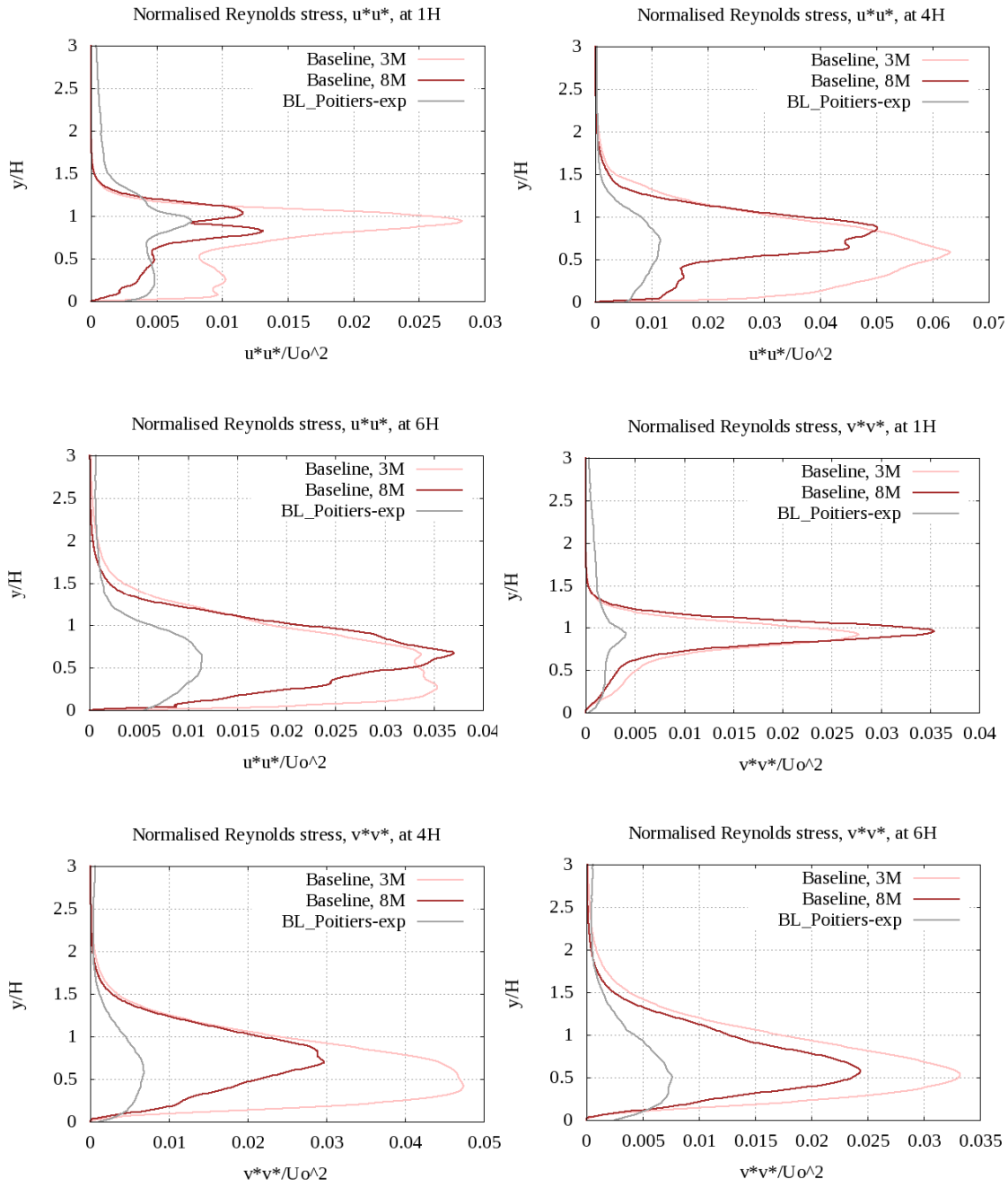

Figure 4.17 Normal Reynolds stresses at three different locations

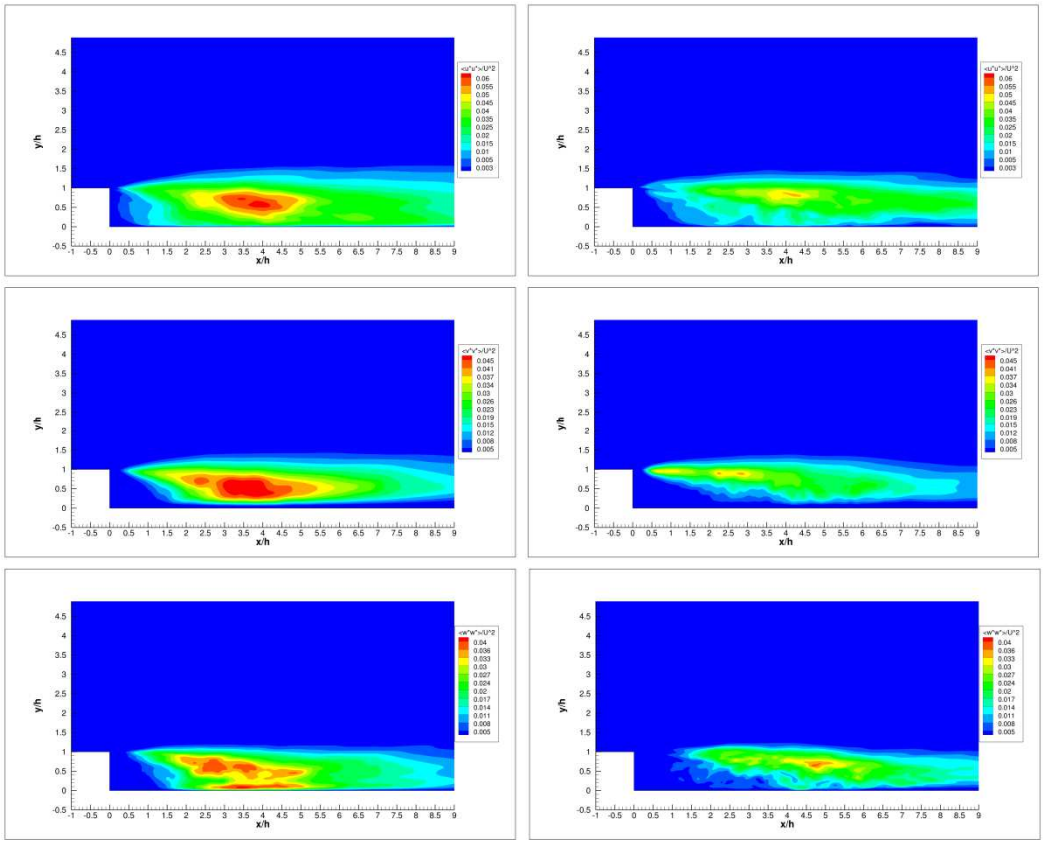

Figure 4.18 Normalised normal Reynolds stresses <u'u'>, <v'v'> and <w'w'> for the 3M mesh –left column- and the 8M mesh – right column- baseline cases

Also, the turbulent shear stress <*u'v'*> profiles, Fig.4.19, and contours, Fig. 4.20 is shown.

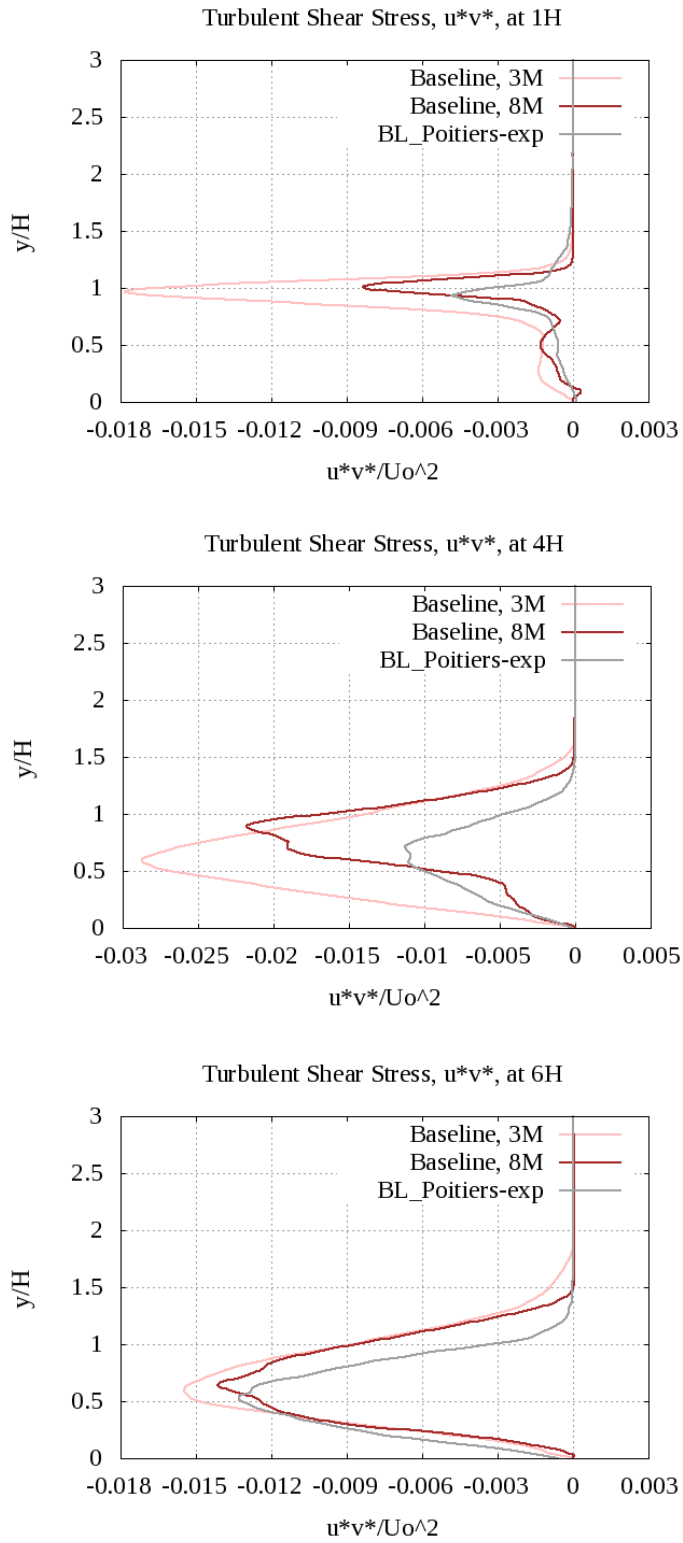

Figure 4.19 Normalised turbulent shear stress profiles at three locations

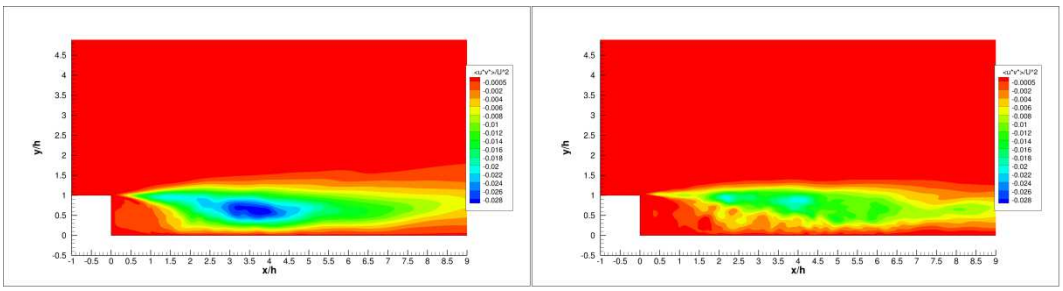

Figure 4.20 Normalised turbulent shear stress, <u'v'> for the 3M mesh –left- and the 8M mesh –right- baseline cases

As it can be seen, Fig. 4.17, with regards to the three components of the normal Reynolds stresses, the coarser mesh over-predicts their value especially in the primary recirculation region. It can also be seen for both cases that the normalised <*u'u'*> component of the Reynolds stresses is overall greater than the normalised <*v'v'*>. This was already observed by Barri et al (2010) where it was found by means of a DNS that the Reynolds stresses and the shear stress <*u'v'*> show a "high turbulence level after the step due to the high mean shear rate in the mixing layer emanating from the step".

However, regarding turbulent shear stress, Fig. 4.19, the finer mesh produces smaller values in the recirculation area which is in agreement with the under-prediction of the normal stresses and it means the 3M has over-predicted the mixing causing therefore an under-prediction of the reattachment area.

Finally the turbulent structures are analysed by means of the vorticity magnitude iso-surface coloured with the streamwise velocity for a value of 30,

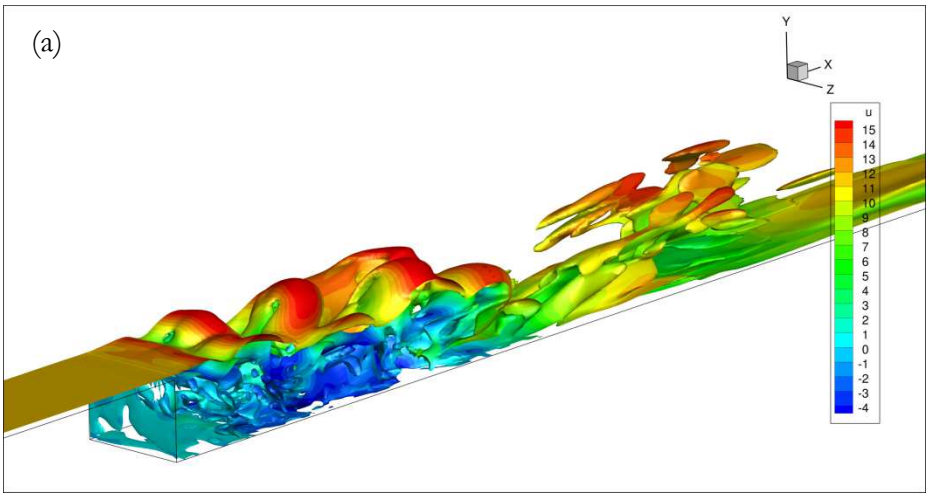

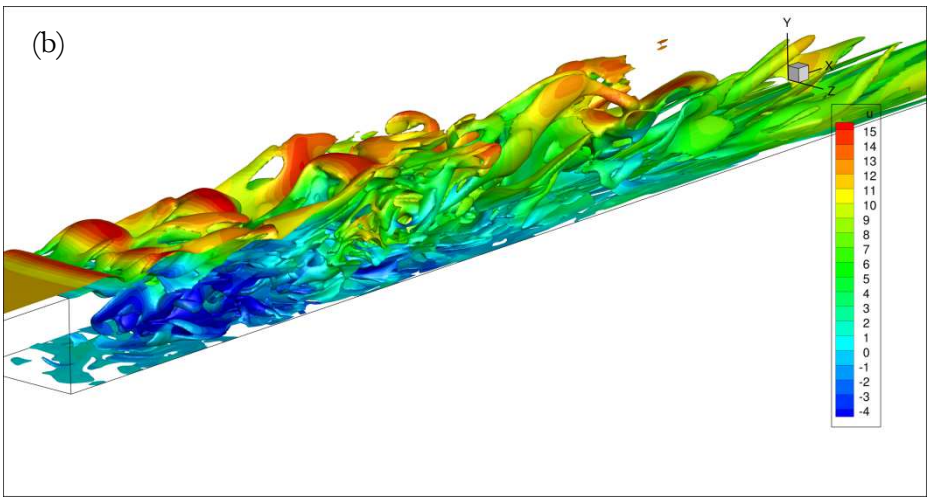

Figure 4.21 Iso-surfaces of vorticity magnitude at 30 for (a) coarser and (b) finer meshes

As it can be seen, the finer mesh resolves more turbulent structures –especially the small turbulent structures- allowing a better understanding of the flow field which of great interest in this thesis.

4.3.3.3.2 Steady plasma actuation comparison: 3M versus 8M meshes

A comparison with steady forcing was also carried out to study the effects of the plasma using both meshes. First of all, the time-averaged streamlines will be shown as we previously did for the baseline case. As this was an initial assessment of the meshes, only one Singh and Roy's constant, $C_{ROY}=7.0x10^{-8}$, was chosen to study the mesh influence on steady plasma.

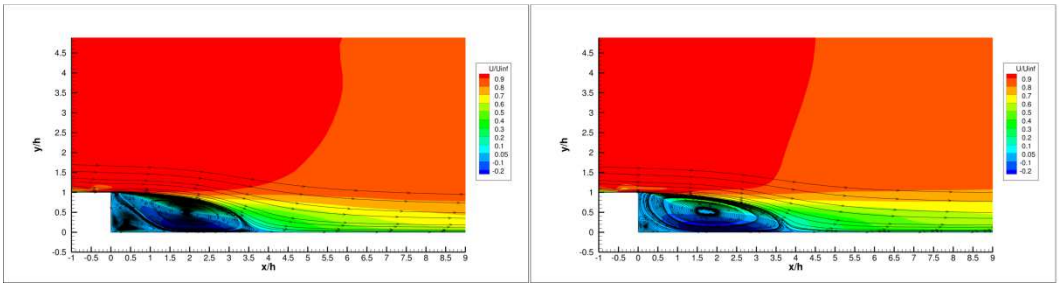

Figure 4.22 Time-averaged streamlines for 3M and 8M meshes with steady plasma, respectively

Fig. 4.29 shows again that the 3M mesh under-predicts the reattachment length when compared to the 8M mesh.

No experimental data was provided in this case to make a comparison of the streamwise velocity components when plasma was applied in steady mode. Reynolds stresses were available though so a comparison was carried out.

The normal and shear Reynolds stresses profiles and contours will be shown, Fig. 4.23-4.26,

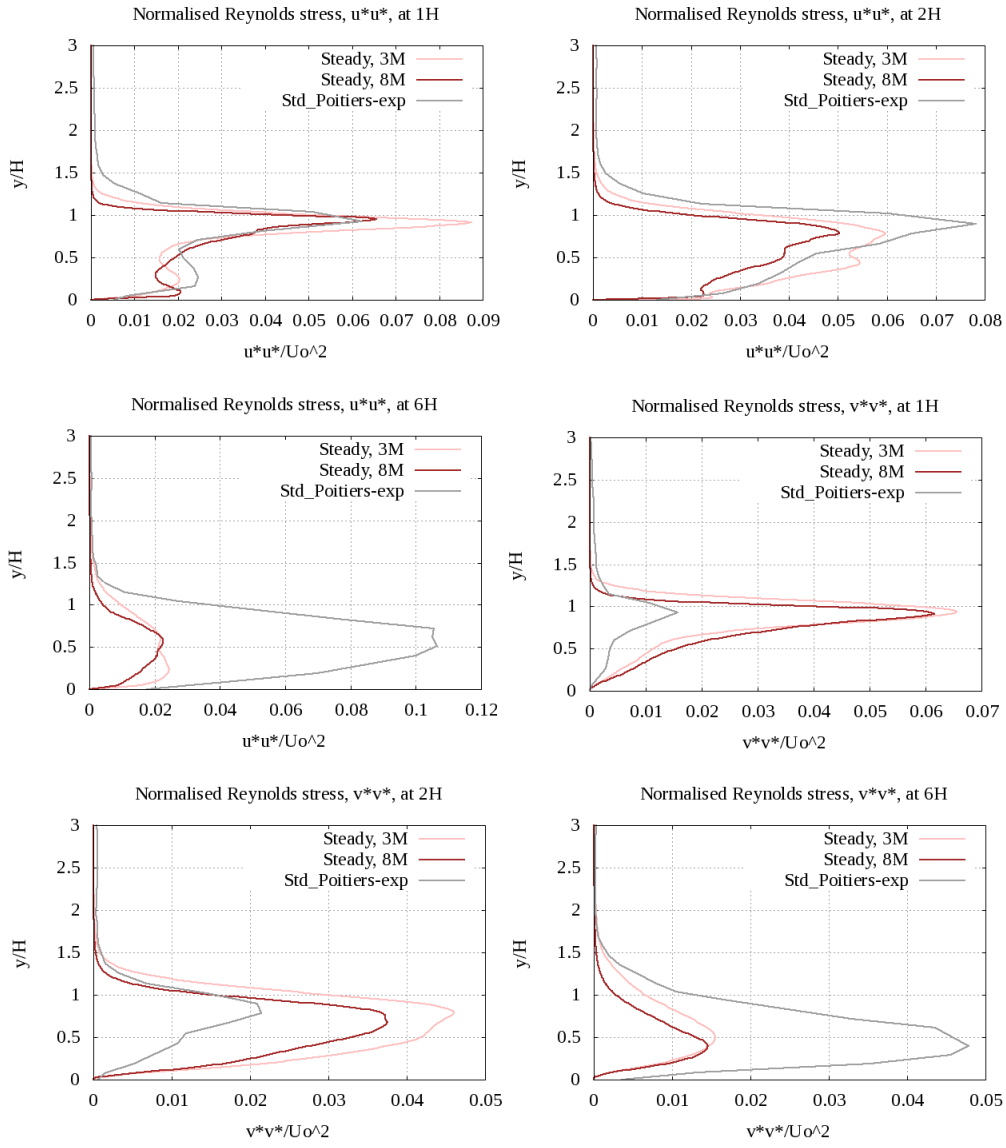

Figure 4.23 Normalised Reynolds stresses <u'u'> and <v'v'> at 1H, 2H and 6H locations.

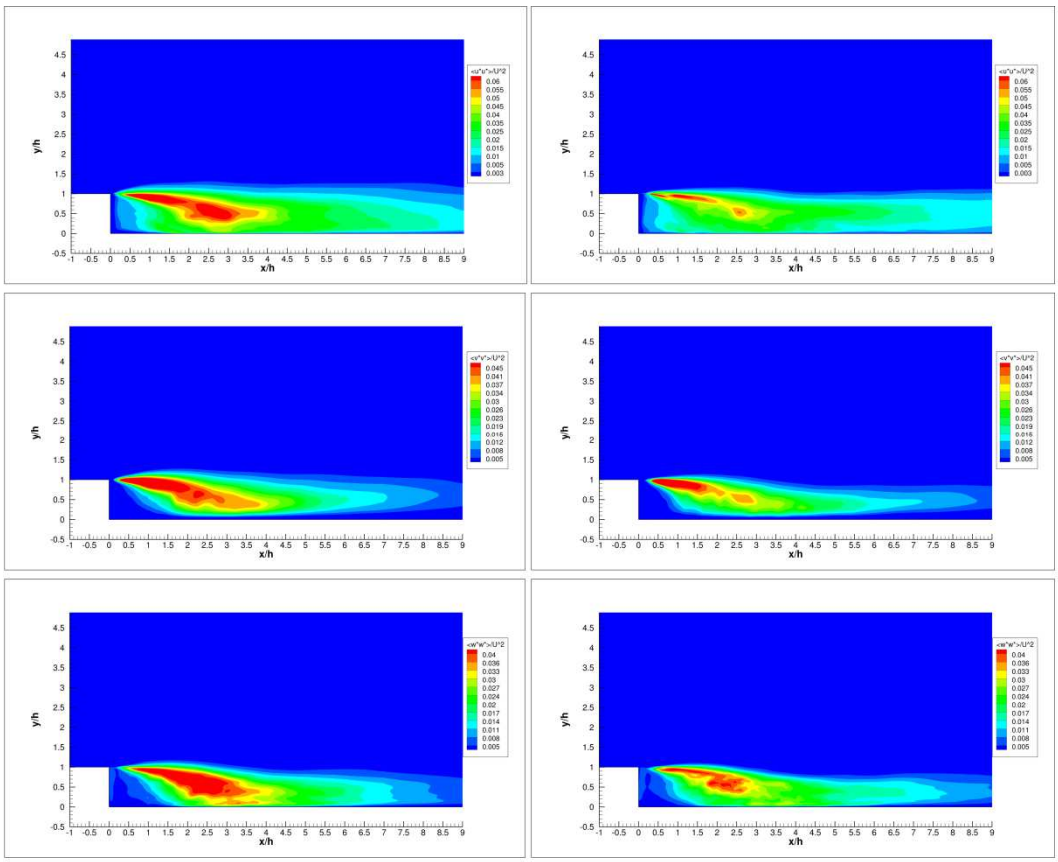

Figure 4.24 Normalised normal Reynolds stresses <u'u'>, <v'v'> and <w'w'> for the 3M mesh –left column- and the 8M mesh – right column- steady plasma cases

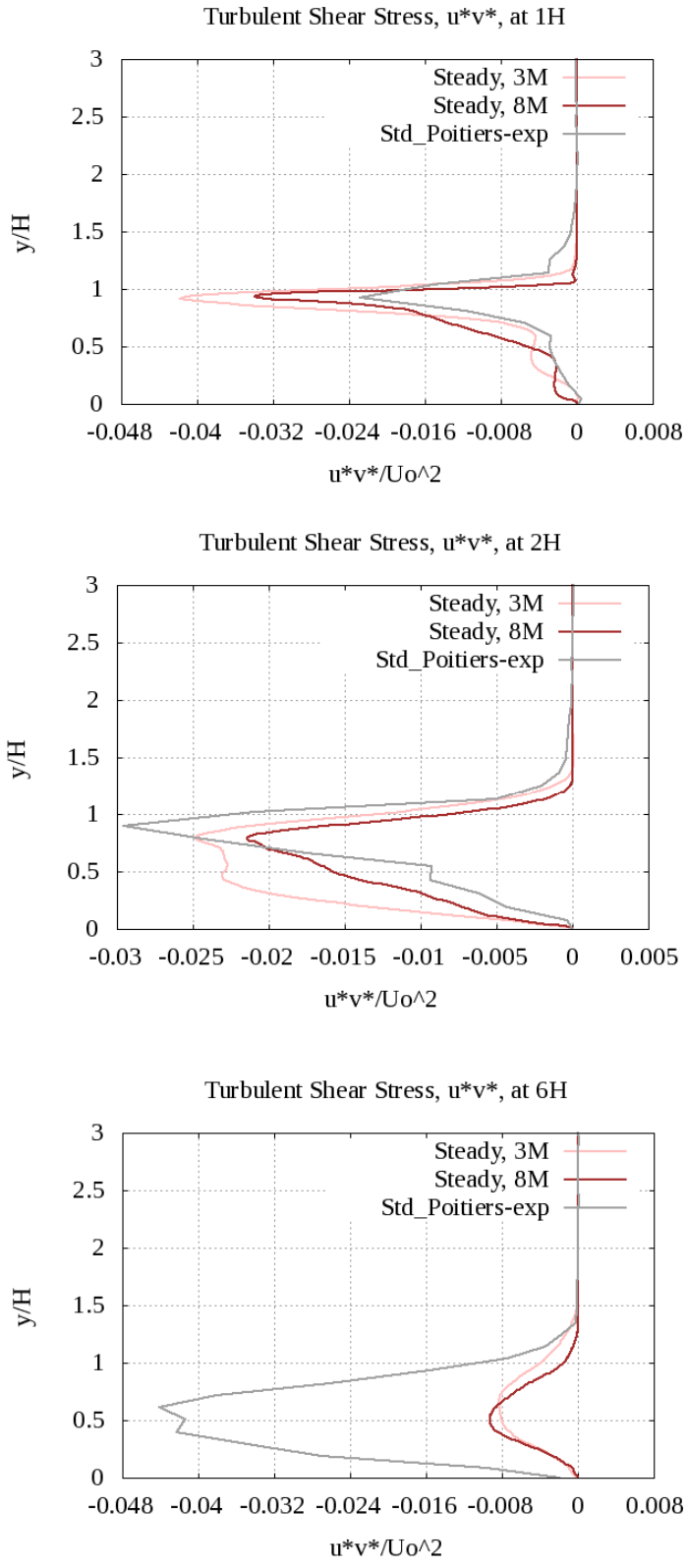

Figure 4.25 Normalised turbulent shear stress <u'v'> at 1H, 2H and 6H

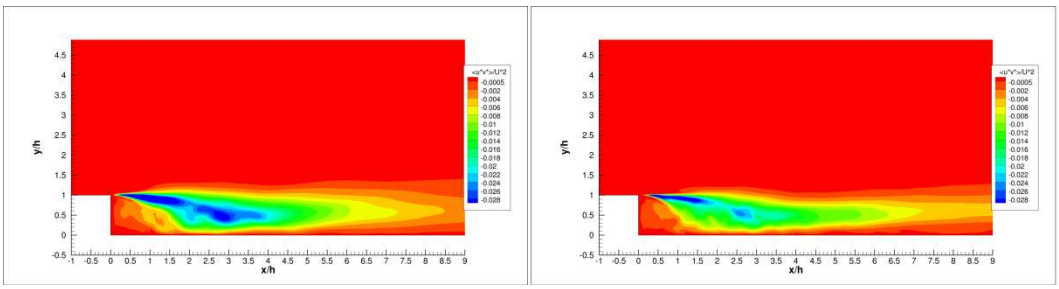

Figure 4.26 Normalised turbulent shear stress, <u'v'> for the 3M mesh –left- and the 8M mesh –right- steady plasma cases

This case is likely to be highly turbulent and therefore the number of cells in the spanwise direction is very relevant to solve the turbulent structures and to capture their three dimension character and this is the reason why the 3M mesh is not accurate enough when used in this study. This will be also appreciated in the following figure, Fig. 4.27, where the vorticity is depicted for a proper comparison,

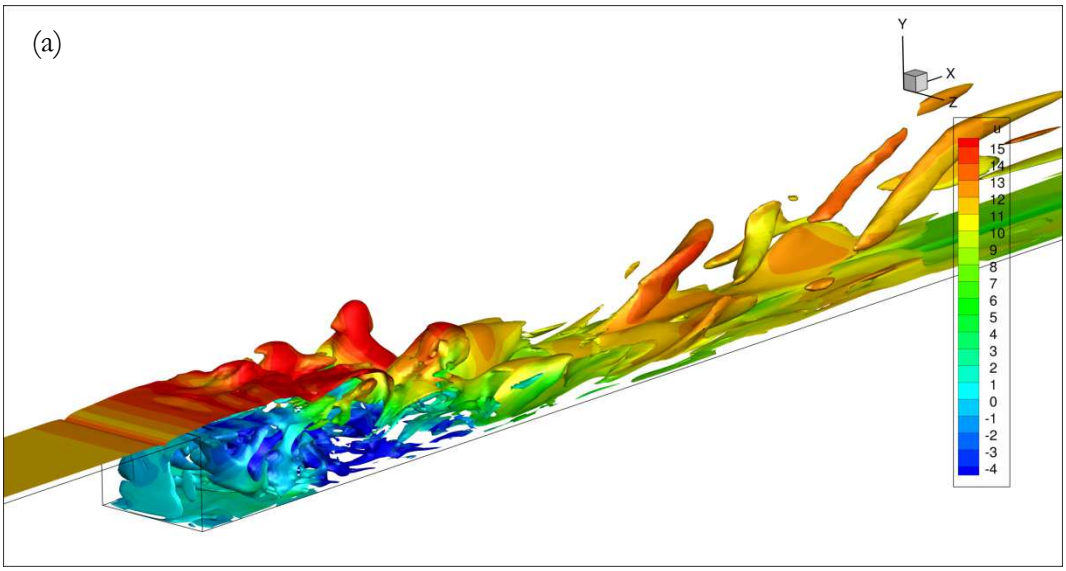

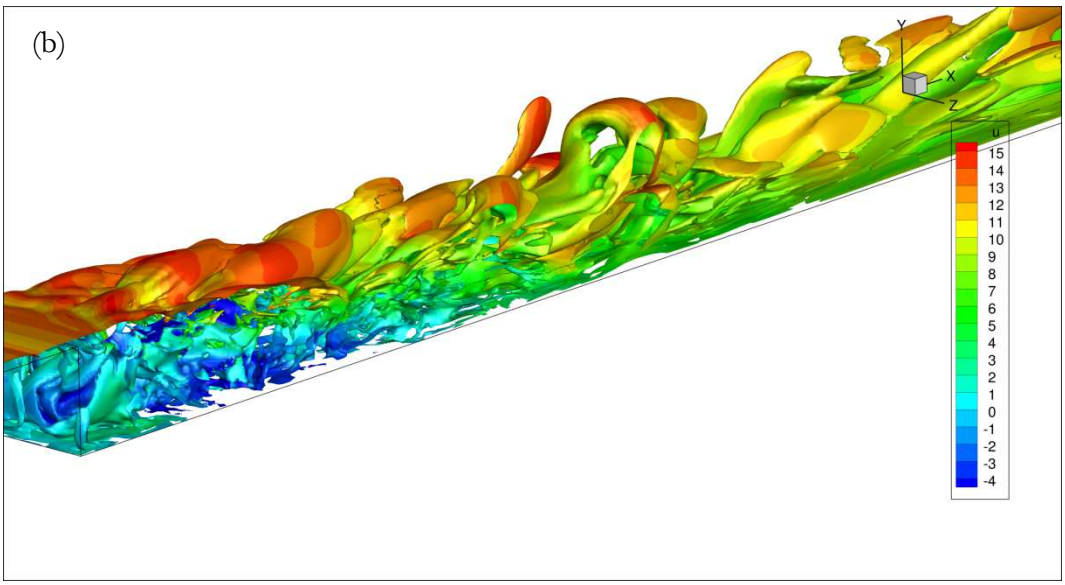

Figure 4.27 Iso-surface of vorticity magnitude at 30 for steady plasma using (a) a 3M mesh and (b) an 8M mesh

As it happened with the baseline case, the use of the finer mesh allowed a better insight into the resolution of the smaller turbulent structures. A coarser mesh is not able to capture them and as one of our interests was to gain a better and detailed understanding of the turbulent structures generated by the flow control devices and the effectiveness of such devices to manipulate flow separation which is similar to saying the size of the recirculation region, the 8M mesh produced more interesting and physically reliable results as it will be also seen later on in this Chapter.

4.3.3.3.3 Final mesh assessment and selection of 8M mesh

It has been shown in the previous sections of this chapter that a finer mesh produces better and more realistic results for this study. Hence, the 8M mesh was chosen to go deeper into the understanding of the backward facing step flow with a DBD actuator in this investigation.

As it was also shown in section **4.3.3.3.2**, the constant $C_{ROY}=7.0x10^{-8}$ under-predicts the reattachment length when compared to the experimental data therefore two smaller constants were tested to finally adjust Roy's model in three dimensional simulations using the 8M mesh.

4.3.3.4 Singh and Roy's model adjustment for the 8M mesh

Three different Singh and Roy's constants, Table 4.6, were investigated in order to perform the closest to experiment results simulation.

	Baseline (simulation)	**C_{ROY}= $7x10^{-8}$**	**C_{ROY}= $2.2x10^{-8}$**	**C_{ROY}= $7x10^{-9}$**	**Shyy, 65% efficiency**
X_R (H-based)	6H	4.1	5.7	6.3	6
% reduction	-	31.7%	5%	-5%	0%

Table 4.5 Singh and Roy's constants for 3D model adjustment cases

A simulation with Shyy's model using the 8M mesh was also carried out to provide a further understanding the performance of both models.

In order to choose a constant, the flow reattachment and time and spanwise averaged streamlines were compared to the experimental data.

Fig. 4.28 displays the time and spanwise averaged streamlines of the flow field for the three different constants. As it can be immediately see, $C_{ROY}=7.0x10^{-8}$ under-predicts the experimental results, $X_R=5.6H$, which means the constant is too high and the induced plasma force using that constant is greater than the experimental force. On the other hand, $C_{ROY}=7.0x10^{-9}$ barely affects the reattachment length when it is compared to the baseline flow, $X_R=5.85H$. However, $C_{ROY}=2.2x10^{-8}$ produces a reattachment length of ~5.75H which matches very well the experimental results

(a)

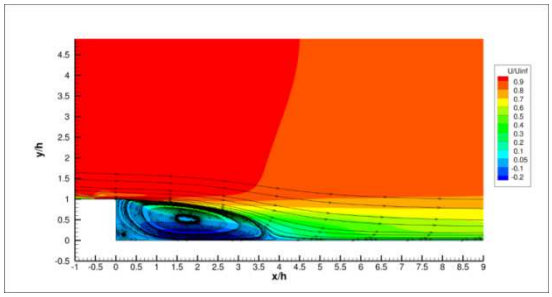

(b)

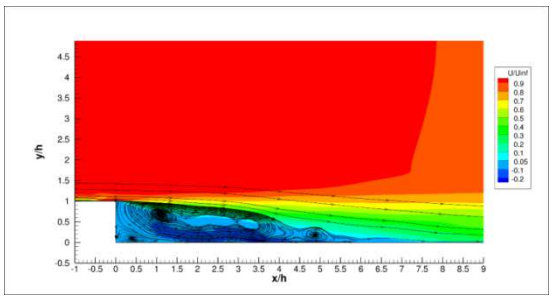

(c)

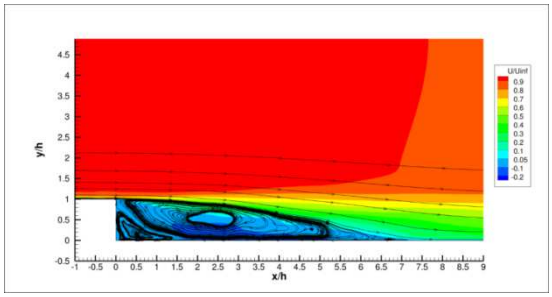

(d)

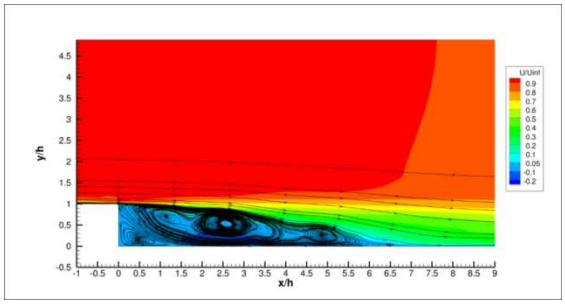

Figure 4.28 Time and spanwise averaged streamlines: (a) C_{ROY}=7x10^{-8}, (b) C_{ROY}=2.2x10^{-8}, (c) C_{ROY}=7x10^{-9}, (d) Shyy model, 65% efficiency

Velocity profiles at three relevant locations -1H, 2H and 6H- show the effects of the different constants,

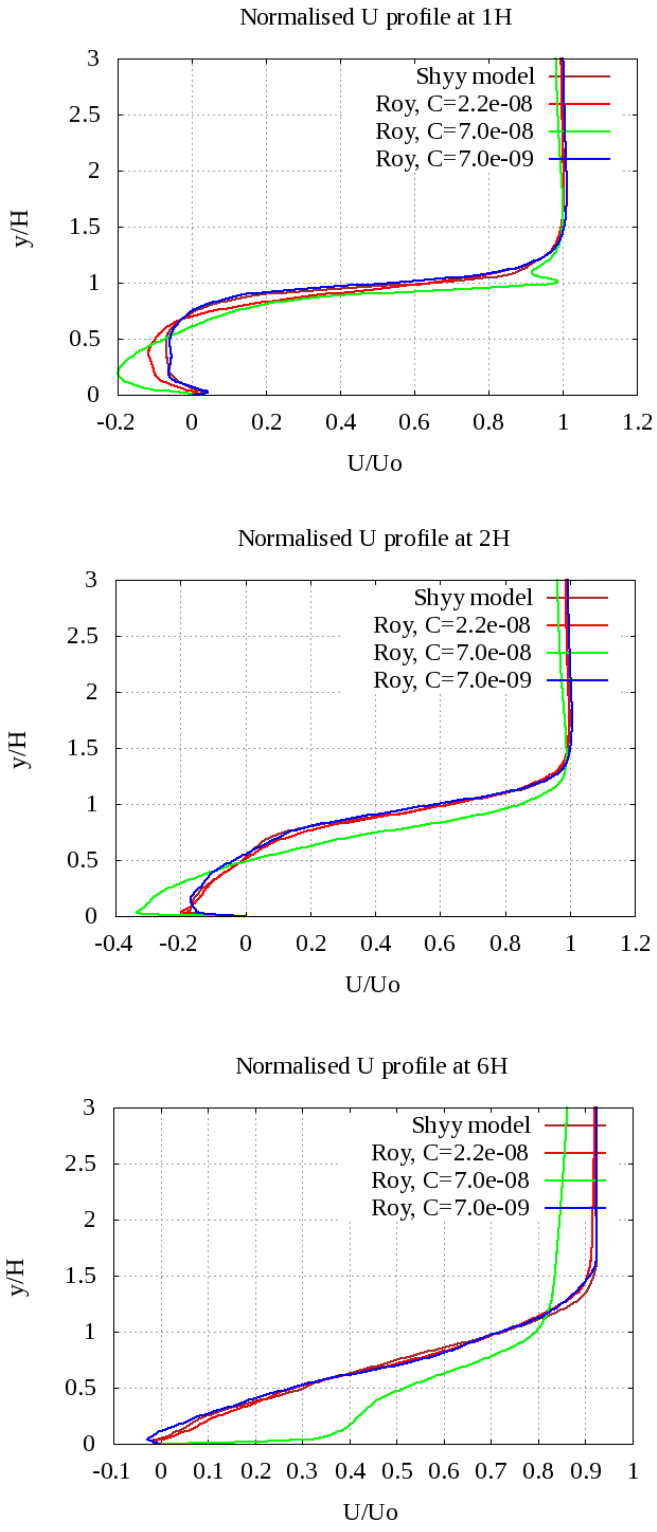

Figure 4.29 Velocity profiles at 1H, 2H and 6H for the three different Singh and Roy's constants and Shyy model

It can be seen that $C_{ROY}=7.0x10^{-8}$ has a bigger influence in the flow than the two other constants. The plasma force generated using that constant is stronger adding more momentum into the flow hence producing a higher streamwise velocity and a smaller reattachment length as it can be seen at 6H, where the flow is already attached and a new boundary layer is developing.

Finally, the Reynolds stresses are compared to the measured stresses at three different locations, Fig. 4.30 and Fig. 4.31.

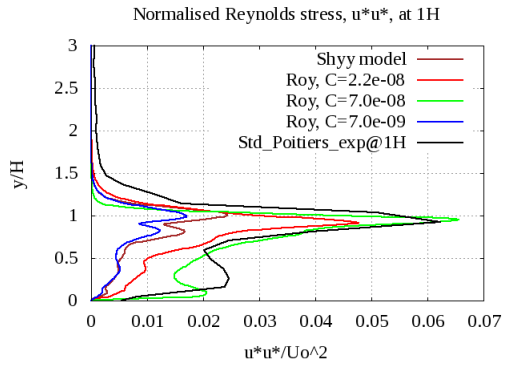
Normalised Reynolds stress, u*u*, at 1H
Shyy model
Roy, C=2.2e-08
Roy, C=7.0e-08
Roy, C=7.0e-09
Std_Poitiers_exp@1H
y/H
u*u*/Uo^2

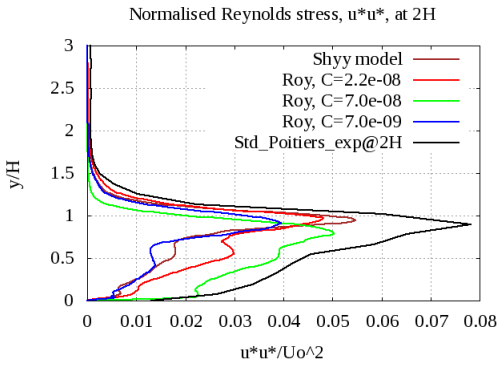
Normalised Reynolds stress, u*u*, at 2H
Shyy model
Roy, C=2.2e-08
Roy, C=7.0e-08
Roy, C=7.0e-09
Std_Poitiers_exp@2H
y/H
u*u*/Uo^2

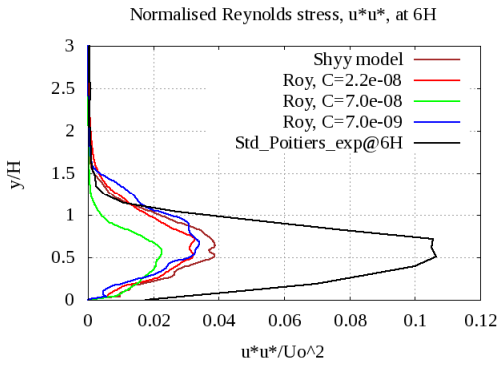
Normalised Reynolds stress, u*u*, at 6H
Shyy model
Roy, C=2.2e-08
Roy, C=7.0e-08
Roy, C=7.0e-09
Std_Poitiers_exp@6H
y/H
u*u*/Uo^2

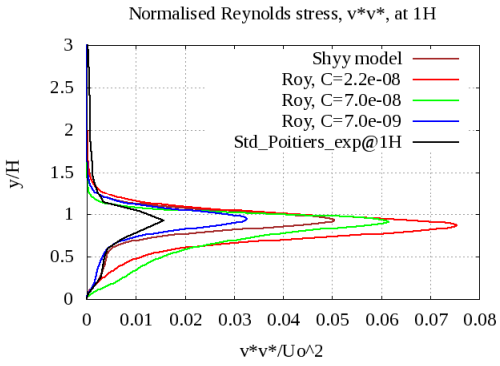
Normalised Reynolds stress, v*v*, at 1H
Shyy model
Roy, C=2.2e-08
Roy, C=7.0e-08
Roy, C=7.0e-09
Std_Poitiers_exp@1H
y/H
v*v*/Uo^2

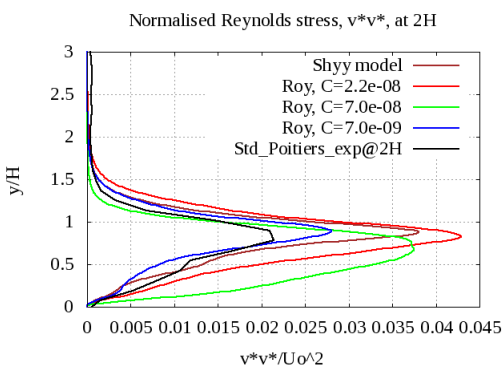
Normalised Reynolds stress, v*v*, at 2H
Shyy model
Roy, C=2.2e-08
Roy, C=7.0e-08
Roy, C=7.0e-09
Std_Poitiers_exp@2H
y/H
v*v*/Uo^2

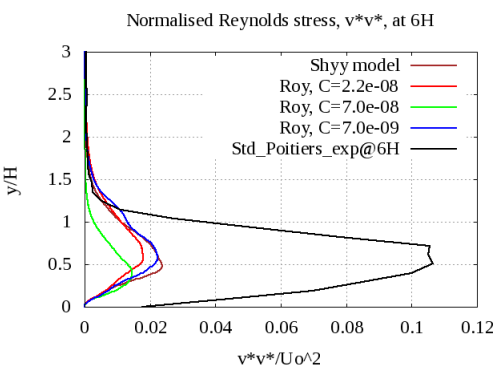
Normalised Reynolds stress, v*v*, at 6H
Shyy model
Roy, C=2.2e-08
Roy, C=7.0e-08
Roy, C=7.0e-09
Std_Poitiers_exp@6H
y/H
v*v*/Uo^2

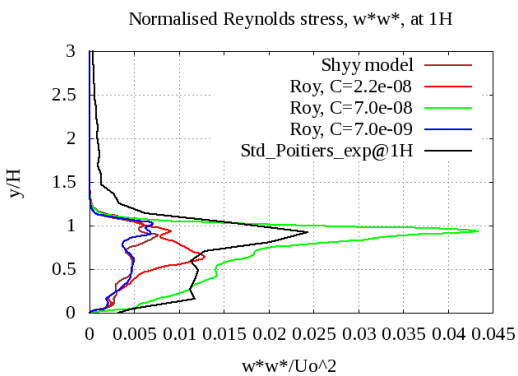
Normalised Reynolds stress, w*w*, at 1H
Shyy model
Roy, C=2.2e-08
Roy, C=7.0e-08
Roy, C=7.0e-09
Std_Poitiers_exp@1H
y/H
w*w*/Uo^2

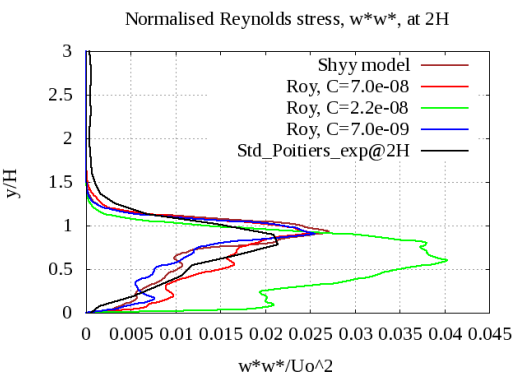
Normalised Reynolds stress, w*w*, at 2H
Shyy model
Roy, C=7.0e-08
Roy, C=2.2e-08
Roy, C=7.0e-09
Std_Poitiers_exp@2H
y/H
w*w*/Uo^2

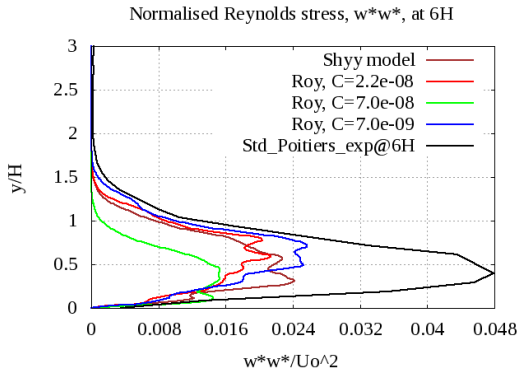

Figure 4.30 Normalised Reynolds stresses at 1H, 2H and 6H for three different Roy's constants, Shyy model and experiment

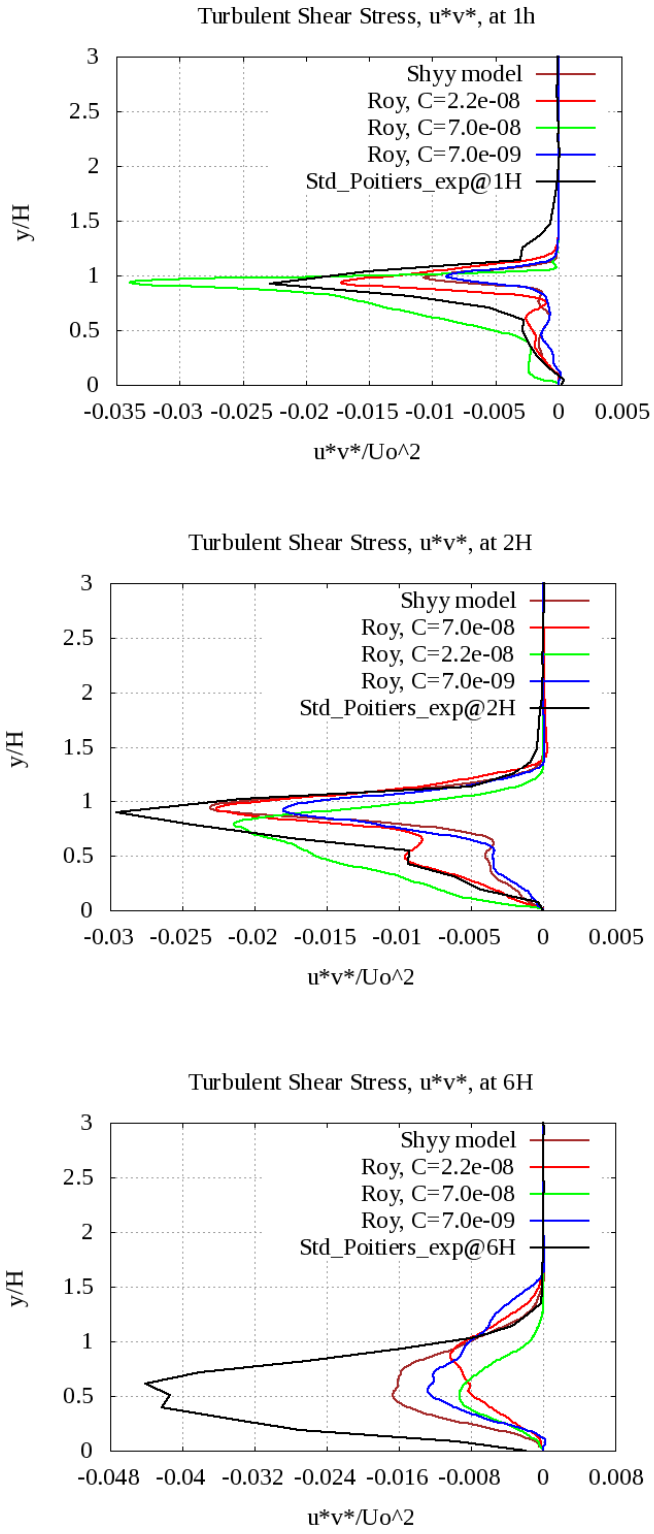

Figure 4.31 Normalised turbulent shear stress <u'v'> at 1H, 2H and 6H for three different Roy's constants, Shyy's model and experiment

The normalised <*u'u'*> component is under-predicted by simulations at the three locations except at 1H where the case with C_{ROY}=7.0x10^{-8} shows a very good comparison with experiment.

With regards to normalised <*v'v'*>, all simulations over-predict the experimental profile within the recirculation region but at 6H all of them are under-predicted. It can be also seen the effects of the performance of plasma when using different constants: the bigger the constant the greater over-prediction is observed.

The other component, normalised <*w'w'*>, is largely over-predicted at 1H by the highest constant, C_{ROY}=7.0x10^{-8}, but all cases show more alteration in the profile when compared to the other normal components of the normalised Reynolds stress. At 2H all the cases but the C_{ROY}=7.0x10^{-8} case show really good agreement with the experimental profile, being C_{ROY}=2.2x10^{-8} the case which shows the best agreement. Finally at 6H and as it happens also previously, all simulations under-predict the value of this Reynolds stress normal component.

Fig. 4.40 shows the normalised Reynolds shear stress <*u'v'*>. The "M" shape at the peak in the experimental profile at 6H is captured by all cases except the C_{ROY}=7.0x10^{-8} case which shows a smooth curvature in the peak, being once more the case which is farther from the experimental measurements.

In all the Reynolds stress profiles, the different shapes, peak and valleys of the curves are due to the interaction between vortices generated by the different value of the generated plasma force and also depending on which model has been used, i.e., Singh and Roy or Shyy.

Overall, the case with C_{ROY}=2.2x10^{-8} shows a better agreement with the experimental data. Therefore, this constant was selected in order to perform any simulation with the DBD plasma actuator when operating in steady mode.

4.3.3.5 Final results and discussion: comparison with experimental data

A final comparison of just this case with the baselines –experimental and computational- and the quasi-steady experimental case is carried out in the next section of this chapter. A further investigation of the turbulent structures, velocity

and Reynolds stress distribution, reattachment region and skin friction coefficient for the case C_{ROY}=2.2x10^{-8} is fully described in this section.

4.3.3.5.1 Analysis of turbulent coherent structures of the flow

"A vortex exists if streamlines mapped onto a plane normal to its core exhibit a circular or spiral patter under an appropriate reference frame" [Robinson, 1991]. In a turbulent boundary layer the motion of fluid is intermittent; however, large scale motions can be identified and they are strongly organised, being hence characterised by a coherent nature. Coherent structures in a simple flow can be reduced to four basic structures such as line vortex, ring vortex, hairpin vortex and helical vortex. A combination of these four elements prompts more complex turbulent coherent structures observed in any kind of flow. Several structures can be identified in wall-bounded flows such as streaks, bursts, pockets, large scale sweeps in the region dominated by viscosity or large scale of motions and mushroom eddies in the outer region of the flow, [Falco, 1989; Jimenez et al, 1993; Rogers & Moser, 1994; Robinson, 1991; Brook & Hanratty, 1993; Smith et al, 1991; Adrian, Meinhart & Tomkins, 2000]. The analysis of the coherent structures [Fiedler, 1987] and the identification of the vortices in the flow [Haller, 2004; Chakraborty et al, 2005] for the CFD simulations are performed here.

Q-criterion [Hunt et al, 1988] was used in this study to identify the turbulent structures in the flow field. This criterion was the first three dimensional criterion to identify coherent structures in a turbulent flow. It is a local approach based on velocity gradient tensor, a Galilean invariant vortex identification technique [Haller, 2005]. The method identifies vortices by defining them as a spatial region where the Euclidean norm of the vorticity tensor dominates over the Euclidean norm of the rate of strain tensor. It is expressed via the following equation,

$$Q = \frac{1}{2}[|\Omega|^2 - |S|^2] > 0 \qquad (5.1)$$

In the Q-criterion, the pressure in the eddy must be lower than the ambient pressure; however Q>0 does not ensure a pressure in the eddy lower than the ambient [Jeong and Hussain, 1995]. In most of cases, this statement is included.

Fig. 4.32 displays a comparison Q-criterion at (a) 1000, (b) 100,000 and (c) 200,000 for the baseline flow and the steady plasma case.

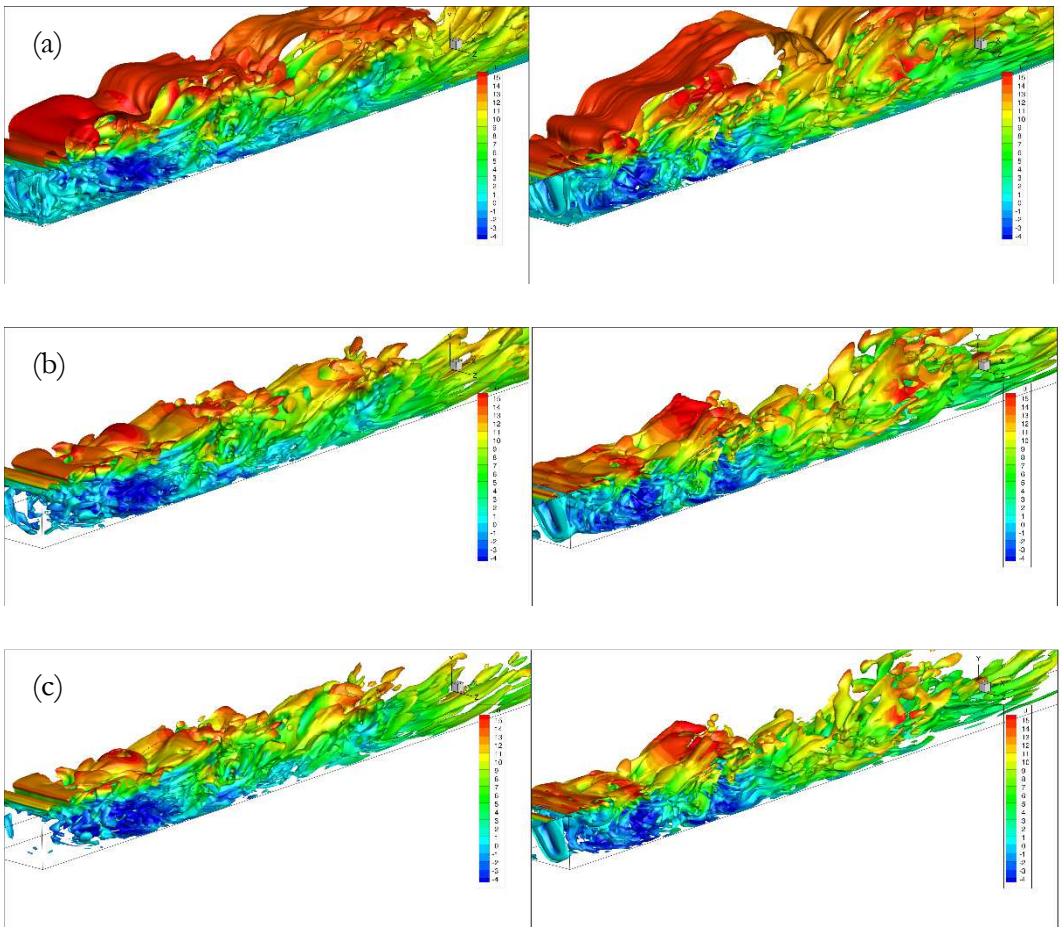

Figure 4.32 Q-criterion of baseline case–left column- and the steady plasma actuation –right column- at (a) 1000, (b) 100,000 and (c) 200,000. Iso-surfaces coloured by streamwise velocity.

Before the step for the baseline case, quasi-two dimensional vortex tubes are formed and then shed from the step edge. Then, these tubes interact with the structures in the recirculation region, break down and hairpin structures and Falco eddies [Falco, 1979] are observed further downstream. It is also observed than the lower parts of these larger structures produce the shear layer in the recirculation and break into smaller structures towards the wall for both uncontrolled and controlled simulations. Overall, in the plasma actuation cases, the aforementioned quasi-two dimensional vortex tubes are flattered due to the acceleration of the flow in the near-wall boundary layer that steady plasma induces. Also, the hairpin-like structures are formed also after the step and are predominant over the typical eddies. Finally, steady

forcing influences the flow after the reattachment area and larger structures appear after the primary air bubble when compared to the baseline case.

4.3.3.5.2 Velocity profiles

Unfortunately, there was no available data for the steady forcing experimental velocity profiles. Velocity profiles are depicted at nine different x/H locations, where the experimental data for the baseline flow was measured. At 8H, 10H and 14H only the baseline and steady plasma –simulation- profiles are compared.

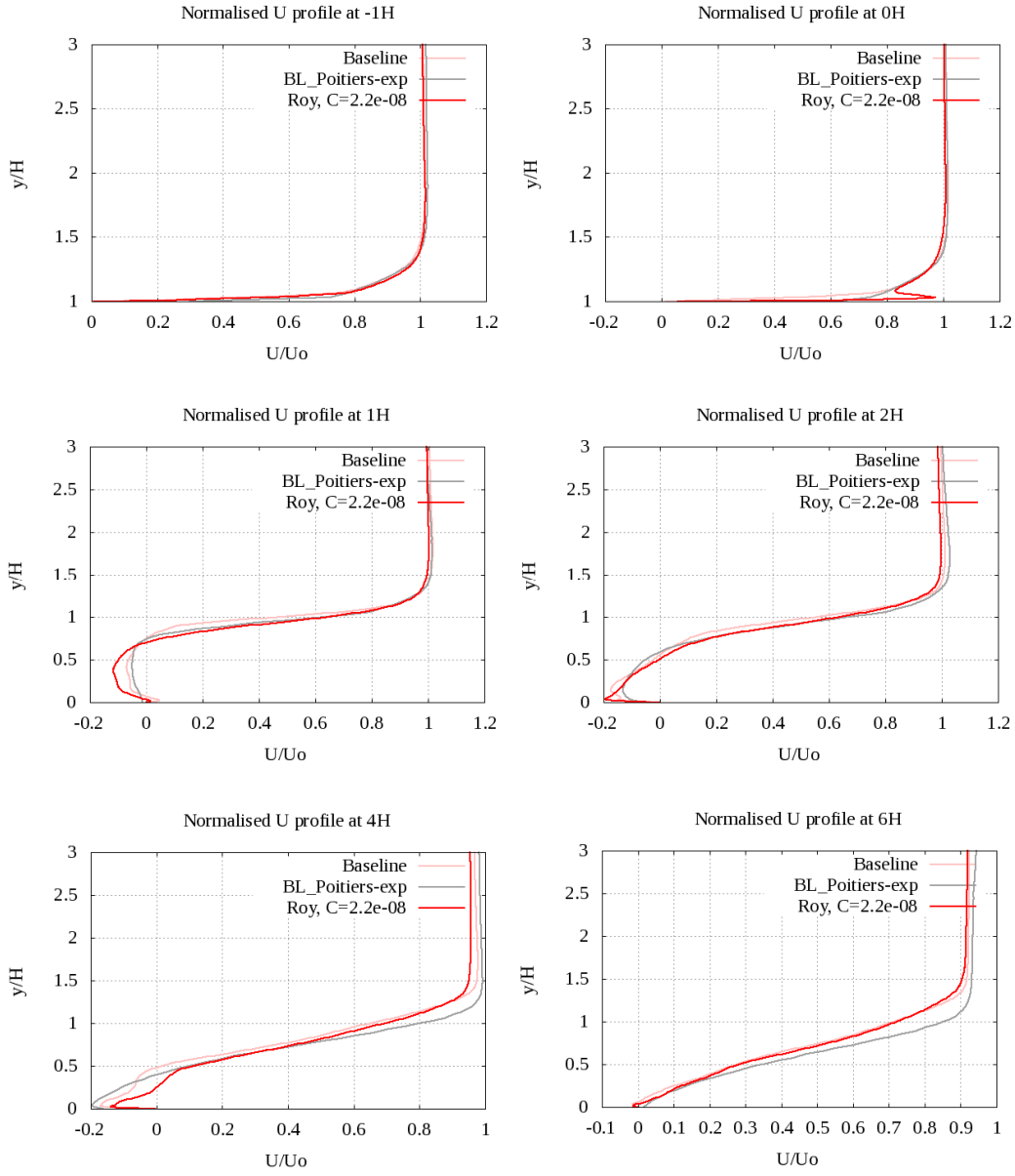

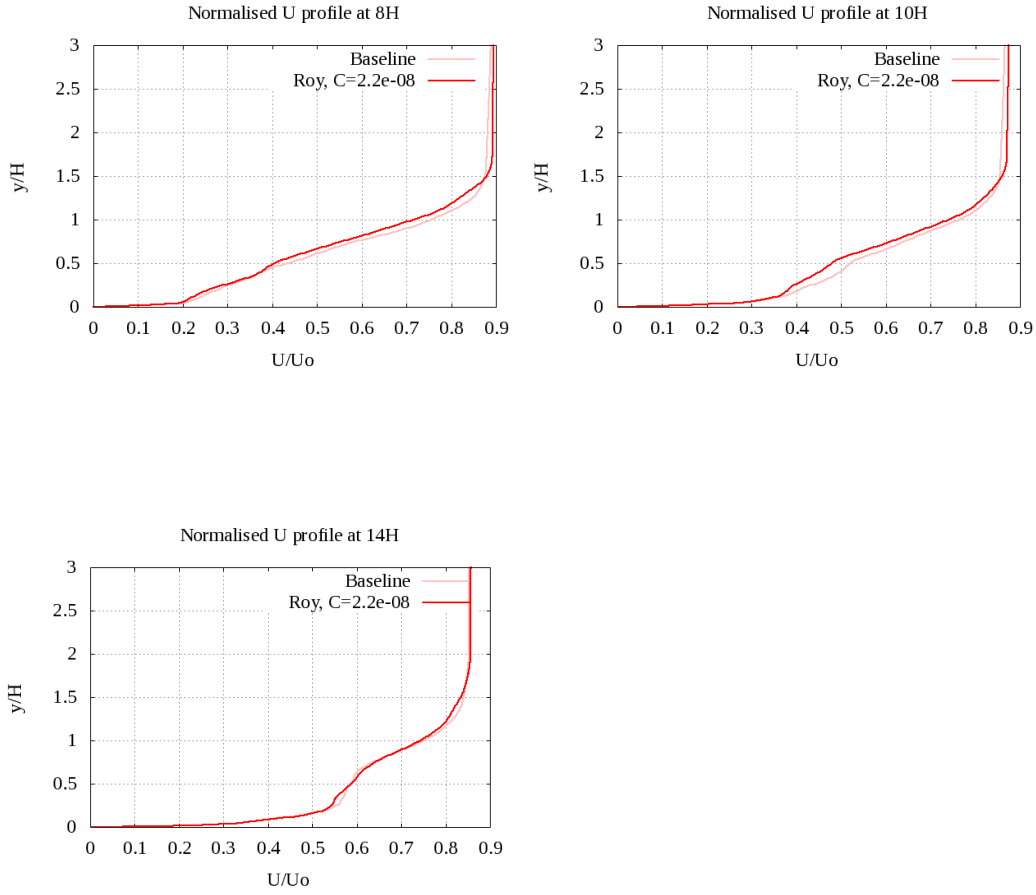

Figure 4.33 Comparison of velocity profiles of baseline cases –simulation and experiments- and steady plasma force – simulation and experiment- at -1H, 0H, 1H, 2H, 4H, 6H, 8H, 10H, 14H

At -1H, velocity profiles of the three set of data are practically identical. It was previously said that the data at the inlet was provided by Poitiers and it shows that the development of the flow before the step edge is very accurate, the boundary thickness from experiments was 13mm and it can be seen all simulations match it perfectly. At this location, the flow has not reached the plasma actuator therefore it is obvious that the velocity profile is coincident with the baseline case profile.

At step, the effects of plasma are clearly seen: the flow near the wall suffers a dramatically acceleration and streamwise velocity increases up to a 95% of the free-stream velocity.

Once the flow moves downstream of the step, at 1H the baseline simulation matches very well the experimental profile and the baseline secondary bubble appears to be larger than the plasma secondary region. This will be clearly seen later on when the

flow streamlines is depicted in section **4.3.2.3** of this chapter. At the location of 2H, simulation shows good agreement with experimental data and plasma shows this time higher negative values of velocity near to the wall and the shear layer is located closer to the wall than the baseline cases due to the effects of plasma.

Closer to the reattachment point, at the location 4H, the velocity of the plasma case in the near wall region and within the circulation bubble increases. This implies that the flow will be attached to the wall before the baseline cases. Further downstream at 6H, simulations show a small negative value, which indicates the presence of small embedded eddies near the wall. The velocity profile from experiments, on the other hand, shows positive values at all y/H locations indicating the flow is fully attached to the wall is such location.

Finally at 8H, 10H and 14H only the simulation profiles are compared. Both uncontrolled and controlled cases have a similar growing boundary layer recovery.

4.3.3.5.3 Reattachment region and skin friction distribution studies

This section comprises the analysis of the reattachment area for the baseline and steady plasma forcing cases and compares the simulation results with the experimental database. Besides, an exploration on the skin friction coefficient was carried out and analysed.

In Fig. 4.34 the streamlines of both experiments and simulations are shown. The baseline flow reattaches to the wall at 5.8H in the experiments and at 6H in the simulation. This over-prediction was acceptable and the reason was explained in the previous section of this chapter. With regards to plasma, the experimental reattachment length occurs at 5.6H and at 5.7H at simulation. This slight difference is caused by the grid high-stretching ratio in the shear layer slowing down the flow velocity and hence increasing the length of the reattachment. The secondary bubble is well predicted in both uncontrolled and controlled cases: for the baseline simulation it is located at ~1.6H which is equal to the experimental baseline; and for plasma in the experiments a smaller secondary bubble appears due to the effects on plasma and it reattaches at 1H as well as in simulation results.

Despite of the slight differences in the primary reattachment length, very good and satisfactory agreement was found between simulations and experiments.

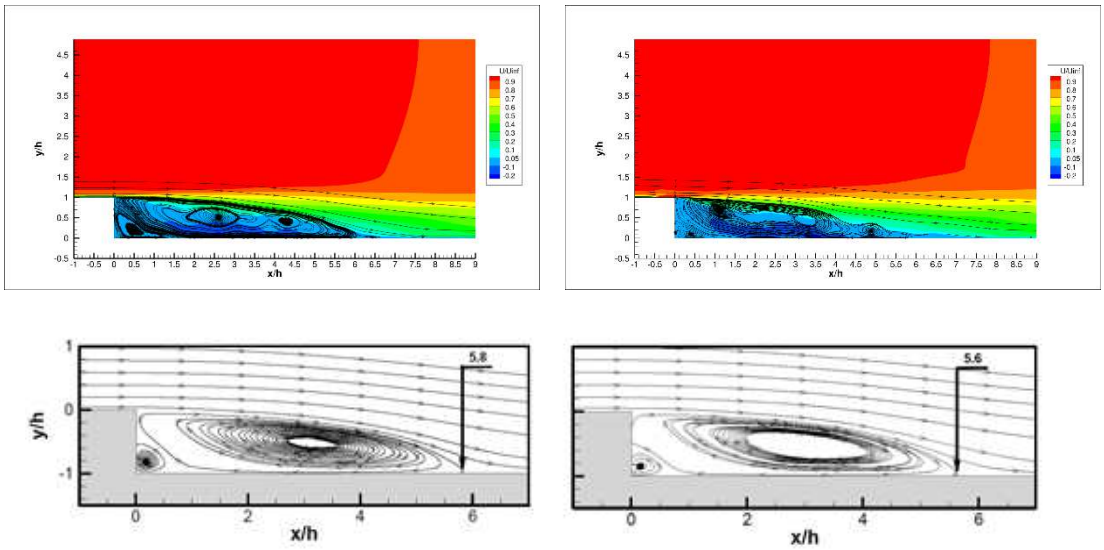

Figure 4.34 Streamlines of flow field: baseline –left column- and steady plasma actuation –right column- comparison. Top row: simulations; bottom: experimental data

The time and spanwise averaged skin friction coefficient distribution along the streamwise direction is depicted in Fig. 4.35. Before the step, it can be seen the very strong effects on plasma skin friction: the velocity in the near wall region increases dramatically hence does the skin friction. The skin friction curves for both cases show a zigzag shape along the x-direction. It is due to the lack of uniformity of the streamwise velocity near the wall despite of it was time averaged. This non-uniformity distribution is caused by the strong 3D characteristics of the flow. Besides, these 3D iDDES simulations required a large amount of computational time hence due to the limitation of resources available and despite the simulation ran for a long time, the results show that the statistical convergence might not have been fully achieved and for this reason the results do not show a fully smooth skin friction distribution for the mean values. This issue will be also observed on the synthetic vortex generators in the next chapter of the thesis.

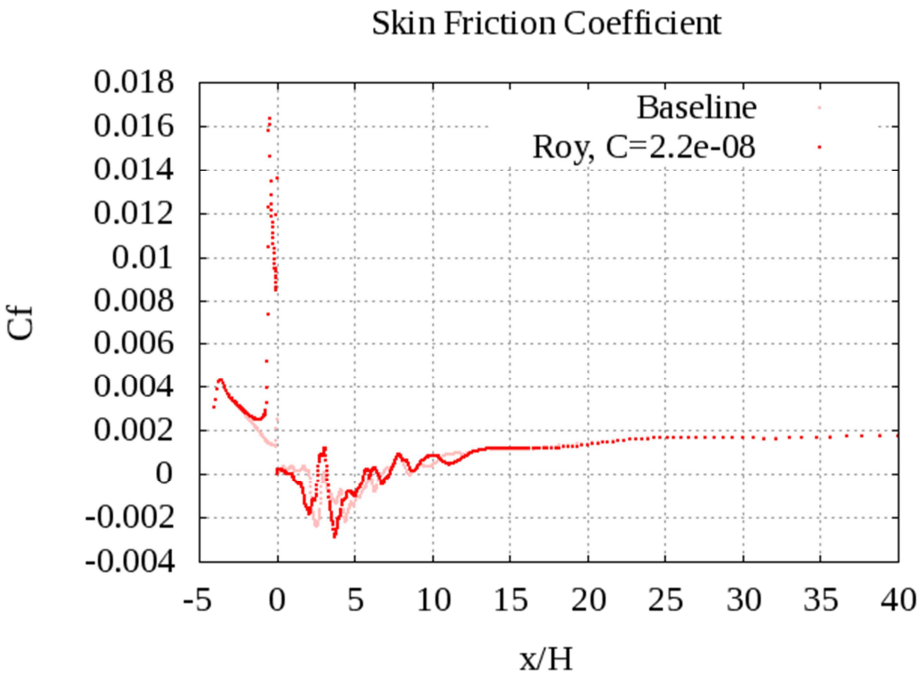

Figure 4.35 Skin friction coefficient distribution along the streamwise direction.

An x-z view of the skin friction distribution can be seen in Fig. 4.36 for the baseline and the plasma case simulations. The effects of plasma are also observed in the plasma actuator location before the step: skin friction peaks in this area as shown in previous graph, Fig. 4.35.

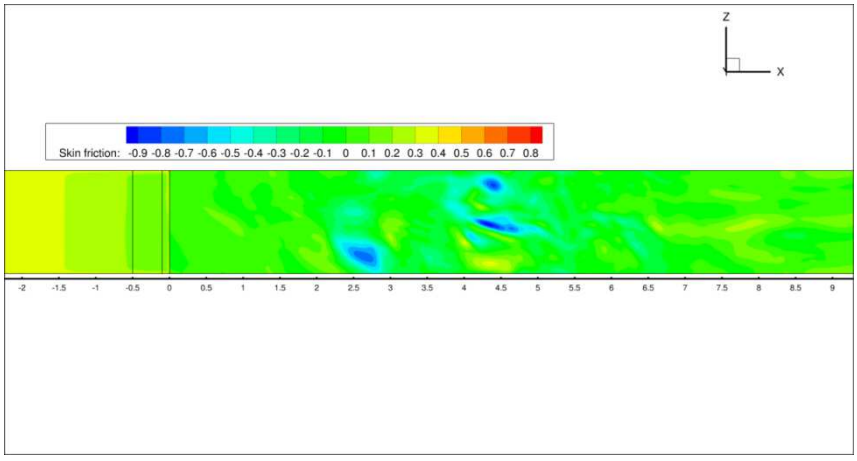

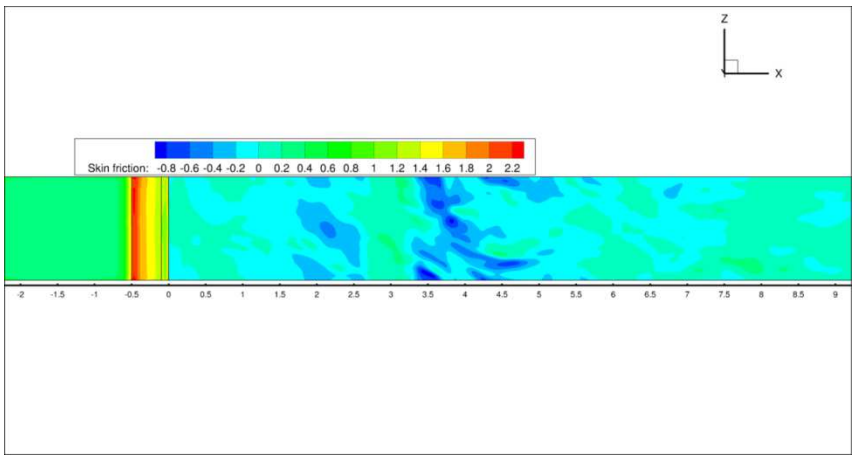

Figure 4.36 x-z plane showing inverse skin friction distribution

An non-homogeneous distribution of the skin friction is observed downstream of step indicating the high unsteadiness of the flow field in both cases.

4.3.3.5.4 Reynolds stress

A comparison of the Reynolds stress profiles at x=1H, 2H and 6H for the baseline and steady plasma actuation is shown in this section. Reynolds stress contours in the vicinity of the step are also analysed for both uncontrolled and controlled cases, but only experimental data is available for the turbulent shear stress $\langle u'v' \rangle$.

Fig.4.37 shows the normal components of the Reynolds stresses at the three aforementioned locations.

Regarding the normalised $\langle u'u' \rangle$ component, at 1H similar profiles for both baseline and experimental baseline and for experimental and simulation plasma actuation are found. At 2H, the Reynolds stress from the baseline simulation is over-predicted in comparison with the experimental measurement and for plasma actuation, the data from the controlled simulation shows reasonably agreement with the experimental profile. At the location of x/H=6, the baseline case profile from computation is over-predicted but the plasma profile is under-predicted.

With regards to the $\langle v'v' \rangle / U^2$. Simulations over-predict this component at 1H and 2H where the peak of this component appears, however experiments and simulations show good agreement in the near wall region and above y/H=1.5. It can be also seen that plasma cases produce larger values of $\langle v'v' \rangle$ than the baseline cases. However,

at 6H, simulation of plasma is again, as it happened with the $<u'u'>$ component, under-predicted and the baseline simulation profiles is over-predicted.

Finally, there was no experimental data for the component $<w'w'>/U^2$ but still the data from the simulations is depicted to evaluate the effects of plasma actuation. At 1H and 2H, experiments and simulations show good agreement, but again at the reattachment area location, simulation under-predicts experimental values for the normalised $<w'w'>$. In the near-wall region at the three locations this component is less smooth than the other two components of the normal Reynolds stresses. This feature is also captured by the experimental measurements.

Overall, and especially in the recirculation locations -1H and 2H- the prediction of the Reynolds stress is acceptable. At 6H, Reynolds stresses from simulations are under-predicted, fact which is probably caused by the acceleration of the velocity in the streamwise direction although further investigation was required and findings will be shown later on in this thesis in order to address this discrepancy between experiments and simulations with DGDES.

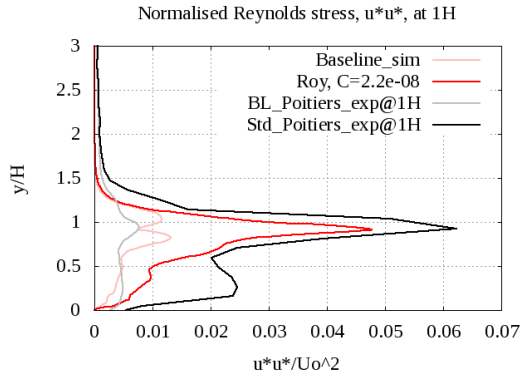
Normalised Reynolds stress, u*u*, at 1H
Baseline_sim
Roy, C=2.2e-08
BL_Poitiers_exp@1H
Std_Poitiers_exp@1H
y/H
u*u*/Uo^2

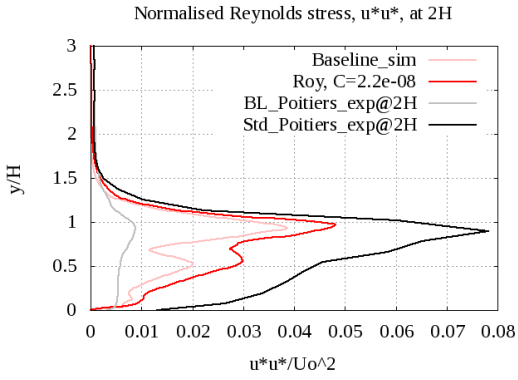
Normalised Reynolds stress, u*u*, at 2H
Baseline_sim
Roy, C=2.2e-08
BL_Poitiers_exp@2H
Std_Poitiers_exp@2H
y/H
u*u*/Uo^2

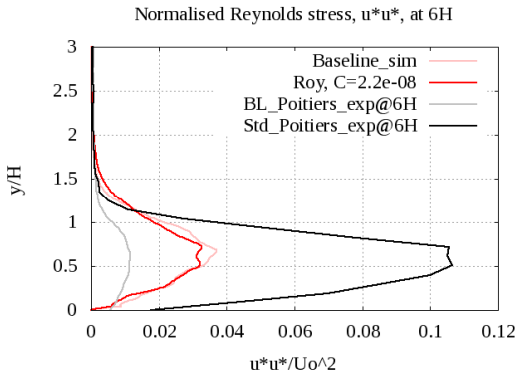
Normalised Reynolds stress, u*u*, at 6H
Baseline_sim
Roy, C=2.2e-08
BL_Poitiers_exp@6H
Std_Poitiers_exp@6H
y/H
u*u*/Uo^2

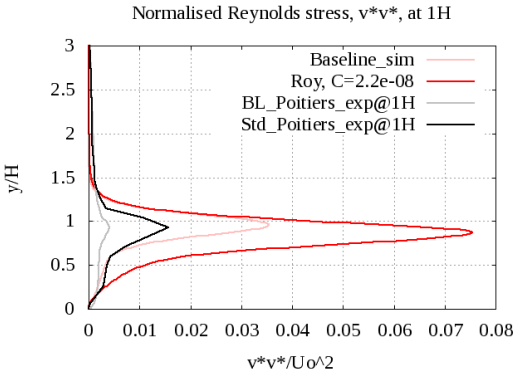
Normalised Reynolds stress, v*v*, at 1H
Baseline_sim
Roy, C=2.2e-08
BL_Poitiers_exp@1H
Std_Poitiers_exp@1H
y/H
v*v*/Uo^2

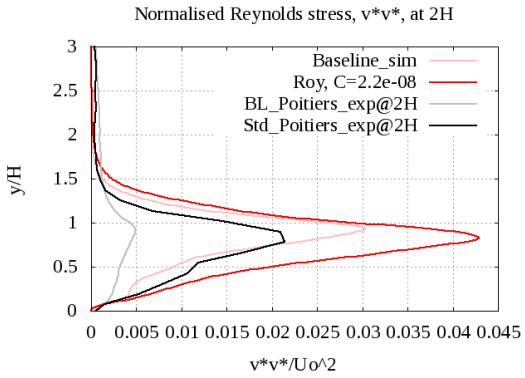
Normalised Reynolds stress, v*v*, at 2H
Baseline_sim
Roy, C=2.2e-08
BL_Poitiers_exp@2H
Std_Poitiers_exp@2H
y/H
v*v*/Uo^2

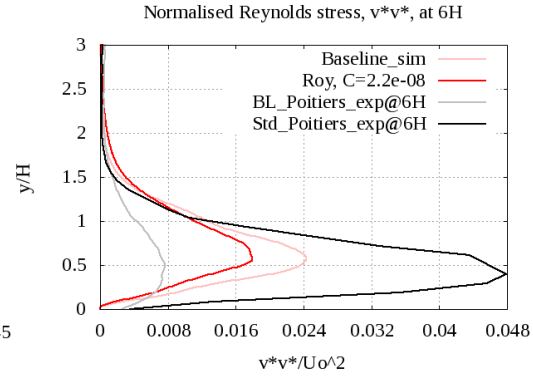
Normalised Reynolds stress, v*v*, at 6H
Baseline_sim
Roy, C=2.2e-08
BL_Poitiers_exp@6H
Std_Poitiers_exp@6H
y/H
v*v*/Uo^2

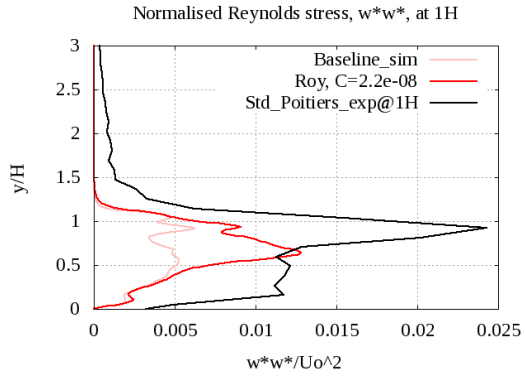
Normalised Reynolds stress, w*w*, at 1H
Baseline_sim
Roy, C=2.2e-08
Std_Poitiers_exp@1H
y/H
w*w*/Uo^2

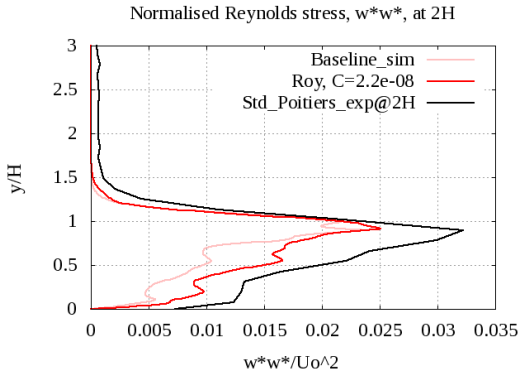
Normalised Reynolds stress, w*w*, at 2H
Baseline_sim
Roy, C=2.2e-08
Std_Poitiers_exp@2H
y/H
w*w*/Uo^2

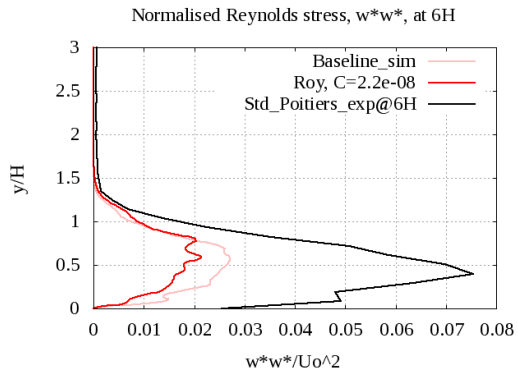

Figure 4.37 Comparison of normalised Reynolds stresses <u'u'>, <v'v'>, <w'w'> at 1H, 2H and 6H for baseline and steady plasma

Fig. 4.38 shows the contours of the three normalised Reynolds stresses: first row is normalised $\langle u'u' \rangle$, second is $\langle v'v' \rangle$ also normalised and the third row is the component $\langle w'w' \rangle / U^2$. Looking at the nine contours, an overall increase of Reynolds stress is observed for the controlled cases. The effects of plasma are clearly seen in all the components, especially $\langle u'u' \rangle$, where there is an important increase of its values near the step edge and immediately after it. It is also seen that Reynolds stresses are larger in the vicinity of the bottom corner of the step, indication of a smaller secondary bubble for the controlled cases as shown in previous sections of this chapter.

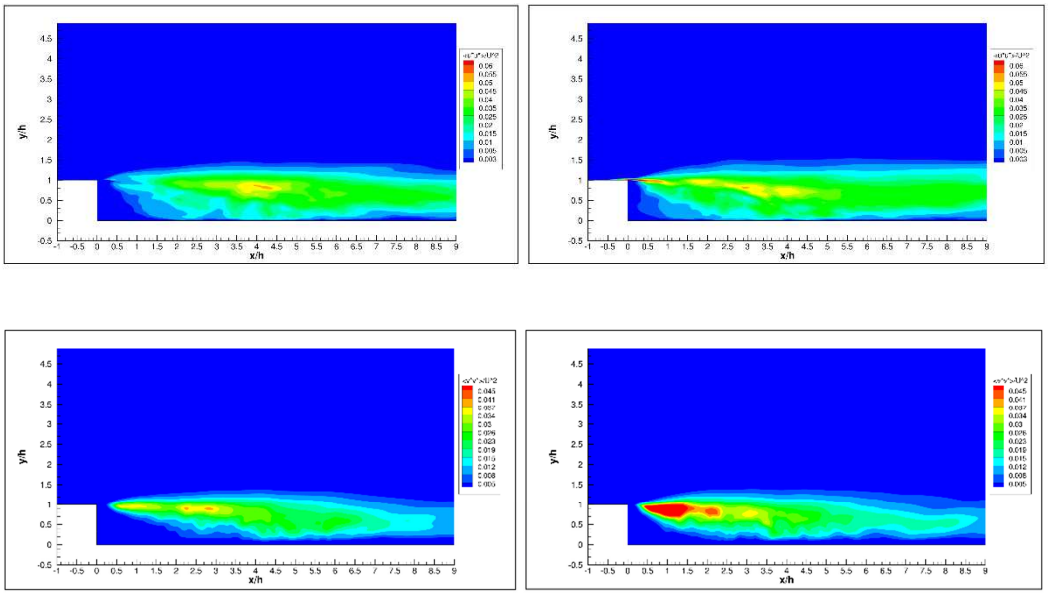

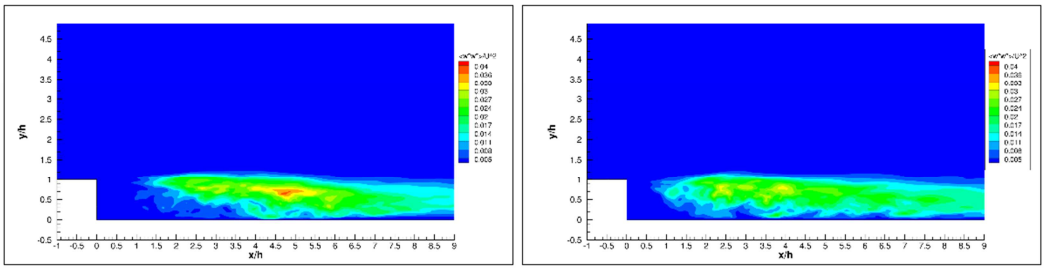

Figure 4.38 Time and spanwise averaged normalised Reynolds stress contours <u'u'>, <v'v'>, <w'w'>

With regards to Reynolds shear stress $\langle u'v' \rangle / U^2$, Fig. 4.39, simulations shows very similar profiles to the experimental profiles within the recirculation region, at 1H and 2H, for controlled and uncontrolled cases. At 6H, baseline simulation shows very good accuracy with respect to the experimental measurement; nevertheless, as it happened with the normal components of Reynolds stress, experimental data shows a larger normalised $|\langle u'v' \rangle|$ than simulation although the valley within the mixing layer at y/H=0.5 is captured. It is also remarkable to mention that turbulent shear stress is very well predicted in the near the step at 1H and 2H especially for the plasma cases and it is very accurately matched by the baseline data from simulations at 6H.

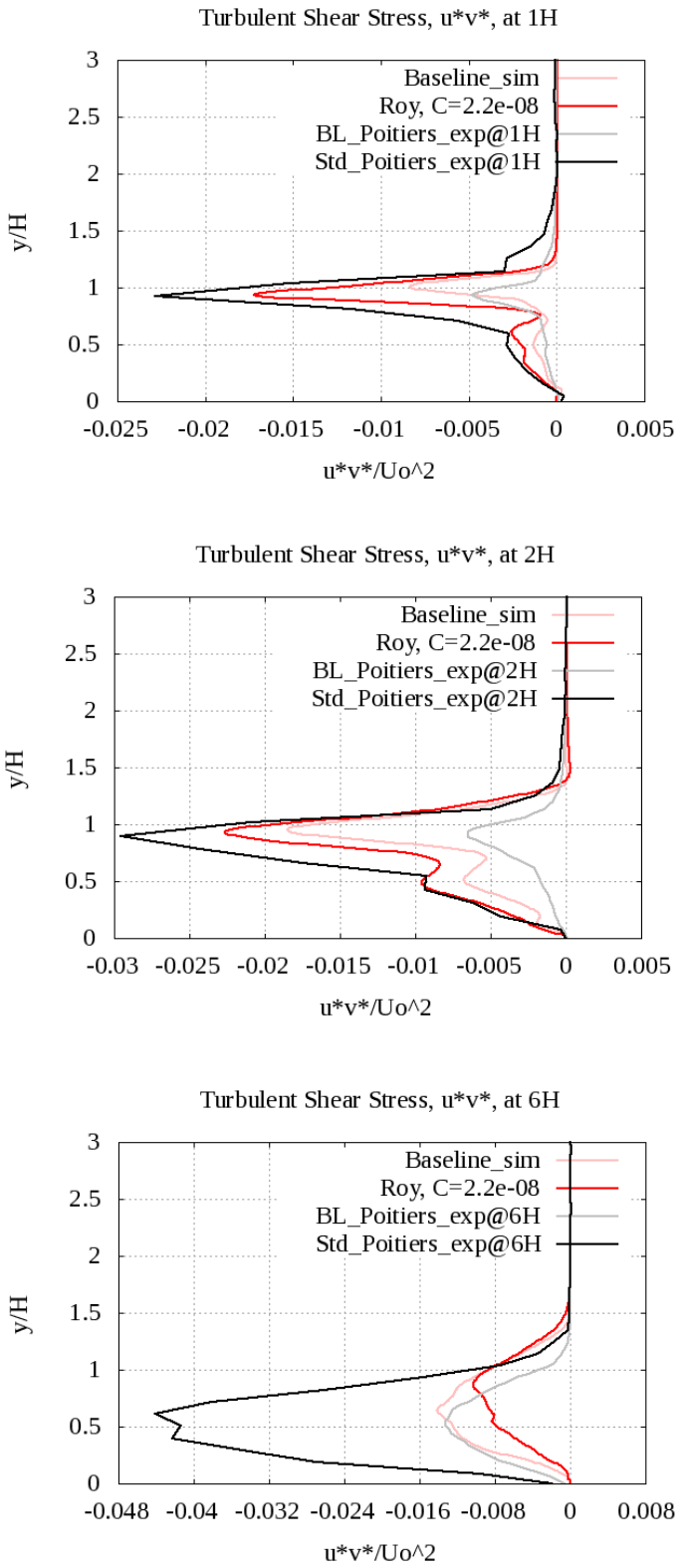

Figure 4.39 Comparison of normalised Reynolds shear stress <u'v'> at 1H, 2H and 6H for baseline and steady plasma

Finally the contours of normalised <*u'v'*> are depicted in Fig.4.40. Only the contours for the baseline case were available from the experimental side. Simulation results have been time and spanwise averaged. In order for the images to be comparable, it must be said that the range of experiments when normalised dividing by U^2 is (-0.012,0). The shape of the distribution of the shear stress is very similar for the baseline simulation and the baseline measurements. With regards to plasma cases and despite of the long time-average performed, the simulation shows a non-homogeneous distribution in the near-wall region within the recirculation region caused by the small embedded eddies shown as well in Fig. 4.34 – Flow streamlines. An increase of the shear stress is also captured near the bottom corner of step which means there is a mixing improvement causing a reduction of the reattachment point.

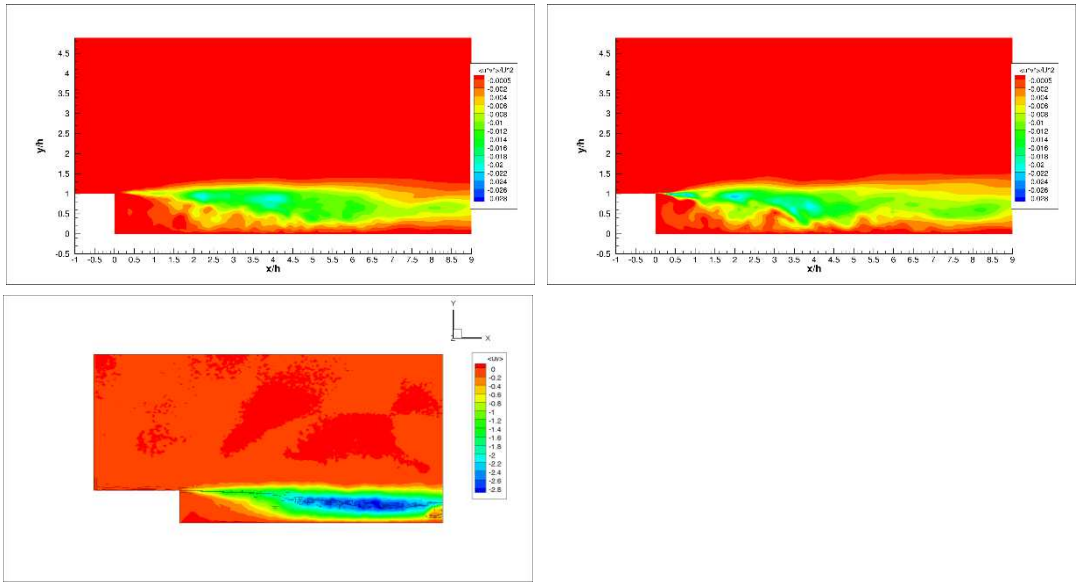

Figure 4.40 Normalised Reynolds shear stress <u'v'> contours (top row: simulations, bottom: experimental data) of uncontrolled – left column- and controlled –right- case

4.3.4 Three dimensional study: DBD plasma actuation over a backward facing step (Poitiers) applying unsteady actuation of plasma

Finally, to complete this Chapter, an investigation of modulated forcing of plasma was also performed. As it was mentioned back in Chapter 2, a DBD plasma actuator could be operated in two different ways: steady (or quasi-steady, experimentally speaking) forcing and unsteady forcing. So far, all simulations in this chapter were

performed with steady forcing of plasma. Experimentally, pulsating plasma produced a smaller recirculation region and a larger reduction of Reynolds stress therefore a series of CFD simulations will be performed and compared with the experimental database expecting the same or very similar effects. Visbal et al, 2006 and Riherd et al, 2011, carried out numerical investigation of pulsated plasma, showing a better separation control than and better effectiveness than when a steady forcing is applied. These studies also showed that the application of modulated plasma have a quick transient respond producing a quicker reattachment of the flow when compared to the steady force.

Simulations for this section were based in the experimental studies from the same partner, the University of Poitiers at the previously described wind-tunnel facilities. The configuration of the case was therefore taken from their published work "Pulsed dielectric barrier discharge for manipulation of turbulent flow downstream a backward facing step" [Bernard et al., 2014]. Unsteady forcing of plasma influences in the large turbulent structures of the flow, thus the expected effects are different from those caused by steady plasma. The most promising results were experimentally obtained at a frequency of the pulsation of 125Hz with a duty cycle of the 50%, which means in every pulse, plasma is on the 50% of the period of that cycle and off the rest 50% of time and so on. The experimental results showed a reduction of a 20% of the reattachment length applying modulated plasma with that frequency.

A simulation of modulated plasma using the experimental set up was performed to assess the reliability of Singh and Roy's plasma model when applying unsteady plasma forcing. Initially and to begin the analysis, the chosen constant for the model was also $C_{ROY}=2.2x10^{-8}$ as it produced the best results when plasma was operating in steady mode. Further on it was shown that for modulated plasma, the constant for this model must be higher so that the plasma effects are stronger as the actuation when the plasma is modulated operates on and off with the pulsation frequency. The model must be then adjusted so that it can be compared to the experimental database, showing sensible and realistic flow physics.

The computational mesh was the previously described 8M mesh and therefore all the inflow conditions and boundary conditions remained the same. The results were as

before and to maintain consistent comparisons, time and space averaged after 8 flow-through time periods, considering the simulations had reached an statistically steady state at that stage although due to the limit of resources and computational time availability, some unsteadiness was observed in the simulation results.

4.3.4.1 Analysis of the modulated plasma produced by Singh and Roy's model and comparison of results against Poitiers experimental database and MARS 3D Shyy's modulation of plasma results.

As Singh and Roy's model simulations with unsteady plasma had not been performed before, the starting point for its study was utilising the same value of the C_{ROY} constants for steady actuation. Later on, due to the lack of accuracy seen in the results using constants whose values were close to the steady plasma cases, a further investigation of their appropriate value to match experimental results was carried out. The complete set of evaluated constants is shown in the table below, Table 4.7.

Singh and Roy's constant analysis for modulation of plasma				
Simulated C_{ROY} values	C_{ROY}= 2.0×10^{-8}	C_{ROY} = 3.5×10^{-8}	C_{ROY} = 5.0×10^{-8}	C_{ROY} = 7.5×10^{-8}

Table 4.6 Modulation of Plasma: Selection of Singh and Roy's model constant

As mentioned in the previous section, modulation of plasma was expected to produce a smaller recirculation region. Singh and Roy's model can produce very unsteady and not physically sensible results depending on the model's constant, showing again a high sensitivity to the value of the constant yet showing more accurate results when compared to Shyy's model as it will be shown in the following sections.

In the initial cases using $C_{ROY}=2\times10^{-8}$, $C_{ROY}=3.5\times10^{-8}$, the simulations produced an over-prediction of the reattachment location, even larger than the baseline case. It was seen that the primary bubble size was largely over-predicted, Fig. 4.41, the free shear layer shape showed a wavy shape with smaller vortices inside the recirculation region, creating not only one but up to five smaller bubbles within this region immediately after the step. The flow streamlines with the velocity contours for these two constants is displayed next,

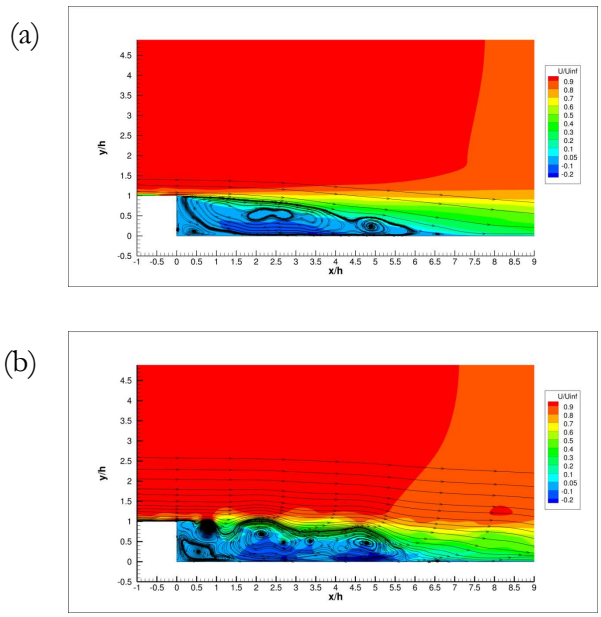

Figure 4.41 Flow streamlines and normalised streamwise velocity contours for modulated plasma using Roy's model using three different constants (a) C_{ROY}=2.0x10^{-8} (b) C_{ROY}=3.5x10^{-8}

As it can be seen, the two cases did not produce reliable results. This is caused by the weak effects of the plasma on the flow field using the values previously used for steady plasma and now used to simulate the injection of modulated plasma. The second set of constants were chosen to be larger so that, by strengthening the effects of plasma reducing the instabilities, the simulation results get closer to the experimental results and to the real physics of the controlled case when the plasma device operates in pulsating mode. These two constants produced results very close to the experimental measurements. The next figure, Fig. 4.42, shows the streamlines and the normalised streamwise velocity component field contour. Because of the closeness to the experimental flow field in which the reattachment length was 4.8H, the constant C_{ROY}=5.0x10^{-8} was chosen for this study.

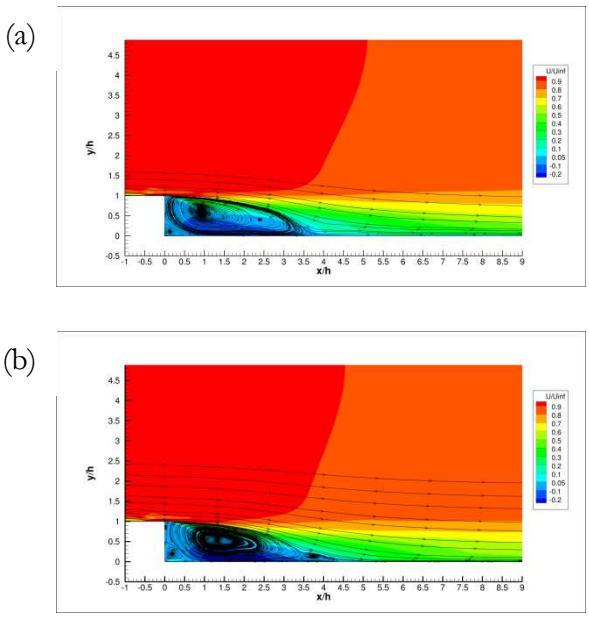

Figure 4.42 Flow streamlines and normalised streamwise velocity contours for modulated plasma using Roy's model using three different constants (a) C_{ROY}=5.0x10^{-8} (b) C_{ROY}=7.5x10^{-8}

For modulated plasma, the constant of the model was found to have to be larger than the constant for steady forcing of plasma. Basically, this is due to the instabilities induced by the weak pulsated plasma: when the plasma is steady, the force remains constant over time allowing the flow to evolve and develop reaching a steady state. However, when the plasma force is pulsating, there is an introduction of high momentum every period of the pulsated frequency which affects the whole domain and the large structures of the flow are highly perturbed causing high instabilities. A larger force will avoid this effect leading to more realistic flow behaviour.

4.3.4.1.1 Analysis of turbulent coherent structures of the flow

The same analysis structure of the results carried out for steady plasma will be followed for analysis of the modulation of plasma results. Firstly the turbulent coherent structures of the two different – Singh and Roy's with C_{ROY}=5x10^{-8} and Shyy's model - cases is analysed by means of the Q-criterion at 1000, Fig. 4.43 and at 100,000, Fig. 4.44.

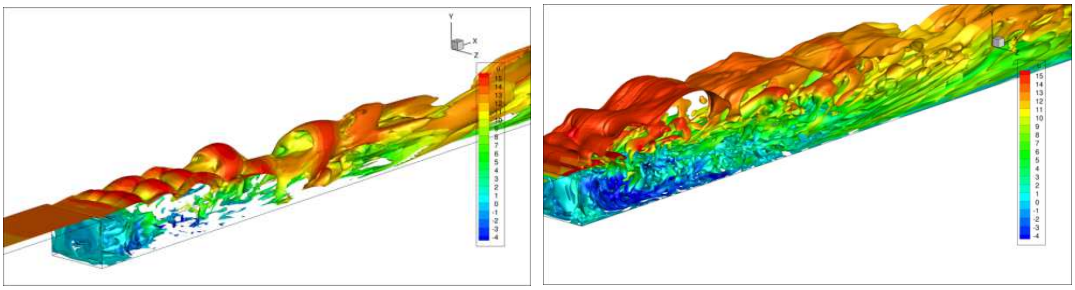

Figure 4.43 Q-criterion at 1,000 comparison: Shyy's model (left) versus Singh and Roy's model (right)

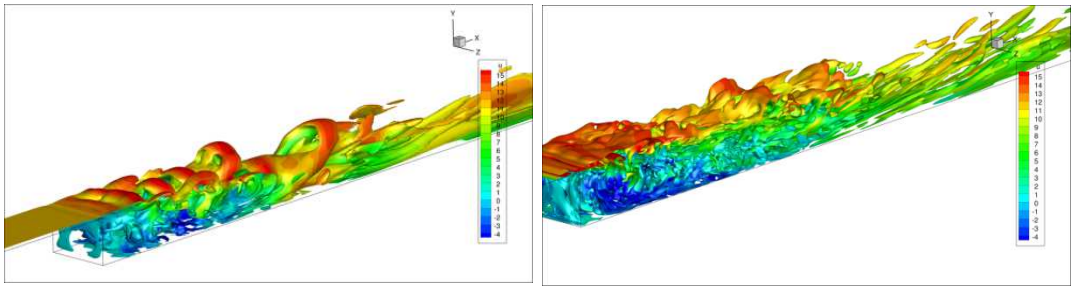

Figure 4.44 Q-criterion at 100,000 comparison: Shyy's model (left) versus Singh and Roy's model (right)

In both figures, Fig. 4.43 and Fig. 4.44, in Shyy's model case the small scale structures within the circulation zone are destroyed and do not even appear; on the other hand, much smaller structures appear in Singh and Roy's case. This is mainly due to the mesh density difference: the 3M mesh used for Shyy's model – this simulation was inherited from previous studies for the MARS project – is not able to capture such small turbulent structures whereas the 8M mesh – used for Singh and Roy – does. Nevertheless, pulsated plasma produces smaller structures in this region if we compare this with the baseline and the steady forcing of plasma (Fig. 4.32 and below Fig 4.45).

It is also observed in the figures, especially at Q-criterion at 1000, how the pulsation of the plasma produces large scale structures at the free shear layer. Their wavy shape is related to the duty cycle of the device: a pulsated injection of plasma produces wave-like turbulent structures downstream of the actuator whereas the turbulent structures for a steady forcing of plasma showed large structures but really long and flatter – not as wavy-. These large structures however are rapidly destroyed downstream, showing a good recovery of the flow after the reattachment area. This fact will be again mentioned then the velocity profiles at different streamwise

locations are shown. At that point, it will be seen that Singh and Roy's model has got a better recovery of the flow after the circulation area.

The actuation of pulsated plasma creates much smaller structures after the step and inside the recirculation region indicating a high dissipative flow. Larger structures appear in the free stream region as it was mentioned when the steady and unsteady forcing of the plasma device was described in Chapter 3; however these large structures are rapidly destroyed if the case is compare to the uncontrolled case. This fact can be seen in the following figure,

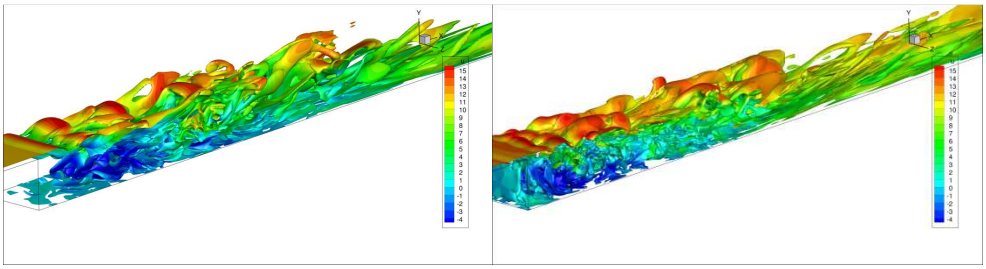

Figure 4.45 Iso-surface of vorticity: uncontrolled case (left) and controlled (modulated) case (right)

4.3.4.1.2 Velocity profiles

In this section velocity profiles are depicted at four crucial x/H locations: 1H, 2H, 4H and 6H where the experimental baseline and the experimental pulsated plasma measurements were taken, Fig 4.46. At each location, both experimental and simulation baseline cases, Shyy's model case, Singh and Roy's model case and the experimental profile with modulated plasma actuation is depicted.

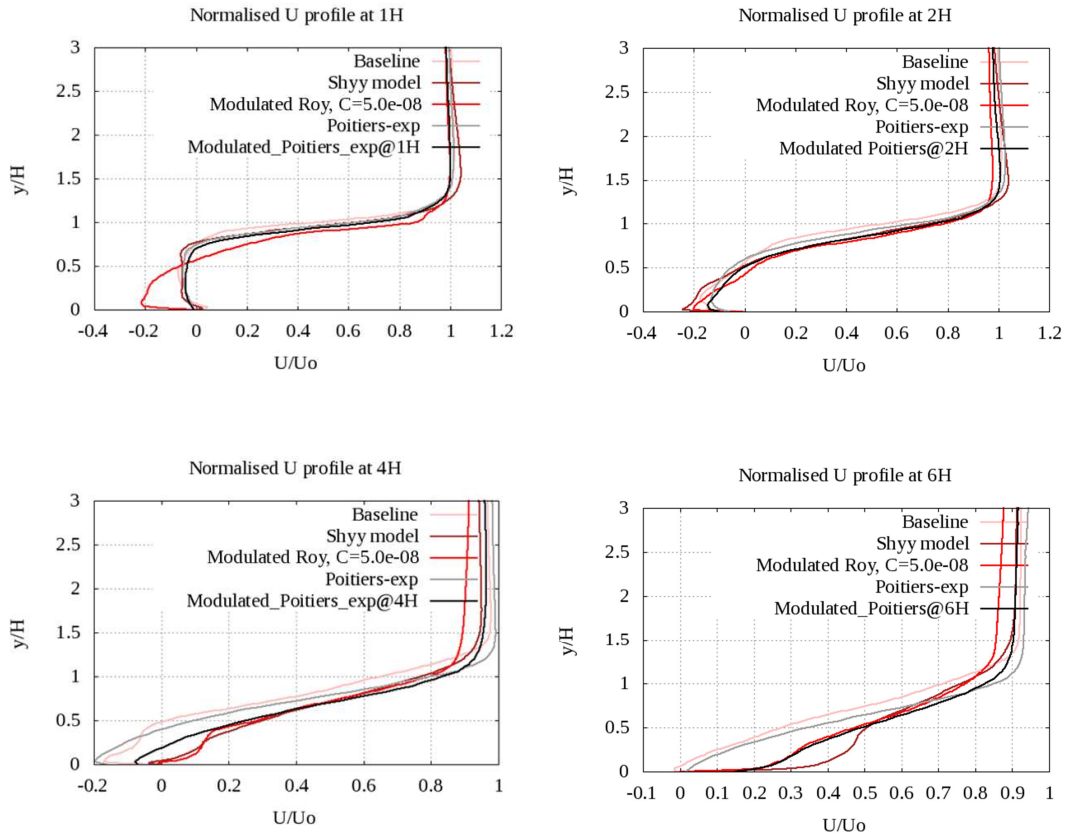

Figure 4.46 Normalised streamwise velocity at 1H, 2H, 4H and 6H

At location 1H, the plasma effects on the flow are not strong as all the profiles have got a similar shape, almost equal. Simulation and experimental data are very close for all the cases except for the Singh and Roy's model. This is due to the strong effects of plasma in the region near the step, causing a smaller secondary recirculation region on the corner right after it. The secondary bubble is hence "smashed". Moving downstream, at 2H, Singh and Roy's model starts to be closer to the experimental velocities, especially in the near wall region. Shyy's model produces smaller velocities in such region. For the baseline cases, both experimental and simulation data are in very good agreement.

At 4H, near the reattachment point, the baseline cases are again very close to each other and it is seen that for both experimental and computational results, modulated plasma effects cause higher velocities hence a smaller circulation bubble after the step region as expected. In this case, Shyy and Singh and Roy's model have a very

similar distribution near the wall and Shyy's model is closer to the experimental profile in the free stream region.

Finally at 6H, a location where all the cases have already passed the reattachment region and the flow is again developing, Singh and Roy's model shows an exceptional agreement in the recovery of the boundary layer – it can be observed in the figure that Singh and Roy's model follows the same distribution of the experiment. Again the computational profile show very good agreement with the experimental velocity distribution.

As a conclusion, Shyy's model predicts the behaviour of the flow better within the circulation region, in particular near the step, producing a more realistic prediction of the flow behaviour as it is been shown. On the other hand, the effects of the plasma produced by Singh and Roy's model are stronger near the edge of the step resulting in a smaller secondary bubble in the corner right after the step edge – this can be clearly seen when the velocity streamlines are depicted in the next section. These results are related to the way the plasma is modelled: Shyy's model restricts the plasma effects to a triangular region, whereas Singh and Roy's model plasma actuation affects the whole domain and its effects diminish proportionally as the flow moves further from the actuator location. The plasma effects are also related to the way the force of the plasma is calculated as it was shown in Chapter 3 where the models were explained: Singh and Roy's model force is related to the fourth of the applied voltage and the aforementioned distance to the actuator; Shyy's model only depends on the voltage and frequency of the device and it is constraint by the triangle geometry.

As the flow moves downstream towards the outlet, Singh and Roy's shows a better prediction of the flow behaviour and it matches the experimental boundary layer development after the reattachment of the flow to the bottom wall after the step. This effect makes perfect sense as Shyy's plasma effects weaken earlier due to the restricted area of actuation of the plasma force.

4.3.4.1.3 Reattachment region and skin friction distribution studies

The resulting reattachment length matched the experimental length, Fig. 4.47, when the constant value was 5.0×10^{-8}, Fig 4.48. The normalised velocity streamlines for the experiment without control and the 3D CFD simulation were shown in Fig. 4.12.

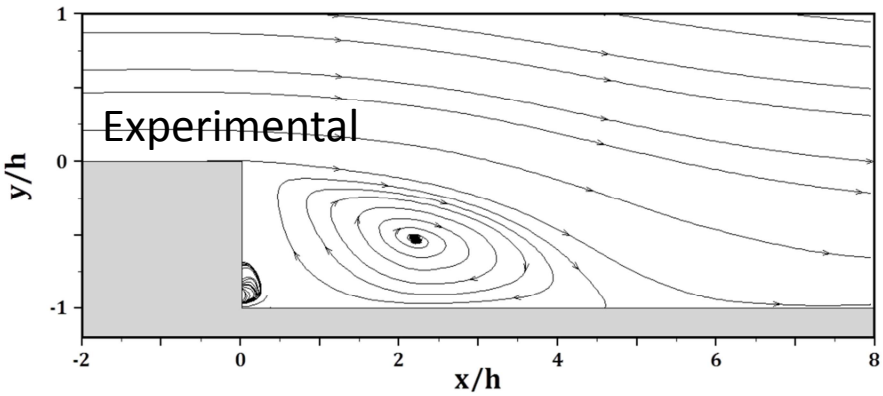

Figure 4.47 Experimental flow streamlines

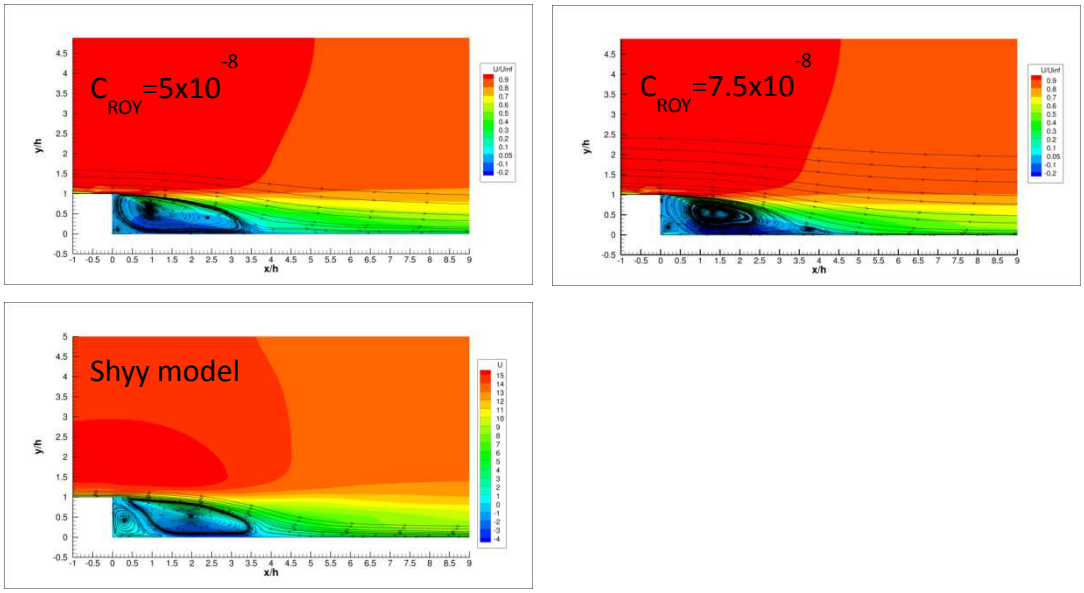

Figure 4.48 Streamlines of flow field and Normalised U contours; top– Singh and Roy's model using two different constants; bottom; Shyy's model

Singh and Roy's model shows a smaller secondary bubble right after the step than Shyy's model, which means the momentum added due to the plasma is higher in Singh and Roy's model causing a larger acceleration after the device's location and hence smashing the bigger bubble and reducing the size of the smaller in the corner.

Plasma effects in Singh and Roy's model are visible at the device location even after performing the time and space averaging whereas when Shyy's model is used, the effects are not visible.

Singh and Roy's model constant value of $7.5x10^{-8}$ produces a very thin recirculation area at the end of the big bubble, enlarging then the overall reattachment length for the case. Because of all these matters and for this particular problem we can conclude – although this argument will be strengthen when more evidence is provided when the whole analysis of the results is performed - that the constant for Singh and Roy's model $C_{ROY}=5x10^{-8}$ is the optimum value.

With regards to the skin friction, Fig 4.49 shows the skin friction coefficient distribution for both the baseline and the modulated plasma simulations along the streamwise direction. It can clearly be seen the reduction of the recirculation region in the modulated plasma case compared to the baseline case. For the baseline case the flow reattaches at 5.8H whereas when the plasma is actuating the reattachment length is 4.8H after the step. This is in complete agreement with the experimental results where the recirculation region reduction was of a 20% as it also occurs in the computational cases.

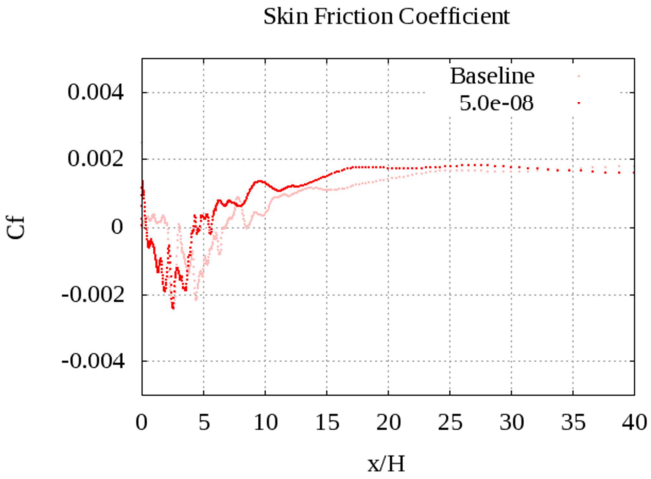

Figure 4.49 Skin friction coefficient distribution along streamwise direction comparison of baseline and modulated plasma actuation

4.3.4.1.4 Reynolds stress

In this section the normalised Reynolds stress profiles at different locations on the streamwise direction and contours in the x-y plane are analysed. Both normal and

<*u'v'*> shear stress normalised components will be shown and discussed. The profiles shown include the simulation and experimental data for both baseline and modulated plasma so that the effects of the actuation of plasma can be analysed. Shyy's model results are also included to therefore make a comparison between the performance of both models, Singh and Roy and Shyy.

The different profiles locations were selected according to the availability of experimental measured data. These locations are 1H, 2H, 4H and 6H after the step. Regarding the contours, all of them are time and space averaged and no experimental data was provided in this occasion.

Normal Reynolds stresses profiles are analysed in first place. The experimental baseline data was available for the <*u'u'*> and the <*v'v'*> components and only <*u'u'*> for the controlled case. For the spanwise component of the Reynolds stresses, there was not available experimental data at all so only the simulation results will be shown.

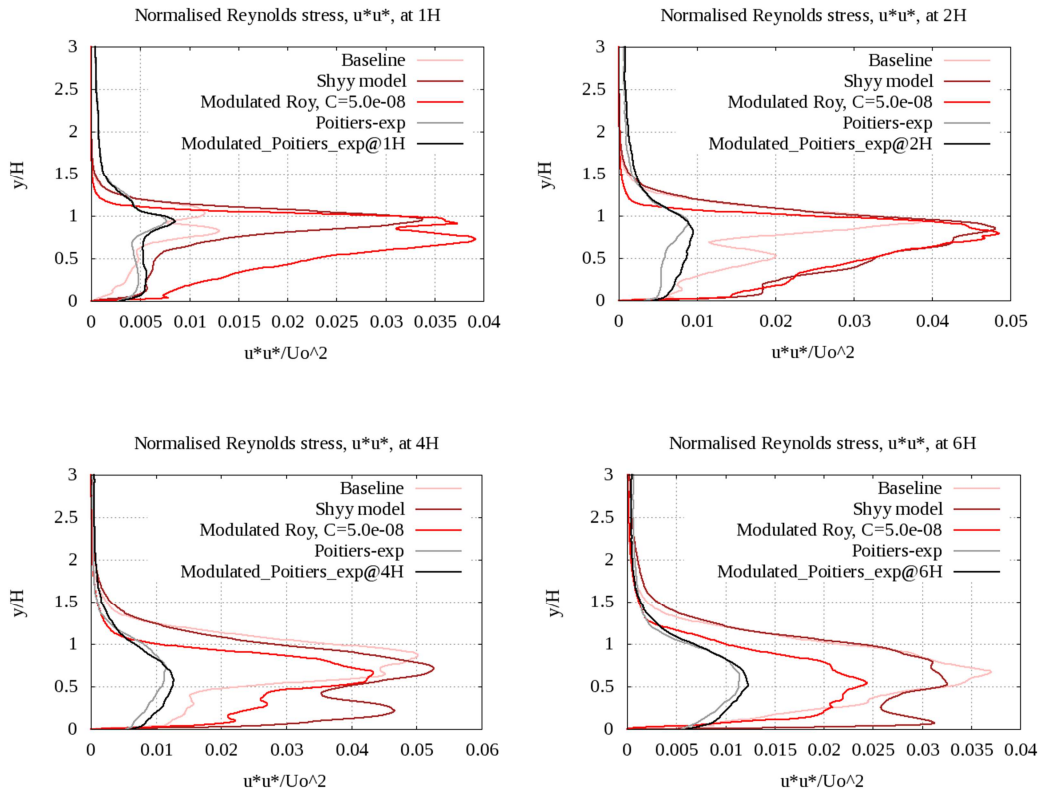

Figure 4.50 Normalised <u'u'> Reynolds stress component at 1H, 2H, 4H and 6H

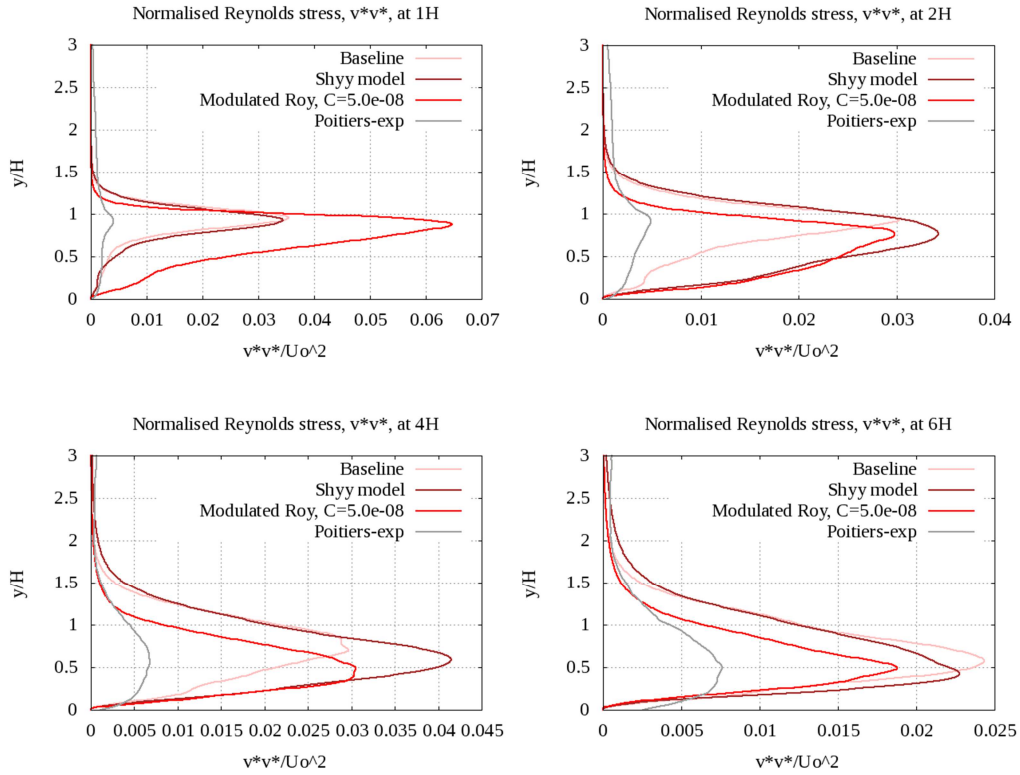

Figure 4.51 Normalised <v'v'> Reynolds stress component at 1H, 2H, 4H and 6H

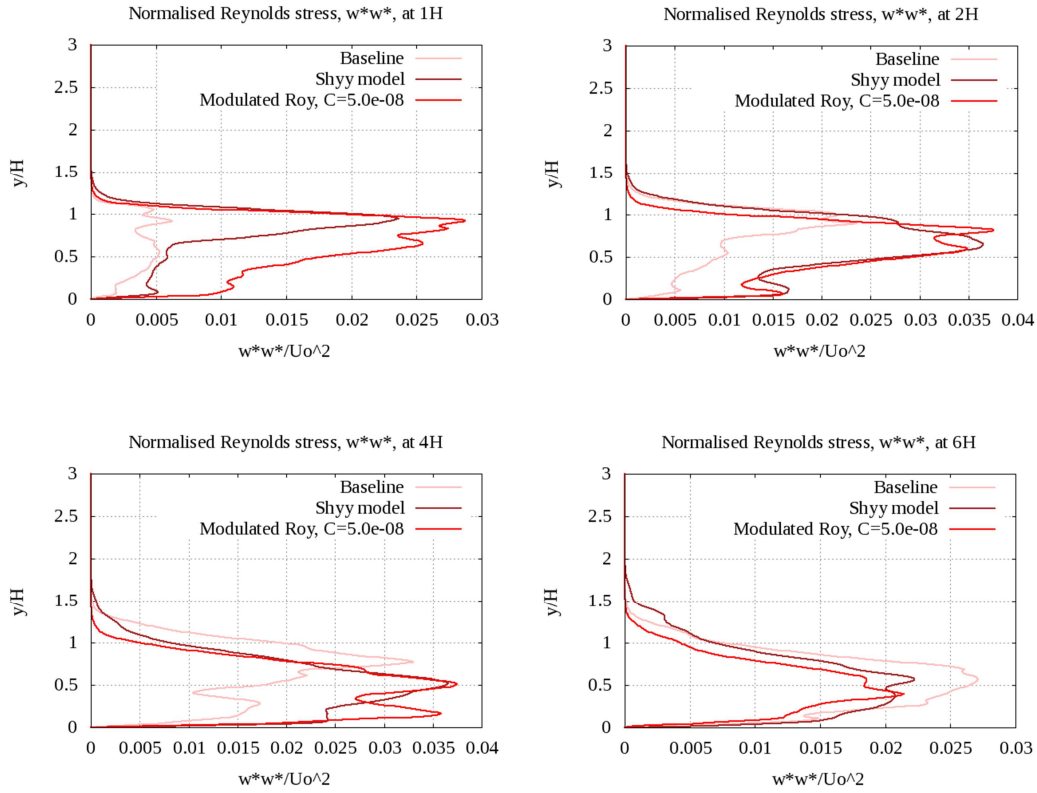

Figure 4.52 Normalised <w'w'> Reynolds stress component at 1H, 2H, 4H, 6H (simulation data only)

The plasma model produces an over-prediction of the turbulence intensity when compared to the experimental data. This issue was not as obvious when plasma was operating in steady mode, but still the normalised Reynolds stresses were over-predicted. The reason why this is happening is because Spalart Allmaras model will over-predict the growth rate of high speed shear layers, [Nichols, 2012]. Also, another issue with Spalart Allmaras model is that when there is a rapid change in length scales associated with the transition from wall bounded to free shear proves to be problematic as it has been addressed in previous work [Yan et al, 2014;. Wang, 2009]

For the <*u'u'*> normalised component, the experimental results show to have larger values in the near wall region in the four locations. This feature is captured by the simulations. Singh and Roy's model starts to get closer to the experimental data after the reattachment point, providing again evidence of a better flow recovery after the separation. Singh and Roy's and Shyy's model produce different profiles at all locations although the maximum normalised value and location is similar in both

models at the free shear layer. The effects on the normal <*v'v'*> component using Shyy's model do not have strong effects as the profiles are really close to the baseline case; Singh and Roy's model, on the other hand, when it is compared to the baseline case show an over-prediction near the step, similar values further downstream and an under-prediction after the reattachment region. Finally for <*w'w'*> normalised component, Singh and Roy's model and Shyy's model produce similar results. This is related to the two dimensional characterisation of the plasma body force, having lower effects on the spanwise and the largest effects on the streamwise and normal to the flow directions as expected.

A comparison of the Shyy's and Singh and Roy's normal Reynolds stresses contours is shown next. For <*u'u'*> contour, Shyy's model shows larger Reynolds stresss in the free shear layer after the step between 2H and 4H than Singh and Roy's model. This effect is also shown in both 2H and 4H profiles. In the region where the secondary bubble is located, Shyy's Reynolds stresses are higher than for the other plasma model.

The normal component <*v'v'*> is definitely higher for Singh and Roy's model than Shyy's model in the area closer to the step, 1H. Shyy's model shows a bulk of high values of this component further downstream, near the reattachment area. This is reflected on the profiles. Finally, the <*w'w'*> distribution is quite irregular for both models.

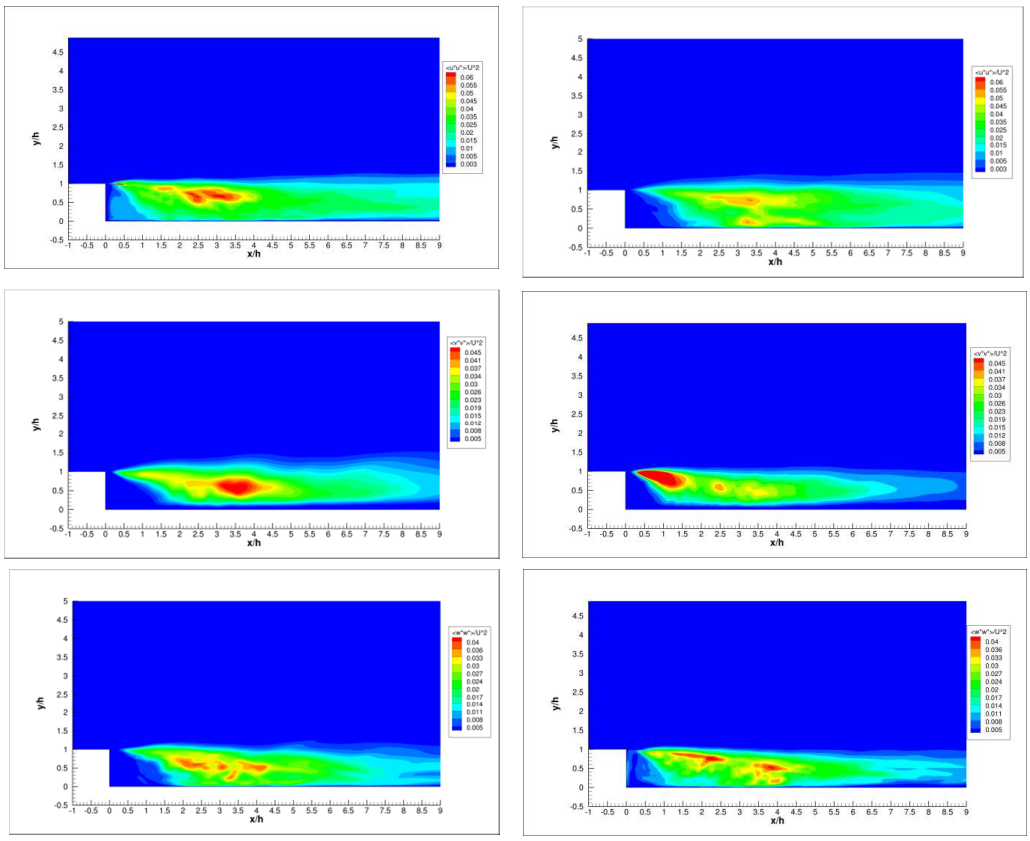

Figure 4.53 Contours of normalised Reynolds stress components: Shyy's model (left) and Singh and Roy's model

The same analysis is now performed for the normalised shear stress <*u'v'*>. It can be seen than for the experimental case, the absolute value of <*u'v'*> is larger for the controlled case than the baseline values. This shows that, effectively, the DBD plasma actuator in enhancing the turbulent vertical advection of streamwise turbulent momentum which shows so one of the aims of this thesis is proven: manipulating the dynamic turbulent structures a reduction of the separated region is achieved. This behaviour is also captured by the simulation, although again the absolute value of the shear stresses is over-predicted. Within the recirculation region, Singh and Roy's model over predicts the value of the shear stress, however, closer to the reattachment point at 4H, the model reproduces the same profile as the experimental modulated plasma. After the separated region, Singh and Roy's model profiles are under-predicted when compared to all experimental and computational cases. In this case, Shyy's model produces similar profiles inside the separated region but then over-predicts this parameter near and after the reattachment region and shows a similar behaviour to Singh and Roy's model near the wall at 6H.

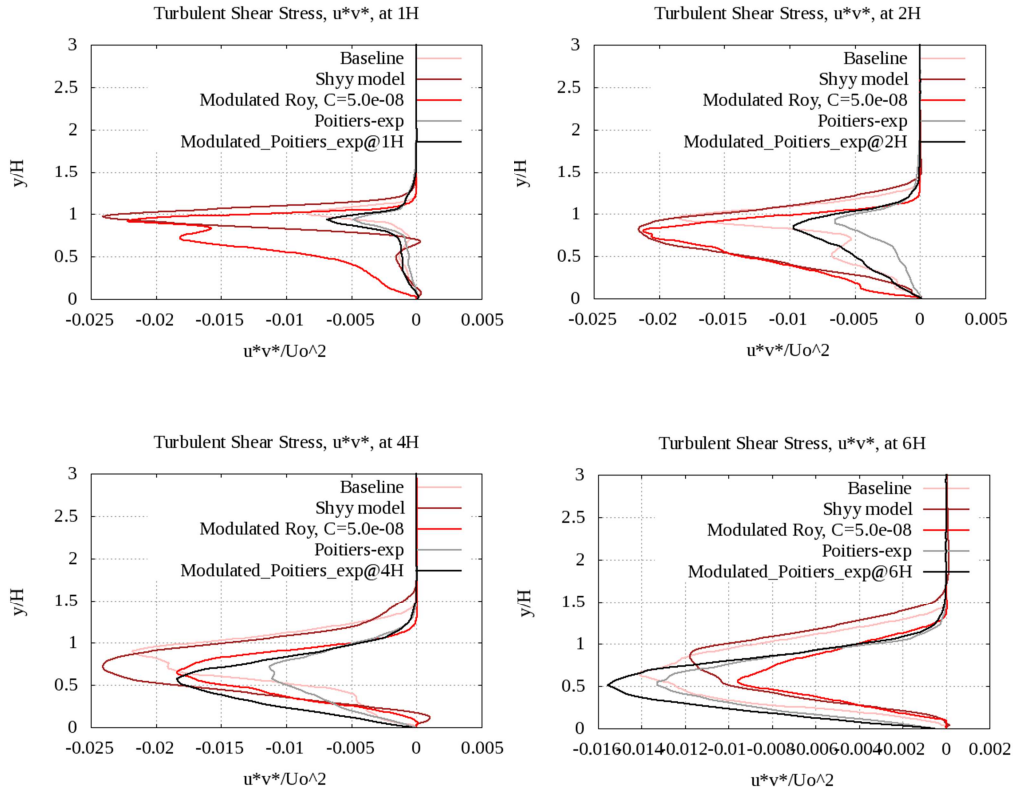

Figure 4.54 Normalised Reynolds shear stress u'v' component at 1H, 2H, 4H and 6H

To finish this section, the shear stress contours for the region of interest in the domain is shown. The experimental contours are included in this occasion. The distribution of the Reynolds shear stress is similar to the experimental case when Singh and Roy's model is used in the computation. There is a reduction of the shear stress in the edge of the step which is capture by Singh and Roy's model but it is not by Shyy's model. There is also a bigger reduction of the shear stress in the free shear layer shown in the experimental contour which matches better the results produced by Singh and Roy's model. Shyy's model seems to produce less vertical flux of horizontal momentum than the experimental results; however, Singh and Roy's model captures and reproduces this effect although the distribution on the shear layer is not as smooth as it was captured in the experiments.

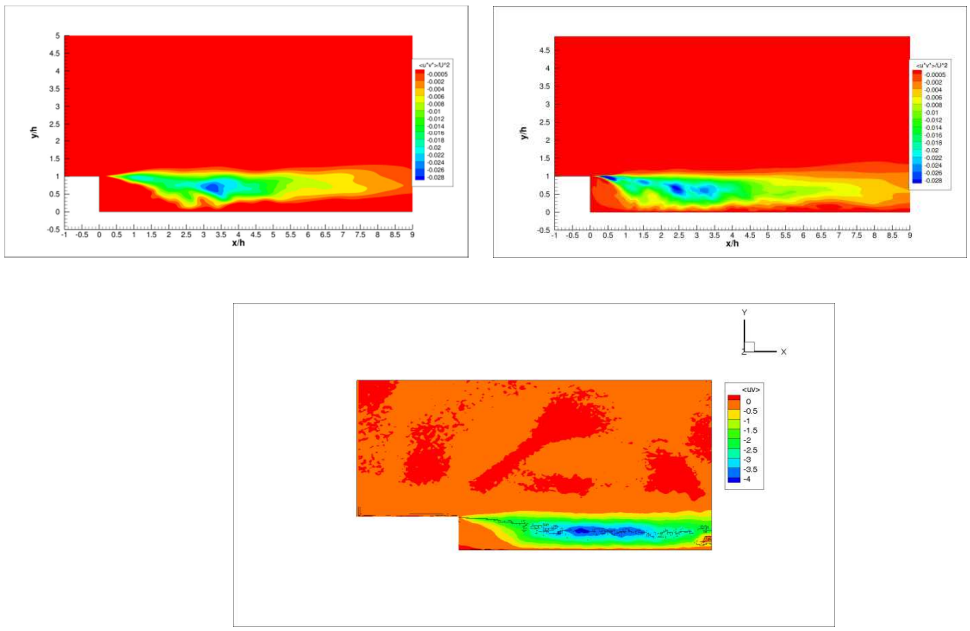

Figure 4.55 Normalised Reynolds shear stress u'v': Shyy's model (left) and Singh and Roy's model

Reynolds shear stress is responsible of the transport of turbulent fluctuations in the y direction. An absolute increase, i.e., a larger absolute value of $<u'v'>$ has shown an improvement of the mixing on the shear layer region causing a reduction of the skin friction which obviously implies a reduction of the separation region.

4.4 Conclusions

An investigation of the effects on a flow over a backward facing step of a single DBD plasma device located upstream of the edge of the step was carried out.

Simulations were carried out and afterwards compared according to the experimental partner in the MARS project, the University of Poitiers, for this particular case. In order to simulate the actuation of plasma in the flow field, a phenomenological model was implemented in the CFD in-house code utilised to run all calculations in this study. Roy's model was the model selected to simulate the plasma actuator.

Initial two dimensional simulations were performed to adjust and validate Roy's model. A set of constants were tested and the results from these simulations showed

good agreement with experimental data for steady forcing actuation of plasma and they also matched the already implemented Shyy's plasma model results. A reduction of a 3.3% of the reattachment point was achieved by applying a constant of value $C_{ROY}=1x10^{-8}$.

One of the aims of this chapter was to provide a deep assessment of Singh and Roy's model effects on the flow over the step, a three dimensional study was carried out. Initially, a 3M mesh was generated by an extrusion from the 2D grid and also an 8M mesh was used to study the mesh dependency for both baseline and steady plasma actuation cases. The 8M mesh showed to provide more accurate results for the uncontrolled and the controlled cases; therefore this grid was selected to look deeper into the features of plasma on a flow over a BFS. A different set of constants was also analysed for the three dimensional cases and $C_{ROY}=2.2x10^{-8}$ provided very good agreement and reliability when it was compared to the available experimental database, reducing the reattachment length a 5% compared to the baseline; value which was acceptable as in experiments the reduction was a 3.4% when applying steady plasma. In the simulations of steady plasma, the actuation of plasma in the experiment had a frequency of 1kHz which is considered quasi-steady. Singh and Roy's model does not include the frequency of the applied voltage but it considers the plasma actuation to be purely steady yet it showed very good agreement with the experimental database.

Finally, a modulation of plasma with 125Hz pulsation frequency was investigated testing as well two initial different Singh and Roy's constants but the model showed to over-predict the reattachment length when plasma was applied in unsteady mode using low values of the constant of the model. A further investigation hence was performed, as the effects of plasma using Singh and Roy's model were not strong enough resulting in highly unsteady flow. A set of two larger constants was investigated finding finally an appropriate value which showed very good agreement with the experimental results from the University of Poitiers. Singh and Roy's model showed to be more advantageous in the recovery area after the flow reattaches to the wall downstream of the recirculation region.

The difference between models lies on the region of actuation of the plasma in the model and also on the mathematical formulation. In Shyy's model, the region of actuation of plasma is restricted to a triangular region and a blending function controls whether the plasma is present or not. This is a quite strict constraint however easier to control as it was shown in this chapter as Singh and Roy's model adjustment was much trickier and complicated than the adjustment of Shyy's model. In Singh and Roy's model, the plasma actuation is more realistic as it affects the whole domain and it is a function of the distance of certain point in the domain to the actuator location. Because of this, the effects of plasma affect more the whole mean flow when Singh and Roy's model is used than when Shyy's model is used.

In Shyy's model the created plasma force is strongest near the edge of the exposed electro and it weakens as it moves beyond the embedded electrode. On the other hand, according to the mathematical model of Singh and Roy's model, the plasma EHD force will be maximum in the middle of the distance of the two electrodes on top of the dielectric and will vary all over the domain depending on the position within it. Another difference is the parameters on which each model depends on: Shyy's model depends on the electric field and on the applied AC frequency: in its formulation, the plasma force is linearly related to these two parameters. On the other hand, Singh and Roy's model is a function of the dielectric material properties, two empirical constants adjusted for a quiescent environment and it is related to the applied critical applied voltage to the fourth power, making the model extremely sensitive to the applied voltage and requiring the introduction of a constant to adjust the effects of the induced body force. This model does not consider the AC frequency.

As final most remarkable conclusions, in this chapter it has been shown that experimental and numerically a single DBD plasma actuator induces a wall jet flow with steady or periodic fluctuations that clearly influences the flow fields on a backward facing step as. The reattachment point can be reduced by 20% when applying modulated plasma due to the strong influence of the discharge on the shear layer development and resulting Reynolds stresses: higher velocities before the step enhance the flow mixture so that the energy is conveyed from the mean flow to the

recirculation area. The shear stress thus increases in the shear layer region causing a reduction of the reattachment length and a reduction of the skin friction coefficient. With regards to the analysis of steady plasma using Singh and Roy's model, it has been shown that despite the model does not take into account the frequency of the applied voltage, the model produces very accurate and reliable results. This is a clearly advantage not only with regards to the reliability of the prediction of the flow behaviour but also computationally speaking because there is less computational expenses as frequency is not included in the formulation of the model. Another remarkable finding is that the application of modulated plasma produces better results than a steady application; the real advantage of this is that only a portion of the energy – which will depend on the duty cycle of the pulsation – applied to the steady plasma is the energy needed for the pulsation of the plasma, leading to energy saving and potential use of this device in the pulsating mode for any real application.

5 Active flow control with Spanwise Vortex Generators over a backward facing step

5.1 Introduction

A flow over a backward facing step was chosen to study the flow control with spanwise vortex generators, SVG. The experimental work was carried out by Prof Ming at Nanjing University of Aeronautics and Astronautics, NUAA, in China. This study was performed within the MARS framework.

First of all, a baseline simulation was performed and then, SVG were configured and a controlled case simulation was carried out using DGDES. Limited data from the experimental side was provided, in particular for the controlled case; however, 3D SVG simulations will procure a further understanding on the effects of SVG in a BFS flow.

5.2 Case Configuration

5.2.1 Description, review and adjustment of the device: passive vortex generators, cavities and blockages and active vortex generators.

Spanwise vortex generator is the second active flow control device investigated in this thesis. A description of the device is provided in this section.

A classic vortex generator, VG (Fig. 5.1, Fig. 5.2) is an aerodynamic device which consists of a small vane placed on top of a surface of an airplane fuselage or any other vehicle such as cars and they can be also installed on a propeller blade of a wind turbine. [Peppler, 1996]. Basically, when the air is flowing over the surface where the VG is installed, this device forces the creation of vortices which will delay the separation of the flow over the surface and hence, delaying the aerodynamic stall of the wing. The effects of the vortex generators in the flow over a backward facing

step has been also studied both experimental and computationally, [Zulkefli et al, 2009]

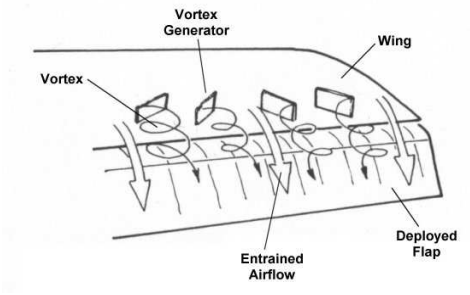

Figure 5.1 Vortex generator on a wing scheme

Figure 5.2 Vortex generators on the vertical fin of a Boeing 727-100

Basically, flow control using steady streamwise vortex generators is well known in the aeronautical field, [Rao, 1988; Lin, 1990; Lin, 1991; McCormick, 1992; Kerho, 1993; Ashill et al, 2001; Ashill, 2002; Yao, 2002; Allan, 2002] and have been widely investigated. In general in a turbulent flow, there is a large loss of energy associated with the separation of the boundary layer. For such reason, flow separation control in fluid mechanics has been and it still is nowadays extremely important for the aerospace industry. VGs are used to control boundary layer separation at a wide range of flow speeds [low speed: Lin, 1999; Jenkins, 2002. Supersonic flow: McCormick, 1992; Mounts, 1992]. As well VGs were analysed to establish the relation between the parameters of the device and the resulting flow characteristics. [Ashill, 2001, 2002; Yao, 2002; Allan, 2002], the aircraft performance improvement and also noise control [Holmes, 1987] and distortion reduction [Anabtawi 1999; Hamstra, 2000].

Similar to the vortex generators, different types of passive control have been studied such as cavities or rods [Isomoto, 1989] and blockages in a channel [Griffith et al, 2004, 2007]. In 2003, Neumann and Wengle found that a minimum distance between the step edge and a control fence – a small obstruction upstream of the step inducing turbulence in the flow – is required to achieve the maximum reduction of the recirculation bubble downstream of the step. Yokoyama et al, 2007, found the formation of a small vortex after a resctangular bump placed before the step edge. Once the vortex went beyond the step edge, it broke into faster and slower vortices causing a compression effect which led to a reattachment reduction.

Several studies focused on researching for more effective flow control beyond fixed vortex generators were carried out by Mochizuki et at, (2006). An experimental investigation of the effects caused by a streamwise vortex generator with periodic perturbation on Reynolds stresses in a turbulent jet wall was performed. In the study, the device is an oscillating vortex generator of a delta wing shape. The triple decomposition mentioned in the introduction of this thesis was analysed [Reynolds and Hussain, 1972] and together with the averaging of the flow, periodic variations in the strength were observed as a direct consequence of the periodic oscillation of the VG. As a conclusion of such study, effects on the oscillating vortex generators were captured at different Reynolds stress components.

Back in Chapter 2, where several of the most common active flow control devices were described, similar cases to the current study in this thesis were highlighted, [Ianoka, 2004; Weier et al, 2011]. The novelty of the present research relies on the fact that the periodical perturbations were introduced in the flow by a flat surface oscillating vertically to the flow direction – with a 2mm gap between the surface and the bottom wall – in order to analyse the effects of the spanwise vortex generator in the reattachment length as well as Reynolds stresses. In this study, it was assumed that the spanwise vortex generator was as rectangular strip – no thickness – located exactly above the edge of the step, with a 2mm gap between the SVG and the wall, exactly like the experiment configuration but the thickness of the surface is zero. The configuration and geometry of the simulated device is explained in detail in the next section.

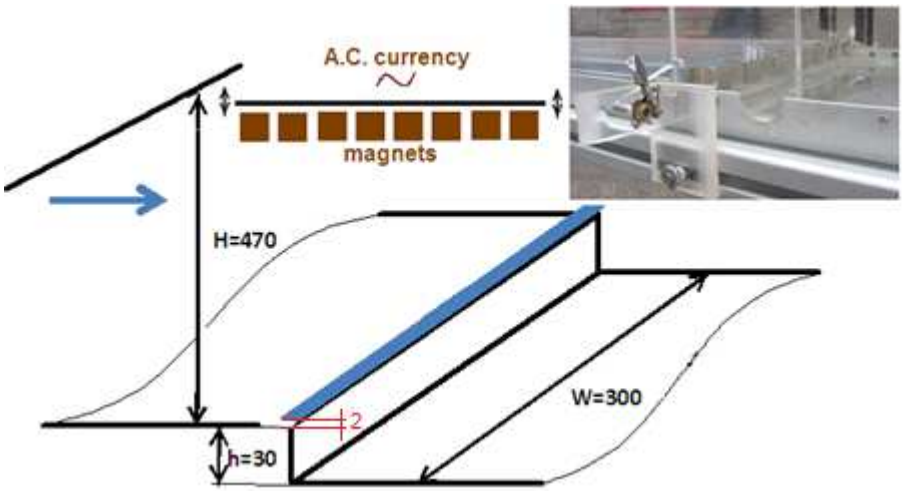

Figure 5.3 Spanwise Vortex Generator (SVG) setup in NUAA wind-tunnel

In this thesis, spanwise vortex generators, Fig. 5.3, were simulated according to Nanjing University of Aeronautics and Astronautics experimental case.

5.2.2 Geometry and Computational Domain

All the experimental work for this study was carried out at NUAA facilities. Fig 5.4 shows a picture of the wind-tunnel where the experiments took place.

Figure 5.4 Wind-tunnel facilities at Nanjing University of Aeronautics and Astronautics

The wind tunnel had a total height of 0.47m and a span width of 0.30m. The step height was 0.03m. Experiments were carried out at a free stream velocity of 19.8m/s and the Reynolds number based on step height was 39,000. In this case, the

boundary layer thickness at step edge location was around 2H according to the experimental readings.

A diagram of the SVG configuration can be seen in previous Fig. 5.3. Experimentally, the SVG consisted of a metal tape stretched over a strip of magnets placed along the span of the wind tunnel. The magnets had a width of 0.005m and were located at 0.002m away from the wall. A.C. current is applied to the metal tape generating a Lorentz force that moves the tape up and down. The frequency and magnitude of the movement is controlled by the applied current. The experimental frequency of 280Hz produced oscillation of the strip and the amplitude was 0.002m.

In order to perform the simulations, it was assumed that the SVG performed as a flat surface 0.005m long located just before the step edge at 0.002 mm over the wall with a frequency of oscillation as the experimental, 280Hz and maximum amplitude of 0.002m. See figure below, Fig. 5.5,

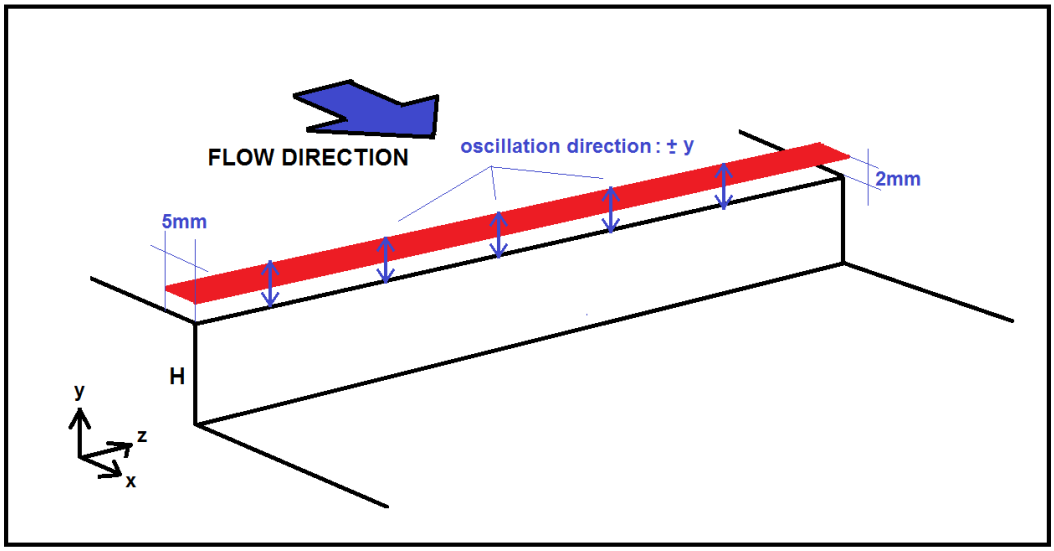

Figure 5.5 Schematics of the simulated SVG

Regarding the computational mesh, the 8M mesh utilised for the DBD plasma study was also used in this study as it provided with very reliable results. Fig. 5.6 shows the computational mesh and an instantaneous capture at 0.29s of a detail of the step region when SVG were activated in simulations.

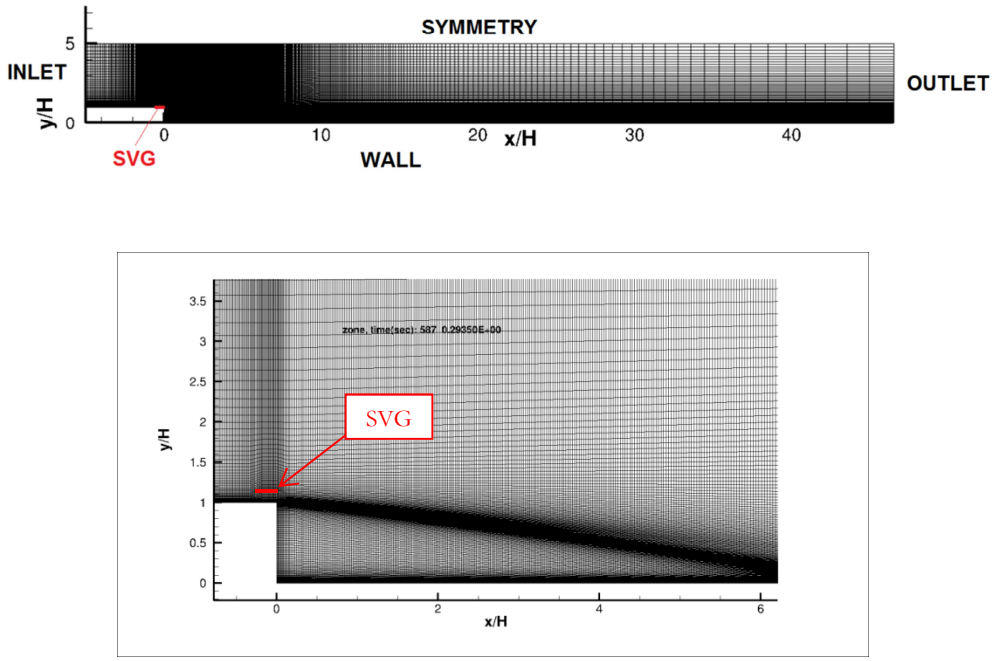

Figure 5.6 Computational mesh and detail of step region when SVG are in operation

A further description of the mesh can be found in **Chapter 4**, section **4.3.3.3 Study of mesh dependency: 3 million versus 8 million cells grids**

5.2.3 Boundary Conditions and Time step selection

The free stream velocity was 19.8m/s. For the inflow, experimental velocity profiles were provided and used as the inlet boundary conditions. The top surface was set up as symmetry boundary condition. The bottom wall of the wind tunnel and the vertical wall of the step were configured as no-slip walls. The outlet was set as non-reflective convective boundary conditions and the sides were assigned periodic boundary conditions. Finally the actuator was defined as moving wall with the experimental amplitude and frequency.

The time step was $0.01H/U_0$ and time averaging was calculated for $400H/U_0$ after the flow swept the whole domain five times.

5.3 Implementation of Spanwise Vortex Generators in DGDES

When the experimental device SVG was described in previous sections, it was said the SVG were located 0.002m over the wall moving up and down with 0.002m amplitude at a frequency of 280Hz. In DGDES, the configuration was the same. A 0.005m long by the span length long surface was defined along the spanwise and it was placed 0.002m over the wall. The oscillation in time corresponds to a sinusoid wave of maximum amplitude of 0.002m, the SVG amplitude; therefore its position is given by,

$$y_{SVG} = A_0 \sin(2\pi f t + \varphi) \tag{5.118}$$

Where A_0 is the maximum amplitude of the SVG, f is the frequency of the actuator, t is the physical time and φ is the initial phase angle if at some point an exploration of the deployment effects of the SVG from different locations wanted to be investigated.

So the velocity of the SVG is obtained by deriving its y position, Eq. (5.1), by time,

$$V_{SVG} = \frac{dy_{SVG}}{dt} = 2\pi f A_0 \cos(2\pi f t + \varphi) \tag{5.2}$$

An example of the actuation of the SVG was already displayed in Fig. 5.5 where a detail of the grid at the step region was shown and it can be appreciated how the SVG defined region is moving upwards at that exact time position.

5.4 Results and Discussion: comparison with experimental database

5.4.1 Analysis of coherent structures

An analysis of the turbulent structures was carried out to evaluate the effects of the spanwise vortex generators. As it was performed in Chapter 4, Q-criterion [Hunt et al, 1988] was used to identify the aforementioned structures. In Fig 5.6, Q-criterion of the baseline –left column- is depicted versus the controlled case –right column- for three different values of Q: (a) Q=1000, (b) Q=100,000 and (c) Q=200,000. The figures are coloured by the streamwise velocity values.

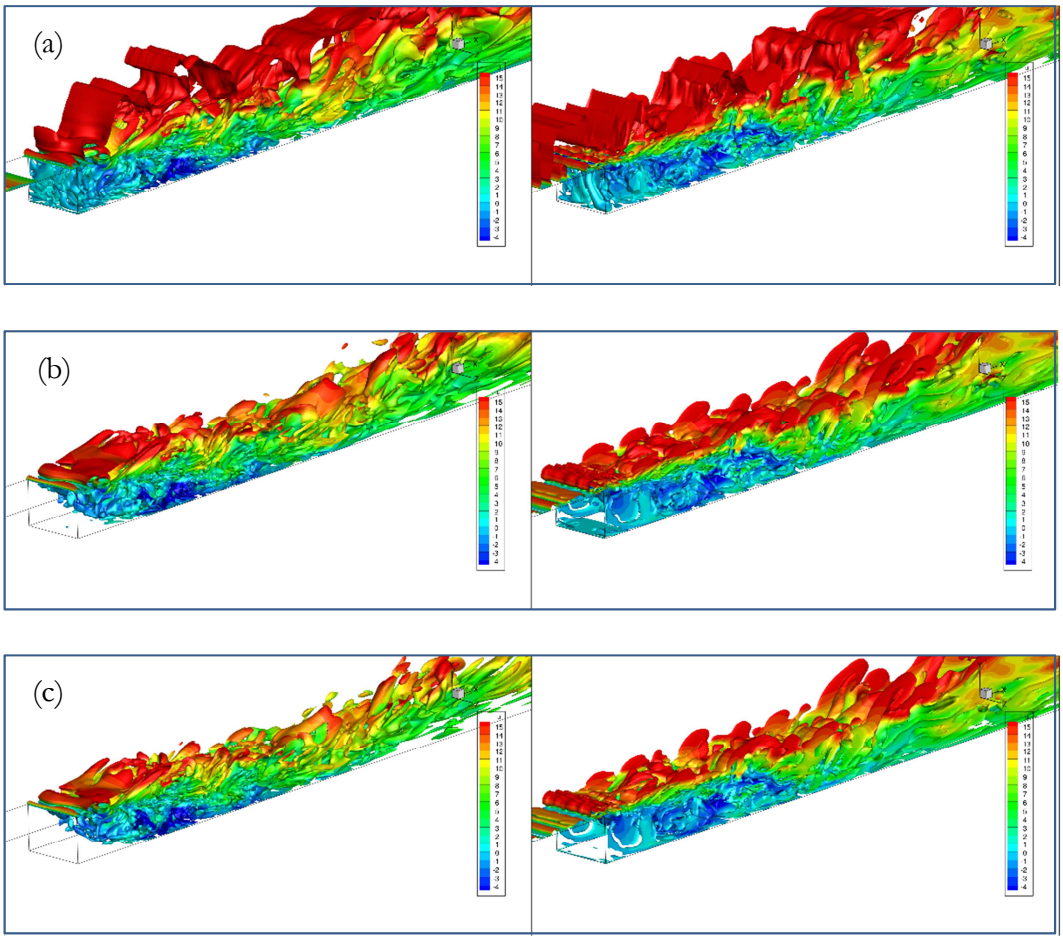

Figure 5.7 Q-criterion of baseline –left column- versus SVG case at (a) 1000, (b) 100,000 and (c) 200,000. Iso-surfaces coloured by streamwise velocity

At (a) it can be seen for the controlled case that at regions close to the SVG, tube-like vortices appear and develop further downstream of step into a long wobbly sheet which has a periodic shape caused by the oscillation of the SVG whereas the uncontrolled case does not show many of this structures but hairpin turbulent structures below a layer of high velocity. For Q=100,000, for the baseline case more obvious than at Q=1000 hairpin structures can be seen downstream of step. There is a bigger destruction of turbulent structures on the uncontrolled case, especially near the step which means the device introduces large instabilities in the mean flow hence there are more turbulent structures in the flow field. The effects of SVG are appreciated for the controlled case: a pseudo-homogeneous layer of mushroom eddies is formed downstream of step. The lower parts of these structures move also towards the wall breaking into much smaller structures. From the reattachment area and downwards, bigger structures are present for the controlled case. Finally at

Q=200,000, similarly as it happened at (b), hairpin-like structures are clearly observed for the uncontrolled case. Smaller structures are formed downstream of the reattachment area, unlike in the controlled case, where again a layer of turbulent structures –mushroom eddies and hairpin further downstream- is appreciated at y=H. An enhanced mixing region is observed in the recirculation area is observed in the controlled case compared to the baseline flow.

5.4.2 Velocity profiles

A comparison of the velocity is done at nine different locations: -1H, at step, at 1H, 2H, 3H, 4H, 5H, 6H and at 9H. Experimental data was not available at all these locations and data for the controlled case was not provided. Also, it must be said that the experimental measurements were performed using hot wire, the obtained reading are absolute hence when looking at and analysing the following normalised velocity profiles, inside the recirculation region where the velocities are negative, the experimental data should have the negative value of what it actually is. Looking close at the figures, the negative values of the experimental baseline case will match the simulation velocity profiles at most of the streamwise locations. After the recirculation point, the experimental readings show greater velocity values due to the inability of the hot wire to measure the velocity at the wall – where obviously the value is zero.

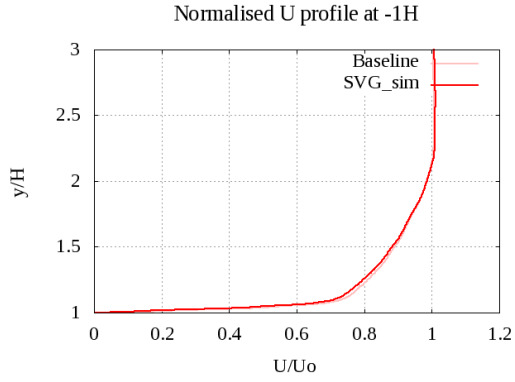
Normalised U profile at -1H
Baseline
SVG_sim
y/H
U/Uo

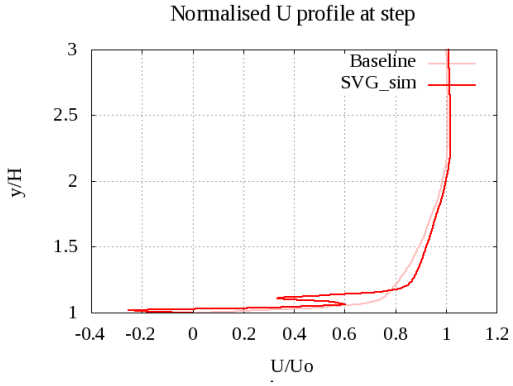
Normalised U profile at step
Baseline
SVG_sim
y/H
U/Uo

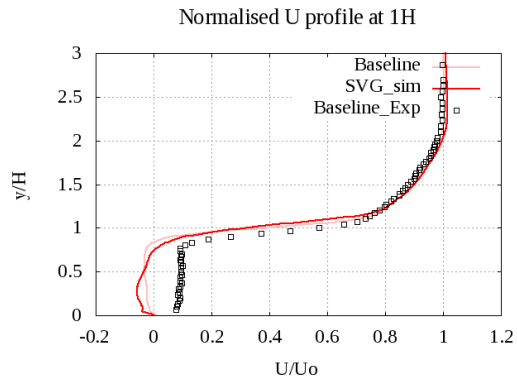
Normalised U profile at 1H
Baseline
SVG_sim
Baseline_Exp
y/H
U/Uo

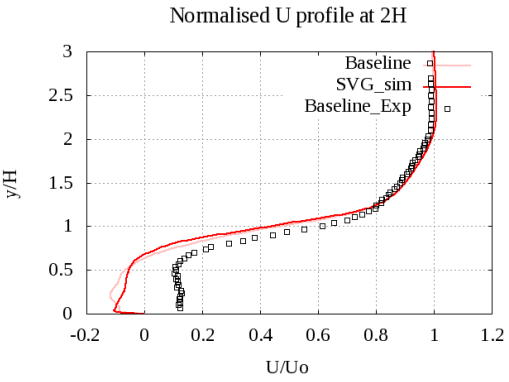
Normalised U profile at 2H
Baseline
SVG_sim
Baseline_Exp
y/H
U/Uo

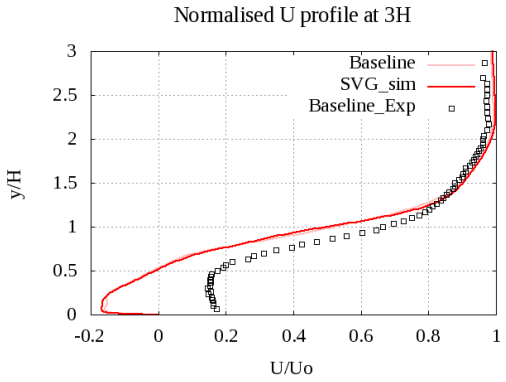
Normalised U profile at 3H
Baseline
SVG_sim
Baseline_Exp
y/H
U/Uo

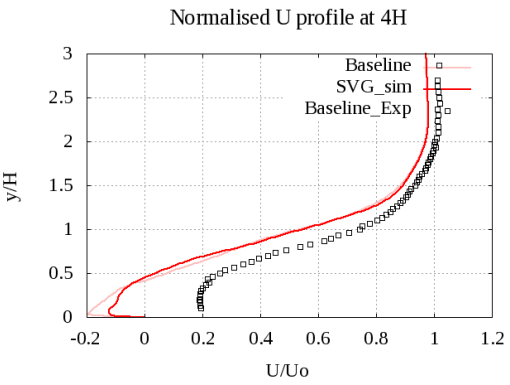
Normalised U profile at 4H
Baseline
SVG_sim
Baseline_Exp
y/H
U/Uo

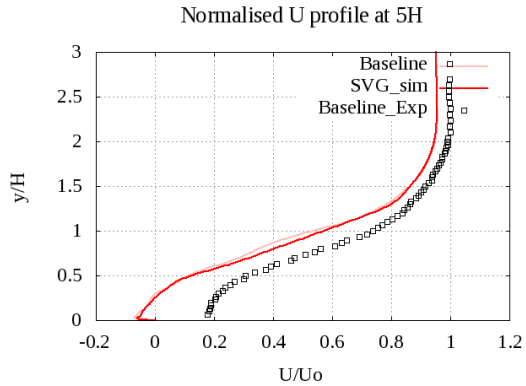
Normalised U profile at 5H
Baseline
SVG_sim
Baseline_Exp
y/H
U/Uo

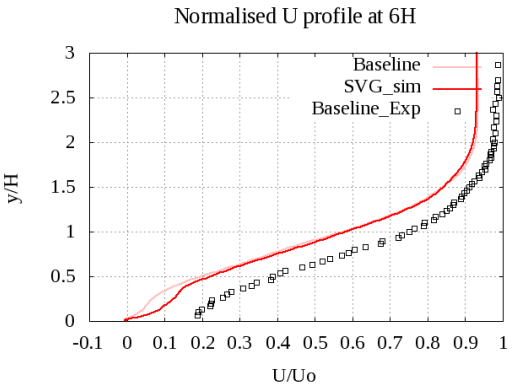
Normalised U profile at 6H
Baseline
SVG_sim
Baseline_Exp
y/H
U/Uo

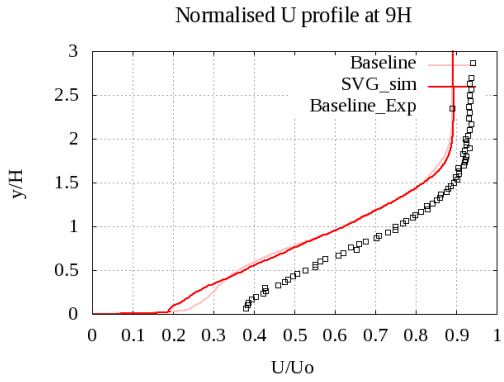

Figure 5.8 Normalised velocity profiles at nine different locations. Baseline (simulation and experiment) versus SVG simulation profiles

The effects of the SVG are very evident at the step location, where a big perturbation of the velocity is seen. There is not much variation of the velocities between the baseline flow and the SVG flow but reattachment point is better shown in next section where it is further analysed.

5.4.3 Reattachment region and skin friction distribution studies

In this section the streamlines of both simulations are depicted and compared, Fig. 5.8. Then, the skin friction coefficient distribution along the streamwise direction is shown, Fig. 5.9.

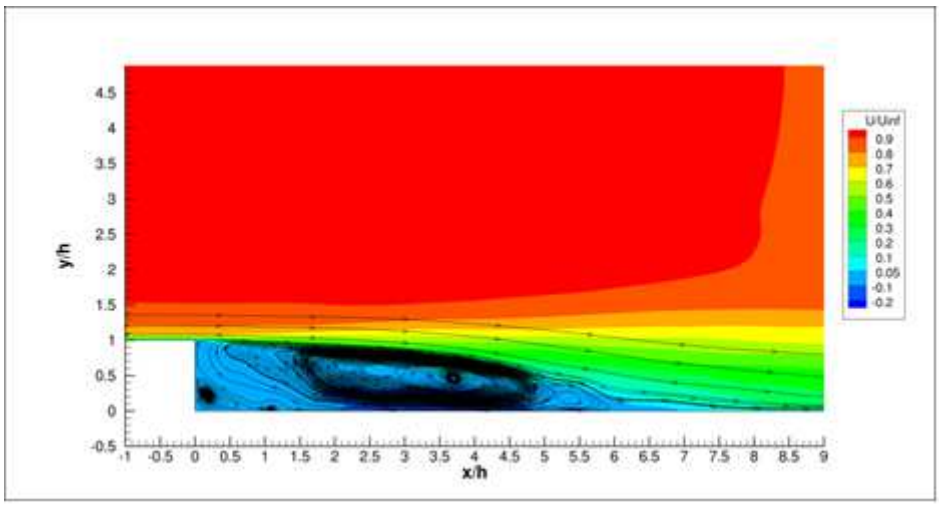

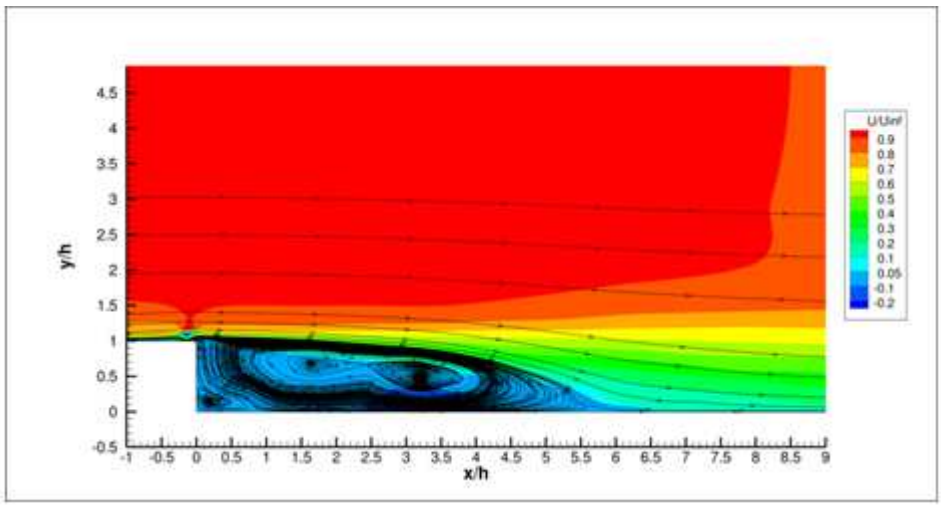

Figure 5.9 Streamlines of flow field: baseline –top- and controlled case –bottom

It is observed that the actuation of SVG reduces the recirculation bubble size and also the secondary bubble is smaller for the controlled case. For the baseline case, the flow attaches to the wall at 7H, although there is a series of smaller embedded eddies after the reattachment point as this issue is captured and shown at the skin friction distribution along the x direction in next figure, Fig. 5.9. The controlled case flow reattaches to the bottom wall at 6H, which is a reduction of 12.5%. The experimental reduction of the reattachment length was 16% hence simulation results are reasonably acceptable.

With regards to the skin friction distribution, experimental measurements were taken by means of the oil film technique. The experimental partner warned the computational side that this technique is a relative quantitative measurement as calibration is needed for absolute value of skin friction. When looking at the next graph next, one must bear in mind that the comparison between the skin friction coefficients between the experiments and the simulations is only relative and qualitative, not absolute. It is only shown for comparative purposes: the relative reduction was acceptable as mentioned previously.

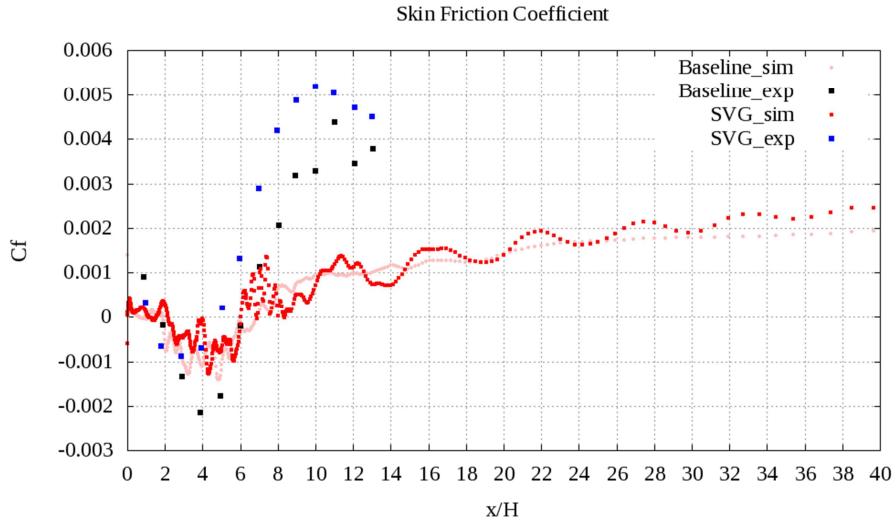

Figure 5.10 Skin friction coefficient distribution along x/H. Simulations versus experimental data (figure shown only for qualitative comparison)

Fig 5.10 shows a strong zigzag shape which is more obvious for the controlled case. This is due to the actuator effect but it is also influenced by the non-homogeneous distribution of the velocity near the wall in the spanwise direction which, in spite of having been time-averaged, it still shows a non-uniform distribution. This oscillatory distribution although not as strong as there were not physical movement in the domain was also captured in the previous Chapter of this thesis and the limitation of computing resources which would lead to a not fully statistically converged results was addressed.

The effects of the actuation of the SVG are also captured in the skin friction distribution for the controlled case. This is consistent with turbulent structures observed when Q-criterion was analysed, where such vortices remained in the domain even far down the reattachment region due to the frequency of the actuator and its addition of instabilities in the flow field.

The recovery of the experimental baseline and controlled cases seem to be much faster and the value of the skin friction coefficient quickly increases. This fast recovery does not seem to be realistic and it will only be taken as a qualitative concept, i.e., the flow starts to develop a new boundary layer after the reattachment point.

Skin friction coefficient is a parameter which has been found difficult to assess in DGDES although it was initially validated for the Driver and Seegmiller's case, [Driver and Seegmiller, 1985]. All the 3D simulations have shown a lack of smoothness in the skin friction coefficient distribution along the streamwise direction even though the results have been time and spanwise averaged when the mesh size is large. This issue is still under investigation although it is related to the non-smooth distribution of velocity along the spanwise direction when the mesh wide and the cell sizes are not too small producing relatively high difference in velocity values from the neighbouring cells. As a proof, this effect does not appear in 2D, where just a slice of 1mm was used as computational mesh or as it was shown in the section 2 of the previous chapter of this thesis. In the two dimensional simulation for this particular case, the skin friction coefficient showed a smooth curve but the reattachment length is, especially in the controlled case, largely over-prediction of the reattachment point was produced. This large over-prediction of X_R is due to the fact that two dimensional simulations will not let the flow develop in the spanwise direction thus it is squeezed and the recirculation region is enlarged. This can be seen in the Appendix at the end of this thesis.

5.4.4 Reynolds stress

An analysis of the Reynolds stresses is finally carried out to complete the analysis of the effects of SVG on a flow over a BFS. Firstly, the normal components –profiles and time- and span- averaged contours- are analysed and the turbulent shear stress is also depicted. Regarding the experimental data for the profiles, it was only available for the baseline at six locations which are the ones shown in this section: 1H, 3H, 4H, 5H, 6H and 9H; and the normal component $\langle w'w' \rangle$ was not experimentally measured.

Fig 5.11 to Fig. 5.13 show the normalised by U_0^2 normal component profiles. All simulations over-predict normal components at locations when compared to the experimental data. The effects of the motion of the SVG is captured on simulation results in the near-wall region, having stronger effects on $\langle u'u' \rangle$ and $\langle w'w' \rangle$.

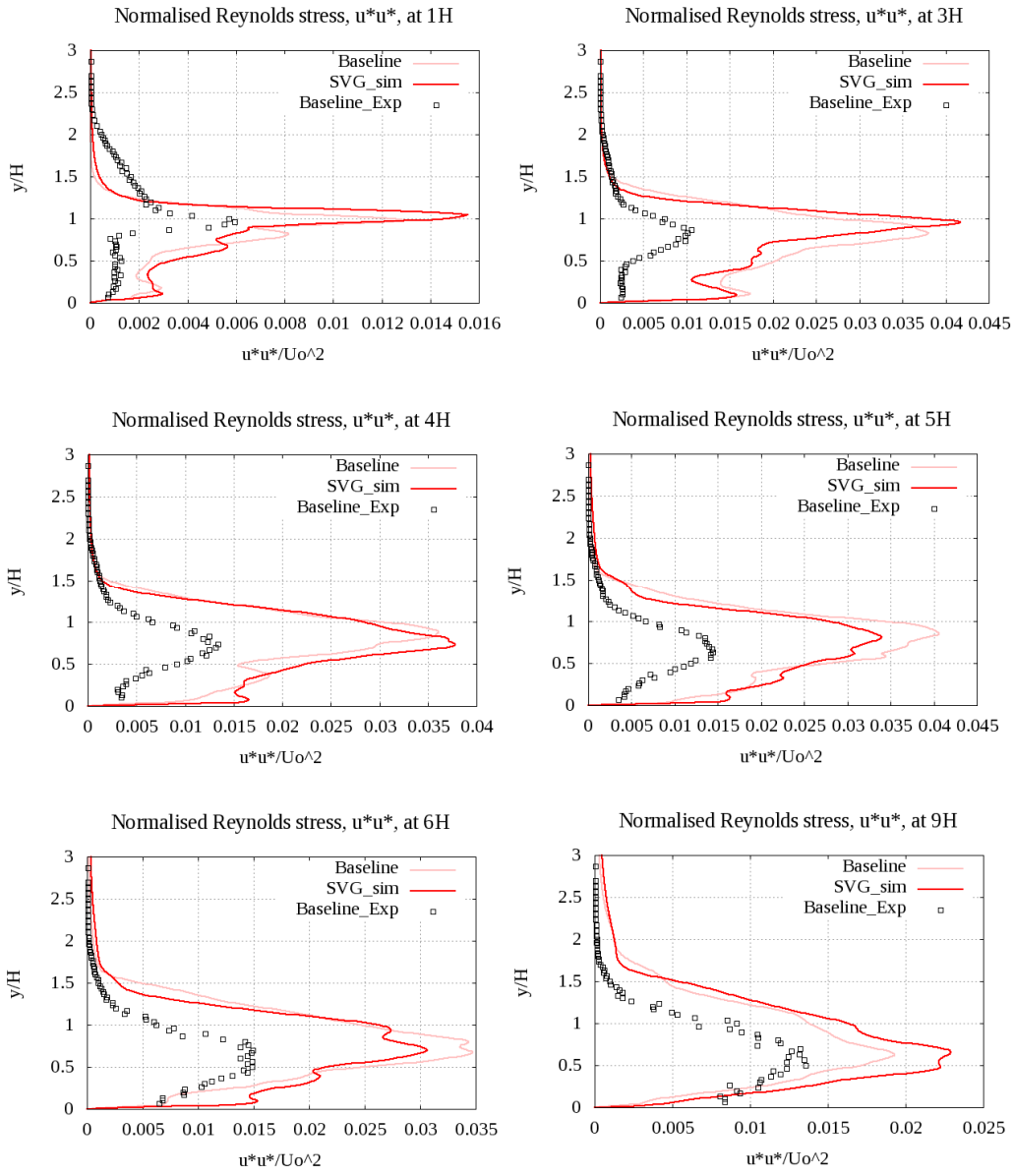

Figure 5.11 Comparison of normalised Reynolds stress <u'u'> component at six x/H locations

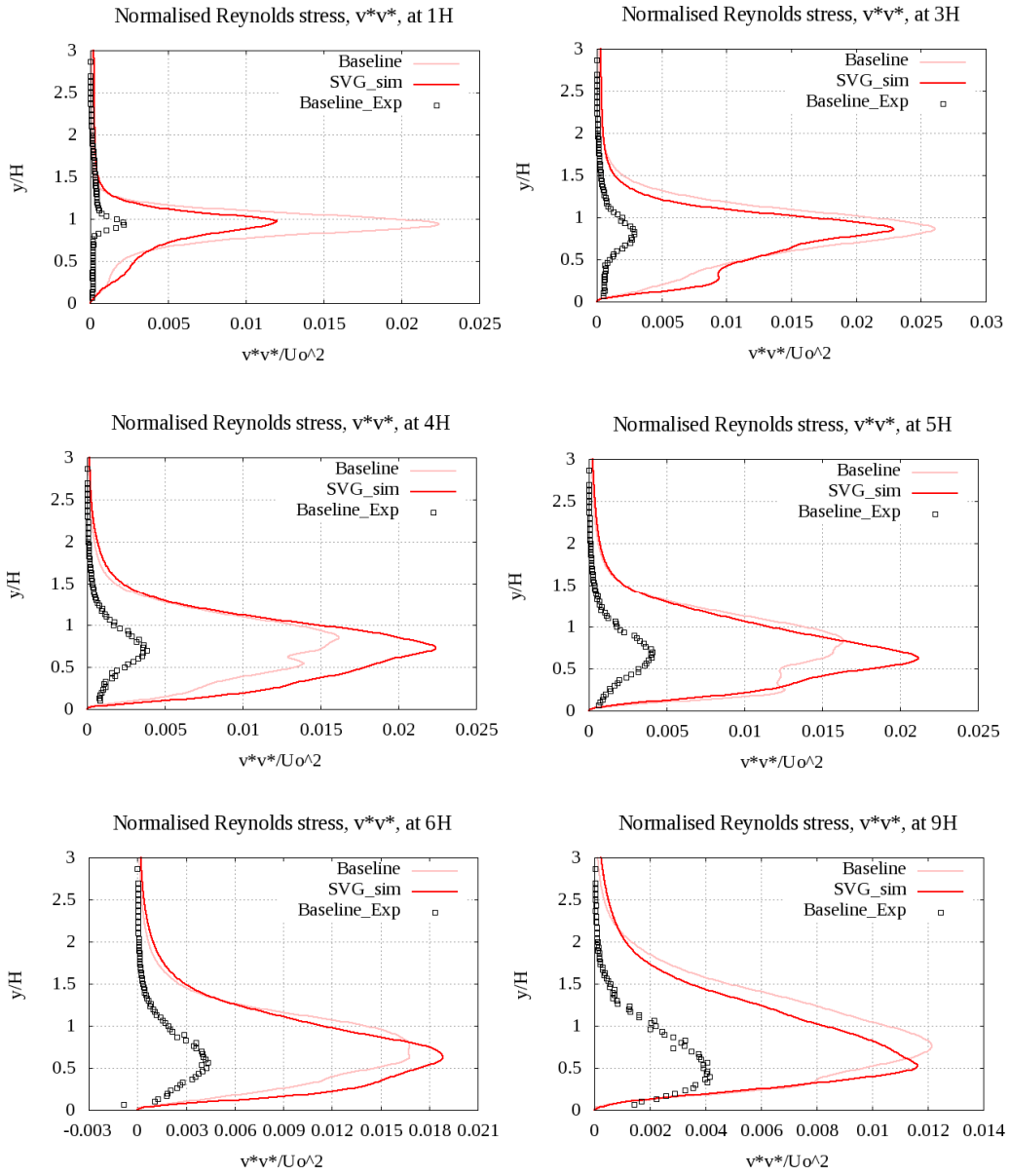

Figure 5.12 Comparison of normalised Reynolds stress <v'v'> component at six x/H locations

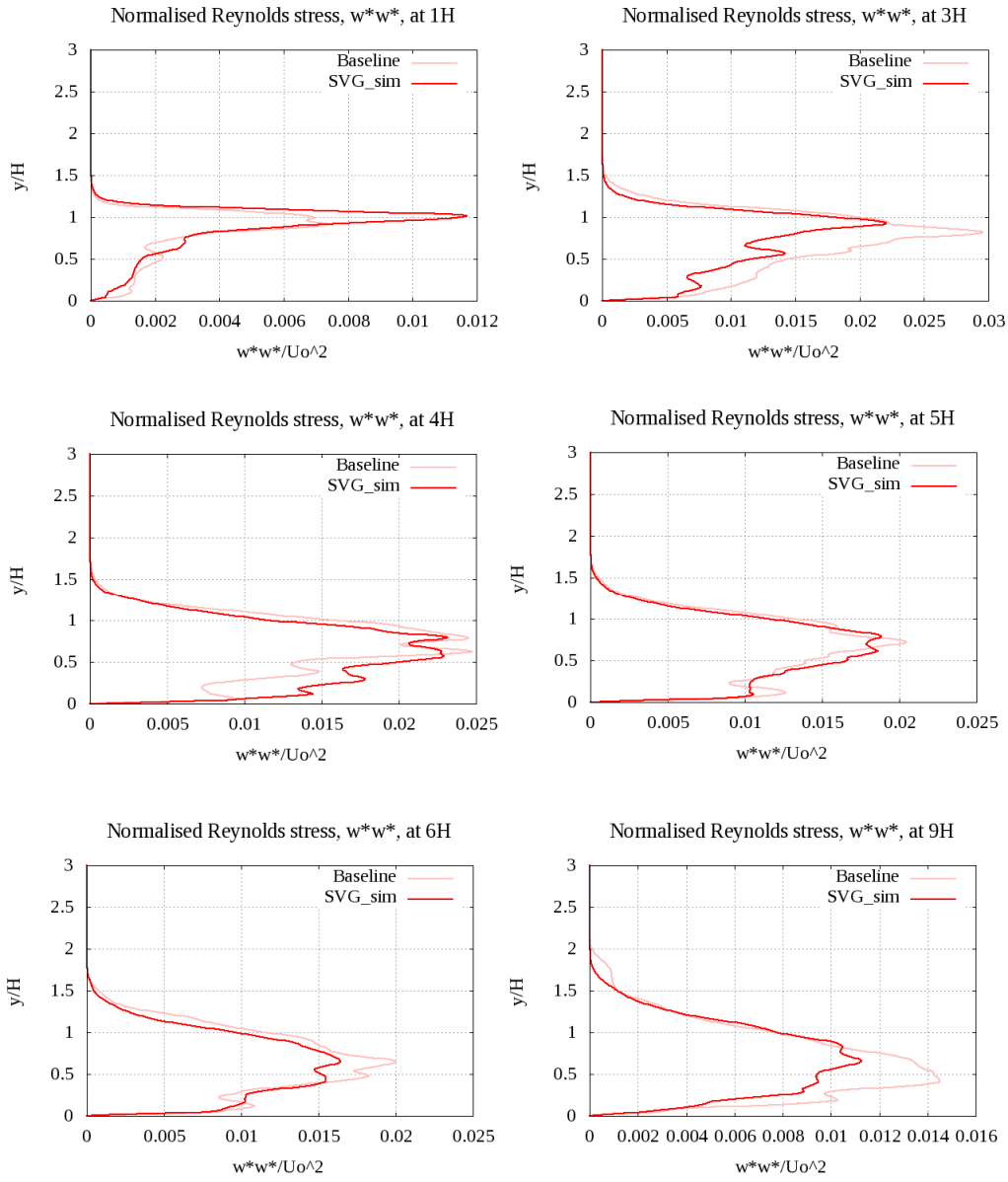

Figure 5.13 Comparison of normalised Reynolds stress <w'w'> component at six x/H locations

The normal Reynolds stress of the three components is quite similar for the controlled and uncontrolled cases and the SVG influence is difficult to be assessed in the streamwise location. The effects of the actuator on the three components are better and easily seen on the contours of the Reynolds stresses, Fig 5.13, where an increase of the three components is observed near the actuator location and a reduction is observed after the step in the recirculation region. After the flow reattaches completely, the Reynolds stress distribution is similar to the uncontrolled case for the three normal components. No experimental contours were provided.

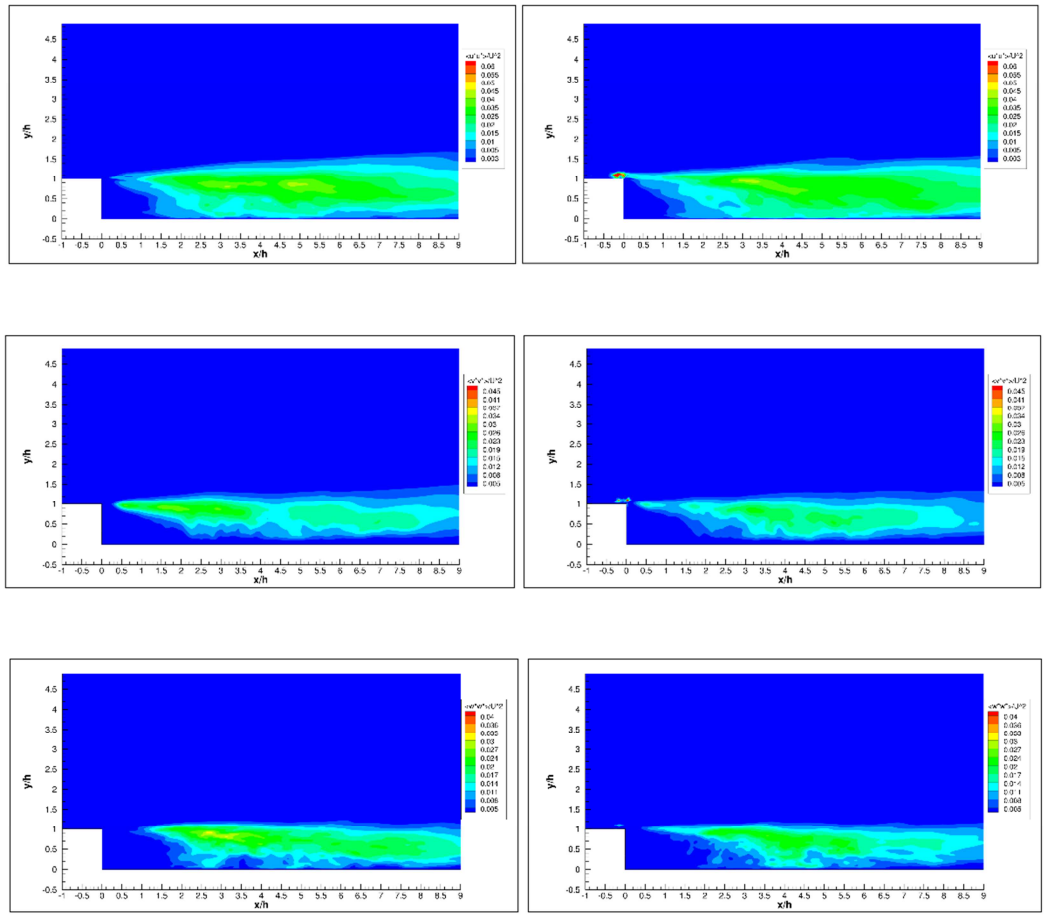

Figure 5.14 Time and spanwise averaged Reynolds normal stress contours $\langle u'u' \rangle / U_0^2$, $\langle v'v' \rangle / U_0^2$, $\langle w'w' \rangle / U_0^2$. Baseline – left- versus SVG –right- cases

With regards to Reynolds shear stress, the profiles, Fig. 5.14, show a matching trend of the curves with the experimental baseline shape. However, $|\langle u'v' \rangle|$ is over-predicted at all locations as it happened with the rest of components. The controlled case shows a larger turbulent shear stress near the wall within the primary bubble at most of locations, interpreted as an enhancement of the mixing in the recirculation area. This fact can be also seen when the turbulent structures where plotted in previous figures of this chapter, Fig. 5.6. After the reattachment area, the controlled and uncontrolled shear stress profiles are very similar and the experimental profile is also reasonably close to the simulation. This might be an indicator of possible measurement errors although DGDES has shown to tend to over-predict Reynolds stresses in separated flows.

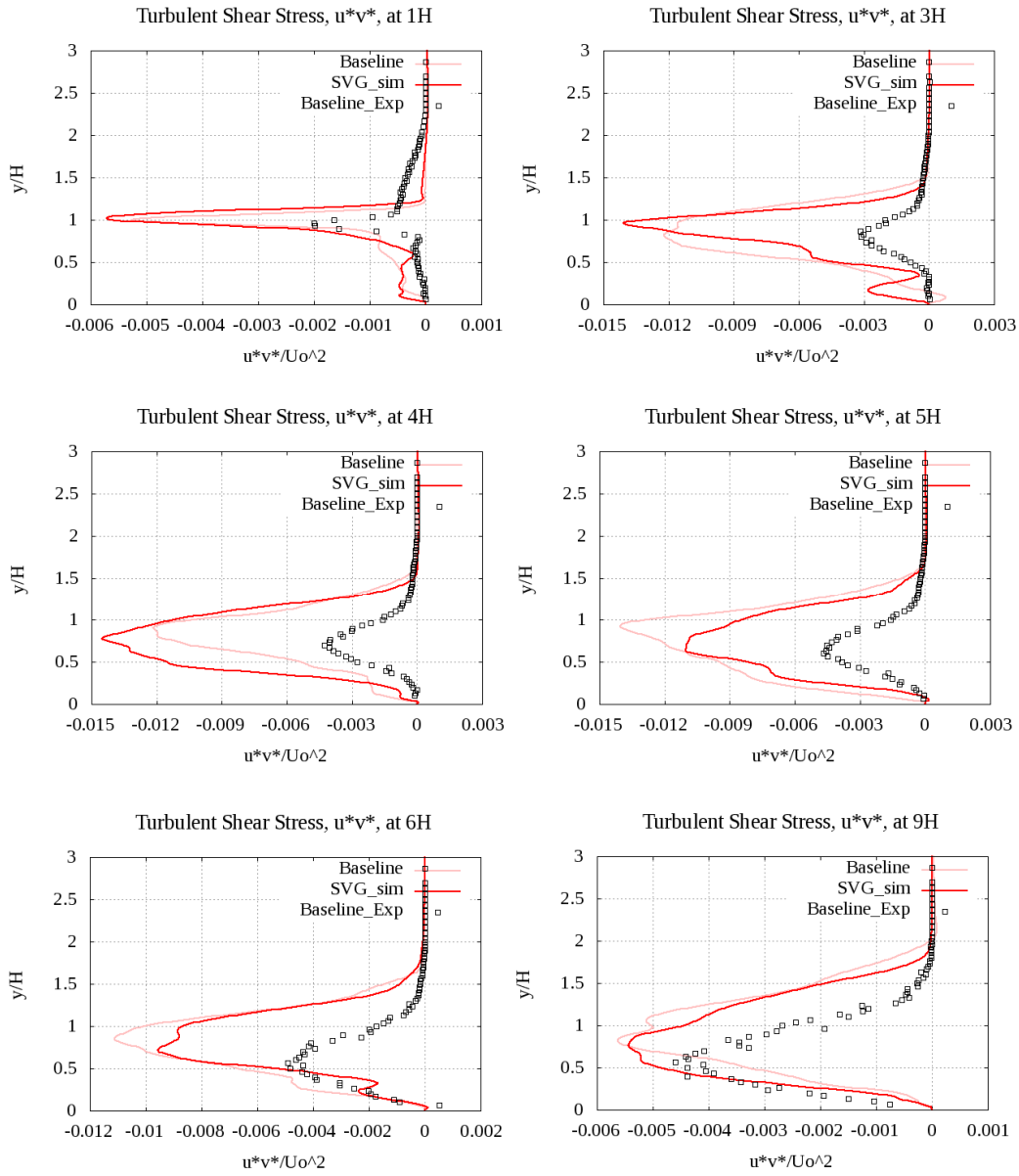

Figure 5.15 Normalised Reynolds shear stress <u'v'> profiles at six different x/H locations

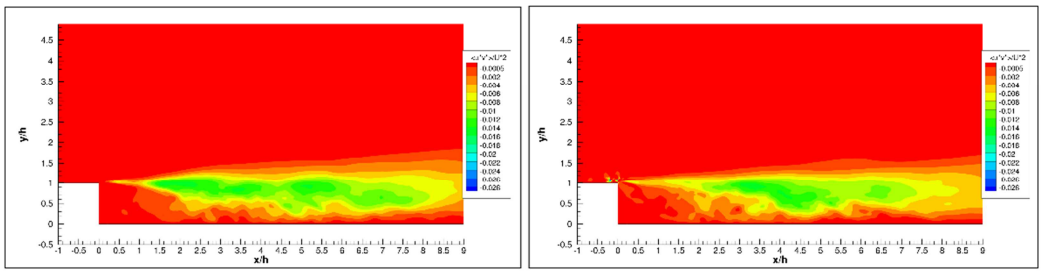

Figure 5.16 Time and spanwise averaged Reynolds shear stress $\langle u'v' \rangle / U_0^2$ contour: Baseline compared to SVG actuation

In Fig 5.15 the shear stress contours are shown. It can be seen there is an overall increase of this Reynolds component within the separation area, confirming again that there exists and improvement of the flow mixing, in particular near the reattachment region. Turbulent shear stress is also increased at the SVG location.

5.5 Conclusions

A novel device known as spanwise vortex generators has been investigated in this chapter. Experimental data was very limited and not 100% reliable as it has been discussed in previous sections of this chapter but simulations provided a proper insight into the features of the SVG effects on a flow over a backward facing step.

For all simulations, an 8M mesh was used. According to experiments a reduction of 16% of the reattachment length was achieved by the application of this device upstream of the step and simulations provided a reduction of 12.5%, which is reasonably accurate due to the lack of information from the experimental side. Turbulent structures and Reynolds stresses captured the effects of the oscillation of the SVG and the skin friction coefficient distribution also captured such effect downstream of the step and even further downstream near the end of the computational domain. The installation of this device has shown to generate a highly turbulent flow and the produced turbulent structures remain in the domain further downstream of the step than the DBD plasma device case.

With regards to Reynolds stresses, the difference of the baseline and controlled cases was not significant, but as mentioned in the previous paragraph, the motion of the SVG is captured especially in the near-wall regions.

Spanwise vortex generator induces an organised motion into and interacts with the separated shear layer from the upper corner of the step. The reattachment point moves upstream and the skin friction downstream increases.

6 Final conclusions

6.1 Summary of work and achievements

The objective of this work was to study the actuation and effects of two different active flow control devices on a flow over a backward facing step using RANS and SA-URANS method for two dimensional simulations and the hybrid RAN/LES IDDES approach simulations. The reliability of the results has been validated by means of comparisons of the simulated cases with different wind tunnel experimental databases.

Overall, the flow control over backward facing step has been computationally investigated and validated with the ultimate goal of obtaining a deep insight into the mechanism of Reynolds stress manipulation by inducing disturbances into the separated shear layer after the step. The relationship of the Reynolds stresses with flow separation and reattachment has been proven: the increased absolute values of the normalised Reynolds shear stress, caused by a plasma actuator or a spanwise vortex generator will result in shortened recirculation zone and reattachment point movement upstream.

In this chapter the achievements for each control device will be discussed.

6.1.1 Single DBD plasma actuation achievements

In first place a comparison of the Driver and Seegmiller's baseline case by assessing the performance of two different approaches, RANS using a commercial code and URANS using our in-house code, over the backward facing step was carried out as an initial study to acquire knowledge about the flow behaviour and characteristics. Due to the aims and objectives of this thesis, the chosen software for all the simulations performed in this study was the in-house code DGDES using iDDES.

Then, a single DBD actuator was placed on the wall before the step edge. Experimentally, the application of the steady plasma actuation was quasi-steady. However, when Singh and Roy's model was implemented, plasma actuation was

considered purely steady and constant. When the modulation of plasma was investigated, using Singh and Roy's model only takes into consideration the frequency of the pulsation and not of the frequency of the applied AC voltage as also assumed for experimental quasi-steady plasma.

Steady forcing of the plasma simulation showed a reduction of 5% of the reattachment point which is in good agreement with the reduction of the experiment, 3.4%. An enhanced mixing was achieved and the relationship between the application of plasma and the Reynolds stresses was found: steady plasma actuation increases the Reynolds stress components at relevant locations along the streamwise length. Regarding the relationship of the actuation of plasma and the size of the primary circulation bubble, the larger the plasma actuation force is, the smaller reattachment length is. This feature was observed when Singh and Roy's model was adjusted to match the experimental results. So CFD simulations offer a further exploration of the effects of plasma than an experimental study can offer, as the possibility of a wide range of control parameters is available. The application of Singh and Roy's model for real quasi-steady plasma actuation is purely steady in the model as already mentioned previously; however, in spite of this assumption the results of the simulations were very accurate and computationally more efficient and faster than any other more complex model. The production of very good results in a reasonable timeframe is a very good advantage of the model.

With regards to modulation of plasma with Singh and Roy's model showed excellent agreement with the experimental reattachment length, opposite to Shyy's model in which the reattachment length could not be matched to the experiments and a comparison for the MARS project was only qualitatively achieved.

The use of both models operating in pulsated mode showed relevant effects on the larger turbulent scales as observed in the experimental results and a larger reduction of the separated region as captured in the experiments carried out at the University of Poitiers – 20% experimental reduction. Singh and Roy's model with an appropriate constant showed also a 20% reduction of the reattachment area. The normalised absolute value of the Reynolds shear stress was larger when the case was

controlled by the modulated plasma actuator providing the achievement of one of the main aims of this study.

And last but not least, the application of modulated plasma produced a larger reduction of the reattachment region using less energy than steady plasma showing a potential application for real life scenarios.

6.1.2 Spanwise Vortex Generators actuation achievements

Simulations of a novel device, spanwise vortex generators were performed. In the simulation, the SVG was considered to be a flat surface located exactly where the experimental SVG were located: the actuator was located 2mm above the step edge. Results showed a very significant effect on the separation bubble in comparison with the baseline case. The motion of the device was captured by certain parameters such as the skin friction distribution and several components of Reynolds stress. In this case, the experimental database was limited and therefore a complete assessment of the device when utilised in real life is harder to be provided. However, reasonable good agreement was shown with regards to separated region reduction and a slightly larger Reynolds shear stress in the recirculation area when the flow was under the SVG influence.

6.2 Future work

Several ideas for the continuation of the work carried out in this thesis are described here.

Regarding DGDES itself the implementation of several variations of the turbulence model to tackle a wider range of problems is proposed and could be investigated. It has been seen in this thesis that Spalart-Allmaras turbulence model over-predicts the Reynolds stress when the flow separates at the edge of the backward facing step. This issue was also found by Bardina et al, (1997). This model showed to under-predict separation and over-predict reattachment in massive separated flows [Srinivasan et al, 1995] or when shockwaves occur, [Ma, 2014]. Due to this issues, different model calibrations are available in the literature [Javaherchi, 2010] and it could be a very interesting and beneficial for the future use of DGDES to implement

such calibrations into the code. Also, density corrections variations have been already proposed and their introduction into the software could allow a better and more accurate prediction and simulation of compressible flows, [Kumari, 2013; Catri, 2000] or near wall improvements, [Edwards and Chandra, 1996]. Many other variations for Spalart-Allmaras with their corresponding technical papers can be found at [Turbulence Langley Research Centre, Turbulence Model: The Spalart-Allmaras model]

DGDES is a code in constant development and according to the desired investigation, the implementation of new mathematical schemes, turbulence models, control devices, boundary conditions, moving mesh techniques, etc. can be achieved according to the research requirements. This is a massive advantage for PhD students and researchers in general when an in-house code is compare to any commercial codes: as the software is open-source – and although good programming language knowledge and advanced IT skills are required - any type of changes, new model implementations of any kind and any other modifications can be introduced. This is particularly interesting for the world of Academia.

6.2.1 Suggestions for DBD plasma actuation

With regards to future work for plasma actuation, a few suggestions will be described in this section.

First of all, all the 3D simulations could be continued from the latest point the calculations were analysed in this thesis to investigate the issue with the non-uniform distribution of the skin friction coefficient after having been time and space averaged. It was mentioned in Chapter 4 that this non-smoothness could have been caused by not having reached a fully convergence of the results due to the limitation of computational resources available to carry out this work but this is yet to be fully proved. The simulations in this thesis took around three months until the results did not show any more vortex shedding after the step and the recirculation region shape was maintained over time hence the time averaged was performed.

Secondly, an enhancement of Singh and Roy's model could be investigated in order to take into account the AC voltage frequency and include the effects of this frequency into the simulation.

Thirdly, in this thesis the exposed electrode is upstream of the grounded electrode as shown in Fig 3.2 and the actuator is placed in the horizontal wall before the step. However a CFD exploration of different configurations of the DBD plasma actuator could be carried out such as placing the DBD on the same wall but at different x/H locations with respect to the step edge or an installation of the device on top wall of the computational domain; it could also be located at the vertical wall of step and even the electrode position could be inverted and the effects of plasma could be deeply understood and studied.

Regarding the geometry, the length of the electrodes could be investigated as well as their installation not parallel to the wall but with an inclined angle with respect to the horizontal wall of the BFS. Different shapes of the device could be also tested such as horseshoe [Roy, 2009] or zigzag shaped plasma actuators.

A creation of a hybrid plasma model using Shyy's model within the separated region of the flow and Singh and Roy's model in the rest of the domain would be a very interesting study to carry out. A blending function depending on the distant to the plasma actuator could be introduced to control the switch between one model and the other.

The effects on plasma could be also investigated when the device is installed on top of an aerofoil or on any other type of surface to research.

6.2.2 Suggestions for SVG actuation

SVG further investigation is even broader than the exploration of the plasma field. In this thesis, the device setup was the same as the experimental setup but there are many options to study the flow control effects of the devices.

As previously suggested for the plasma device, the simulations for the SVG could be continued from the latest time they were carried out in this thesis to look into the skin friction distribution when the results are time and space averaged. The

simulation of this device is computationally more demanding than the plasma simulations as the code has to read the mesh due to its movement every time step of the simulation, requiring more computational resources and more computational time as a consequence.

Different frequencies and amplitudes of the applied voltage device can be investigated as well as the location of the actuator in the geometry of the BFS. The SVG could be located further from wall and at different x/H locations. Also, its geometry can be explored, what would the effects be of a wider strip of magnets? How many of them could be placed in the computational domain and what would the effects be? What would be the optimum configuration? As it can be seen, a lot of possibilities arise from this flow control device and a much deeper exploration of its effects can be carried out.

Besides, the installation of the SVG on different geometries such as an aerofoil could be investigated, perhaps leading to more realistic flight configurations.

Appendix: Two dimensional simulation of SVG: an exploration of the skin friction coefficient distribution along the streawise direction.

The three dimensional simulations with DGDES have shown for all cases, except for the validation of Driver and Seegmiller's case by Wang, (2013, that even though the results have been time and span-averaged, the distribution of the skin friction coefficient along the x direction of flow is certainly not smooth. This issue, however, does not happen when the skin friction is depicted for the two dimensional cases. Hence, this issue in 3D may be caused as it was mentioned in this thesis by the strong turbulent characteristics of the flow. Also, when a flow control device comprises some kind of motion, such as the SVG did, the oscillation is captured not only by the skin friction, but also by the Reynolds stresses.

Nevertheless, in order to sustain this statement, a two dimensional simulation of the baseline and controlled case of the SVG device was carried out and the skin friction was extracted.

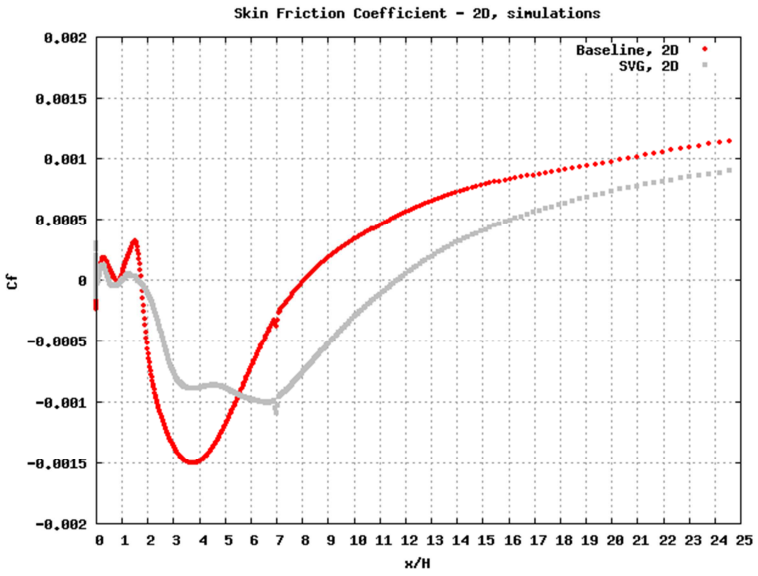

App. 1 Skin friction distribution for 2D simulations. Baseline and SVG cases

It is seen in App2.1 that both cases over-predict the circulation bubble. Besides, the controlled case produces a large reattachment length because as it was mentioned in Chapter 4, turbulence in a 3 dimensional phenomenon and by restricting to a thin mesh, the flow is squeezed and it is not able to develop in the third spatial component, z.

In spite of the separation being largely over-predicted, as the width of the mesh is just 1mm, when the skin friction is time-averaged and a slice in z=0 is extracted, the distribution along the free stream direction is completely smooth and the previous hypothesis is therefore vindicated.

References

Adrian, R. J., Meinhart, C. D., Tomkins, C. D., "Vortex organization in the outer region of the turbulent boundary layer.", *J. Fluid Mech. 422*, *1–54*. 2000.

Allan, B. G., Yao, C-S., Liin, J. C., " Numerical simulation of vortex generator vanes and jets", AIAA Paper 2002-3160, 1st AIAA Flow Control Conference, St. Louis, MO, June 24-27, 2002.

Anabtawi, A. J., Blackwelder, R. F., Lissaman, P. B. S., Liebeck, R. H., " An experimental investigation of boundary layer ingestion in a diffusing S-duct with and without passive active control", AIAA Paper 90-0739, 37th AIAA Aerospace Sciences Meeting and Exhibit, Reno, NV, January 11-14, 1999

Anderson, J. D., "Fundamentals of Aerodynamics", 4th Edition, McGraw-Hill Higher Education

Armaly, B.F., et al. "Experimental and theoretical investigation of backward facing step flow", *J. Fluid Mech, 127 (473), 20*, 1983.

Ashill, P. R., Fulker, J. L., Hackett, K. C., "Studies of flow induced by sub boundary layer vortex generators (SBVGs)", AIAA Paper 2001-0887, 39th AIAA Aerospace Sciences Meeting and Exhibit, Reno, NV, January 8-11, 2001.

Ashill, P. R., Fulker, J. L., Hackett, K. C., " Research at DERA on sub boundary layer vortex generators (SBVGs)" AIAA Paper 2002-0968, 40th AIAA Aerospace Sciences Meeting and Exhibit, Reno, NV, January 14-17, 2002.

Bakhshan, Y., Niazi, S., Mahmeli, M., "Control of Turbulent Flow in a Stepped Duct with Using the Suction and Injection", *J. Basic. Appl. Sci. Res., 2(4) 3268-3275*, 2012.

Bardina, J.E., Huang, P. G. and Coakley, T.J., "Turbulence Modeling Validation, Testing, and Development", NASA Technical Memorandum, 1997.

Barri, M. et al., "DNS of backward-facing step flow with fully turbulent inflow", *Int. J. Numer. Meth. Fluids*; 64: 777-792, 2010.

Batchelor, G.K., "The Theory of Homogeneous Turbulence", Cambridge University Press, 1953.

Batina, J.T, "Unsteady Euler algorithm with unstructured dynamic mesh for complex-aircraft aerodynamic analysis", AIAA Journal, 1991. **29**(3): p. 327-333, 1991.

Batina, J.T, "Unsteady Euler airfoil solutions using unstructured dynamic meshes." AIAA Journal, 1990. **28**(8): p. 1381-1388, 1990.

Benard, N., Sujar-Garrido, P., Bayoda, K.D., Bonnet, J.P., Moreau, E., " Pulsed dielectric barrier discharge for manipulation of turbulent flow downstream a backward facing step", AIAA paper 2014-1127, 2014.

Benard, N., Braud, P., Jolibois, J, and Moreau, E., (2008) 'Airflow Reattachment along a NACA 0015 Airfoil by a Surface Dielectric Barrier Discharge Actuator – Time-Resolved Particle Image Velocimetry Investigation', AIAA paper 2008-4202, 2008.

Benard, N., Bonnet, J.P., Touchard, G., and Moreau, E., "Flow control by dielectric barrier discharge actuators– Jet mixing enhancement," AIAA Journal , Vol. 46, No. 9, pp.2293-2305, 2008.

Benard, N., Braud, P., Pons, J., Touchard, G., and Moreau, E., "Quasi-steady and unsteady actuation by surface non-thermal plasma discharge for control of a turbulent round air jet", *J. of Turbulence, Vol. 49*, 2007.

Benard, N., Mizuno, A., Moreau, E., 'A large-scale multiple dielectric barrier discharge actuator based on an innovative three-electrode design', *Journal of Physics D: Applied Physics, Vol. 42*, 235204, 2009.

Blazek, J, "Computational Fluid Dynamics: Principles and Applications: Principles and Applications." Oxford, UK: Elsevier Science, 2001

Boussinesq, J., "Theorie de l'ecoulement tourbillonnnatnt el tumultuex des liquids", Gauthier-Villars et fils, Paris, 1897.

Bradshaw, P., Ferriss, D.H. and Atwell, N.P., "Calculation of boundary layer development using the turbulent energy equation", *J. Fluid Mech, 28 (3)*, 593–616, 1967

Breuer, M., Jovivi, N., Mazaev, K., "Comparison of DES, RANS and LES for the separated flow around a flat plate at high incidence", International Journal for Numerical Methods in Fluids 43:357, 388, 2003

Brook, J. W., Hanratty, T. J. "Origin of turbulence-producing eddies in a channel flow", *Phys. Fluids A* **5**, 1011–1022.), 1993.

Cadirci, S., Gunes., "Active flow control with an oscillating backward facing step", ASME 2012 11th Biennal Conference on Engineering Systems Design and Analysis, ESDA 2012.

Catris, S. and Aupoix, B., "Density Corrections for Turbulence Models," Aerospace Science and Technology, Vol. 4, 2000, pp. 1-11.

Chakraborty, P., Balachandar, S., Adrian, R.J., "On the relationships between local vortex identification schemes", *J. Fluid Mech.* (2005), vol. 535, pp. 189–214, 2005.

Chiang, T. P., Sheu, T. W. H., "A numerical revisit of backward-facing step flow problem", *Physics of Fluids, Vol. 11, No. 4, pp 862-874*, 1998.

Choi, H., Moin, P. and Kim, J., "Active Turbulence Control for Drag reduction in Wall-bounded Flows", *J. Fluid Mech.*, Vol 262, pp. 75-110, 1994.

Chung, K. B., Sung, H. J., "Control of turbulent separated flow over a backward-facing step by local forcing", *Experiments in Fluids 21* (1996) 417-426.

Corke, T. C., Enloe, C. L., Wilkinson, S. P., "Dielectric Barrier Discharge Plasma Actuators for Flow Control", Annu. Rev. Fluid Mech. 2010. 42:505–29, 2010.

Dandois, J., Garnier, E. and Sagaut, P., "Numerical simulation of active separation control by a synthetic jet", Journal of Fluid Mechanics, Vol. 572, 2007, pp. 25-58, Cambridge University Press.

Dejoan, A., Leschziner, M.A.,"Large eddy simulation of periodically perturbed separated flow over a backward-facing step", International Journal of Heat and Fluid Flow 25 (2004) 581–592.

Dinef, P. and Gospodinova, D., "Electrode Configurations and Non-uniform Dielectric Barrier Discharge Properties", FACTA UNIVERSITATIS (NIS) ˇ SER.: ELEC. ENERG. vol. 22, no. 2, August 2009, 217-226, 2009.

Driver, D.M. and Seegmiller, H.L., "Features of a reattaching turbulent shear layer in divergent channel flow.", AIAA Journal, 23, 163 – 171, 1985.

Driver, D.M., Seegmiller, H.L., and Marvin, J.G., "Time-dependent behavior of a reattaching shear layer." AIAA Journal, 25, 914 – 919, 1987.

Durrani, N.I. and Qin, N., "Behaviour of detached-eddy simulations for mild trailing-edge separation." *Journal of Aircraft*, 48 (1), 193 – 202, 2011.

Durrani, N.I. and Qin, N., "Comparison of Hybrid RANS-LES Methods for Massively Separated Flows." Progress in Hybrid RANS-LES Modelling., 257 – 266, 2012,

Durrani, N.I., "Hybrid RANS-LES simulations for separated flows using dynamic grids." Thesis (PhD). The University of Sheffield, 2009.

Edwards, J. R. and Chandra, S. "Comparison of Eddy Viscosity-Transport Turbulence Models for Three-Dimensional, Shock-Separated Flowfields," AIAA Journal, Vol. 34, No. 4, 1996, pp. 756-763.

Emami-Naeine, A., McCabe, S. A., de Roover, D., Ebert, J. L., Kosut, R. L., "Active Control of Flow Over a Backward-Facing Step", Decision and Control, 2005 and 2005 European Control Conference. CDC-ECC '05. 44th IEEE Conference on 12-15 Dec. 2005, 7366 – 7371.

Enloe C.L., McLaughin T. E., VanDyken R.D., Kachner K. D., Jumper E.J. and Corke T.C., "Mechanisms and Responses of a Single Dielectric Barrier Plasma Actuator: Plasma Morphology", AIAA Journal, Vol. 42, No. 3, pp. 589-594, 2004.

Erfani, R. et al, "Development of DBD plasma actuators: The double encapsulated electrode", Acta Astronautica 109 (2015) 132–143, 2015.

Fadai-Ghotbi, A., et al., "Revisiting URANS computations of the backward-facing step flow using second moment closures", 2008.

Fadai-Ghotbi, A., et al., "A Hybrid RANS-LES Model Based on Temporal Filtering." In: S.H. Peng, P. Doerffer and W. Haase, eds. Progress in Hybrid RANS-LES Modelling., Vol. 111 of Notes on Numerical Fluid Mechanics and Multidisciplinary Design, 225 – 234, 2010.

Falco, R.E., "A review of the current state of knowledge of turbulent boundary structure", Summary of the AFOSR/MSU Research Specialists Workshop on Coherent Structure in Turbulent Boundary Layers, AFOSR-TR-80-0290, 1979.

Falco, R.E., "The role of outer flow coherent motions in the production of turbulence near a wall", Coherent Structures of Turbulent Boundary Layers (eds C.R. Smith and D.E. Abbott) AFOSR, Lehigh, 1978.

Fiedler, H.E., "Coherent structures in Turbulent Flows", Prog. Aerospace Sci. Vol 25, pp 231, 269, 1988.

Frink, N.T., "A Fast Upwind Solver for the Euler Equations on Three-Dimensional Unstructured Meshes" , AIAA paper 91-0102, 1991.

Forte, M., Jolibois, J., Pons, J., Moreau, E., Touchard, G., Cazalens, M., "Optimization of a dielectric barrier discharge actuator by stationary and non-stationary measurements of the induced flow velocity: application to airflow control", Exp Fluids (2007) 43:917–928, 2007.

Gad-el-Hak, M., "Introduction to Flow Control," Gad-el-Hak, M., Pollard, A., Bonnet, J., editors. Flow control fundamentals and practices, pp. 199–273, 1998.

Gad-el-Hak, M. and Bushnell, D., "Separation Control: Review", ASME Journal of Fluids Engineering, Vol. 113, pp. 5-30, 1991.

Gad-el-Hak, M., "Passive, Active and Reactive Flow Management", Cambridge University Press, Cambridge, 2003.

Germano, M., "Properties of the hybrid RANS/LES filter. Theoretical and Computational Fluid Dynamics", 17, 225–231, 2004.

Germano, M., et al. "A dynamic subgrid-scale eddy viscosity model", Physics of Fluids A: Fluid Dynamics, 3 (7), 1760–1765, 1991.

Gregory, J. W. et al., "Force Production Mechanisms of a Dielectric-Barrier Discharge Plasma Actuator", AIAA paper 2007-185, 2007.

Griffith, M. D., Hourigan, K., Thompson, M. C., " Numerically Modelling Blockage Effects on the Flow Between Flat Plates", 15th Australasian Fluid Mechanics Conference, the University of Sydney, Sydney, Australia, 13-17 December 2004.

Griffith, M. D,Thompson, M. C., Leweke, T., Hourigan, K., Panderson, W., "Wake behaviour and instability of flow through a partially blocked channel", *J. Fluid Mech.* (2007), *vol.* 582, *pp.* 319–340

Gritskevich, M.S., et al., "Development of DDES and IDDES Formulations for the k − ω Shear Stress Transport Model." Flow Turbulence and Combustion, 88 (3), 431 – 449, 2012.

Haller, G., "An objective definition of a vortex", *J. Fluid Mech.(2005),* Vol. 525, pp.1–26, 2005.

Hamstra, J. W., Miller, D. N., Yagle, P. J., Truax, P. P., Anderson, B. H., Wendt, B. J., "Active flow control technology demonstration", ICAS-2000-6. 11.2, 22nd International Congress of the Aeronautical Sciences, Harrogate, UK, August 27-September 1, 2000.

Harten A., "On a class of high resolution total-variation-stable finite-difference schemes", SIAM , Journal of Numerical Analysis, 21(1):1 23, 1984.

Holmes, A. E., Hickey, P. K., Murphy, W. R., Hilton, D. A., "The application of sub-boundary layer vortex generators to reduce canopy Mach rumble interior noise on

the Gulfstream III", AIAA Paper 87-0084, AIAA 25th Aerospace Sciences Meeting, Reno, NV, January 12-15, 1987.

Hoskinson, A. R., Hershkowitz, N., "Flow Measurements and Plasma Simulations of Double and Single DBD Plasma Actuators in Quiescent Air", 46th AIAA Aerospace Sciences Meeting and Exhibit, pg 1370, Reno, NV, 2008.

Hunt, J. C. R., Wray, A. A. & Moin, P. "Eddies, stream, and convergence zones in turbulent flows." Center for Turbulence Research Report CTR-S88, pp. 193–208. 1988.

Iaccarino, G., Ooi, A.,. Durbin, P.A, Behnia, M., "Reynolds averaged simulation of unsteady separated flow", International Journal of Heat and Fluid Flow 24 (2003) 147-156, 2003.

Inaoka, K., Nakamura, K., Senda, M., "Heat transfer control of a backward-facing step flow in a duct by means of electromagnetic actuators", International Journal of Heat and Fluid Flow 25 (2004) 711-720.

Jameson, A., "Time dependent calculations using multigrid, with applications to unsteady flows past airfoils and wings.", AIAA-Paper 91-1596, 1991.

Jameson, A., Schmidt, W., and Turkel, E., "Numerical Solutions of the Euler Equations by Finite Volume Methods using Runge-Kutta Time Stepping Schemes",. AIAA Paper 81-1259. **1981.**

Javaherchi, T., "Review of Spalart-Allmaras Turbulence Model and its Modifications", University of Washington, March 2010.

Jenkins, L., Gorton, S. A., Anders, S., "Flow control device evaluation for an internal flow with an adverse pressure gradient", AIAA Paper 2002-0266.

Jeong, J., Hussain, F., "On the identification of a vortex", *J. Fluid Mech.* **285**, 69–94, 1995.

Jimenez, J., Wray, A. A., Saffman, P. G. & Rogallo, R. S. "The structure of intense vorticity in isotropic turbulence.", *J. Fluid Mech.* **255**, 65–90. Rogers & Moser (1994); 1993.

Jones, W. P. and Launder, B. E., "The Prediction of Laminarisation with a tow-equation Model of Turbulence", International Journal of Heat Mass Transfer 15, 301-314, 1972.

Kerho, M., Hutcherson, S., Blackwelder, R. F., Liebeck, R. H., "Vortex generators used to control laminar separation bubbles", J Aircr 1993; 30(3): 315-9.

Kim, J. Y., Ghajar, A. J., Tang, C., Foutch, G. L., "Comparison of Near-Wall Treatment Methods for High Reynolds number Backward Facing Step",. International Journal of Computational Fluid Dynamics, Vol. 19, No. 7, 493–500, 2005.

Kumari, N., Nair, M.T., "Application of Density Corrected Spalart-Allmaras Model to Flow Past Ogive Cylinder at High Angles of Attack", Journal of Applied Fluid Mechanics, Vol. 6, No. 3, pp. 375-384, 2013.

Launder, B.E., Sharma, B.I., "Application of the Energy-dissipation Model of Turbulence to the Calculation of Flow Near a Spinning Disc",. Lett. Heat Mass Transf. 1, 131-138, 1974

Le, H., Moin, P., Kim, J., "Direct numerical simulation of turbulent flow over a backward facing step", *J. Fluid Mech* , Vol 330, pp. 349-374, 1997.

Leonov, S.B., Yarantsev, D.A., "Quasi-DC discharge in high-speed flow for combustion enhancement", ICPIG 15-20, 2007.

Li, X., Gu, C.and Xu, J., "Development of Roe-type scheme for all-speed flows based on preconditioning method", Computers and Fluids, 38 (4), 810-817, 2009.

Lien, F.S., Leschziner, M.A., "Assessment of the turbulence-transport models including non-linear RNG eddy viscosity formulation and second-moment closure for flow over a BFS", 1994.

Lin, J. C., "Control of turbulent boundary layer separation using micro-vortex generators", AIAA Paper 99-3403, 30th AIAA Fluid Dynamics Conference, Norfolk, VA, June 28 – July 1, 1999.

Lin, J. C., Howard, F. G., Selby, G. V., "Small submerged vortex generators for turbulent flow separation control", J Spacercr Rockets, 1990; 27(5): 503-7.

Lin, J. C., Howard, F. G., Bushnell, D. M., Selby, G. V., "Investigation of several passive and active methods for turbulent flow separation control", AIAA Paper 90-1598, AIAA 21st Fluid Dynamics, Plasma Dynamics and Lasers Conference, Seattle, WA, June 18-20, 1990.

Lin, J. C., Selby, G. V., Howard, F. G., " Exploratory study of vortex-generating devices for turbulent flow separation control", AIAA Paper 91-0042, AIAA 29th Aerospace Sciences Meeting, Reno, NV, January 7-10, 1991.

Liou, M.S., Steffen, C.J., "A new flux splitting Scheme", *Journal of Computational Physics*, 107 pp23-39, 1993.

Liou, M.S., Van, Leer B., "Choice of Implicit and Explicit Operators for the Upwinding differencing scheme", AIAA paper, 88-0624, 1988.

Liou, M.S., "A further development of the AUSM+ scheme towards robust and accurate solutions for All Speeds", AIAA 2003-4116, 2003.

Liu, Y., Vinokur, M., "Upwind algorithms for general thermo-chemical nonequilibrium flows", AIAA paper, 89-0201, 1989.

Liu, X., Qin, N., and Xia, H., "Fast dynamic grid deformation based on Delaunay graph mapping", Journal of Computational Physics, 2006. **211**(2): p. 405-423, 2006.

Ma, L., Lu, L., Fang, J., Wang Q., "A study on turbulence transportation and modification of Spalart–Allmaras model for shock-wave/turbulent boundary layer interaction flow", Chinese Journal of Aeronautics, 27(2): 200–209, 2014

McCormick, D. C., "Shock-boundary layer interaction control with low-profile vortex generators and passive cavity" AIAA Paper 92-0064, 30th AIAA Aerospace Sciences Meeting and Exhibit, Reno, NV, January 6-9, 2012

Mehrez, Z., Bouterra, M., El Cafsi, A. E., Belghith, A., Le Quéré, P., "ACTIVE CONTROL OF FLOW BEHIND A BACKWARD FACING STEP BY USING A PERIODIC PERTURBATION" , ARPN Journal of Engineering and Applied Sciences, Vol. 5, No. 2, pp. 21-29, February 2010.

Menter, F.R., Kuntz, M., "Adaption of eddy-viscosity turbulence models to unsteady separated flow behind vehicles", Aerodynamics of heavy vehicles: trucks, buses and trains, 2004.

Menter, F.R. and Egorov, Y., "The Scale-Adaptive Simulation Method for Unsteady Turbulent Flow Predictions. Part 1: Theory and Model Description." Flow Turbulence and Combustion, 85 (1), 113 - 138, 2010.

Menter, F.R. and Kuntz, M., "Adaptation of eddy-viscosity turbulence models to unsteady separated flow behind vehicles." In: Symposium on the aerodynamics of heavy vehicles: trucks, buses and trains, Berlin, 2004.

Menter, F.R., "Two-equation eddy-viscosity turbulence models for engineering applications." AIAA Journal, 32, 1598 - 1605, 1994.

Menter, F.R., Kuntz, M., and Langtry, R., "Ten years of experience with the SST turbulence model." In: 4th International Symposium on Turbulence Heat and Mass Transfer, 625 - 632, 2003.

Mertz, B. E., Corke, T. C., "Single-dielectric barrier discharge plasma actuator modelling and validation" J. Fluid Mech. (2011), vol. 669, pp. 557–583, 2011.

Merzari, E., Khakim, A., and Ninokata, H., "Unsteady Reynolds-averaged Navier-Stokes: toward accurate prediction of turbulent mixing phenomena." *Int. J. Process Systems Engineering,* 1 (1), 100–123, 2009.

Miles, R.B., "Flow control by energy addition into high-speed air", AIAA 2000-2324, 2000.

Ming, X., "Flow control over backward facing step by synthetic jet", The 12th International Symposium on Fluid Control, Measurement and Visualization, Nara, Japan, 18-23 Nov. 2013.

Mochizuki, S., Yamada, S., and Osaka, H., "Reynolds Stress Field in a Turbulent Wall Jet Induced by Streamwise Vortex With Periodic Perturbation," Experiments in Fluids, 40, 372-382, 2006.

Moreau, E., "Airflow control by non-thermal plasma actuators", J. Phys. D: Appl. Phys. 40 605, 2007.

Mounts, J. S., Barber, T. J., " Numerical analysis of shock-induced separation alleviation using vortex generators", AIAA Paper 92-0751, 30th AIAA Aerospace Sciences Meeting and Exhibit, Reno, NV, January 6-9, 1992.

Neumann, J., Wengle, H., "DNS and LES of Passively Controlled Turbulent Backward-Facing Step Flow", *Flow, Turbulence and Combustion* **71:** 297-310, 2003.

Nichols, R. H., "Turbulence Models and Their Application to Complex Flows", University of Alabama at Birmingham, NASA, 2012

Nicoud, F. and Ducros, F., "Subgrid-scale modelling based on the square of the velocity gradient tensor. Flow", Turbulence and Combustion, 62, 183–200., 1999.

Noh, W.F., "CEL: A Time-dependent Two-Space Dimensional Coupled Eulerian-Lagrangian -Code", Methods in Computational Physics, pp 117-179, 1964.

Okada, K., Fujii, K., Miyaji, K., "Computational Study of the Separated Flow Structure Induced by the Synthetic Jet on a Backward-Facing Step", Flucome 2009, 10th International Conference in Fluid Control, Measurements and Visualization, August 17-21, 2009, Moscow, Russia.

Opaits, D. F., "Dielectric Barrier Discharge Plasma Actuator for Flow Control", NASA/CR—2012-217655, 2012.

Panjwani, B., Ertesvag I.S., Gruber, A., Rian K.E., " Large Eddy Simulation of Backward Facing Step Flow", MeklT09, Fifth National Conference on Computational Mechanics, Trondheim, 2009.

Panguluri, S, Reasor, D., LeBeau Jr., R.P., "Investigation of Grey Area Construction on the performance of Detached eddy Simulation", AIAA 2007-4095, 2007.

Peppler, I.L., "From the ground up", pg 23. Aviation Publishers Co. Limitied, Ottawa Ontario, 27th Revised Edition, 1996.

Pons, J., Moreau, E., Touchard, G., "Asymmetric surface dielectric barrier discharge in air at atmospheric pressure: electrical properties and induced airflow characteristics", J. Phys. D: Appl. Phys. 38 3635, 2005.

Pope, S.B., "Turbulent Flows", Cambridge University Press, 2000.

Prandtl, L., "Fluid Flow in very little friction", Verhandlungen des dritten internationalen Mathematiker- Kongresses in Heidelberg, .1904

Prandtl, L.,. "Fluid motion with very small friction". In: Third international mathematics congress, Heidelberg, 484–491. Schubauer and Skramstand, 1947.

Qin, N. and Xia, H., "Detached eddy simulation of a synthetic jet for flow control." Proceedings of the Institution of Mechanical Engi.neers, Part I: Journal of Systems and Control Engineering, 222 (5), 373 – 380, 2008.

Rao, D. M., Kariya, T. T., "Boundary-layer submerged vortex generators for separation control – an exploratory study" AIAA Paper 88-3546-CP, 1988.

Reynolds, O., "On the dynamical theory of incompressible viscous fluids and the determination of the criterion." Philosophical Transactions of the Royal Society of London. A, 186, 123 – 164, 1985.

Reynolds, W.C., and Hussain, A.K.M.F. "The Mechanics of an Organized Wave in Turbulent Shear Flow, Part 3: Theoretical Models and Comparison with Experiments", *J Fluid Mech*, 54(2):263-288, 1972.

Riherd, M., Roy, S., Rizzetta, D., Visbal, M., "Study of transient and unsteady effects of plasma actuation in transitional flow over an SD7003 airfoil", AIAA Paper 2011-1075, 49th AIAA Aerospace Meeting including the New Horizons Forum and Aerospace Exposition, 4-7 January 2011, Orlando, Florida.

Robinson, S. K. "Coherent motion in the turbulent boundary layer.", *Annu. Rev. Fluid Mech.* **23**, 601–639, 1991.

Roe, P.L., "Approximate Riemann Solvers, Parameters velcorts and Difference Schemes", *Journal of Computational Physics*, 1981.

Roth, J. R., "Aerodynamic flow acceleration using paraelectric and peristaltic electrohydrodynamic effects on a one atmosphere uniform glow discharge plasma", *Phys. Plasmas* 10, 2117, 2003.

Roy, S., Gaitonde, D. V., "Force interaction of high pressure glow discharge with fluid flow for active separation control", Phys. of Plasmas, 13, 023503, 2006.

Roy, S., Singh, K. P., Gaitonde, D. V., "Air Plasma Actuators for Effective Flow Control", AIAA paper, 2007-184, 2007.

Roy, S., Singh, K. P ., "Modeling plasma actuators with air chemistry for effective flow control", J. Appl. Phys. 101, 123308, 2007.

Roy, S. and Wang, C.C, "Bulk flow modification with horseshoe and serpentine plasma actuators", *J. Phys. D: Appl. Phys.* 42, 2009.

Sakuraba, K., Fukazawa, K., Sano, M., "Control of turbulent channel flow over a backward-facing step by suction or injection", Heat Transfer – Asian Res. 33 (8), 490-504, 2004.

Santhanakrishnan, A., Jacob, J. D., " Flow Control Using Plasma Actuators and Linear/Annular Plasma Synthetic Jet Actuators", 3rd AIAA Flow Control Conference, pg. 3033, San Francisco, CA, 2006.

Schlichting, H., Gersten, K., "Boundary Layer Theory", 8th rev. and enlarged ed., McGraw-Hill Book Company, Inc., 2000.

Schmitt, G.F., "About Boussinesq's turbulent viscosity hypothesis: historical remarks and a direct evaluation of its validity", Comptes Rendus Mechaniques 335, 9-10, 617-627, 2007.

Shur, M., Spalart, P.R., Strelets, M. and Travin, A., "Detached-eddy simulation of an airfoil at high-angle of attack", 1999.

Shur, M.L., Spalart, P.R., Strelets, M.K., Travin, A.K., "A hybrid RANS/LES approach with delayed-DES and wall-modelled LES capabilities", International Journal of Heat and Fluid Flow 29, 1638-1649, 2008.

Shur, M., et al., "A hybrid RANS-LES approach with delayed-DES and wall modelled LES capabilities." International Journal of Heat and Fluid Flow, 29, 1638 – 1649, 2008.

Shur, M., et al., "A rapid and accurate switch from RANS to LES in boundary layers using an overlap region.", Flow, turbulence and combustion, 86 (2), 179 – 206, 2011.

Shyy, W., Jayaraman, B., and Andersson, A., "Modelling of glow discharge-induced fluid dynamics", *J. Appl. Phys.* 92, 6434, 2002.

Singh, K.P. and Roy, S., "Force approximation for a plasma actuator operating in atmospheric air", *J. Appl. Phys.* 103, 013305, 2008

Smagorinsky, J. "General circulation experiments with the primitive equations", Monthly Weather Review, 91, 99, 1963.

Smith, C. R., Walker, J. D. A., Haidari, A. H. , Sobrun, U. "On the dynamics of near-wall turbulence." Phil. Trans. R. Soc. Lond. A **336**, 131–175, 1991.

Spalart, P.R., Allmaras, S.R., "A One-Equation Turbulence Model for Aerodynamic Flows", AIAA-92-0439,1992.

Spalart, P.R., Jou, W-H, Strelets, M., Allmaras, S.R., "Comments on the feasibility of LES for wings, and on a hybrid RANS/LES approach". Advances in DNS/LES, 1997.

Spalart, P.R., et al., "A new version of detached-eddy simulation, resistant to ambiguous grid densities.", Theoretical and Computational Fluid Dynamics, 20, 181 – 195, 2006.

Srinivasan, G.R., Ekaterinaris, J.A., McCroskey, W.J., "Evaluation of turbulence models for unsteady flows of an oscillating airfoil", Computers & Fluids Vol. 24, No. 7, pp. 833-861, 1995

Sujar-Garrido, P., Bernard, N., Laurentie, J. C., Bonnet, J.P., Moreau, E., "Modifications du tenseur de Reynolds turbulent en aval d'une marche descendante par actionneur plasma", 13ième Congrès Francophone de Techniques Laser, CFTL 2012 - ROUEN, 18 – 21 Septembre 2012.

Toro, E.F., "Riemann Solvers and Numerical Methods for Flui Dynamics, Springer-Verlag, 1997.

Tota, P. V., "Turbulent Flow Over a Backward-Facing Step Using the RNG k-ε Model", Flow Science Inc., 2009.

Toschi, F., Piomelli, U., Iaccarino, G., "Backward facing calculations using the shear improved Smagorinski model", Center for Turbulence Research Proceeding of the Summer Program, 2006.

Travin, A., Shur, M., Strelets, M., Spalart, P.R., "Detached Eddy Simulations past a circular cylinder",. Flow Turbul. Combust. , 63:293-313, 1999.

Uruba, V., Jonas, P., Mazur, O., " Control of a cannel flow behind a backward facing step by suction/blowing", International Journal of Heat and Fluid Flow 28 (2007) 665-672.

Valencia, A., "Effect of pulsating inlet on the turbulent flow and heat transfer past a backward-facing step", *Int. Comm. Heat Mass Transfer*, Vol. 24, No. 7, pp. 1009-1018, 1997

Visbal, M. R., Gaitonde, D.V., Roy, S., "Control of transitional and turbulent flows using plasma-based actuators", AIAA Paper 2006-3230, 5-8 June, San Francisco, CA, 2006.

Wang D., Lu L., Li Q., "Improvement on S-A model for predicting corner separation based on turbulence transport nature" , AIAA 2009-4931, 2009.

Wang, L., Hu, R., Li, L., Fu, S., "Detached Eddy Simulation of Flow past a Backward-Facing Step with a Harmonic Actuation", 29th Congress of International Council of the Aeronautical Sciences, St. Petersburg, Russia, September 7-12, 2014.

Wang, W., "Passive and active flow control studies using hybrid RANS/LES simulations, Thesis (PhD), The University of Sheffield, 2013.

Weier, T., Albretch, T., Gerbeth, G., Wittwer, S., Metzkes, H., Stiller, J., "The electromagnetically forced flow over a backward-facing step", 7th International Symposium on Turbulence and Shear Flow Phenomena (TSFP-7), Ottawa, Canada, 2011.

Weiss, J.M., Smith, W.A., "Preconditioning applied to variable and constant density flows", AIAA Journal, 33, 2050-2057, 1995.

Wilcox, D.C., "Turbulence Modelling for CFD" , 1998.

Xia, H., "Dynamic grid detached eddy simulation for synthetic jet flows." Thesis (PhD). The University of Sheffield, 2005.

Yakhot, V., Orszag, S. A., "Renormalization Group Analysis of Turbulence",. I Basic Theory, J. Sci. Comput. 1, 3-51, 1986

YAN Hao, LIU Yangwei1, FANG Le, LU Lipeng, "Modification of Spalart-Allmaras Turbulence Model for Predicting S825 Airfoil Aerodynamic Performance", Applied Mechanics and Materials Vols. 543-547 pp 189-194 (2014)

Yao, C-S., Lin, J. C., Allan, B. G., " Flowfield measurement of device-induced embedded streamwise vortex on a flat plate", AIAA Paper 2002-3162, 1st Flow Control Conference, St. Louis, MO, June 24-27, 2002.

Yokoyama, H., Tuskamoto, Y., Kato, C., Iida, A., "Self-sustained oscillations with acoustic feedback in flows over a backward-facing step with a small upstream step", Physics of Fluids **19**, 106104 (2007)

Yoshioka, S., Obi, S., Masuda, S., "Momentum transfer in the periodically perturbed turbulent separated flow over the Backward-facing step", *Proc. TSFP1 pp 1321-1326*, 1999.

Yoshioka, S., Obi, S., Masuda, S., "Organized vortex motion in periodically perturbed turbulent separated flow over a backward-facing step", *Int. Journal of Heat and Fluid Flow, Vol. 22, pp. 301-307*, 2001

You, D. and Moin, P., "A dynamic global-coefficient subgrid-scale eddy-viscosity model for large-eddy simulation in complex geometries", Physics of Fluids, 19, 065110, 2007.

Zulkefli, N. F., Tai, E. N., Mujeebu, M. A., Abdullah, M. Z., Ahmad, K. A., "Numerical and experimental investigations of passive flow control devices on a backward facing step", International Journal of Engineering and Technology 01/2009; 6(2):21-29.

Links and user guides

NASA, Driver and Seegmiller's data:
http://www.grc.nasa.gov/WWW/wind/valid/backstep/backstep01/bstepdata.txt

ANSYS 13 – FLUENT Tutorial Guide

Langley Research Centre, Turbulence Modelling: The Spalart-Allmaras model
http://turbmodels.larc.nasa.gov/spalart.html